LES Modelling of Wake Vortex Surfing for Formation Flight Applications

Chan Jia Cheng

xxxxxxxx

This thesis is submitted in fulfilment of the requirements for the Degree of Doctor of Philosophy

School of Engineering

College of Science and Engineering

University of Glasgow

April 2026

Acknowledgement

My sincere appreciation goes to Dr. Henrik Hesse and Dr. Victor Wang Peng Cheng for their invaluable supervision, guidance, and encouragement throughout the research journey. The intelligence, clarity of thought and analytical rigour demonstrated by Dr. Henrik in addressing research challenges, together with the dedication and strong research direction on CFD provided by Dr. Victor, has shaped the values I seek to uphold in my own work. Their combined expertise, patience, and high expectations have profoundly influenced both the development of this project and my growth as a researcher. Warm thanks are also extended to Dr. Kiran Ramesh, my secondary supervisor, for his constructive feedback and steady support thoughtful review of my research progress.

This research was conducted under the Industrial Postgraduate Programme (IPP), co-funded by the Economic Development Board of Singapore (EDB) and ST Engineering Aerospace Ltd. I gratefully appreciate for the scholarship and research funding for various conferences and training programmes. I would like to express sincere gratitude to Dr. Kenneth Low and Dr. James Tan for their industrial supervision, as well as for the valuable opportunities and experiences gained within the company. Appreciation is also conveyed to Ms. Lee Hui Fung, and Mr. Frederic Foo for their continual support, understanding, and the resources provided throughout the project.

Special thanks to Dr. Benjamin Tan Kin Jon for sharing his insights on the PhD journey, and for providing crash course to familiarise with OpenFOAM and Linux operating system. Extended acknowledgement to Dr. Lim Yau Shiang and Mr. Jeremy Lim from Singapore Institute of Technology for their facility and technical support during the wind tunnel experiments. Further appreciation to Dr. Stefanie Düssler and Mr. Ben Preston from Imperial College London for their technical advice and assistance with the SHARPy package.

Finally, heartfelt appreciation for my parents, Sing Hwa and Meng Chow, whose unwavering faith, encouragement, and belief in my path have carried me through every stage of this journey. To my wife, Vivian, thank you for your steadfast love, patience, and support. Your presence is the greatest blessing, and you have always been my greatest source of strength.

Abstract

The industry mission toward sustainable aviation has intensified interest in wake surfing operation as a potential method for reducing carbon emissions. Wingtip vortices constitute the fundamental aerodynamics mechanism governing the wake interactions between aircraft. However, the prediction of wake-vortex evolution over extended distances remains technically challenging due to the highly unsteady nature of vortical flows, which are sensitive to turbulence dissipation and inflow specification. This research investigates the characterisation, modelling, and efficient computational simulation of wingtip vortex behaviour, with specific emphasis on vortex surfing in extended longitudinal fields. A combined experimental-computational approach is adopted to address the challenges of accurately predicting vortex development over long distances at reduced computational cost.

A novel perspective upright correction technique for wind tunnel test is introduced to enable geometrically upright vortex images from a single camera positioned at arbitrary viewing angles. This method greatly simplifies experimental setup and improves the precision of wake-spiral characterisation. Experimental results reveal that the true vortex core may behave differently from the visible wake spiral, underscoring the importance of numerical analysis for vortex core characterisation.

To address the numerical characterisation, a Computational Fluid Dynamic (CFD) methodology is developed using OpenFOAM to resolve the wake vortex dynamics from the leading wing using Unsteady Reynolds-Averaged Navier-Stokes (URANS) and Large Eddy Simulation (LES) turbulence models. The CFD framework is constructed to capture the spiral morphology of the vortex core, the tangential velocity magnitudes, axial velocity deficits and downstream trajectory and evolution. The more recent formation flights have a substantial longitudinal separation of up to a few kilometres. Resolving the flight dynamics using LES is computationally prohibitive due to the vast spatial and temporal scales. For efficient simulation for repetitive upstream flow field over the extended flight formation, inlet conditioning framework was developed. The precursor method successfully transfers fully developed LES vortex inflow to a downstream main domain, retaining coherent turbulence with negligible dissipation. A complementary synthetic method, based on Fourier-series reconstruction of velocity fluctuations, demonstrates feasibility but encounters limitations within the vortex core where fluctuation behaviour is highly unstable.

In wake surfing simulations, the leading wing remains largely unaffected, whereas the trailing wing benefits substantially from the induced upwash. The optimal configuration identified in this study corresponds to a lateral overlap of approximately 10% wingspan at matched flight level, yielding a significant improvement in lift-to-drag ratio.

To further reduce the computational cost, the inflow conditions can be initialised through the combination of the mean vortex fields derived from the Unsteady Vortex Lattice Method (UVLM) and the turbulent fluctuations from the LESs. Although the UVLM tends to accelerate the vortex core growth, the simulation case may achieve the realistic vortex representation through a careful selection of the inlet plane from the UVLM.

Contents

List of Figures

List of Tables

Nomenclature

Latin

a	Local speed of sound; fluctuations amplitude
b	Wingspan, m
c	Wing chord, m
C_D	Drag coefficient
C_{D0}	Profile drag coefficient
C_{Di}	Induced drag coefficient
C_f	Friction coefficient
C_L	Lift coefficient
C_l	Rolling moment coefficient
C_p	Pressure coefficient
f	Frequency, Hz
i, j, k	Unit vectors
k	Turbulent kinetic energy
L	Lift, N
M	Mach number (u/a)
N	Number of grid points
P	Pressure, Pa
p	Static pressure, Pa; pre-peak exponent
R	Spatial correlation coefficients
Re	Reynolds number ($\rho uc/\mu$)
r	Radial coordinate (positive outwards)
S	Reference area
T	Integral time scale
t	Time, s
u	Velocity, ms^{-1}
x	Longitudinal coordinate (positive downstream)

y	Lateral coordinate (positive toward right wingtip)
z	Vertical coordinate (positive upward)

Greek

α	Angle-of-attack, °
β	Spatial oscillation wavenumber
Δ	Discretised grid size
θ	Polar angle
λ	Rate of spatial decay
ξ	Dimensionless vortex radial position
ρ	Density
σ	Variance
τ	Shear stress; stress tensor; time lag
ϕ	Phase lag
ω	Vorticity, s^{-1}
∂	Partial derivative operator

Sub- & Super-Scripts

’	Fluctuation component
ac	Aerodynamic centre
c	Chord-based
i, j, k	Index notation
Lam.	Laminar
max	Maximum
min	Minimum
ref	Reference
sgs	Sub-grid scale
syn	synthetic
rms	Root mean square
x, y, z	Components in the respective Cartesian directions
θ	Tangential based

∞	Freestream reference conditions

Abbreviations

AR	Aspect Ratio
ADS-B	Automatic Dependent Surveillance-Broadcast
AFF	Autonomous Formation Flight
AFRL	Air Force Research Lab
AFIT	Air Force Institute of Technology
AIAA	American Institute of Aeronautics and Astronautics
AoA	Angle of Attack
ATC	Air Traffic Control
AWSE	Air-Wake Surfing Efficiency
BW	Blended Winglet
CAD	Computer Aided Design
CAPFIRE	Cargo Aircraft Precision Formation for Increased Range and Efficiency
CFD	Computational Fluid Dynamics
CG	Centre-of-Gravity
CONOPS	Concept of Operations
CPU	Central Processing Unit
DARPA	Defence Advanced Research Projects Agency
DES	Detached Eddy Simulation
DLR	Deutsche Forschungsanstalt für Luft- und Raumfahrt
DNS	Direct Numerical Simulation
FL	Flight Level
IATA	International Air Transport Association
IC	Inlet Condition
ICAO	International Civil Aviation Organization
LDA	Laser Doppler Anemometry
LES	Large Eddy Simulation
LTS	Long Term Support
MMT	Million Metric Tons

MS	Main Simulation
NACA	National Advisory Committee for Aeronautics
NASA	National Aeronautics and Space Agency
NM	Nautical Miles
NW	No Winglet
OpenFOAM	Open-source Field Operation And Manipulation
PIV	Particle Image Velocimetry
PSP	Pressure Sensitive Paint
RANS	Reynolds-Averaged Navier Stokes
RAM	Random Access Memory
RH	Relative Humidity
RMS	Root Mean Square
RTA	Required Time of Arrival
RV	Rendez-vous
SA	Spalart-Allmaras
SACCON	Stability and Control Configuration
SATCOM	Satellite Communications
SAVE	Surfing Aircraft Vortices for Energy
SGS	Sub-Grid Scale
SSD	Solid State Drive
SST	Shear Stress Transport
TCAS	Traffic Alert and Collision Avoidance System
UAV	Unmanned Aerial Vehicle
URANS	Unsteady Reynolds-Averaged Navier-Stokes
USAFTPS	United States Air Force Test Pilot School
VLM	Vortex Lattice Method
UVLM	Unsteady Vortex Lattice Method
WER	Wake Energy Retrieval

Declarations

I hereby declare that, apart from the introductory material in Chapters 1 and 2, the work presented in this thesis represents my own original research. It has not been submitted in whole or in part for any other academic award. Any ideas, data, or quotations derived from the work of others are fully acknowledged and appropriately referenced.

Jia Cheng CHAN

Chapter 1

Introduction

Commercial aerospace remains a major contributor to global carbon emissions, with nearly 39 million flights recorded in 2018 [1], and an associated 918 million metric tons (MMT) of CO_2. This amount equates to approximately 2.4% of global emissions from fossil fuel consumption, an astonishing rise of 32% in just five years. This emissions growth rate is almost 70% greater than the current ICAO forecasts. Slightly more than 80% of the emission is contributed by passenger aircraft. The greenhouse gas emissions from commercial aviation are expected to triple by 2050 under the trajectory of its rapid growth [2], potentially accounting for 25% of the global carbon budget.

The Covid-19 pandemic severely disrupted the growing number of flights. However, the air traffic has rebounded to pre-pandemic levels in 2024 [3] and expected to sustain a long-term growth. Both Airbus [4] and Boeing [5] predict the global aircraft fleet to be doubled from now to 2040, driven by rising passenger and logistics demand and expanded air transport networks. This rapid growth will inevitably result in denser air traffic and increased greenhouse gases emissions, which stands in contrast to the commitments of aviation sector to achieve net-zero carbon emissions by 2050 [6] to meet the sustainability goal set by ICAO.

In achieving the sustainability targets, the industry must pursue strategies that significantly enhance aerodynamic and fuel efficiency without imposing substantial cost increases on operators or passengers. One promising concept is formation flight [7, 8] by wake vortex surfing [9, 10], in which a trailing aircraft positions itself within the beneficial upwash generated by the wingtip vortices of a leading aircraft. By exploiting this induced upwash, the trailing aircraft can reduce lift-induced drag and achieve measurable fuel savings.

However, practical implementation of formation flight requires accurately predicting the location, strength, and evolution of the wake vortex system to identify the optimal “sweet spot” for maximum aerodynamic benefit. Both experimental investigations [11] and computational studies [8, 12] have examined vortex dynamics, core trajectory, and decay behaviour to better characterise the flow environment encountered by a trailing aircraft. These insights continue to motivate deeper investigation into wake vortex physics, including turbulence modelling, inflow specification using high-fidelity simulations for a more efficient yet accurate formation flight aerodynamics estimations.

1.1 Vortex Surfing

A classic example of vortex surfing is observed in long-distance migratory birds. More than a century ago, aerodynamics pioneers observed and documented the migratory birds flying in a V-shaped formation and investigated how the formation improves flight efficiency. Wieselsberger [13] was one of the first to demonstrate this notion in a proper setting. A flock is typically organised into a V-shaped formation led by a strong head bird as shown in Figure 1.1. The trailing birds then position themselves to intercept the upwash generated by the wingtip vortices of the bird ahead, thereby gaining additional lift force and reduce the energy exerted. This aerodynamic advantage is propagated throughout the formation, enabling the flock to travel significantly more efficient, for additional mileage with the same amount of energy. Wieselsberger formalise the vortex surfing concept by applying the Prandtl's lifting line theory to represent three birds in a V formation flight. The analysis demonstrated that trailing birds benefiting from the updraft from the leading bird's trailing vortices. Each bird in the V formation would also experience approximate equipartition of drag resulting in lesser induced drag. However, the estimated power savings were later shown to be conservative due to methodological simplifications.

Figure 1.1 Migratory birds in V formation.

Subsequent studies refined these aerodynamic estimates for the flock formation. By applying standard unsteady wing theory, Lissaman and Shollenberger [14] reported that a three-bird formation could achieve approximately 26% power savings, with potential range increases up to 71% as more birds join the formation. Hummel [15, 16] further examined drag reduction for trailing birds in arbitrary position of varying weight and aspect ratio. The author discovered that lateral wing spacing has the greatest impact on the overall flight power reduction and that lighter birds gain proportionally more benefit from the upwash generated by larger, heavier leading bird.

Based on field observations, Hainsworth [17, 18, 19] reported that some Canadian Geese flew with wingtips overlapped, which can achieve an optimum power saving of 35%. This has violated

Lissaman's theory [14] of maximum savings in a line abreast formation with zero wing tip spacing. Years later, Cutts and Speakman [20] studied on pink-footed geese that always fly outboard of the ideal position and reported that the geese achieved a 14% of power savings induced from the flock. The values are similar to Weimerskirch et al.'s research [21], reported 11.4% to 14.5% heart rate reduction for imprinted white pelicans flying in formation. These deviations from ideal positioning suggest that birds may prioritise positional stability and reduced control effort over strictly maximising aerodynamic benefit. The consistent evidence that formation flight yields meaningful energetic advantages provides a compelling foundation for analogous strategies in aviation, where exploiting wake-induced upwash could contribute to reduced fuel consumption, extended range, and lower greenhouse-gas emissions.

1.2 Formation Flight

Inspired by the energy-saving mechanisms observed in migratory birds, powered flight began to explore the possibilities of formation flight as early as the mid-20th century [16, 22, 23]. As illustrated in Figure 1.2, the updraft of the vortices produced by the leading aircraft's wingtip causes a forward rotation of the lift vector to the trailing aircraft, resulting in a smaller angle of attack and induced drag [24]. The trailing aircraft in the formation flight can therefore exploit the whirlwinds of turbulence produced by leading aircraft in achieving reduction in induced drag and better fuel flow savings. The potential to achieve advantageous aerodynamic effects without making significant changes to existing aircraft makes the formation flight operations particularly attractive.

Figure 1.2 Aircraft on vortex surfing [25].

Similar principle as the migratory birds, the aircraft formation flight incorporates a leading aircraft and one or more trailing aircraft. The formation spacing is usually defined in terms of the leading aircraft wingspan b, or wing chord c. The longitudinal displacement, x/b denotes the streamwise distance between the trailing aircraft's nose to the leading aircraft's nose (see Figure 1.3b & Figure 1.3c). For instance, an $x/b = 20$ indicates that the trailing aircraft is flying at a distance 20 wingspans down the stream aft the leading aircraft.

The lateral spacing, y/b is defined as the lateral distance between the leading aircraft's starboard wingtip to the trailing aircraft port's wingtip or vice versa (see Figure 1.3a & Figure 1.3c). A negative value of y/b indicates the aircraft wing is overlapping with each other and a zero value means the wingtip of the aircraft are aligned.

Finally, the vertical offset, z/b represents the relative altitude of the trailing aircraft with respect to the leading aircraft (see Figure 1.3a & Figure 1.3b). As the pair of counter-rotating vortices shed by the leading aircraft induce a downward drift on the trajectory of vortices over streamwise distance or time [26], the z/b position would mostly a negative value where the trailing aircraft positioned below the flight path altitude of leading aircraft.

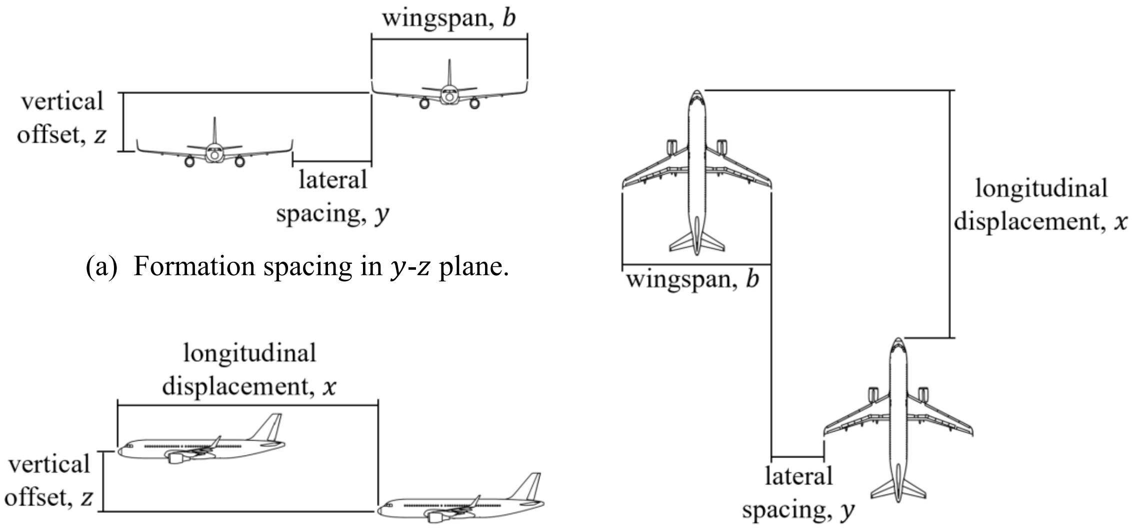

(a) Formation spacing in y-z plane.

(b) Formation spacing in x-z plane.

(c) Formation spacing in x-y plane.

Figure 1.3 Overview of formations in different direction.

During vortex surfing, the imbalanced inflow (see Figure 1.2) will also cause a rolling moment on the trailing aircraft. This must be counteracted with appropriate aileron and rudder deflections [9]. The strength of the rolling moment varies strongly with the relative position to the leading aircraft or in the wake. There may be areas where the rolling moment exceeded the aircraft's compensation capabilities and must therefore be avoided. In real world, the leading and trailing aircraft in a formation are likely to be of different model, size, aerodynamic characteristics and performance. Table 1.1 presents several formation configurations involving varied aircraft counts and types. Such permutations create a numerous possible formation strategy. Consequently, a trailing aircraft may fly slightly offset from the theoretically optimal energy-saving position in exchange for a more flexible handling requirements and reduced pilot or control-system workload.

Table 1.1 Formation configurations [26].

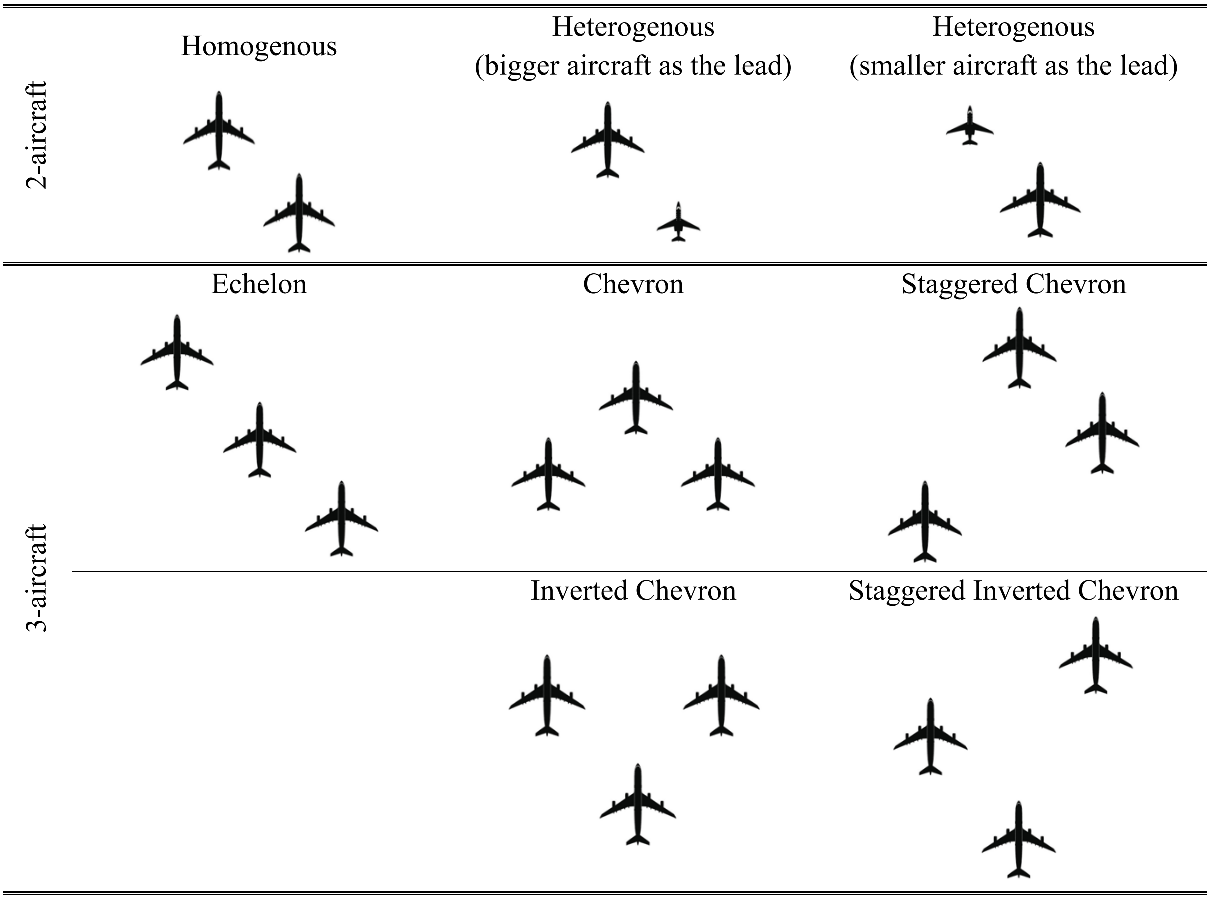

Over the past few decades, several institutes, organisations and aerospace companies have undertaken flight test programs to investigate the aerodynamic benefits and operational feasibility of the vortex surfing technique in formation flight. These efforts span a progressive evolution, from early research focused on military fighter aircraft in close formations and the flight test, later progressed to transport aircraft in extended formations of thousands of feet of longitudinal separations. With higher confidence and technological readiness level, the flight demonstrations eventually leading to commercial passenger aircraft.

One of the earlies documented formation flight tests effort was conducted by the Deutsche Forschungsanstalt für Luft- und Raumfahrt (DLR) in 1996 with Do-228 and Do-28 fighter jet [15]. Subsequently in 2001, NASA launched the Autonomous Formation Flight (AFF) program [27] to have an in-depth investigation of the air-wake surfing efficiency (AWSE) with F/A-18 airplanes [28]. The United States Air Force Test Pilot School (USAF TPS) also performed flight tests [29] to validate the tight formation performance of T-38 Talon aircraft calculated by the Air Force Institute of Technology (AFIT) [30]. A few years later, The USAF TPS again conducted homogenous formation flight tests using F-16 aircraft [31], followed by a heterogenous formation of F-16 led by KC-135. These formation flight tests were carried out in a relatively close proximity, of which the maximum longitudinal displacement is merely $x/b = 4.2$. Please refer to Table 1.2 for the summarised flight tests information such as formation spacing and fuel savings metrics.

To extend the use of vortex surfing to transport aircraft with a operationally meaningful streamwise spacing, NASA incorporated with the U.S. Air Force in 2010 [32] and initiated the project Cargo Aircraft Precision Formation for Increased Range and Efficiency (CAPFIRE) employing C-17 transport aircraft. Two years later, the U.S. Air Force Research Lab (AFRL) and Defence Advanced Research Projects Agency (DARPA) have established a new program called Surfing Aircraft Vortices for Energy (SAVE) [33, 34]. This program conducted the same formation flight concept as CAPFIRE but with a substantially longer longitudinal separation, of 4,000 – 8,000 feet. The relevant flight test information including the speed and altitude is provided in Table 1.2.

Table 1.2 Summary of the formation flight projects.

Year	Project	Aircraft		Alt. (feet)	Speed (knots)	Spacing			Fuel Savings
		Lead	Trail			x/b	y/b	z/b	
1996	DLR	Do-228	Do-28	-	-	3	≈ 0	-	15% – manual flight 10% -– feedback controller
2001	NASA, USAF	F/A-18	F/A-18	-	-	< 4.2	-0.2 – -0.1	-0.1 – 0	18%
2001	AFIT	T-38 Talon	T-38 Talon	10,000	360	3	0.86	-	1st trailing a/c – 15% drag / 13.8% fuel 2nd trailing a/c – 17.5% drag savings
2004	USAF TPS	F-16	F-16	-	300	3	-0.135	-	16%
				-	210			-	34%
2004	USAF TPS	KC-135	F-16	-	300	< 4.2	-0.167	-	26%
2010	CAPFIRE – NASA, USAF	C-17	C-17	25,000	275	5.9 – 17.7	-0.3 – 0.1	0 – 0.4	7% – 8%
2012	SAVE – AFRL, DARPA	C-17	C-17	30,000	500	21 – 42	-0.135	-	5% – 10%
2018	Boeing	C-17	B777F	28,000 – 39,000 *	450 – 500 *	-	<0.7	-	4% – 6%
present	fello'fly – Airbus	A350	A350	35,000 – 41,500 *	488 – 513 *	43 – 57	0.25 – 0.5	-0.5 – -0.25	≈ 5%

** Based on cruising conditions values, as information not provided*

Leveraging the extensive C-17 flight test datasets produced from the SAVE program, Boeing initiated further flight tests involving a C-17 as the leading aircraft, followed by a B777 aircraft [35] to validate the fuel savings at different test points based on the in-house CFD calculations, which is in the range of 4% - 6%. Boeing [36] also advanced on the Traffic Alert and Collision Avoidance System (TCAS) software and evaluated the effectiveness of an ADS-B-based wake prediction to enable SAVE operations and formation flight capabilities across multiple aircraft platforms. Two Boeing 777F aircraft were flown in formation to assess the accuracy of the ADS-B-derived wake position estimates and to verify the station-keeping performance in proximity to the wake. The flight test results showed highly accurate lateral wake localisation which validated the pre-flight modelling estimation.

Most recently, Airbus has conducted considerable efforts in advancing vortex surfing research and operations through the Wake Energy Retrieval (WER) program [37] to reduce aviation emissions. As part of this initiative, Airbus organised the fello'fly flight demonstrations [37, 38] in 2020 and 2021 in collaboration with Frenchbee, SAS, DSNA, NATS and EUROCONTROL. The campaign involved two A350 aircraft – MSN1 as the leader and MSN59 as the follower, flying from Toulouse, France to Montreal, Canada under a set of operational procedure. The trials have achieved more than six tonnes of CO_2 reduction on a single transatlantic mission, corresponding to fuel savings of over 5% for long haul flights. The practical test also proved that the WER in an operational environment is viable with appropriate procedures and regulations.

Airbus has published the concepts of operations (CONOPS) [38] of WER after the success of the fello'fly demonstrations. As shown in Figure 1.4, the CONOPS outlined the sequence of operational stages, namely pre-departure, post-departure pairing callout, rendezvous, separation responsibility transfer, join-up, formation keeping and separation.

During the pre-departure phase, the pairing assistance tool (PAT) evaluates flight plans and identifies the most beneficial pairing configurations. Upon airborne, both aircraft must pre-position on the same track with the support and supervision from ATC. The follower aircraft must be initially positioned 1,000 feet lower than the leading aircraft in Flight Level (FL). The follower aircraft must also remain laterally outside of the vortex upwash region at this stage. After occupying the so-called "pre-OPTI position", the follower aircraft then accelerates to catch-up with the leading aircraft until the longitudinal separation of 1.5 -2.0 NM is achieved.

At this point of formation setting, the rendezvous phase is completed, and the pair of aircraft will now be communicated within themselves and the responsibility for managing their formation spacing is now transferred from the ATC to the pilots. The pair formation will be treated as one flight entity in the airspace and only reported to the ATC by the leading pilots. The follower aircraft can now slowly and safely manoeuvre itself laterally and vertically into the updraft region of the leading aircraft's wake, which is the "OPTI position" for WER operations. The typical OPTI position for the follower aircraft will be marginally outboard of the leading aircraft (60 – 100 feet) and slightly below the leading aircraft's altitude (50 – 100 feet). The WER formation will be maintained throughout the cruising until the track diverges or one of the aircraft needs to descend when approaching the destination. In such cases, the follower aircraft will move to the pre-OPTI position and further move to the empty space below the formation FL. This will split the paired formation into two individual aircraft that report to the ATC who will coordinate with both aircraft independently for the rest of the flight and landing.

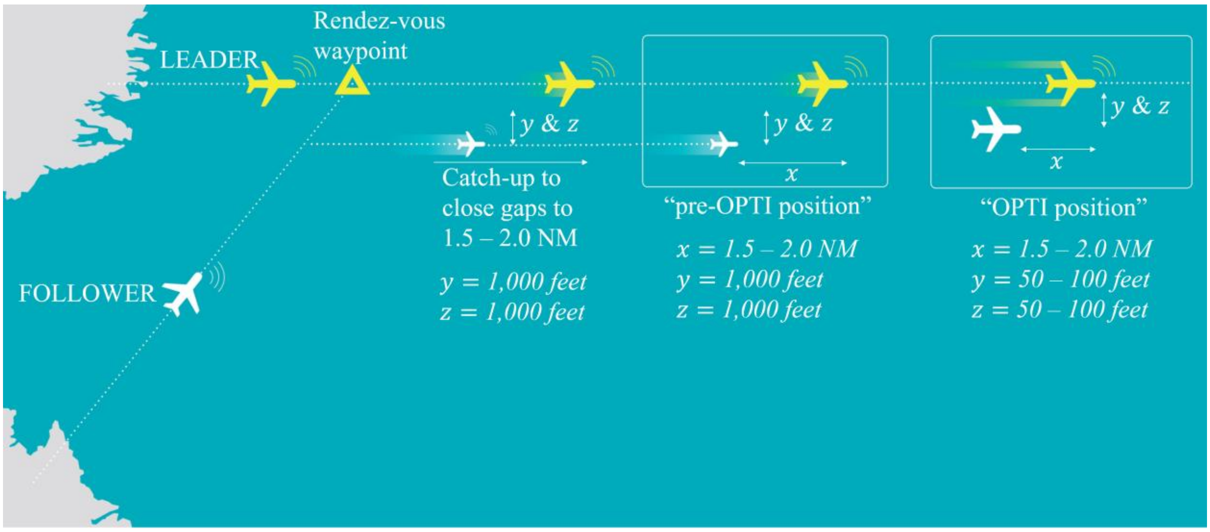

Figure 1.4 Airbus 'fello fly' concept of operations [38].

To sum up, wake vortex surfing remains in the early stages of commercialisation and operational deployment. Its potential benefits including enhanced flight endurance, extended range, increased payload capacity, tighter airspace utilisation, improved fuel efficiency, reduced emissions and climate impact are well recognised [26]. Theoretically, the execution of vortex surfing is possible with the current available technology, but operational reliability and robustness remain key challenges. In particular, a more accurate prediction of wingtip vortex behaviour and a deeper understanding of its aerodynamic influence on the trailing aircraft are required in achieving consistent and safe performance. Consequently, high fidelity CFD studies and complementary experimental or modelling efforts are essential to strengthen confidence in the system, support certification pathways and enable reliable large-scale implementation.

1.3 Wingtip Vortices

To generate lift force that can keep an airplane aloft, the airplane wings are designed in such a way that when fluid moves over it, the fluid accelerates over the upper surface relative to the lower surface. The acceleration of fluid movement creates a lower pressure on the upper surface of the wing compared to the lower surface, creating a net upward lifting force that increases exponentially with the local velocity. However, the pressure differential also induces spanwise flow. The flow on the lower (pressure) surface tends to slip outboard toward the wingtips, while flow on the upper (suction) surface moves inboard toward the wing root. This spanwise movement contributes to the formation of wingtip vortices, as illustrated in Figure 1.5.

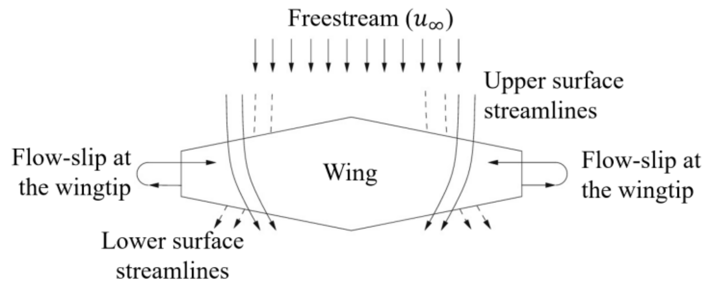

Figure 1.5 Front and top view of the wingtip vortices flow pattern [39].

When the airflow accelerates over the wing, the resulting adverse pressure gradient will eventually lead to the boundary layer separation and the formation of inwards rotating airflows, also known as wingtip or trailing vortices [40]. The vortices can exhibit a crossflow velocity of up to $100m/s$ in the core region [41]. Between the two counter-rotating vortices, a downward component of flow-field velocity is induced while the flow-field outboard of the vortex core is moving upward, as illustrated in Figure 1.6.

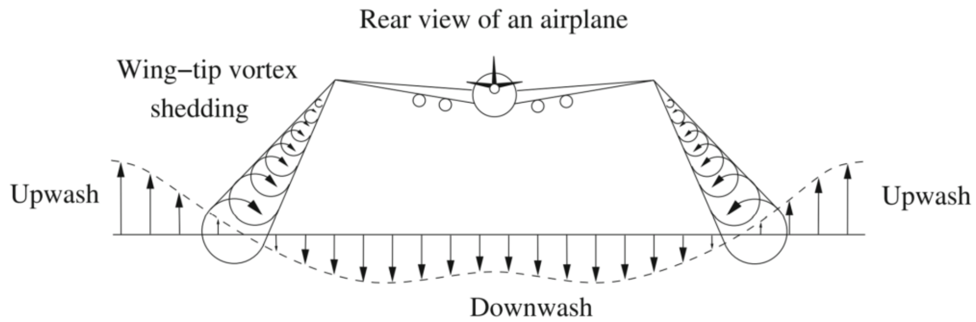

Figure 1.6 Wingtip vortex shedding with upwash and downwash field [39].

The formation and development of wingtip vortices can be divided into four regions as illustrated in Figure 1.7. The wake shed from the generating wing is experiencing the roll-up process in the near field, and it will develop and form into vortices with strong vorticity in the extended near field. This region is where the close formation flight performed by the fighter jet aircraft mentioned in Section 1.2. The trailing vortices will continue to grow in size but reduce in strength at a very slow rate in the mid and far field regions. This flow field can persist for a very long distance, of up to $x/b = 100$ in the downstream. In vast majority of the commercial formation flight projects, the follower aircraft is flying in this region for the vortex surfing effect. It is postulated the mid/far field have a bigger range of beneficial region with lesser rolling impact for the aircraft to ride on. The aerodynamic gains are compromised as compared to the extended near field, but with improved safety and comfort. Thereafter, the vortices enter the decay region where the strength diminishes, and the wake vortex dissipates rapidly.

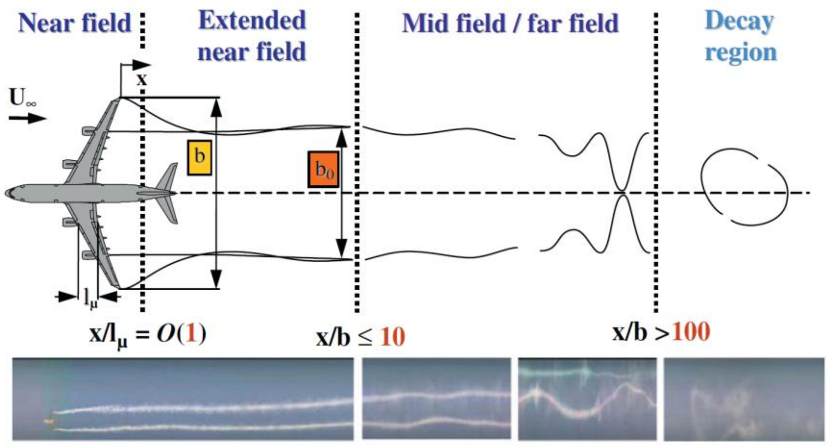

Figure 1.7 Stages of wake vortex lifespan [41].

Before the wingtip vortices decay substantially, the velocity gradient between the upwash and downwash can cause structural stress or even failure to any aircraft flying across it as shown in Figure 1.8. In addition, the downwash and the vortices can pose loss of lift and unsteady roll to the following aircraft. This situation can constitute a major hazard, especially during take-off and landing. According to Lamb's vortex model estimation [42], the wake vortices would take much longer than three minutes for the wake to decay to a safe level, this translates to about six to nine NM at landing velocity. To avoid such wake encounters, regulations require aircraft to maintain a certain distances behind each other during cruising and set time intervals to allow the vortices to decay to a safe level for landings and take-offs.

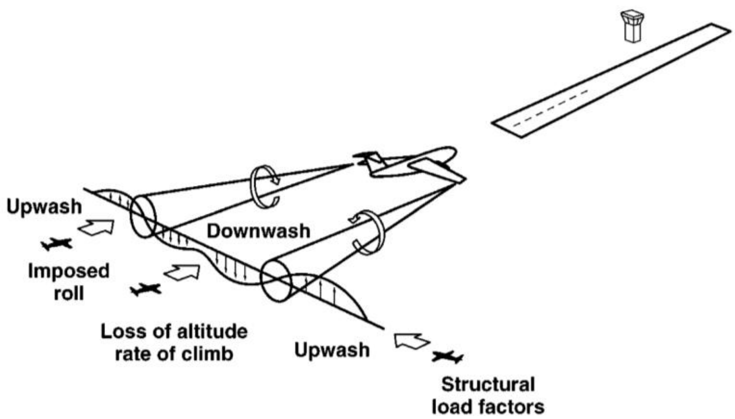

Figure 1.8 Aircraft encountering wingtip vortices [43].

Wingtip vortices also generate additional drag to the aircraft, known as induced drag. The industry has designed various wingtip devices to increase the effective wingspan, optimise the lift distribution and mitigate the unwanted induced drag [44]. The few well-known winglet designs included blended winglets, wingtip fences and raked wingtips [45]. Blended winglet is attached to the wing tip with smooth transition curve which reduce the aerodynamic interference at the joint [46]. Wingtip fence on the other hand extends in upward and downward from the wingtip. The raked wingtip is a newer design which featuring a continuous blended tip section with a higher sweptback angle than the rest of the wing. This design can be found on the most recent commercial aircraft, such as Boeing 787 Dreamliner and Airbus A350.

Even with the most effective wingtip devices, the trailing vortices can persist for several wingspans downstream and create abrupt changes in the flow field that may pose hazards to other aircraft. However, these vortices also present an opportunity for wake surfing where trailing aircraft deliberately position themselves within the upwash region to reduce induced drag and save fuel. Wake surfing is primarily conducted during the cruising phase, when aircraft maintain a clean, level-wing configuration with the angle of attack equal to the angle of incidence. This configuration reduces uncertainties in vortex generation, yet a detailed understanding of wake strength, spatial decay, and downstream evolution remains essential. Thorough characterisation of vortex formation and development is therefore critical for safely and effectively exploiting the aerodynamic benefits of the upwash region.

1.4 Wake Vortices Characterisation and Modelling

The fundamentals of wake vortices have traditionally been investigated using experimental studies and theoretical interpretations. The typical experimental techniques include wind tunnel testing and in-flight measurements [47]. Whereas the foundational mathematical principle is based on Lanchester-Prandtl lifting line theory [39], which subsequently derives to methods such as the Unsteady Vortex Lattice Method (UVLM) [48]. Improved understanding of airflow dynamics has enabled the verifications of theoretical hypothesised fluid dynamics formulations, which lead to renowned viscous flow theories such as the Navier-Stokes equations [49]. The development of Computational Fluid Dynamics (CFD) has further facilitated the numerical solutions of these complex and iterative equations [50]. CFD can provide reliable results given the mesh and solver are appropriately configured, but the uncertainties in accuracy of the results still exist in certain cases. Hence, it is necessary to conduct validation and verification on CFD baseline setup against experimental or published theoretical data before proceeding with simulation case variations. In short, CFD should be viewed as a complementary tool rather than a replacement for other experimental and theoretical methodologies.

1.4.1 Experimental Methods for Characterisation

There are a few experimental methods for visualisation, characterisation, and quantification of wingtip vortices. One approach is by observing the exhaust condensation wakes in flight test. Scorer and Davenport [51] investigated on the wake vortex dynamics and presented that the exhaust from aircraft engines would condense at low temperature ($< -40°C$) and persist when the relative humidity (RH) level is above 30% [52]. It is postulated that the aerodynamic feature of the wake is effectively represented by the condensation trails, as only a negligible amount of the total energy is consumed for the condensation production, and the atmospheric conditions are largely the same.

Another common experimental method for vortex research is wind tunnel testing [53]. It is an established experimental method that enables controlled visualisation, characterisation, and quantification of wingtip vortices. It is also highly reliable for capturing the irregular features of the turbulent wingtip vortices. There are several common techniques to experimentally characterise wingtip vortices, including Laser Doppler Velocimetry (LDV), Laser Doppler Anemometry (LDA) and Particle Image Velocimetry (PIV). Despite the differences in technology, these methods are typically based on the similar working principle [54]. Smoke, dye, or any other form of particulate is introduced at the inlet of the wind tunnel test section, and a laser sheet will illuminate at a plane of interest to track the movement of fluid particles and quantify the vortex properties. Different techniques [55-59] are then used to measure and characterise the vortices at the plane.

Sohn and Chang [55] conducted a low-speed wind tunnel experiment using a three-component PIV system to capture the formation and structure characteristics of wingtip vortices at different angles of attack and wingtip configurations, with multiple camera viewing angles. Bhagwat et al. [56] also utilised a stereoscopic PIV system to measure the aerodynamic loading of a wing under an influence of another wing-vortex wake system. Panagiotou et al. [57] presented a 3D LDA point measurement system to investigate the velocities, vorticity, and circulation quantity of the trailing vortices over different designs of Unmanned Aerial Vehicles (UAVs) at different angles of attack. More recently, Nagarathinam et al. [58] demonstrated the use of LDV to measure the mean streamwise velocity and the root-mean square of their fluctuations. Collectively, these studies demonstrated that wind tunnel testing combined with advanced flow visualisation techniques can effectively capture the trailing vortices.

However, the mentioned systems come at a cost in terms of required time, budget, and infrastructure. Serrano-Aguilera et al. [59] proposed a cost-effective alternative using a smoke wire technique with a single digital camera. The wingtip vortex is illuminated by a laser-sheet, and it is captured through the reflections from a tilted mirror behind the wing, as shown in Figure 1.9. This method and system have greatly reduced the cost compared to LDA or PIV, but the precise calibration of the camera and mirror in the downstream may be challenging and unattainable for some wind tunnel facilities.

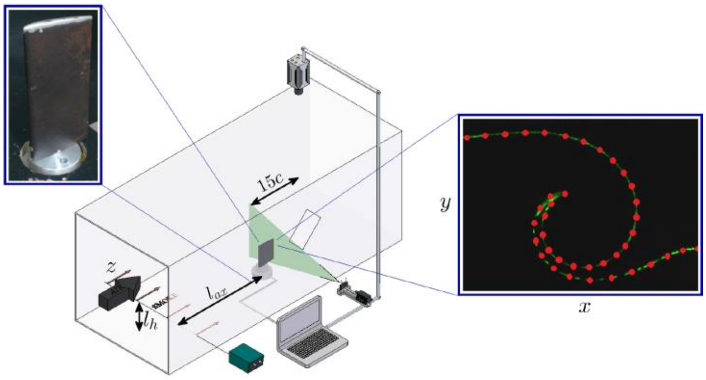

Figure 1.9 Wind tunnel setup with laser sheet, and camera [59].

Hence, a novel methodology for perspective upright correction (PUC) is proposed and demonstrated for experimental wind tunnel testing in Chapter 2, detailing the wind tunnel setup, including the placement of the laser plane and the camera, and the post-processing procedure that corrects for slanted views of the vortex plane. This approach allows a single camera to be positioned anywhere in the test domain with minimal alignment and calibration effort. By accurately capturing vortex evolution, this method provides clearer insight into the wake structure, facilitating the determination of optimal trailing aircraft positions for formation flight or vortex surfing applications.

1.4.2 Numerical Modelling

Despite the high reliability of the wind tunnel test in characterising the wingtip vortex, it is limited by a finite test section length, restricting the study of wingtip vortices development only in the near field region of limited chord lengths downstream effectively. Hence, numerical methods such as Computational Fluid Dynamics (CFD) or Unsteady Vortex Lattice Method (UVLM) emerge as alternative to complement the wind tunnel test in examining the evolution of wingtip vortices in the extended field and beyond.

CFD is a numerical methodology that simulates the fluid dynamics condition by solving the governing equations with the computational power. CFD techniques are now often used in engineering industry such as aerospace, turbomachinery, automobiles, and marine. It has become an increasingly important design tool in engineering, as well as a significant research tool in some physical sciences studies. It is relatively inexpensive, and the costs are expected to be lowered as the computers get more powerful. Furthermore, CFD [60] allows to examine any location in the region of interest and interpret its performance through a set of thermal and flow parameters, whereas experiments only permit data to be extracted at a limited location in the system where sensors and gauges are placed. In addition, CFD allows great control over the physical process, and provides the ability to isolate specific phenomena for study. After validating with published experimental results, the accuracy of the proposed turbulence modelling CFD framework will be evaluated in formation flight scenarios.

While CFD is required to accurately resolve the wake vortex turbulence, its computational requirements may become too costly for formation flight in extended domain. For such simulations, a reduced-order model is advantageous to provide a rapid estimation of the mean flow field. The Unsteady Vortex Lattice Method (UVLM) is a lower fidelity numerical tool that models the wingtip vortices more efficiently compared to the CFD methods due to its advantage of relatively ease in solving Laplace's equation. It provides a simplified approach that significantly reduces computational cost and time, making it a more practical choice for cases where high fidelity is not critical, but efficiency is prioritised. The essential vortex characteristics modelled by UVLM will be ported over to a CFD simulation at a further downstream position to offer an early-stage analysis on the vortex surfing effect.

1.4.2.1 Reynolds-Averaged Navier-Stokes (RANS)

The most widely used CFD turbulence modelling approach is the Reynolds-Averaged Navier-Stokes (RANS) framework. RANS averages the overall small-scale fluctuations and model the non-linear influence from the small-scale fluctuations, in the governing equations, that can alter the large-scale fluid motion [61]. The commonly used turbulence models include k-epsilon (k-ε) model, k-omega (k-ω) model, and Spalart-Allmaras. k-ε turbulence is a two-equation model to compute the turbulent velocity and length scales, respectively, with a relatively quicker calculation time. The drawback of k-ε is that it only valid for the fully developed turbulence region and not accurate in the near-wall area. k-ω turbulence model incorporates modifications for low-Reynolds number effects, compressibility, and shear flow spreading. It can predict free shear flow spreading rates for far wakes in close agreement with measurements and is thus applicable to wall-bounded flows and free shear flows. k-ω model has been further developed to refine the formulation in the near-wall region with the free stream independence of the far field. This shear stress transport (*SST*) model can predict more variety of flows with higher accuracy and reliability.

1.4.2.2 Large Eddy Simulation (LES)

A large eddy simulation (LES) method relies on the spatial filtering of the turbulence energy to directly resolve both the near-wall boundary layers and massively separated flows. LES is more promising in capturing and solving the vortex shedding, flow recirculation and critical unsteady flow structures, and the solution is more representative of the entire vortex flow field [61]. However, the requirement for a highly defined mesh grid size and time step significantly increases the computational cost, making LES prohibitive without access to high-performance computing resources.

The superior capability of LES in resolving the large-scale turbulent structures and vortex dynamics in the downstream has been combined with the RANS model for near-wall regions in large aerodynamic domains, leading to the development of the Detached Eddy Simulation (DES) [62]. In DES, all the near wall boundary layers are resolved by RANS to achieve adequate solutions with higher computational efficiency. This is appropriate as long as the streamwise pressure gradient remains small, but for flows with substantial adverse pressure gradients that could eventually lead to separation and the downstream vortices, the predictive accuracy of the models usually degrades [63]. Hence, the separated regions (detached eddies) are assigned to LES, which is able to reproduce the massive turbulence with much higher accuracy and to predict the vortex shedding and flow recirculation accurately [61].

In Chapter 3, the author will first validate the performance of LES model with different unsteady RANS turbulence models in capturing the persistent vortex mechanism in the downstream for wingtip vortex prediction. The most accurate model will be implemented in the wake vortex surfing cases to investigate aerodynamic effects and determine the optimal position of the leading-trailing wing in vortex surfing formation. The same framework [8] will also be used to validate against the wind tunnel experimental results [11], aiming to compare the near field vortex behaviour observed in the wind tunnel test, particularly the wake spiral contour characterised by the smoke particles.

1.4.2.3 Unsteady Vortex Lattice Method (UVLM)

The Lanchester-Prandtl lifting line theory [39] described the mechanism of trailing vortices in the lift generating process by resembling a finite wing with an endless number of horseshoe vortices allocating across the line of aerodynamic centre throughout the entire wingspan, as shown in Figure 1.10. Each horseshoe vortex consists of a bound segment along the lifting line and trailing vortex legs extending downstream, collectively capturing the essential behaviour of a finite wing and the induced downwash.

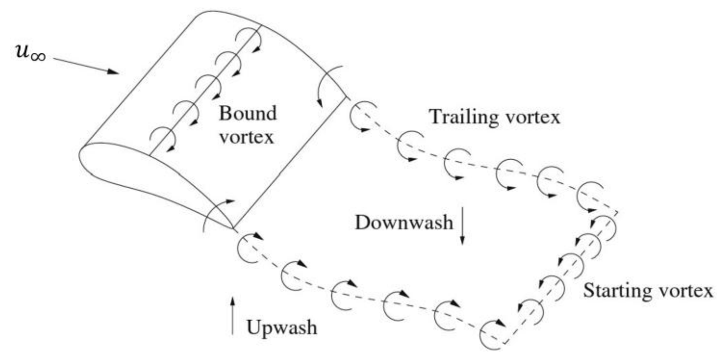

Figure 1.10 Horseshoe Vortex Model [39].

Building on the lifting line theory, the unsteady vortex lattice method (UVLM) [64, 65] utilised a lattice of horseshoe vortices across a lifting surface such as the aircraft wing. UVLM treats the lifting surface as an infinitesimally thin sheet and neglects aerofoil thickness effects, assuming the flow to be inviscid, incompressible, and irrotational. Small-angle assumptions are typically applied to both the angle of attack and sideslip angle [66, 67]. As shown in Figure 1.11, the cambered lifting surface is discretised into quadrilateral panels and the induced velocities at each control point are computed using Biot-Savart law This formulation provides an efficient means to estimate unsteady aerodynamic loads and the evolution of trailing vortices with significantly lower computational cost compared to high-fidelity CFD approaches.

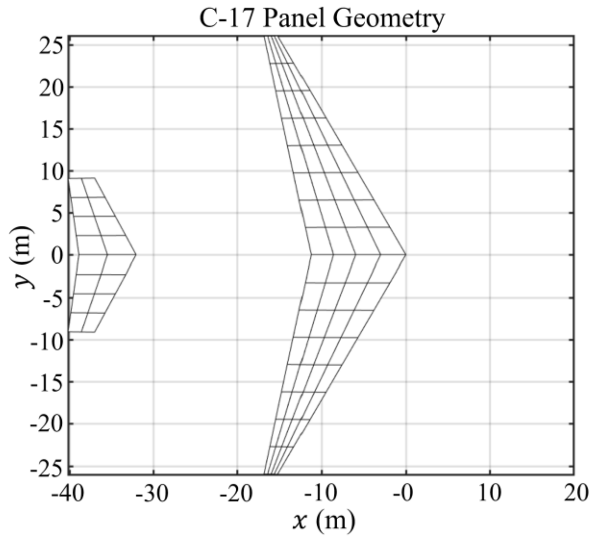

Figure 1.11 Panel geometry and distribution for C-17 aircraft lifting surface [24].

Fleischmann and Lone [24] performed a parametric study using an UVLM program to replicate the SAVE flight test formation with two simplified Boeing C-17 aircraft lifting surfaces geometry. The trailing aircraft in the study is 1250m behind the leading aircraft. Tens of thousands of wake vortex panels over hundreds of time steps were implemented to derive the drag reduction and the fuel consumption savings on the follower aircraft. As illustrated in Figure 1.12, the calculated data is plotted on y-z plane and superimposed against the actual flight test result. The model under-predicted the magnitude of measured savings, but the spatial contour of the fuel reduction map is in general agreement and with reasonable fidelity.

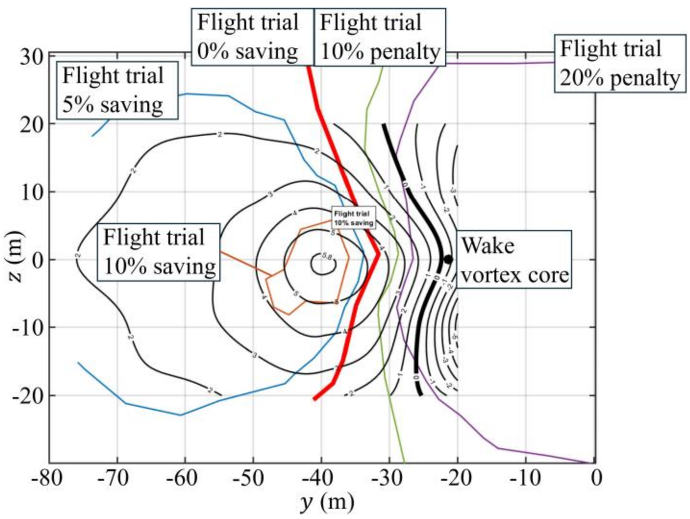

Figure 1.12 Follower aircraft fuel savings percentage predicted in the parametric study (black) vs. SAVE flight trials (colour), in 1,250m longitudinal separation from leading aircraft [24].

In Appendix A, UVLM as a lower order modelling will be used to generate the initial wingtip vortices. The mean flow-field data from UVLM will then be combined with the turbulent fluctuations from the LES at a later stage as the inlet mapping boundary conditions for the main simulation.

1.4.2.4 Applications of Numerical Modelling

Over the past few decades, CFD simulations [68-72] have been conducted to investigate the optimal positioning of trailing aircraft and associated aerodynamics implications in formation flight. With the available data from SAVE program, Halaas et al. [68] employed Reynolds-Averaged Navier Stokes (RANS) for the C-17 formation simulations, incorporating the follower aircraft trim conditions and validated mean wake dynamics against flight test data with 95% confidence on the wake dynamics. Singh et al. [69] used multi-fidelity simulations including Vortex Lattice Method (VLM) and RANS for close tandem UAVs formation flight. Both models predict the same location of minimum drag and maximum lift, but RANS is more accurate in the lift and drag calculation, with a smaller deviation from the experimental results. Similarly, Zhang et al. [70] applied RANS to determine the optimal lateral spacing, vertical distance and the optimum formation of simplified tailless delta wing UAVs in the close formation flight. Whereas Vechtel et al. [71] used Large Eddy Simulation (LES) to generate vortex flow fields with small perturbations of the vortex lines, which is a more representative flow field for real formation flight conditions.

These studies indicate that RANS turbulence models remain the most common choice for formation flight due to its computational efficiency. However, the predictive accuracy of RANS often degrades for downstream vortices or flows with substantial adverse pressure gradients [63]. On the other hand, LES [61, 72] model which relies on the spatial filtering of turbulence energy, can reproduce the massive turbulence with a much higher accuracy and predict the vortex shedding and flow recirculation more accurately.

1.5 CFD Inlet Boundary Conditions

As the vortex surfing formation is developing from close range operations [15] into extended range of up to a few miles [73], the corresponding CFD simulation domains grow exceptionally large, particularly in the longitudinal direction. The elongated spatial domains pose substantial computational challenges for realistic formation flight simulations. For turbulence-resolving models such as the LES, both spatial and temporal discretisation must be sufficiently refined to capture the integral length scales of turbulence for accurate representations. Consequently, the dense mesh and fine time steps over the tremendous flight space domain imposes significant computational costs and extended core-hours demands, thereby limiting the practicality for wake surfing simulations.

Inlet boundary conditioning [74, 75] has therefore emerged as an efficient strategy to reduce the computational domain sizes by prescribing the fully developed flow fields on the inlet boundary. As illustrated in Figure 1.13, the overall domain is conceptually divided into an inlet-condition (IC) region and a main-simulation (MS) region. However, generating an appropriate inlet velocity profile with realistic turbulence characteristics remains a significant challenge for LES. This difficulty arises mainly due to the LES explicitly resolves the large-scale eddies that contain most of the turbulent kinetic energy, k which is computed from the velocity fluctuation components (u'_x, u'_y, u'_z) [76].

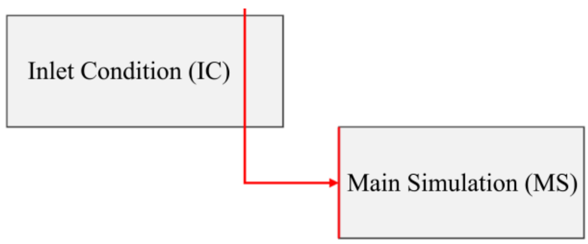

Figure 1.13 Inlet condition and main simulation

The first domain, or the IC domain contains the leading wing or aircraft responsible for generating the wingtip vortices. The flow-field information at a selected downstream plane is extracted and mapped onto the inlet of the second domain. The second domain, referred to as the MS domain, includes the trailing wing or aircraft that positioned within the upwash region of the induced vortices. By splitting the wake surfing scenario into two domains, the formation spacing studies can be conducted using a single IC simulation and paired with multiple MS simulations. This approach allows the trailing aircraft to be evaluated at different positions using only a small fraction of the full spatial domain, instead of repeatedly simulating an entire two-aircraft configuration for each formation spacing configuration.

In LES, prescribing realistic inlet conditions remains complex yet essential [77]. Turbulent fluctuations exhibit strong spatial and temporal coherence, and any inflow that lacks such correlations can severely impact the downstream flow development. The simplest method to introduce turbulence is to superimpose white noise perturbations scaled to the desired turbulence intensity [77]. This method however suffers from the well-known limitation that the injected fluctuations are neither temporally nor spatially coherent, resulting in unrealistic turbulence structures that do not evolve correctly within the computational domain. Uncorrelated turbulent inflow conditions can cause rapid dissipation [77], thereby compromising the overall accuracy of the simulation.

1.5.1 Precursor Inlet Conditioning Method

Tabor and Baba-Ahmadi [74, 75] have concluded that precursor and synthesised methods yield a more realistic flow dynamics compared with simple white-noise perturbations. These approaches preserve the turbulence structures to retain the spatial and temporal coherence required for accurate LES predictions, especially in flows dominated by coherent vortical structures such as aircraft wake vortices.

In the precursor method, a separate upstream simulation is performed to generate a fully developed turbulent flow field from which a time-series of planar velocity data is extracted for the inlet boundary mapping. As the inflow conditions are directly derived from a genuine turbulent simulation, they inherently possess the correct energy spectrum and spatiotemporal correlations. The slice of planar flow-field data is stored at each time step over a significant period and is subsequently read in on the inlet of MS domain.

There are several methods of generating the flow-field parameters. One common approach is the internal mapping or cyclic channel flow methods, where the velocity field at specific planes or outlet is recirculated back to the inlet through mathematical mapping. These methods require only one simulation domain as the source of precursor data is from within the same domain. These are often used in pipe or channel flow studies to achieve a fully developed state with the minimal computational domain length and resource expenditure.

Alternatively, an independent precursor simulation can be performed in a separated IC domain, with the resulting flow field stored in a dedicated database. These data are then fed into the inlet of the main MS domain as physically consistent inlet conditions. A key consideration for this method is that the precursor time series must be of sufficient temporal duration to allow for periodicity, thereby avoiding spurious repetitions that could corrupt the simulation. A more advanced variant of this approach is concurrent library generation, wherein the precursor data is computed "on-the-fly" in tandem with the main simulation, offering a dynamic and potentially more efficient solution.

Villers [78] demonstrated a pre-computed domain with periodic streamwise boundaries to construct a time-series library of the outlet flow fields of adequate duration to drive an entire main simulation. As the inherent periodicity of the datasets can lead to repeated structures, Villers applied a random phase-amplitude jittering technique to mitigate the cyclic artefacts and maintain the stochastic integrity of the inlet turbulence.

1.5.2 Synthetic Inlet Conditioning Method

The synthesised inflow method introduces additional fluctuating velocity terms, commonly constructed using Fourier Techniques or Principal Orthogonal Decomposition (POD) on the mean velocity to represent the turbulent fluctuations. This method allows users to prescribe and modify the fluctuation amplitude, the energy coefficients and spatiotemporal characteristics, thereby enabling greater control over the turbulence structure at the inlet.

Montorfano et al. [79] compared the different inlet boundary models such as fixed mean profile, internal plane mapping with flow quantity of interest and synthetic turbulence generated by superstition of harmonic functions, to investigate the impact on the flow dynamics in the downstream. The study showed that the internal plane mapping has the closest velocity profile to the theoretical law-of-the-wall as well as the fluctuation away from the wall. However, Baba-Ahmadi and Tabor [74] highlighted that the basic mapping method provide only limited control over the inlet flux, and this is deficient to reproduce the accurate turbulence fluctuation. To overcome the weakness, Wang and McGuirk [77, 80, 81] have demonstrated the recycling-rescaling model (R^2M) by applying additional forcing mechanisms such as explicit velocity correction and axial and azimuthal body forces into the system, to recover the appropriate turbulence intensity and length-scale distributions.

Dhamankar and Blaisdell [82] introduced the database approach, whereby pre-existing turbulence database from a prior computation or an experiment are mapped onto the inlet of a CFD domain, regardless of periodic, recycling-rescaling, or synthetic turbulent inflow-based. The turbulent fluctuations can be rescaled and manipulated if necessary. Schluter et al. [83] presented the LES inflow conditions with RANS computational data and proposed a modified procedure, where the velocity data generated from the periodic LES. The data are modified from the coupled, upstream RANS simulation, to result in the desired mean velocity and velocity fluctuation profile.

The literature above has highlighted various methods of mapping the outlet or mid-plane flow-field information onto the inlet, with precursor and synthetic approach. These techniques have shown strong performance in non-swirling flows, particularly in canonical boundary-layer and channel-flow configurations [79-85]. However, for application involving aircraft wake vortices, the inflow field contains strong swirl and vortex-dominated turbulence. Inlet conditioning with such swirling profile would offer substantial reduction in computational cost for vortex surfing simulation and other related applications. However, as far as the author are concerned, there is a notable lack of studies addressing LES inlet treatments specifically tailored for vortex flows. The trailing vortex with its pronounced rotational core and anisotropic turbulence, imposes additional complexity in both the mean velocity specification and the fluctuation reconstruction.

Some progress has been made for confined swirling flows. Pierce and Moin [84] proposed a novel method to generate swirling inflow boundary conditions in LES. The method implemented additional azimuthal body force, which is to conquer the drag from the walls, and axial body force to drive the physical flow. Jiang et al. [85] have specified a swirling velocity profile with desired swirl numbers for DNS or LES. For annular and round jets, a certain swirl number at the inflow can be conveniently implemented by varying the body force which is linearly dependent on the swirl number. The analytical solution agrees well with simulation and experiment results. These mentioned swirling inflow conditions are however not directly applicable for the wingtip vortex flow, as they are specifically designed for confined simulation domains such as the jet combustors, and the swirl number is only suitable for axisymmetric flow.

In Chapter 4, the author addresses the identified gap by developing inlet conditioning methods specifically tailored for vortex-dominated LES inflow conditions. The approach maps the wingtip vortex field from the IC domain onto the inlet of MS domain, to substantially reduce the computational resources needed for repetitive LES simulation while maintaining the physical integrity of the downstream vortex evolution. Subsequently, the time series precursor data are further utilised to formulate a Fourier series expression which can be used to synthetically generate the velocity fluctuations. The vortex developed in the downstream plane of precursor MS is then analysed to validate that the vortex development is correctly captured and to ascertain the accuracy of the precursor inlet conditions for vortex flow.

With the LES methodology validated, the inlet conditioning techniques are employed to significantly reduce the computational memory and core hours required for wake vortex surfing simulations while maintaining satisfactory accuracy across the vortex-dominated flow field.

1.6 Research Objectives and Contributions

With the growing interest in wake surfing for formation flight, significant challenges remain in efficiently capturing wingtip vortices and modelling their evolution over extended downstream distances. In particular, there is a lack of unified framework that integrate the experimental characterisation, numerical prediction, and efficient inflow conditioning approach for vortex-dominated flows. To address these gaps, the present project aims to achieve the following research objectives:

1. Develop an enhanced experimental characterisation methodology by introducing a perspective upright correction approach for vortex visualisation, enabling accurate characterisation of wingtip vortex structure, trajectory, and evolution despite non-ideal camera placement.
2. Establish and validate high fidelity CFD framework for accurate wingtip vortex prediction by assessing turbulence modelling approaches and validating numerical results against published studies and in-house wind tunnel measurements.
3. Develop efficient LES inlet conditioning strategies for vortex dominated flows by extending conventional inflow approaches towards spatially evolving vortical environments while preserving essential vortex turbulence characteristics.
4. Formulate spatial reconstruction strategies for synthetic vortex inflow generation to represent the non-uniform turbulence characteristics across the vortex core and surrounding flow region while reducing dependency on large precursor datasets.
5. Implement the CFD with inlet conditioning strategies to investigate wake-encounter behaviour of a trailing wing positioned at various locations within the formation flight arrangements.
6. Integrate a reduced-order aerodynamic model for rapid vortex flow field generation to provide an efficient and practical alternative for vortex initialisation in formation flight simulations.

The key contributions of this research are the development of an integrated experimental and computational framework for efficient prediction of wake vortex evolution in formation flight applications. A perspective upright correction methodology is developed to improve the accuracy and flexibility of wind tunnel vortex characterisation using a simplified imaging setup. A validated CFD framework is established to capture the key characteristics of wingtip vortices, including their structure, velocity distribution, and downstream evolution. Furthermore, efficient LES inlet conditioning strategies are developed and adapted for vortex-dominated freestream flows, extending conventional inflow approaches beyond canonical turbulent configurations. The proposed precursor and synthetic methods preserve essential vortex turbulence characteristics while reducing the computational cost associated with extended-domain formation flight simulations.

1.7 Thesis Outline

Accurate prediction of aircraft wake vortices is fundamental to understanding vortex surfing and its potential aerodynamic benefits in formation flight. The experimental methodology in this research provides the qualitative insight into the vortex spiral behaviour and quantitative estimates of vortex core size and trajectory. The CFD framework using URANS and LES in the thesis are showing the capability in capturing the essential vortex characteristics observed experimentally, and in addition to more dynamics quantities such as tangential velocity, axial velocity deficit and decay trends.

Today, even with a substantial amount of research on vortex surfing in the aviation industry, the boundary condition strategies for the turbulent vortex-dominated inflow fields remains comparatively under-developed. Existing methods are still largely tailored to canonical boundary layer, channel, or confined jet configurations, and do not fully account for the strong rotational core, anisotropic turbulence, and three-dimensionality inherent in aircraft wake vortices. This research will address that gap by systematically examining inlet-mapping and synthetic fluctuations methodologies specifically for vortex flows. The precursor or synthetic framework to reproduce realistic vortical inflow conditions for LES aims to reduce the computational cost while preserving downstream vortex fidelity. Through this approach, the work contributes new insights and practical tools for accurate and efficient simulation of vortex surfing and other vortex-driven aerodynamic applications.

Chapter 2 presents the experimental characterisation of wingtip vortices using wind tunnel testing. The near field downstream development of wake vortex generated by different wing configurations are examined to provide deeper insight into the underlying physics behaviour of the vortex. The chapter also demonstrates an efficient yet accurate approach to capture and characterise the wingtip vortices with a cost-effective experimental setup. The resulting measurements form a critical validation reference for the trailing vortices modelled via numerical methods later.

Chapter 3 outlines the computational fluid dynamics (CFD) framework for simulating wingtip vortices, including Unsteady Reynolds-Averaging Navier Stokes (URANS) and Large Eddy Simulations (LES) techniques, within the OpenFOAM environment. The chapter details the pre-processing procedures including the geometry preparation and mesh grid generation, followed by the numerical solution of the flow field using several turbulence models over a duration to achieve converged results. Post-processing is performed to interpret the key vortex metrics such as core strength, core size and aerodynamic force trends with angle of attack. The results are validated against published data and the wind tunnel findings from the previous chapter.

Chapter 4 builds on the validated CFD framework and extends it to the development of precursor and synthetic inlet boundary condition for LES. The chapter first demonstrates how the upstream domain with leading wing generates the time-dependent precursor data for coherent inflow conditions. The chapter then investigates synthetic turbulence generation methods to allow controlled scaling of fluctuations while reducing the memory requirements compared with a full series of precursor data. The outcomes provide critical insights into the feasibility of inlet conditioning techniques for wake vortex simulations.

Chapter 5 presents the simulation for formation flight and quantifies the aerodynamic benefits on the trailing wing operating within the updraft region. The analysis evaluates lift enhancement, drag reduction and the overall aerodynamic efficiency under various relative positions. This chapter also employs the established inlet-conditioning framework to demonstrate its capability in accurately reproducing the turbulent intensity, coherence and structural behaviour for vortex surfing effects in the main simulation domain. The demonstration sheds light on the accuracy of the proposed inlet conditioning methodologies in predicting the wake vortex interactions on trailing wing in formation flight.

Chapter 6 summarises the theoretical development and numerical applications presented in this work and highlights the key contributions. The chapter concludes with recommendations for future research, focusing on strategies to further improve the numerical efficiency of the proposed methodology and to extend the application of the CFD framework to broader investigations other than wake vortex surfing and formation flight aerodynamics.

Appendix A introduces the reduced-order model of Unsteady Vortex Lattice Method (UVLM), to provide the initial baseline of mean-flow-field data. The circulation strength derived from the UVLM model is used to populate the planar velocity distribution required for the LES inflow conditions. The UVLM model is potentially an efficient alternative to produce the mean velocity data, and these data can also be augmented with the same synthetic fluctuations to reconstruct the necessary turbulences.

1.7.1 Resources

The primary resources supporting both the experimental workflow and the computational simulations in this thesis are outlined below:

Resources for Experimental Modelling

1. 3D-printing material and services at Singapore Institute of Technology [86]
2. Wind tunnel lab facility and technical support at Singapore Institute of Technology [86]
3. Full-frame mirrorless camera Sony A7c with Sigma 28-70mm f/2.8 Lens [87, 88]
4. Aiguru construction green line laser leveller [89]
5. Adobe Lightroom Classic and Photoshop [90, 91]

Resources for Numerical Modelling

1. Workstation
    - AMD Ryzen™ Threadripper™ PRO 5995WX @2.70GHz, 64-cores, 128-threads [92]
    - Crucial RAM 512GB (8×64GB) DDR4 3200MHz
    - NVIDIA GeForce RTX™ 3050 8GB GDDR6 SODIMM
    - Micron® 7300 Pro SSD 960GB NVMe SED
    - Ubuntu (22.04 LTS and 24.04 LTS)
2. Pre-Processing

- Autodesk® Inventor® Professional [93] for 3D-modelling and geometry setup

3. Solving
   - OpenFOAM (v2206, v9, v10 and v12) [94, 95] for CFD meshing generation, processing and solving
   - SHARPy [96] for UVLM calculation
4. Post-Processing
   - ParaView [97] for data visualisation and quantification of results from OpenFOAM and SHARPy
   - Python [98] with library packages including Matplotlib, NumPy, Pandas, SciPy, etc for data post-processing and plotting for presentation

1.7.2 Publications and Presentations

The work carried out in this research has resulted in the following publications and presentations:

Journal publications

1. J. C. Chan, H. Hesse and P. C. Wang, "LES validation on near-field wingtip vortex evolution with wind tunnel characterization at low Reynolds number," *Aerospace Science and Technology*, vol. 157, 2025.
   DOI: 10.1016/j.ast.2024.109789
2. J. C. Chan, H. Hesse and P. C. Wang, " Synthetic Inlet Conditioning Methods of Vortical Flows in Wake Vortex Surfing by LES," *AIAA Journal*
   [under review at the time of writing]

Conference publications

1. J. C. Chan, H. Hesse and P. C. Wang, "Inlet Mapping of Wingtip Vortices in LES for Wake Vortex Surfing," in *AIAA AVIATION and Ascend 2024 Forum*, Las Vegas, Nevada, 2024.
   DOI: 10.2514/6.2024-4016
2. J. C. Chan, P. C. Wang, J. J. Y. Tan and H. Hesse, "Characterization of LES Inlet Conditions with Mapped Wingtip Vortices using UVLM Mean Flow Field Data," in *Twelfth International Conference on Computational Fluid Dynamics (ICCFD12)*, Kobe, Japan, 2024.
   Link: researchgate.net/publication/383234409
3. J. C. Chan, H. Hesse and P. C. Wang, "Aerodynamic Interactions in Formation Flight for Wake Vortex Surfing," in *AIAA AVIATION 2023 Forum*, San Diego, CA and Online, 2023.

DOI: 10.2514/6.2023-4221

4. J. C. Chan, H. Hesse and P. C. Wang, "Experimental Characterization of Wingtip Vortices with Perspective Upright Correction," in *AIAA AVIATION 2023 Forum*, San Diego, CA and Online, 2023.

   DOI: 10.2514/6.2023-4526

Conference presentations

1. Singapore Aerospace Technology and Engineering Conference (SATEC) 2024

   J.C. Chan, H. Hesse, and P. C. Wang, "Wake Vortex Surfing for Formation Flying," Singapore, 2024.

2. AIAA AVIATION 2023 Forum, Flow Visualization Showcase

   J.C. Chan, H. Hesse, and P. C. Wang, "Experimental Characterization of Wingtip Vortices with Perspective Upright Correction," San Diego, CA, 2023.

Chapter 2

Experimental Characterisation of Wingtip Vortices with Wind Tunnel

Accurate prediction of wingtip vortices is fundamental for future development of wake vortex surfing operations. Full scale experiment such as flight test [99] provides the most realistic observations of wake vortex behaviour. However, it is costly, time-consuming, and subjected to operational constraints such as airspace clearance and weather conditions [52]. Wind tunnel experimentation therefore emerges as the practical alternative to provide a controlled environment for investigation the vortex formation and development.

Despite being the most common and reliable approaches to visualise and characterise the trailing vortices, wind tunnel experiment often present practical challenges, for instances the positioning of the camera and visual access. In this work, a novel correction technique [11] is introduced to address this limitation. The proposed method enables geometrically upright vortex images to be reconstructed from a single camera positioned at arbitrary viewing angles. The qualitative and quantitative results of vortex capture obtained from the wind tunnel experiments also serve as the validation reference for the CFD models in the subsequent chapter.

The wind tunnel facility used in this study is located at the Singapore Institute of Technology [86]. It is an open-circuit subsonic suction wind tunnel as shown in Figure 2.1 (left), with test section measures $1.2m$ in width, $0.8m$ in height and $2m$ in length [53]. A fan of $2m$ in diameter is located at the outlet end, with capabilities to create freestream velocities of up to $u_\infty = 10m/s$. The freestream velocity is monitored using a pitot tube mounted at the at the midstream of the test section. The test section is accessible via the openable panels on both sides. The wind tunnel is also equipped with a smoke generator and probe, which located along the centreline in the upstream, as shown in Figure 2.1 (right) and Figure 2.5. The probe is vertically adjustable along the z-axis, enabling precise control of the smoke-injection height for vortex visualisation and flow-field interrogation.

Figure 2.1 Wind tunnel at Singapore Institute of Technology.

The workflow overview of the wind tunnel test for vortex visualisation is illustrated in Figure 2.2. There are three main stages namely pre-experiment, vortex capture and post-process.

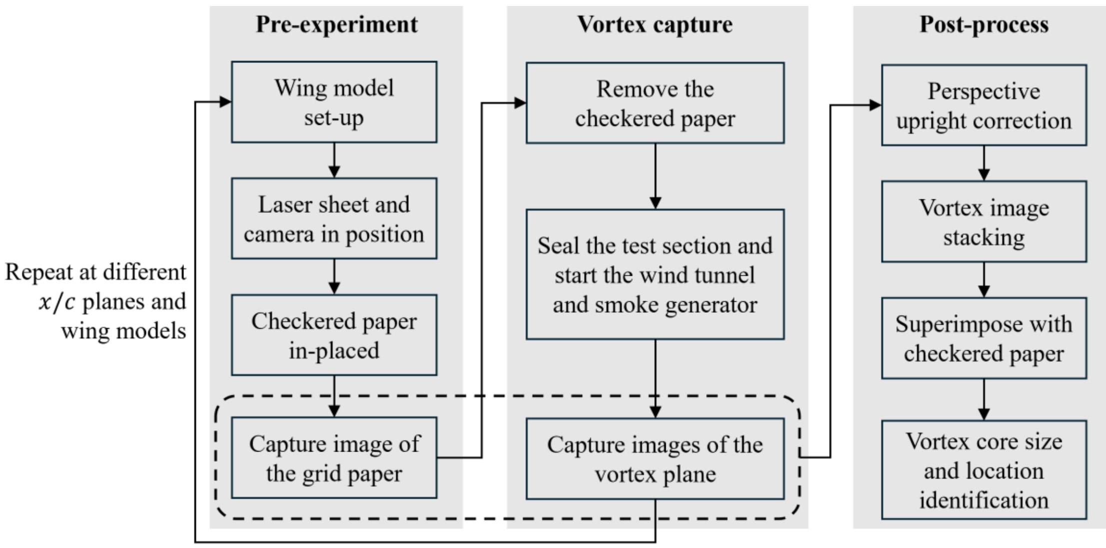

Figure 2.2 Overview of wind tunnel test workflow.

2.1 Pre-Experiment

Winglets or wingtip devices [100] have been introduced since the early twentieth century to minimise the induced drag and improve aerodynamic efficiency. The additional structure is incorporated at the wingtip to reduce the wingtip vortices and minimise the induced drag by preventing the airflow on the pressure surface from slipping to the suction surface. Even with the most effective wingtip devices such as the blended winglets [101], the trailing vortex continues to contain substantial energy that can be exploited for vortex surfing operations. Therefore, prior to investigating vortex surfing behaviour, it is necessary to experimentally examine how different wingtip configurations influence the formation and development of wingtip vortices.

2.1.1 3D Modelling of Wing Geometries

To demonstrate the effect of winglets on the vortex generation, two distinct wing configurations were used in this validation study – a baseline model without a winglet (NW) and a variant equipped with a blended winglet (BW) [101], as shown in Figure 2.3a and Figure 2.3b, respectively. Both wing models were designed with identical geometrical specifications, featuring a chord length c of 0.1m, a wingspan b of 0.5m and an NACA 4412 aerofoil profile. The NACA 4412 aerofoil has been commonly adopted in wind tunnel experiment at low Reynolds number [58], and investigated in numerical studies [102, 103] with a comparable aspect ratio, providing a suitable reference for studying the vortex behaviour. The wingspan was chosen to fit within the test section width while minimising the wing root interference effects. Instead of replicating a specific published experimental setup, the present work simplifies the range of configurations to primarily visualise and characterise the near-field development of wingtip vortices with and without the winglets, rather than to obtain detailed aerodynamic performance measurements. The experimental flow visualisation results provide qualitative reference for the vortex behaviour and serve as a comparison and validation baseline of the numerical simulations presented in the subsequent chapter.

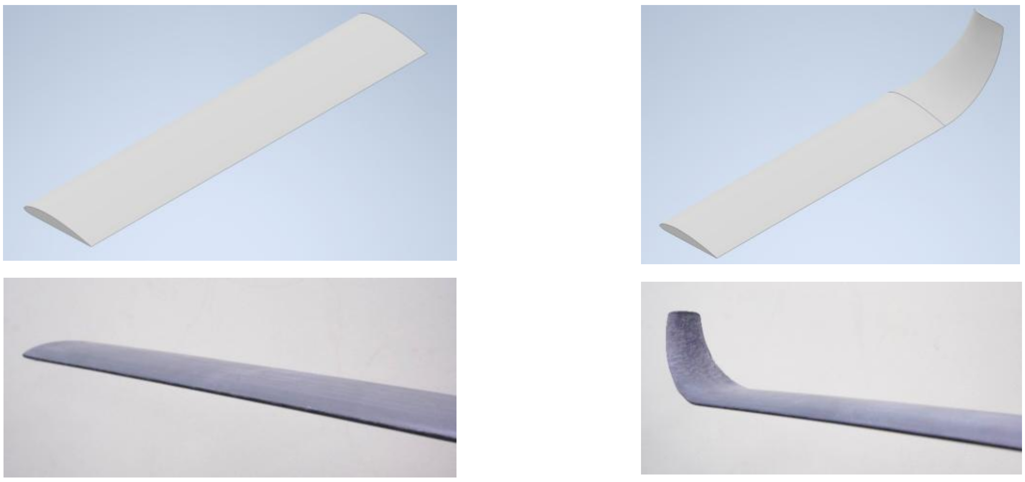

(a) No winglet (NW) (b) Blended winglet (BW)

Figure 2.3 Rectangular NACA 4412 CAD (above) and 3D-printed (below) wing models.

The BW design as illustrated in Figure 2.4 incorporates an upward sweep with a smooth curvature radius of 0.1m in the transition section and taper ratio of 0.5 at the tip. Both wing models were fabricated with polylactic acid (PLA) using additive manufacturing, and their surfaces were finished with micro grit sandpaper to achieve a smooth surface finish and minimise the skin friction effect. The NACA 4412 aerofoil profile also possesses a benefit with relatively flat lower surface, easing the fabrication post-process in maintaining the geometric fidelity with the intended profile.

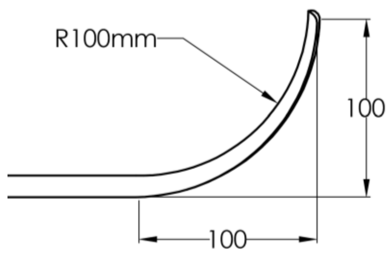

Figure 2.4 BW design with curvature radius = 1c.

2.1.2 Wind Tunnel Setup

The experimental wind tunnel setup is configured as shown in Figure 2.5. The wing model was positioned at the mid height of the test section with a supporting stand, located approximately five chord length ($x/c = 5$) downstream of the smoke probe. The wingtip was precisely aligned with the smoke particle probe centreline to ensure consistent vortex seeding. To visualise the induced vortex in the downstream, a laser leveller emitting continuous green laser-sheet with 2.5mm sheet thickness [89] was employed to illuminate the smoke-seeded vortices at various downstream cross sectional (y-z) planes. The smoke particles visualisations of the experiment are taken place from $x/c = 0$ to $x/c = 10$. With the x/c indicator labelled on the bottom surface of the test section, the positioning of laser sheet and camera can be done effortlessly.

A 24-megapixels mirrorless camera [87] with variable focal length of 28-70mm and maximum aperture of f-stops 2.8 [88] was placed at $x/c = 8$ downstream to the laser emitter to capture the illuminated vortex sheet. The camera live view monitoring and control settings including ISO (sensitivity to light), shutter speed, and aperture were all conducted externally via a remote device to optimise the imaging conditions. The tunnel blockage effect attributable to the imaging setup was less than 0.85%, confirming a negligible impact on the flow field. All experiments were conducted at a chord-based Reynolds number of $Re_c = 6.8 \times 10^4$.

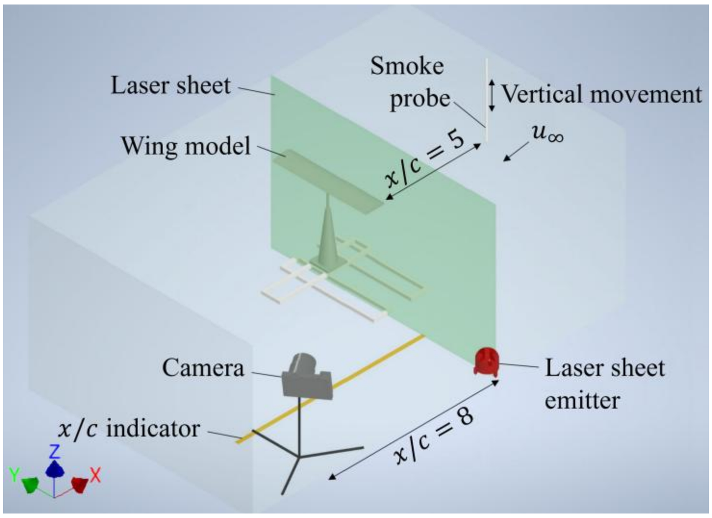

Figure 2.5 Overview of the wind tunnel experiment setup for vortex visualisation.

2.1.3 Problem Identification and Mitigation

Conventional smoke visualisation techniques provide effective qualitative observation of wingtip vortex structures. During the initial attempt to capture the vortex patterns, the imaging device was positioned with its optical axis perpendicular to the laser sheet to ensure an upright view. However, this configuration resulted in the accumulation of smoke particles and severely obscuring the field of view to the laser illuminated vortices. To mitigate this, the camera was relocated to an outboard position on the wing tunnel to have a clearer line of sight. Zaman et al. [104] similarly captured the tip vortex in oblique viewing configuration for aerofoil with different tip shapes and angles of attack. Although this repositioning effectively resolved the occlusion issue, it introduced a non-orthogonal viewing angle to the laser sheet and resulting in a tilted and distorted image from the upright viewing angle to the vortex plane.

To rectify the result, a post-processing step for perspective upright correction was essential to restore an upright orthogonal view, which enable the quantitative analysis of vortex core properties such as vortex core size, location, and flow structures. A checkered paper of 5mm × 5mm with a central origin as illustrated in Figure 2.6 was used in the experiments as the calibration baseline for post-processing. The checkered paper was placed normal to the freestream airflow direction, accurately aligned to the location of the laser sheet plane. The centre of the checkered paper was also fixed in-line with the wingtip trailing edge as shown in Figure 2.7. This arrangement of checkered paper serves as a reference point for the camera’s focal point and as a calibration datum.

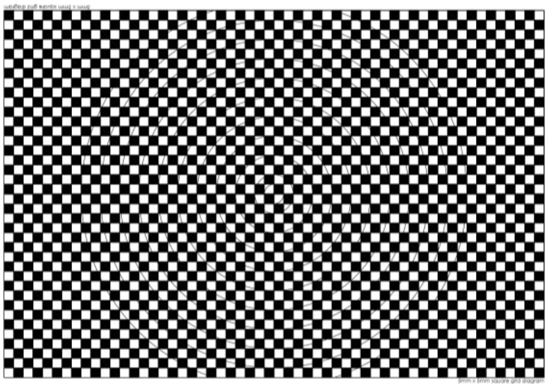

Figure 2.6 5mm×5mm square checkered paper for baseline calibration.

The camera mounted on the tripod will be adjusted to the same height as the wing, positioned at the right most position in wind tunnel test section offset by the tripod, as shown in Figure 2.7. A strap is hooked on the camera as a safety precaution. The camera setting for the wind tunnel test was optimised to ISO 640, shutter speed of 1/160 – 1/250s, aperture of $f/2.8$, zoom focal length of 70mm and with manual focus locked to the centre of checkered paper. The configuration ensured sharp and focused imaging with sufficient light intake and acceptable level of noise. A reference image of the checkered paper was taken as the calibration baseline. The reference checkered paper was removed after the calibration, but the wing, camera and laser remain stationary. The wind tunnel setup was thereafter activated, and the laboratory lighting was switched off to enhance the image contrast without overexposure on the laser-highlighted regions.

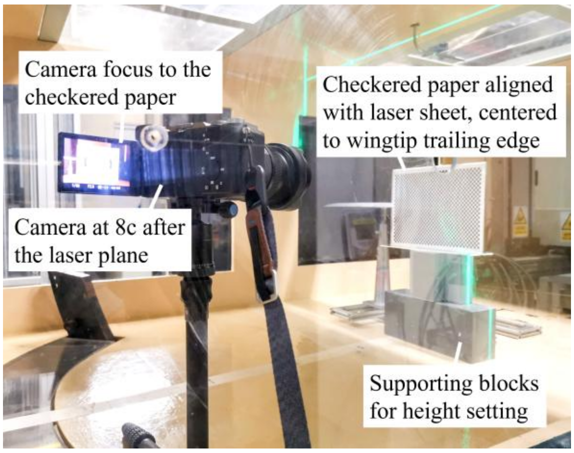

Figure 2.7 Wind tunnel setup – initialisation of the vortex plane.

2.1.4 Validation test for the perspective upright correction method

A validation test was conducted prior to the experimental investigation on accuracy of the perspective upright correction (PUC) method against a native orthogonal view. The validation procedure involved imaging a calibration target consisting of a checkerboard grid and a printer 40mm diameter solid black circle, from both the corrected and native upright perspective. The acquired images were post-processed, and the corrected image from the slanted view was superimposed onto the reference image from the native upright view as shown in Figure 2.8. Dimensional measurements were subsequently performed on both datasets using a digitiser tool [105] for validation purpose.

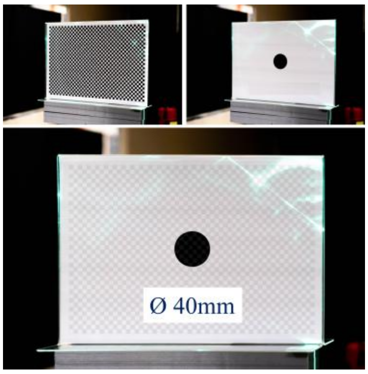

(a) Perspective upright correction.

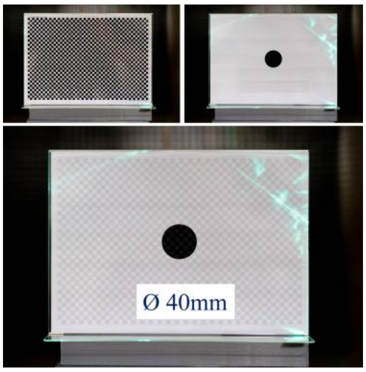

(b) Native upright view.

Figure 2.8 Validation of perspective upright correction accuracy.

Remarkably, the result of PUC method has fared a superior accuracy to the native upright view, with -0.52% to +0.16% of inaccuracy compared to -0.67% to +0.84%. The minimal residual error associated with the PUC method is attributed to the sensitivity limit of the digitisation tool rather than the correction technique itself. These results confirm that the perspective upright correction robustly transforms slanted view images into an accurate upright projection, achieving high fidelity in both the vertical and horizontal axes and thereby validating its application for subsequent quantitative vortex analysis.

Through the checkerboard calibration, the defined homographic transformation of PUC was systematically applied to all vortex images acquired under the identical conditions to ensure consistent geometric fidelity across the dataset.

2.2 Vortex Capture

One limitation encountered in this experiment is that the smoke particle discharged from the probe tip forms only a narrow smoke filament at higher freestream velocities. As a result, the illuminated region is smaller than the actual vortex cross section, which restricts the observable portion of the flow field. To address this, the smoke-generator probe was traversed vertically during image acquisition so that the vortex structure outside the initial smoke filament could be captured. Multiple images at different probe heights were recorded for each measurement plane, with an example shown in Figure 2.9. These images were subsequently post-processed and composited into a single field of view. Using the checkered reference sheet as a spatial baseline, the vortex-core size, flow structure, and spatial location were quantifiable from the superimposed image.

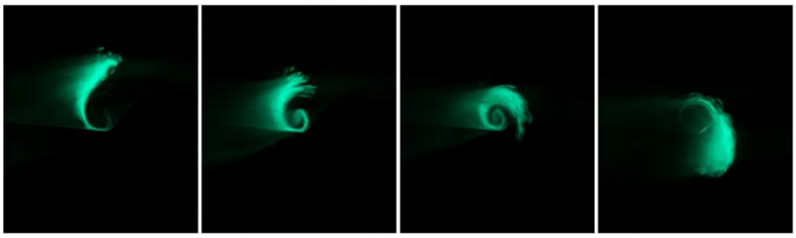

Figure 2.9 Examples of vortices captured for NW wing ($\alpha = 12°$, $x/c = 0$), before PUC.

The experiment procedure was repeated by translating the laser sheet emitter and camera downstream to successive x/c stations, as illustrated in Figure 2.10. At each new placement, the camera alignment and checkered paper reference were re-verified before acquiring both the reference and vortex images. After completing the full set of downstream locations, the experiments were repeated for additional angles of attack, α, and for different wing models.

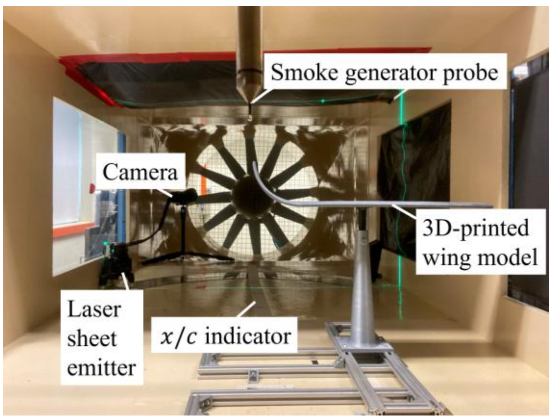

Figure 2.10 Laser sheet and camera shifted downstream taking reference on the x/c indicator, front view.

2.3 Post-Process

As the camera views the vortex plane at an oblique angle, the raw images appear tilted and geometrically distorted as illustrated in Figure 2.11a. The implementation of PUC method enabled accurate extraction of vortex core size, position, and flow structure. In this study, all wind-tunnel images are imported into Adobe Lightroom Classic [90] for correction. For each test configuration, the checkered paper image is first processed using the guided-mode PUC tool, which allows the four boundaries of the checkered sheet to be used as vertical and horizontal guides. Lens-profile correction is also applied to remove any distortion and vignetting. After all the adjustments, the checkered paper turned normal to the camera line-of-sight, with rectified horizontal and vertical alignment. The vortex image before and after the PUC were placed side-by-side in Figure 2.11 for a clear comparison.

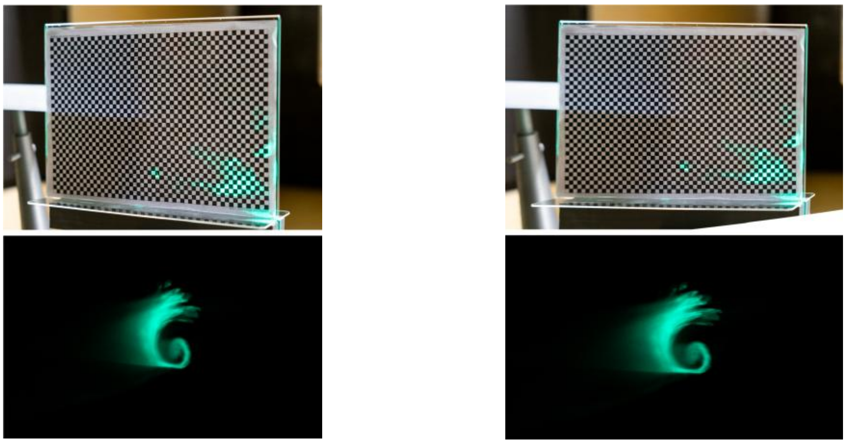

a) Before perspective upright correction. b) After perspective upright correction.

Figure 2.11 Perspective upright correction and cropping in Adobe Lightroom.

The same geometric transformation is then batch-applied to all corresponding vortex images to ensure consistent upright correction across the dataset. Figure 2.12 shows some examples of the corrected view of vortex after applying the perspective upright correction based on Figure 2.9.

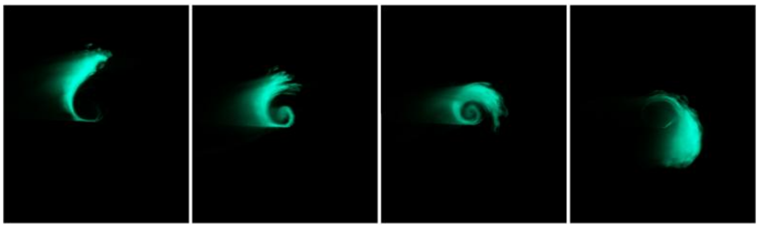

Figure 2.12 Same vortices from Figure 2.9 for NW wing ($\alpha = 12°$, $x/c = 0$), after PUC.

Given each frame of the vortex image captures only part of the instantaneous vortex traced by smoke particles, a single image is insufficient to represent the full vortex structure. Hence numerous images were taken with the smoke generator probe positioned at different vertical positions to map the vortex cross-section more comprehensively. The corrected images are then imported into Adobe Photoshop [91] for composite construction.

At the layer palette, each image is assigned with the lighten blending mode, which selects the brighter pixel intensity at every location. Any darker pixels in previous layers are replaced by lighter values in the new layer, while the lighter pixels are retained. This stacking effects were illustrated in Figure 2.13, enhances the visibility of the smoke-traced vortex boundary and reveals comprehensive structural details.

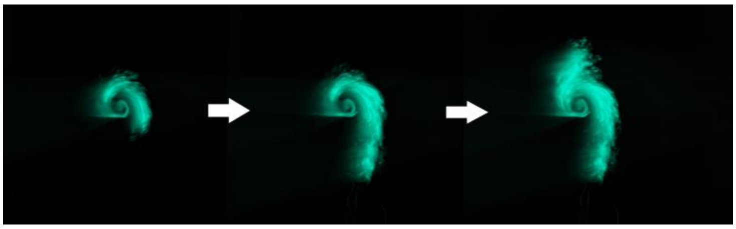

Figure 2.13 Vortex images layer stacking with lighten blend mode.

To capture the entire vortex structure in clarity, up to 30 photos are selected and blended for each x/c location. In the same project file, the checkered paper image is superimposed over the final vortex image with 5% opacity, making the measurement of vortex core size and location possible. The outline of wing geometry is added onto the final image to better visualise the position of the vortex in relative to the wingtip, as shown in Figure 2.14.

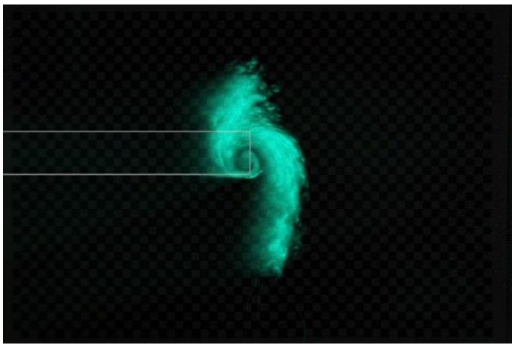

Figure 2.14 Final vortex image superimposed with checkered paper and wing profile.

2.4 Wind Tunnel Experiment Results

The proposed methodology to capture wing vortices was exercised on the NACA 4412 wing in two configurations – one without winglet and one with blended winglet, at angle of attack, α of 2° and 12°. The post-processed images are tabulated in Table 2.1, it can be clearly seen that the vortex shed from the plain wing is more pronounced, with the vortex core readily identifiable across different downstream locations and angles of attack. On the other hand, the wing with blended winglet consistently produces a weaker and less distinct vortex structure, reflecting the winglet's intended function of mitigating the production of wingtip vortices. This observation aligns closely with the findings of Sohn and Chang [55], where the incorporation of winglets reduces the intensity of wingtip vortices and its associated induced drag.

Table 2.1 Vortices captured for NACA 4412 rectangular wing without winglet.

x/c	No winglet (NW)		Blended winglet (BW)	
	$\alpha = 2°$	$\alpha = 12°$	$\alpha = 2°$	$\alpha = 12°$
0	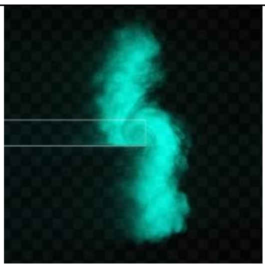	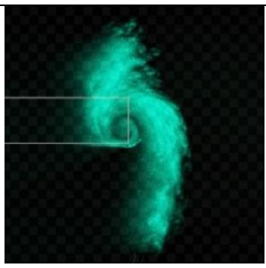	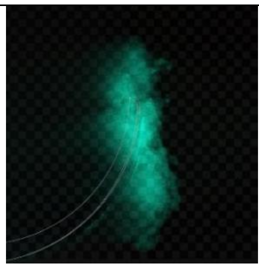	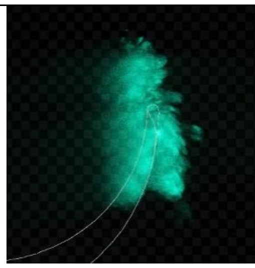
1	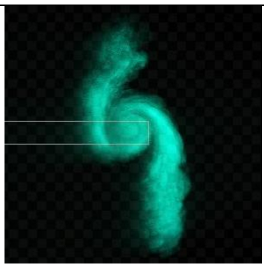	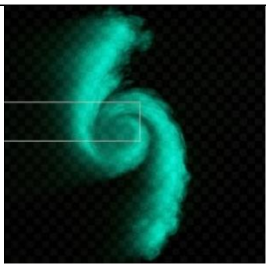		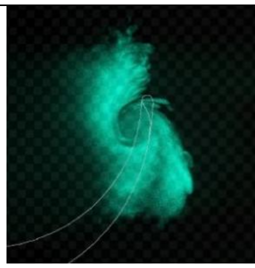
2	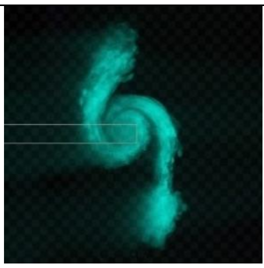	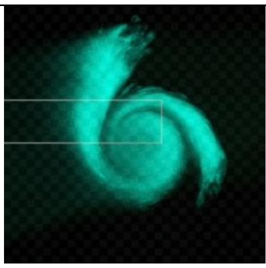	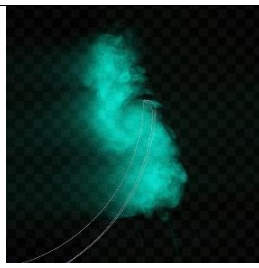	

Continues to the next page

3		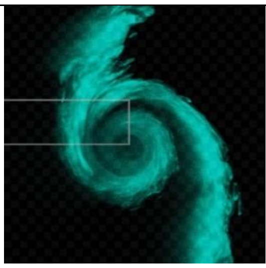	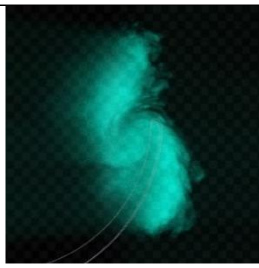	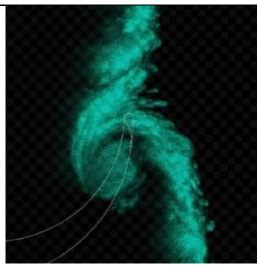
4	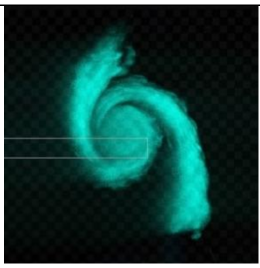	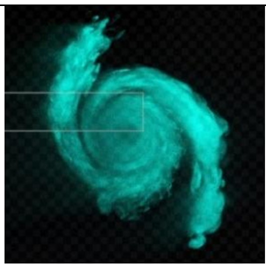	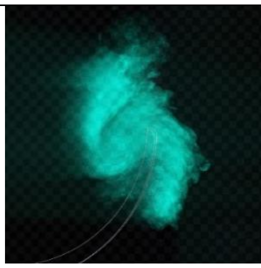	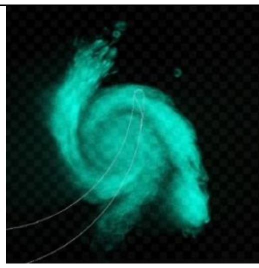

To characterise and quantify the wing vortices, the present study focuses on estimating the vortex size from the processed images. Devenport et al. [106] defined the contour of the wake spiral as the locus of peak axial turbulence stress, which marks the region of strongest unsteadiness within the vortex core. As the smoke particles are tracing the near-tip flow, the visible spiral observed in the wind tunnel represents the highly unsteady and fluctuating axial motion induced by the coherent vortex structures.

Similar interpretations of vortex spirals have been adopted in several wind tunnel studies employing hot wire anemometry to delineate the vortex core and associated turbulent features [55, 57, 59]. The wake spiral in this experiment is less sharply defined due to the use of a smoke probe instead of the hot wire sensor. Nonetheless, the structure of the vortex core remains identifiable and traceable. The vortex boundary is captured through the high-contrast smoke streaks bounded by the darker coherent contours surrounding the core region as shown in Figure 2.15.

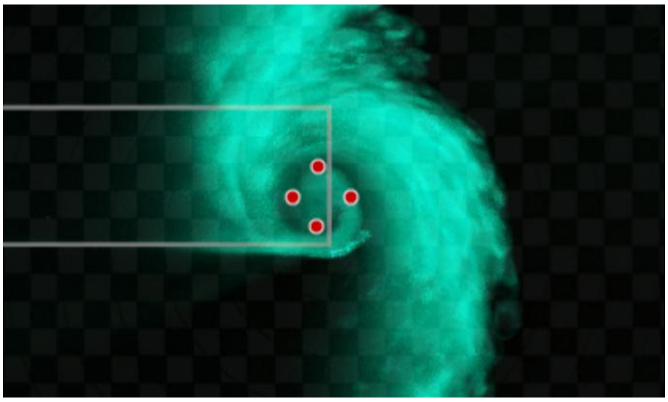

Figure 2.15 Measurement of vortex core size and location.

A digitiser tool [105] is used to plot and extract the four quadrant points of the visible wake spiral, as indicated by the red markers in Figure 2.15. These points data can be processed to identify the centre of vortex core, as well as the characteristic radius of the peak axial turbulence stress in y and z direction. The results are summarized in the Table 2.2 and Table 2.3 respectively.

Table 2.2 Vortex core location in the downstream.

x/c	Location of vortex core in coordinates of $(y/c, z/c)$, w.r.t the wingtip trailing edge position (mm)			
	No Winglet (NW)		Blended Winglet (BW)	
	$\alpha = 2°$	$\alpha = 12°$	$\alpha = 2°$	$\alpha = 12°$
0	(-0.03, 0.04)	(-0.02, 0.09)	(0.01, -0.05)	(-0.02, 0.03)
0.5	(-0.06, 0.06)	(-0.03, 0.08)	(-0.08, -0.07)	(-0.06, -0.01)
1	(-0.10, 0.06)	(-0.11, 0.04)	(-0.05, -0.06)	(-0.05, -0.04)
2	(-0.05, 0.08)	(-0.12, 0)	(-0.09, -0.07)	(-0.18, -0.11)
4	(-0.14, 0.17)	(-0.09, -0.02)	(-0.25, -0.04)	(-0.17, -0.19)
7	(-0.14, 0.18)	(-0.09, -0.03)	(-0.20, 0)	(-0.25, -0.25)
10	(-0.40, 0.21)	(-0.11, -0.02)	(-0.20, 0.16)	(-0.37, -0.26)

Table 2.3 Vortex core size development in the downstream.

x/c	Diameter of vortex core (circle / ellipse) in $(y/c, z/c)$			
	No Winglet (NW)		Blended Winglet (BW)	
	$\alpha = 2°$	$\alpha = 12°$	$\alpha = 2°$	$\alpha = 12°$
0	(0.11, 0.10)	(0.12, 0.12)	(0.03, 0.03)	(0.05, 0.05)
0.5	(0.19, 0.19)	(0.19, 0.19)	(0.09, 0.09)	(0.13, 0.13)
1	(0.22, 0.22)	(0.34, 0.28)	(0.14, 0.12)	(0.18, 0.17)
2	(0.26, 0.26)	(0.49, 0.40)	(0.17, 0.15)	(0.25, 0.25)
4	(0.36, 0.33)	(0.63, 0.53)	(0.22, 0.20)	(0.42, 0.37)
7	(0.47, 0.43)	(0.77, 0.68)	(0.21, 0.18)	(0.56, 0.50)
10	(0.57, 0.48)	(0.85, 0.75)	(0.24, 0.23)	(0.61, 0.59)

However, there is missing velocity information on the vortex profile, particularly the tangential velocity u_θ, which is of significant for wake vortex surfing application. To address the limitation, the well-established Lamb-Oseen model [107, 108] is used to estimate the tangential velocity distribution at each *x/c* downstream location,

$$u_\theta = \frac{\Gamma_V}{2\pi r}\left[1 - e^{-1.26\left(\frac{r^2}{r_c{}^2}\right)}\right] \tag{1}$$

where r_c is the characteristic core radius of determined from the digitised quadrant points, and r is the radial distance of an arbitrary point (y, z) from the vortex core centre (y_0, z_0),

$$r = \sqrt{(y - y_0)^2 + (z - z_0)^2} \tag{2}$$

and the circulation strength Γ_V of the vortex is the estimated at each x/c plane using the Kutta Joukowski's theorem [109] as follows,

$$\Gamma_V = \frac{L_G}{\rho u_\infty b_V} \tag{3}$$

where L_G is typically the weight of the vortices generating aircraft, but for the wind tunnel test here, it represents the lift generated by the wing. ρ is the fluid density, u_∞ is the freestream velocity and b_V is the span between the counter-rotating pair of vortices, which can be calculated from the shifting of the vortex core position.

As the wind tunnel setup does not include a force balance instrument or pressure sensor, the lift force of the plain rectangular wing is inferred from the published aerodynamic data for NACA 4412 wings with comparable aspect ratios and low Reynolds numbers in the range of 10^5 [102, 103, 110]. Based on these references, the approximated lift coefficients, C_L for $\alpha = 2°$ and 12° is 0.5492 and 1.0994 respectively. According to the experimental outcomes presented by Ara et al. [110], the lift of the blended winglet is assumed to be about 8.4% higher than the wing without winglet.

From the experiments and literature, it is noticed that the BW configuration generally exhibits a higher lift coefficient under the same condition and produces a noticeable smaller vortex core radius. Specifically, the BW reduces the core radius by approximately 45% and 31% at $\alpha = 2°$ and 12° respectively. When applied to the Lamb-Oseen formulation, these reduced core dimensions yield higher peak tangential velocities, as illustrated in Figure 2.16. The graphs are plotted with origin at the vortex core and showing the profile of u_θ across the radial position of the wingtip vortices at different x/c plane.

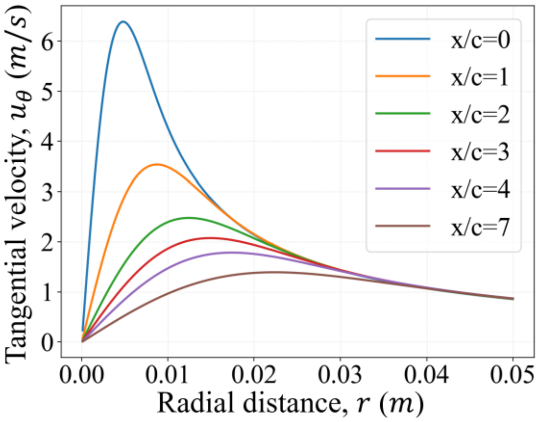

(a) NW, $\alpha = 2°$

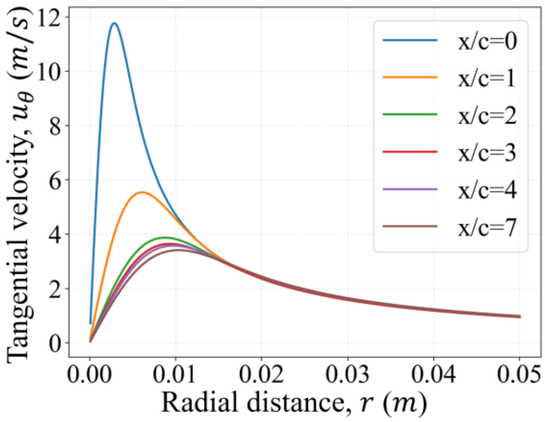

(be) BW, $\alpha = 2°$

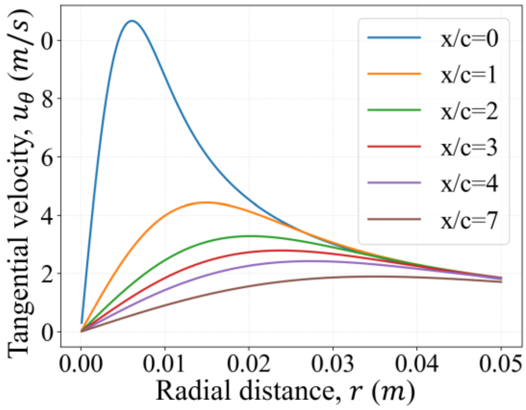

(c) NW, $\alpha = 12°$

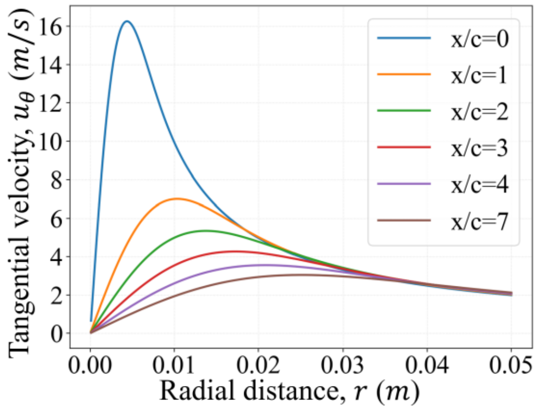

(d) BW, $\alpha = 12°$

Figure 2.16 Tangential velocity profile across core radius, estimated by Lamb-Oseen model.

To provide clearer insight into the flow structure, the Lamb Oseen tangential velocity vector fields are superimposed onto the vortex images in Table 2.4 for both wingtip configurations at $\alpha = 12°$ and at plane $x/c = 0$, 2 and 4. With the vortex core radius extracted directly from the processed images, the resulting velocity fields align well with the observed smoke-traced vortex patterns. The reconstructed fields show a core region of higher tangential velocity and peaked at the circumference of the core diameter, then a surrounding region of decreasing velocity as the distance to the vortex core increases.

Table 2.4 Lamb Oseen vortex model on $\alpha = 12°$, $x/c = 0$, 1, 2 and 3.

x/c	No winglet at α = 12°	Blended winglet at α = 12°
0	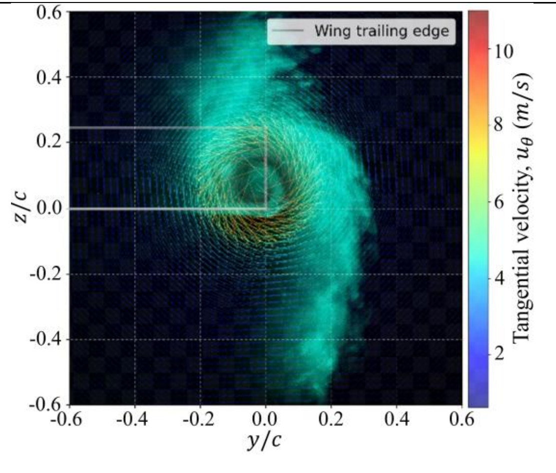	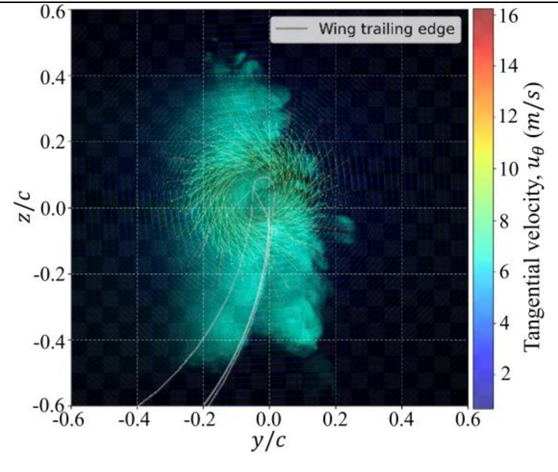
2	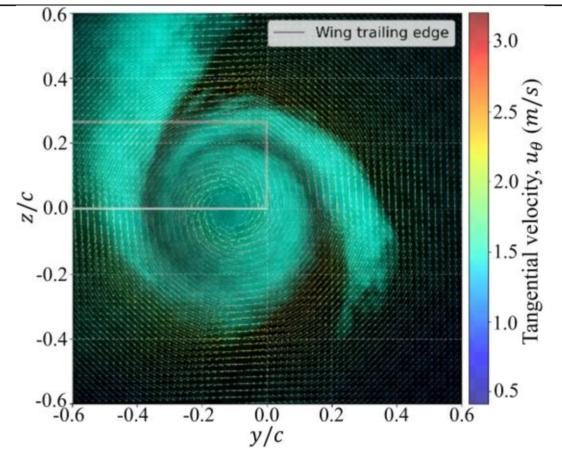	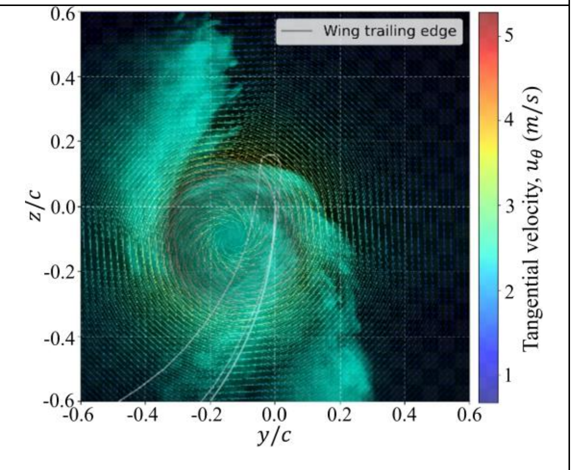
4	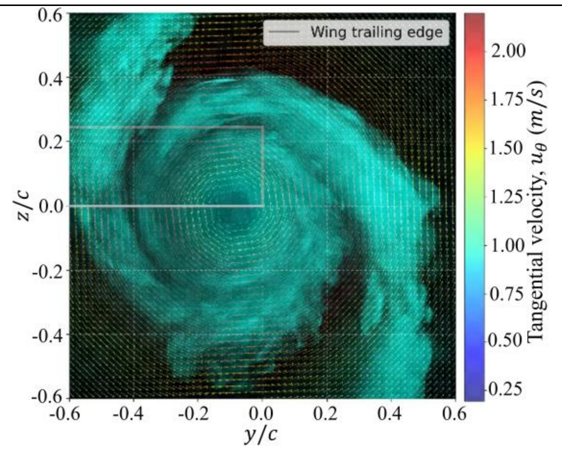	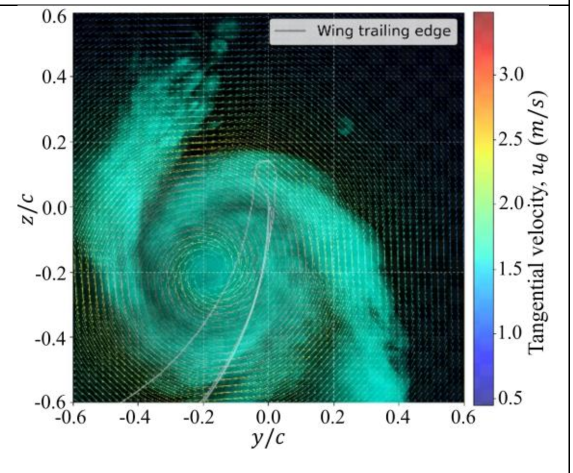

For each vortex core, the core location with respect to the wingtip trailing edge and the corresponding size of core radius were computed and plotted in Figure 2.16, Figure 2.18 and Figure 2.19 to visualise the overview of the vortex core trajectory and its downstream development.

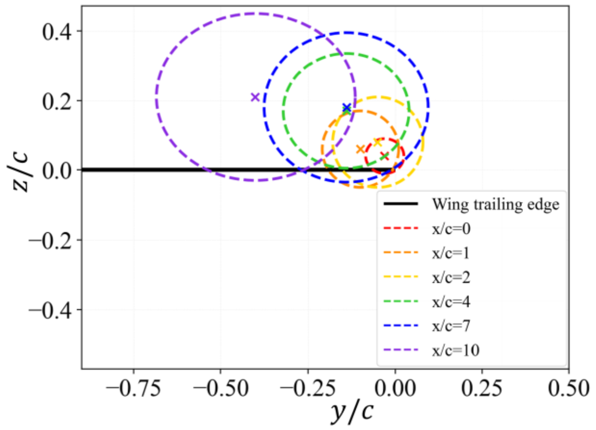

(a) No winglet at $\alpha = 2°$

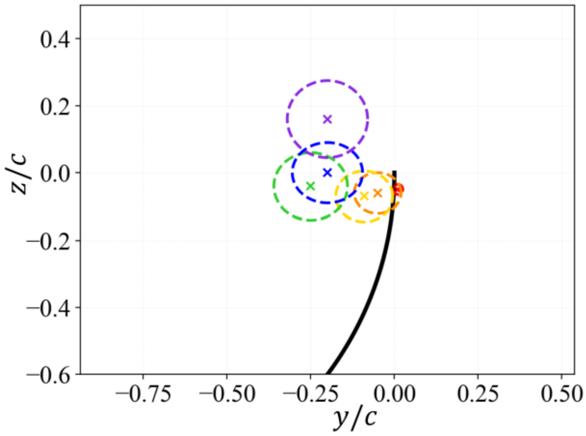

(b) Blended winglet at $\alpha = 2°$

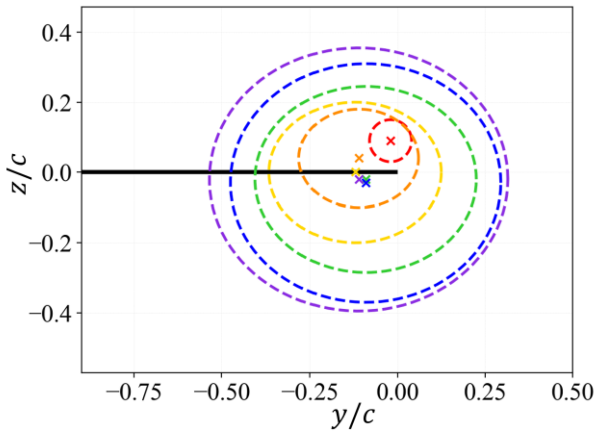

(c) No winglet at $\alpha = 12°$

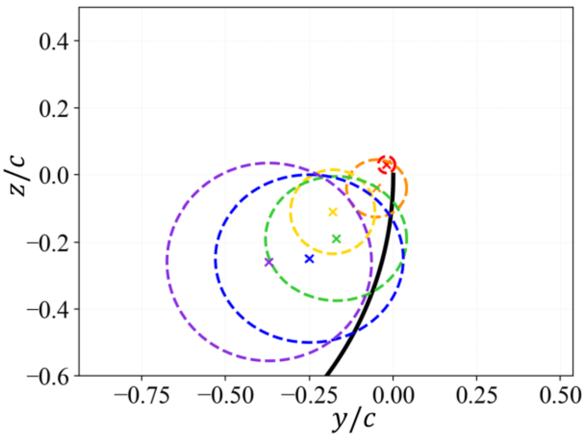

(d) Blended winglet at $\alpha = 12°$

Figure 2.17 Overview of the vortex cores development, rear view.

From Figure 2.17 and Figure 2.19, it is observed that the trailing vortices have consistently moved towards the wing root direction, and this inboard shift is ranged between -0.2c to -0.4c, as the airflow going downstream from $x/c = 0$ to $x/c = 10$. The lateral drift result agrees with O'Regan et al. [111], and it has confirmed that the airflow over the pressure surface tends to roll in toward the fuselage over the wingtip trailing edge. The mechanism consequently causes the vortex to deviate laterally at a rate that decreases with distance downstream, as described by Devenport et al. [106].

Looking at Figure 2.17 and Figure 2.18, the vertical shift of the vortex core reveals an interesting phenomenon that is independent of winglet configurations. At $\alpha = 2°$, the vortex core shifts upwards as it develops downstream, while the vortex core is going downwards for the case of $\alpha = 12°$. A plausible explanation is that a higher angle of attack generates a stronger wingtip vortex and leads to a more pronounced induced downwash. This enhanced downward induced velocity deflects the vortex trajectory downward, in agreement with the classical behaviour of strong trailing vortices [41]. The contrasting behaviour at low α suggests a weaker induced velocity field, allowing residual upwash and secondary flow to influence the vortex ascent.

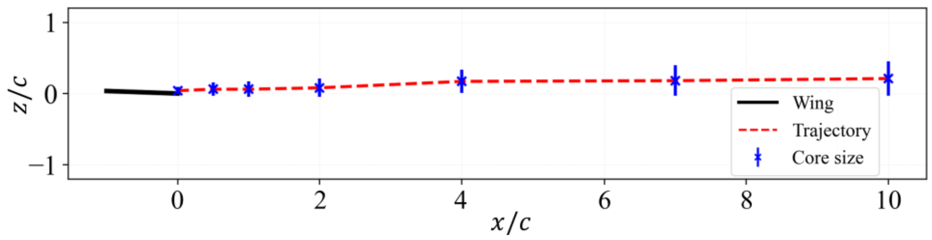

(a) No winglet at $\alpha = 2°$

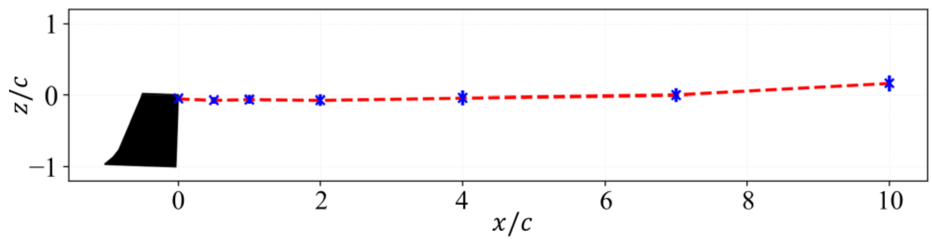

(b) Blended winglet at $\alpha = 2°$

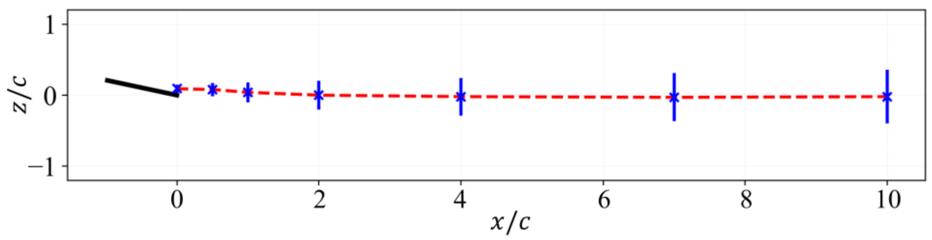

(c) No winglet at $\alpha = 12°$

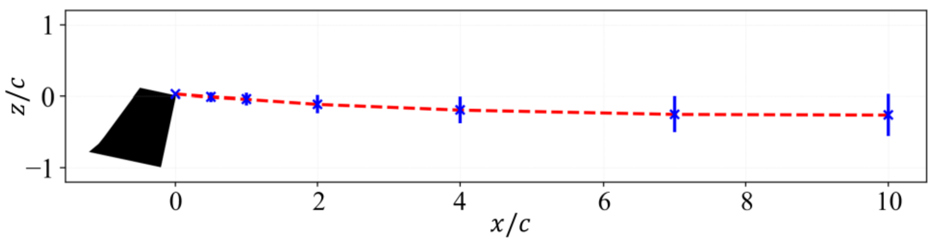

(d) Blended winglet at $\alpha = 12°$

Figure 2.18. Vortex trajectory and development, side view.

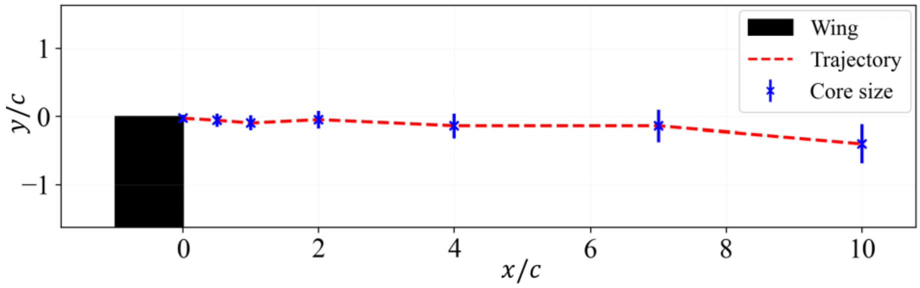

(a) No winglet at $\alpha = 2°$

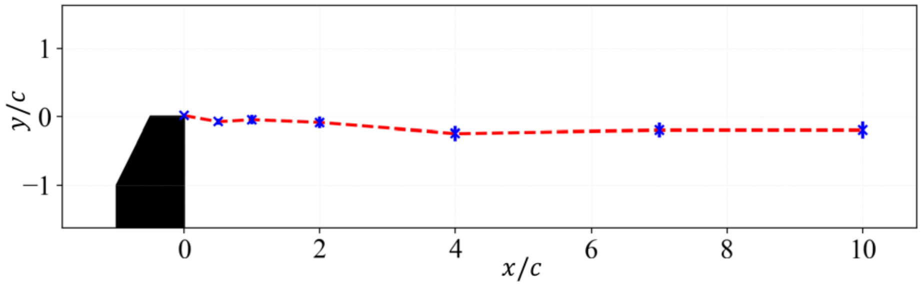

(b) Blended winglet at $\alpha = 2°$

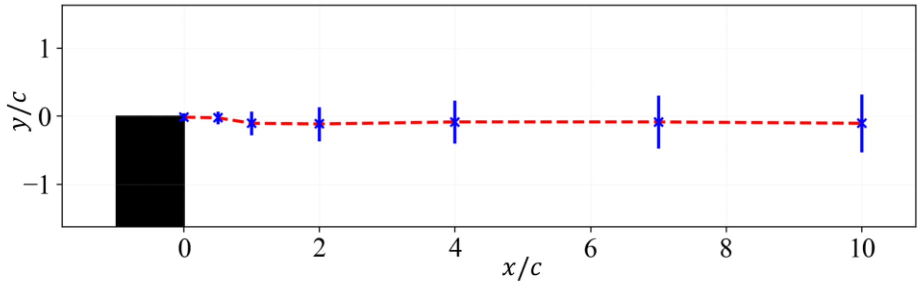

(c) No winglet at $\alpha = 12°$

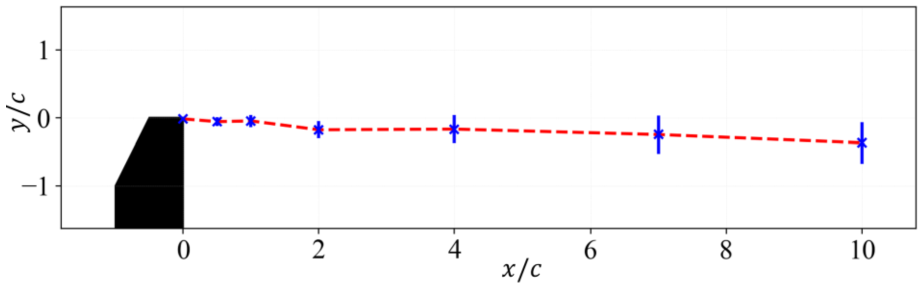

(d) Blended winglet at $\alpha = 12°$

Figure 2.19. Vortex trajectory and development, top view.

2.5 Summary and Recommendations

This work presented a new and cost-effective methodology to capture wing wake vortices in a wind tunnel environment. The proposed perspective upright correction (PUC) method enables the accurate vortex characterisation using a single camera positioned at arbitrary, non-normal viewing angles. By using a checkered reference pattern for geometric initialisation, the approach ensures that the slanted and tilted images can be rectified reliably.

A simple validation test has proved that the accuracy of the image capturing and processing for the slanted view image is comparable with or better than the native upright camera alignment. Moreover, the wind tunnel test with the PUC methodology was demonstrated on a wing model with blended winglets to show the reduction of the core size of the wingtip vortices. The clarity and quality of the acquired flow structures may be further improved using a laser sheet emitter with finer beam width.

The corrected vortex core radius and location are subsequently used to parameterise the vortex physics via the Lamb–Oseen model. Despite the limitations of the numerical model such as the axisymmetric vortex assumption and uniform vortex core shape and size, the result of each x/c plane has shown the growth of vortex size with decaying tangential velocity. The information may provide some guidelines on the vortices encountered by the trailing aircraft in the wake vortex surfing. These insights offer useful guidance on the nature of vortical structures relevant to wake-encounter and wake-surfing applications. The results from the experiment will be cross validated with the established LES framework [8] in Chapter 3 to ensure the accuracy of this cost-effective PUC setup. The comparison includes vortex core shape contours and detailed downstream development for different wing configurations.

To sum up, the contribution of the experimental investigation is not the wind tunnel facility itself, but the development of a correction methodology that improves the interpretation of smoke visualisation results. The corrected images enable more consistent comparison with LES predictions through improved representation of vortex position, shape, and size.

The proposed methodology can be further improved for any future work on wind tunnel experiment. The laser sheet emitter and camera may be placed outside of the wind tunnel to keep the wind tunnel test section clean. Automated image correction tools based on modern computer vision techniques could eliminate the manual post-processing. Finally, integrating this approach with Particle Image Velocimetry (PIV) to capture simultaneous qualitative visualisation and quantitative measurement of the complex, unsteady vortex dynamics downstream of bluff bodies or lifting surfaces.

Chapter 3

Computational Modelling of Wingtip Vortices with LES

The experimental characterisation presented in the previous chapter provides qualitative insight into the wingtip vortices development but are subjected to several inherent limitations. The finite size of the wind tunnel test section restricts the observation of vortex development to the near field region, let alone the space required for formation flight. In addition, the measurements are limited to the visual structure of the vortex rather than detailed velocity and turbulence quantities within the flow field. To overcome these constraint, computational fluid dynamics (CFD) is employed to complement the experimental observations and provide a more comprehensive description of the flow field.

Computational fluid dynamics (CFD) has become an increasingly powerful and promising tool in the current state due to the advanced development of high-performance computing and numerical algorithms. Compared to experimental testing, CFD is relatively inexpensive, and the costs are expected to be lowered as the computers get more powerful. Furthermore, CFD offers broad flexibility for detailed interrogation of the flow field at any location of interest and interpret its performance through a set of thermal and aerodynamic parameters. However, rigorous validation remains necessary to ensure the numerical framework is capable of estimating the underlying physics before applying to the research cases. Therefore, the CFD methodology in present chapter is first validated against published numerical and experimental data, followed by further verification against the wake vortex characterisation obtained from the wind tunnel experiments in Chapter 2.

The primary CFD research instrument used in this thesis is OpenFOAM (Open-source Field Operation and Manipulation) [95], a free, open-source C++ toolbox for the development and customised numerical solvers, and it is also one of the leading and most widely adopted CFD software. OpenFOAM offers an extensive range of solver suite for applications ranging from complex fluid flows involving chemical reactions, turbulence, and heat transfer, to acoustics, solid mechanics, and electromagnetics. It has been successfully applied to the simulation of aerofoil wakes and trailing vortices [61, 112]. The active user community of OpenFOAM has grown steadily and expand its capabilities through producing new models and valuable utilities to complement the official releases.

In CFD, the simulation process is typically divided into three main stages, namely pre-processing, numerical solving, and post-processing. Pre-processing involves geometry preparation, mesh generation and specification of boundary conditions. The numerical solver then computes the governing flow equations, and the resulting flow field is analysed during post-processing to extract the necessary aerodynamic and turbulence characteristics.

For the simulation of wingtip vortices, CFD has been widely applied to investigate vortex formation and downstream development [113, 114]. However, it has be reported that conventional turbulence models often underpredict vortex strength and accelerate vortex dissipation as the flow propagates downstream [63]. This limitation arises from excessive numerical diffusion and turbulence modelling assumptions that damp the rotational core of the vortex [115]. To address this issue, several modelling approaches have been proposed to improve vortex preservation in numerical simulations.

For example, O'Regan et al. [111] presented the CFD model with vorticity confinement model to capture the trailing vortices generated by a symmetrical aerofoil profile of NACA 0012. The CFD model with additional forcing term aims to retain the vortex strength in the downstream. The results covered the normalised axial velocity, vortex trajectory, vortex size and vortex core centre location at $\alpha = 10°$. The literature also incorporates wind tunnel test data, which makes it a comprehensive source for validation. The CFD validation in this thesis is using the standard URANS and LES solvers without modification on the source code. The accuracy of the turbulence models in trailing vortices modelling will be assessed, in order to forming the basis for the subsequent application to formation flight simulations.

3.1 Pre-processing

The first step in establishing the CFD framework is to construct an aerodynamic geometry of interest. This may comprise an isolated wing, a full aircraft model, or any subcomponent relevant to the study. In the present work, a 3D wing with NACA 0102 aerofoil profile is built using Autodesk® Inventor® Professional [116], with a chord length of 0.14m, and semi-span of 0.15m as illustrated in Figure 3.1. The wing model is exported in .obj format before importing to OpenFOAM for computational domain setup and mesh generation.

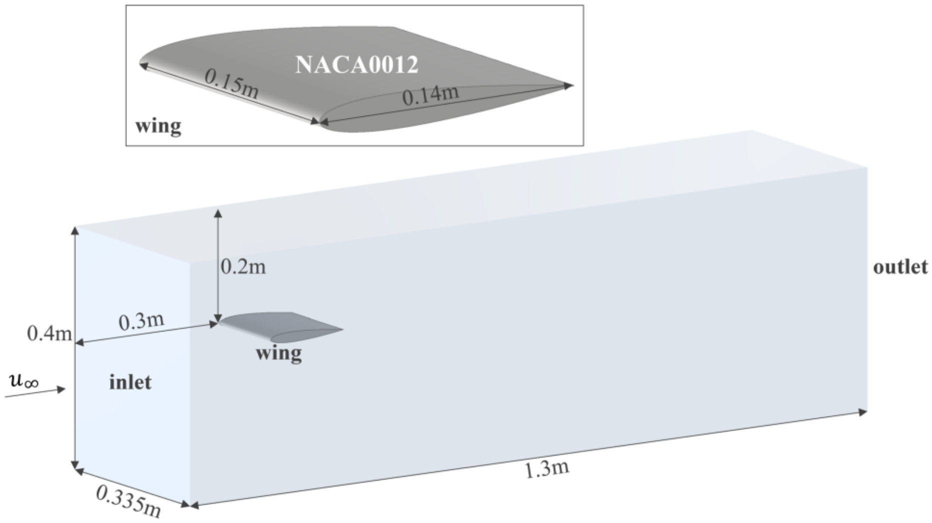

Figure 3.1 Wing model in domain for verification.

The simulation domain and boundary condition for the validation case in Figure 3.1 are constructed to match with the reference configurations [111] as closely as possible. Each surface in the setup is systematically grouped and named, to facilitate the process such as boundary conditions and mesh refinement controls. The top, side, and bottom faces of the outer domain are grouped under the label "wall", while all surfaces associated with the wing geometry are collectively assigned to the "wing" group. The remaining boundary patches – inlet, outlet, and sym (the symmetry plane) are explicitly named to ensure clarity and consistency throughout the pre-processing and solver setup stages. This structured naming convention streamlines subsequent steps such as applying boundary conditions, extracting flow-field data, and automating mesh operations in OpenFOAM.

The domain inlet is prescribed with a uniform freestream velocity of $u_\infty = 34m/s$ which corresponds to a chord-based Reynolds number of $Re_c = 3.25 \times 10^5$. The outlet is conditioned as constant zero pressure and the symmetry plane at the wing root is to represent the mid-span plane of an equivalent full-span wing. The wing geometry is treated with a no-slip boundary condition to resolve the viscous boundary layer and capture the shear-driven roll up that seeds the wingtip vortex system. The remaining walls of the domain are modelled as slip boundaries [117], which appoints zero shearing stress and prevents artificial viscous damping effect on the airflow on the surface.

The domain and geometry are further processed in OpenFOAM through a combination of blockMesh [118] for the base grid and snappyHexMesh [119] for local refinement near the wing and anticipated vortex core region. Previous mesh refinement study [114] indicate that a grid size resolution of 0.21% chord was required in the vortex core region to resolve the downstream propagation of the wingtip vortex in RANS model, but such resolution is prohibitively expensive for the LES case. Other research suggested implementation of adaptive grid refinement (AMR) method [120] or vorticity confinement model [111] to prevent the excessive numerical dissipation. The adoption of adaptive grid refinement yielded comparable results with reduced cell count, but the benefits are limited to flows where refinement is focused around the fixed features [121] such as wing or body. For wake-dominated flows, the continual re-meshing introduces abrupt variations in cell size that may yield discontinuous eddy viscosity fields, potential numerical artefacts, and degraded vortex fidelity [122]. Additionally, the dynamic overhead of frequent refinement escalates the overall computational cost significantly.

Due to the strong dependency of wingtip vortex prediction on spatial resolution, a mesh sensitivity analysis was conducted to assess the influence of mesh refinement on the predicted vortex characteristics. The assessment was performed using the baseline single wing configuration with k-$\omega\ SST$. Four mesh resolutions were considered by varying the local refinement level within the vortex region while maintaining consistent domain dimensions and boundary conditions. The mesh sensitivity was evaluated based on vortex-specific parameters, including the vortex core radius and tangential velocity magnitude, to represent the ability of the numerical model to capture vortex intensity, structure, and downstream evolution.

Table 3.1 Mesh sensitivity study.

Mesh	**Cells**	**Δ/c in vortex core region**	**Vortex core radius, r_c/c**	**$u_{\theta,max}/u_\infty$**
M1	3.0×10^6	1.7%	0.1551	0.4673
M2	3.8×10^6	1.3%	0.1245	0.4654
M3	4.6×10^6	1.1%	0.1103	0.4721
M4	5.4×10^6	1.0%	0.1074	0.4736

With the consideration of the mesh sensitivity study presented in Table 3.1, increasing the mesh resolution results in only minor variations in the predicted vortex characteristics. The vortex core radius and maximum crossflow velocity show minimal changes between the M3 and M4. Hence, the M3 meshing of 4.6×10^6 cells count is adopted, with nearly 80% of the total mesh cell concentrated within the vortex core region, where the local mesh resolution is approximately 0.011c as shown in Figure 3.2. A consistent near-wall mesh resolution on the wing is refined using `snappyHexMesh`, resulting in an average y^+ value of approximately 2-3 across the wing, with local values within the range of 2-5, which remains within the viscous sublayer region ($y^+ < 5$) [123]. Although a value closer to unity is generally preferred for fully resolving the near-wall region, the adopted y^+ resolution provides an appropriate balance on the computational resources with limited impact on the overall vortex shedding characteristics. The same mesh resolution was consistently applied for all turbulence model evaluations to ensure a consistent comparison of vortex prediction performance.

In addition, the refined mesh around the vortex core has a grid size of approximately 1.1% of the chord length, which provides a balance between accuracy and computational tractability for LES. The simulation is advanced using a time step of $1 \times 10^{-5} s$ to ensure the maximum Courant number remains below unity throughout the simulation.

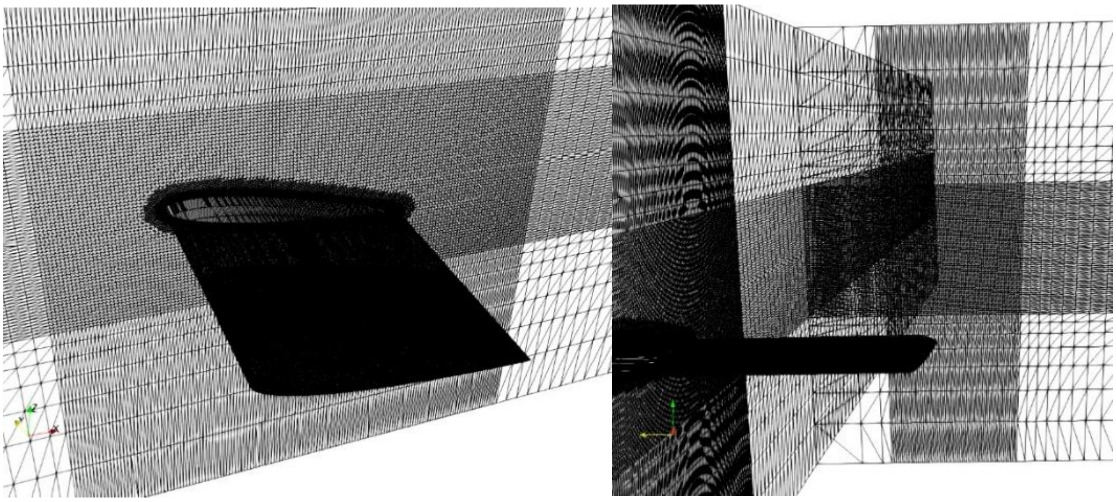

Figure 3.2 Mesh generation with snappyHexMesh for validation.

3.2 Numerical Solving

Based on the validation case settings, the pisoFoam solver [124] – an OpenFOAM transient, pressure-implicit split-operator (PISO) solver for incompressible flow is selected for the CFD simulations. The PISO algorithm is widely adopted for unsteady simulations because it enables efficient coupling between velocity and pressure fields while maintaining numerical stability for transient flows. The solver computes the evolution of the flow field by discretising the governing equations of fluid motion over the computational mesh and advancing the solution in time.

In computational fluid dynamics, the motion of a Newtonian fluid is governed by the Navier-Stokes equations, which express the conservation of mass, momentum and energy [125, 126]. In Cartesian tensor notation, the compressible governing equations may be written as follows,

$$\frac{\partial \rho}{\partial t} + \frac{\partial (\rho u_j)}{\partial x_j} = 0 \tag{4}$$

$$\frac{\partial (\rho u_i)}{\partial t} + \frac{\partial (\rho u_i u_j)}{\partial x_j} = -\frac{\partial p}{\partial x_i} + \frac{\partial \tau_{ij}}{\partial x_j} + \rho f_i \tag{5}$$

where ρ is the density of fluid, u_i is the velocity component in the x_i direction, p is the static pressure, f_i is the body-force component, $E = e + \frac{1}{2}u_k u_k$ is the total energy per unit mass, τ_{ij} is the viscous stress tensor, and q_j is the heat-flux vector. For a Newtonian fluid,

$$\tau_{ij} = \mu\left(\frac{\partial u_i}{\partial x_j} + \frac{\partial u_j}{\partial x_i}\right) - \frac{2}{3}\mu\frac{\partial u_k}{\partial x_k}\delta_{ij} \tag{6}$$

and, under Fourier's law,

$$q_j = -k_t\frac{\partial T}{\partial x_j} \tag{7}$$

where μ is the dynamic viscosity, k_t is the thermal conductivity, and T is the temperature. Eq. (4) represents continuity and therefore enforces conservation of mass, whereas Eq. (5) represents conservation of linear momentum. In practical, these equations are discretized over a finite computational mesh and solved numerically to obtain the spatial and temporal evolution of the flow field. For low-Mach incompressible flow, which is typical of many external aerodynamic simulations including the present research, the density is treated as constant and hence the continuity Eq. (4) for incompressible flow is written as,

$$\nabla \cdot u = 0 \tag{8}$$

where u denotes the velocity vector, while the momentum Eq. (**5**) is expressed as,

$$\frac{\partial u}{\partial t} + (u \cdot \nabla)u = -\frac{1}{\rho}\nabla p + \nu\nabla^2 u + f_i \tag{9}$$

where p represents the pressure, ρ is the density of fluid, and $\nu = \mu/\rho$ being the kinematic viscosity. These equations described the temporal evolution of the velocity and pressure fields in response to inertial, viscous, and pressure-gradient forces.

3.2.1 Unsteady Reynolds-Averaging Navier Stokes (URANS)

Direct numerical solution of the Navier-Stokes equations for turbulent flows is computationally impractical for most engineering applications due to the wide range of spatial and temporal scales involved. Consequently, turbulence is commonly modelled through the Reynolds-averaged Navier-Stokes (RANS), to approximate the effects of unresolved turbulent fluctuations. In the unsteady RANS (URANS) formulation [126], the instantaneous flow variables are decomposed into mean and fluctuating components, $u_i = \bar{u}_i + u_i'$, and the governing equations are time-averaged to obtain the following,

$$\frac{\partial \bar{u}_i}{\partial x_i} = 0 \tag{10}$$

$$\frac{\partial \bar{u}_i}{\partial t} + \bar{u}_j \frac{\partial \bar{u}_i}{\partial x_j} = -\frac{1}{\rho}\frac{\partial \bar{p}}{\partial x_i} + \nu \frac{\partial^2 \bar{u}_i}{\partial x_j^2} - \frac{\partial}{\partial x_j}\left(\overline{u_i' u_j'}\right) + f_i \tag{11}$$

where the additional term $\left(\overline{u_i' u_j'}\right)$ represents the Reynolds stress tensor, which accounts for the momentum transfer caused by the turbulent fluctuations. It is not known a priori and creates the turbulence closure problem. The most common closure for eddy-viscosity models is the Boussinesq hypothesis,

$$-\rho\overline{u_i' u_j'} = 2\mu_t S_{ij} - \frac{2}{3}\rho k \delta_{ij} \tag{12}$$

where μ_t is the turbulent eddy viscosity and $k = \frac{1}{2}\overline{u_i' u_i'}$ is the turbulence kinetic energy and S_{ij} is expressed as,

$$S_{ij} = \frac{1}{2}\left(\frac{\partial \bar{u}_i}{\partial x_j} + \frac{\partial \bar{u}_j}{\partial x_i}\right) \tag{13}$$

Thus, URANS does not alter the form of the governing conservation laws but modifies the stress term in the averaged momentum equation and introduces one or more auxiliary transport equations to determine μ_t. The turbulence model therefore enters the CFD solver through the closure of the Reynolds stresses, and its formulation strongly affects vortex roll-up and downstream dissipation.

Closure models such as the Spalart-Allmaras (S-A), the standard k-epsilon (k-ε) and k-omega shear stress transport (k-ω SST) introduce transport equations to approximate these Reynolds stresses and enable practical computation of turbulence flows. To establish a reliable baseline and assess model sensitivity, several commonly used URANS turbulence models [127] including the abovementioned S-A, k-ε and k-ω SST models. This preliminary evaluation aims to identify the most suitable turbulence formulation for capturing the generation, roll-up, and downstream persistence of trailing vortices.

3.2.1.1 Spalart-Allmaras (S-A) Model

The Spalart-Allmaras (S-A) model [128, 129] is a one-equation eddy-viscosity model developed for aerodynamic flows. Instead of solving directly for k and a second turbulence scale, the model solves a transport equation for a modified turbulent kinematic viscosity, $\tilde{\nu}$. Its standard form may be expressed as,

$$\frac{D\tilde{v}}{Dt} = c_{b1}\tilde{S}\tilde{v} + \frac{1}{\sigma}\left[\frac{\partial}{\partial x_j}\left((v + \tilde{v})\frac{\partial \tilde{v}}{\partial x_j}\right) + c_{b2}\left(\frac{\partial \tilde{v}}{\partial x_j}\right)^2\right] - c_{w1}f_w\left[\frac{\tilde{v}}{d}\right]^2 \tag{14}$$

where d is the distance to the nearest wall boundary, $\tilde{S}$ is a modified vorticity or strain measure, and f_w is a damping function. Within the URANS equations, the S-A model supplies the turbulent viscosity $\mu_t = \rho v_t$, which is then substituted into the Reynolds-stress closure of Eq. (12). Hence, the momentum equation itself is unchanged in structure, but the effective diffusion and production of momentum are altered through the modelled turbulent stress. As there is only one additional transport equation is solved, the S-A model is computationally economical and generally robust for attached or mildly separated flows. Its formulation is closely related to the wall distance and near-wall behaviour, which makes it favourable for boundary layer dominated applications.

The principal limitation of the S-A model [130] is that it represents turbulence using a single transported viscosity-like variable. As a result, it offers less freedom than other two-equation models in flows containing strong non-equilibrium turbulence or large-scale separation. Therefore, the predicted vortex structure and persistence remain sensitive to the mesh resolution.

3.2.1.2 Standard k-epsilon (k-ε) Model

The standard k-ε model [131, 132] is a two-equation eddy viscosity model in which the turbulent viscosity is computed from the turbulence kinetic energy k and its dissipation rate ε. The model transport equations are formulated as,

$$\frac{\partial(\rho k)}{\partial t} + \frac{\partial(\rho \bar{u}_j k)}{\partial x_j} = \frac{\partial}{\partial x_j}\left[\left(\mu + \frac{\mu_t}{\sigma_k}\right)\frac{\partial k}{\partial x_j}\right] + P_k - \rho\varepsilon \tag{15}$$

$$\frac{\partial(\rho \varepsilon)}{\partial t} + \frac{\partial(\rho \bar{u}_j \varepsilon)}{\partial x_j} = \frac{\partial}{\partial x_j}\left[\left(\mu + \frac{\mu_t}{\sigma_\varepsilon}\right)\frac{\partial \varepsilon}{\partial x_j}\right] + C_{\varepsilon 1}\frac{\varepsilon}{k}P_k - C_{\varepsilon 2}\rho\frac{\varepsilon^2}{k} \tag{16}$$

where the eddy viscosity μ_t and the turbulence production term P_k are expressed as,

$$\mu_t = \rho C_\mu \frac{k^2}{\varepsilon} \tag{17}$$

$$P_k = 2\mu_t S_{ij} S_{ij} \tag{18}$$

The role of the k-equation is to account for the transport, production and destruction of the turbulence kinetic energy, while the ε-equation provides the turbulence time scale by describing the rate at which k is dissipated into smaller scales. The two equations collectively determine the eddy viscosity in Eq. (17), which then closes the Reynolds-stress term in Eq. (12). Due to the explicit transport equation and the second equation for dissipation, the standard k-ε model offers more flexibility in free-shear and fully turbulent flows as compared to the S-A model. However, the model is known to be less reliable in the near-wall region unless an appropriate wall treatment is used [133], and it is often less accurate for flows subject to strong adverse pressure gradients or pressure-induced separation such as wake vortices. These characteristics will lead to overly diffusive wakes and weakened coherent vortical structures when compared to higher fidelity model.

3.2.1.3 k-omega Shear Stress Transport (k-ω SST) Model

The k-ω SST model [134] combines the near-wall advantages of the k-ω formulation with the improved free-stream behaviour of the k-ε model through blending functions. According to Menter's formulation [134, 135], the governing transport equations for turbulent kinetic energy k and specific dissipation rate ω are expressed as follows,

$$\frac{\partial(\rho k)}{\partial t} + \frac{\partial(\rho \bar{u}_j k)}{\partial x_j} = P_k - \beta^* \rho k \omega + \frac{\partial}{\partial x_j}\left[(\mu + \sigma_k \mu_t)\frac{\partial k}{\partial x_j}\right] \tag{19}$$

$$\frac{\partial \rho \omega}{\partial t} + \frac{\partial(\rho \bar{u}_j \omega)}{\partial x_j} = \alpha \frac{\omega}{k} P_k - \beta \rho \omega^2 + \frac{\partial}{\partial x_j}\left[(\mu + \sigma_\omega \mu_t)\frac{\partial \omega}{\partial x_j}\right] + 2(1 - F_1)\rho \sigma_{\omega 2}\frac{1}{\omega}\frac{\partial k}{\partial x_i}\frac{\partial \omega}{\partial x_i} \tag{20}$$

where P_k denotes the turbulence production term. The blending function F_1 which transitions the formulation between the inner k-ω and the outer k-ε regions, is defined as,

$$F_1 = \tanh\left\{\left[\min\left[\max\left(\frac{\sqrt{k}}{\beta^* \omega y}, \frac{500\nu}{y^2 \omega}\right), \frac{4\sigma_{\omega 2} k}{CD_{k\omega} y^2}\right]\right]^4\right\} \tag{21}$$

where

$$CD_{k\omega} = \max\left(2\rho \sigma_{\omega 2}\frac{1}{\omega}\frac{\partial k}{\partial x_i}\frac{\partial \omega}{\partial x_i}, 10^{-10}\right) \tag{22}$$

and the turbulent viscosity ν_t is calculated using,

$$\mu_t = \rho a_1 \frac{k}{max(a_1 \omega, S F_2)} \tag{23}$$

where S is the mean strain rate magnitude, and F_2 is the second blending function defined as,

$$F_2 = \tanh\left[\left[\max\left(\frac{2\sqrt{k}}{\beta^* \omega y}, \frac{500\nu}{y^2 \omega}\right)\right]^2\right] \tag{24}$$

The default value for the model coefficients used in pisoFoam are listed in Table 3.2:

Table 3.2 Default model coefficient for the k-ω SST model.

β^*	σ_{k1}	$\sigma_{\omega 1}$	α_1	β_1	σ_{k2}	$\sigma_{\omega 2}$	α_2	β_2	a_1	b_1	c_1
0.09	0.85	0.5	5/9	3/40	1.0	0.856	0.44	0.0828	0.31	1.0	10.0

The zonal formulation enables the near-wall region is resolved using the standard k-ω model and progressively blending to the k-ε formulation in the outer shear layer and far-field wake. The damped cross-diffusion derivative term in the ω equation [136] is the essential component to modify the eddy viscosity formulation to account for the transport effects of the turbulent shear stress. This provides a more accurate flow-field prediction, particularly for cases involving adverse pressure gradients and pressure-induced separations. The intrinsic low Reynolds corrections in the SST model also eliminates the requirement for an additional treatment for the wall damping functions. The SST variant of the standard k-ω model has improved the accuracy and stability for the wake vortex simulation yet with only marginally longer computational run time.

Similar to other URANS closure models, the SST model replaces the unknown Reynolds stresses through Eq. (12). However, the functional form of μ_t in Eq. (23) with the cross-diffusion and blending functions are causing the effective turbulent stress response to differ materially from both S-A and standard k-ε. This generally makes SST more reliable in wall-bounded flows with separation than standard k-ε model, although it still models rather than resolves the unsteady large-scale coherent turbulence.

3.2.1.4 Wake Vortex Results by Different Turbulence Models

The three URANS models share the same underlying conservation laws derived from the Navier-Stokes equations but differ in the way in closing the Reynolds stress term. Using the computational setup as specified in the pre-processing section, the trailing vortices induced by the wing geometry are assessed and analysed. The comparison focusses on the vortex characteristics such as the maximum vertical velocity components, core axial velocity deficit and the vortex core diameter. The numerical results across different turbulence models are compared against the published experimental results of wind tunnel measurements using a five-holes probe (Exp. Fhp.) [111]. The comparison is summarised in Table 3.3.

Table 3.3 Comparison of wake vortex represented by different turbulence models.

	Maximum velocity component u_z, at $x/c = 0$	Core axial velocity deficit, at $x/c = 0$	Vortex core diameter along y-axis, at $x/c = 0$
Exp. Fhp. [111]	$0.5309u_\infty$	$0.7233u_\infty$	$0.1149c$
S-A (current)	$0.2935u_\infty$	$0.8125u_\infty$	$0.1316c$
k-ε (current)	$0.3374u_\infty$	$0.8051u_\infty$	$0.1567c$
k-ω SST (current)	$0.4721u_\infty$	$0.8672u_\infty$	$0.1149c$

From the results presented, the *k-ω SST* model exhibits the closest agreement with the experimental data in terms of the vertical velocity component and the vortex core diameter. In contrast, both the S-A and k-ε predict a lower vertical velocity magnitude and larger core diameter. Since the same mesh resolution of equivalent to $y^+ \approx 2 - 3$ and near-wall treatment were applied consistently across all turbulence models, these differences are primarily attributed to the inherent characteristics of the turbulence models. These discrepancies suggest that the two models are less capable in preserving the vortex strength and tend to produce a more diffusive vortex as it propagates downstream. Although the *k-ω SST* does not outperform the other two models in predicting the axial velocity deficit, the values remain comparable to the other two. Overall, the *k-ω SST* model demonstrates its superior performance in capturing the vortex-induced velocity and maintaining a more confined vortex core structure attributed to its improved balance between near-wall fidelity and free-stream robustness. Therefore, the *k-ω SST* model is selected as the URANS turbulence model for the subsequent simulations.

Nevertheless, all URANS closures retain the central limitation that the large, unsteady coherent turbulence is not resolved directly but represented through eddy viscosity. Consequently, even the vortices in the *k-ω SST* turbulence model continue to dissipate too rapidly. The peak tangential velocity at $x/c = 3$ location reaches only about 50% of the experimental data, indicating that the model fails to preserve vortex strength downstream. This is the well-known limitations of URANS models when applied to strongly swirling, curvature-dominated flows, where excessive eddy viscosity leads to premature diffusion of coherent vortical structures.

To overcome the excessive vortex dissipation issues, O'Regan et al. [120] proposed to adopt adaptive mesh refinement method to further refine the mesh around the vortex core, or alternatively to use vorticity confinement model [137] which introduces additional forcing terms, $\hat{f}_\omega = -\epsilon\rho(\hat{n} \times \vec{\omega})$ into the body-force component in the momentum Eq. (**11**), where ϵ is a confinement coefficient, ρ is the density, $\hat{n}$ is a unit vector pointing in the direction of the gradient of vorticity magnitude, and ω is the local vorticity. This term effectively redirects vorticity towards the vortex centroid, helping mitigate the artificial radial spreading of the vortex caused by numerical dissipation. However, the vorticity confinement flow model exhibited an unexpected axial velocity excess within the vortex core, which contradicts the experimental results as well as the typically reported axial velocity deficit [106, 138]. Other approach includes using a higher fidelity model, where Kolomenskiy et al. [139] suggested a coupled RANS-LES model. This strategy leverages the computational efficiency of RANS for boundary-layer resolution while enabling LES to capture the large-scale coherent structures that dominate trailing-vortex evolution.

3.2.2 Large Eddy Simulation (LES)

Large Eddy Simulation (LES) [140, 141] is derived directly with the same Navier-Stokes governing Eqs. (8) and (9). However, unlike URANS where the entire turbulence spectrum is modelled through Reynolds averaging, LES employs a spatial filtering operation to separate the large, high energy turbulent motions from the smaller unresolved scales [141]. For a general flow variable ϕ, the spatial filtering process decomposes the instantaneous quantity into resolved and unresolved components, as follows,

$$\phi = \tilde{\phi} + \phi^{sgs} \tag{25}$$

where ϕ denotes the resolved, filtered quantity and ϕ^{sgs} denotes the unresolved subgrid-scale (SGS) contribution. In contrast to URANS approaches which models the entire turbulence spectrum, LES resolves the large-scale eddies that contains majority of the energy while modelling only the smaller scales turbulence. This is achieved by applying a spatial filter to the incompressible Navier-Stokes equations [141], yielding the governing Eqs. (8) and (9) to the following filtered equations,

$$\frac{\partial \tilde{u}_i}{\partial x_i} = 0 \tag{26}$$

$$\frac{\partial \tilde{u}_i}{\partial t} + \tilde{u}_j \frac{\partial \tilde{u}_i}{\partial x_j} = -\frac{1}{\rho}\frac{\partial \tilde{p}}{\partial x_i} + \nu \frac{\partial^2 \tilde{u}_i}{\partial x_j^2} - \frac{\partial \tau_{ij}^{sgs}}{\partial x_j} + f_i \tag{27}$$

where the tilde denotes the filtered velocity field and the component τ_{ij}^{sgs} represents the subgrid-scale (SGS) stress tensor. This additional stress term arises due to the nonlinear convective terms in the Navier-Stokes equations and accounts for the momentum transfer between the resolved large-scale motions and the unresolved SGS turbulence. The SGS stress tensor is defined as,

$$\tau_{ij}^{sgs} = \widetilde{u_i u_j} - \tilde{u}_i \tilde{u}_j \tag{28}$$

and represents the effect of unresolved turbulence on the resolved flow field. In the LES modelling, this tensor is typically decomposed into anisotropic and isotropic components,

$$\tau_{ij}^{sgs} = a_{ij}^{sgs} + \frac{2}{3} k_r \delta_{ij} \tag{29}$$

where a_{ij}^{sgs} is the anisotropic SGS stress, k_r represents the subgrid-scale kinetic energy, and δ_{ij} is the Kronecker delta. The anisotropic component a_{ij}^{sgs} is modelled using an eddy-viscosity hypothesis, which correlates with the SGS eddy viscosity μ^{sgs}, and the resolved strain rate tensor $\tilde{S}_{ij}$,

$$a_{ij}^{sgs} = -2\mu^{sgs} \tilde{S}_{ij} \tag{30}$$

where the filtered strain-rate tensor is defined as,

$$\tilde{S}_{ij} = \frac{1}{2}\left(\frac{\partial \tilde{u}_i}{\partial x_j} + \frac{\partial \tilde{u}_j}{\partial x_i}\right) \tag{31}$$

and the isotropic part of the SGS stress tensor is related to the SGS turbulent kinetic energy k_r as follows,

$$k_r = \frac{1}{2} \tau_{ij}^{sgs} \tag{32}$$

In most LES implementations, this isotropic component is absorbed into the modified filtered pressure term because it contributes only a relatively small portion of the total turbulent energy. Consequently, the SGS stress tensor is formulated as follows,

$$\tau_{ij}^{sgs} = -2\mu^{sgs} \tilde{S}_{ij} + \frac{1}{3} \rho \tau_{ij}^{sgs} \delta_{ij} \tag{33}$$

which accounts for the effects of unresolved small-scale turbulence. The SGS stress tensor are commonly modelled using formulations such as the Smagorinsky model [142, 143], which is one of the most widely adopted formulations due to its simplicity and robustness. In this model, the unresolved turbulence is represented using an eddy viscosity μ^{sgs} which is expressed in term of the local strain rate of the resolved flow field, as follows,

$$\mu^{sgs} = \rho (C_s \Delta)^2 \left|\tilde{S}_{ij}\right| \tag{34}$$

where C_s is the Smagorinsky constant, typically taken as 0.18 and Δ being the filter width, commonly approximated by the local grid scale. The magnitude of the filtered strain-rate tensor is defined as,

$$\left|\tilde{S}_{ij}\right| = \left(2\tilde{S}_{ij}\tilde{S}_{ij}\right)^2 \tag{35}$$

substituting the Smagorinsky eddy viscosity into the SGS stress formulation yields the momentum equation for LES in the following form,

$$\frac{\partial \rho \tilde{u}_i}{\partial t} + \frac{\partial (\rho \tilde{u}_i \tilde{u}_j)}{\partial x_j} = -\frac{\partial \tilde{p}}{\partial x_i} - \frac{\partial}{\partial x_j}\left(\tau_{ij} + \tau_{ij}^{sgs}\right) \tag{36}$$

where τ_{ij} denotes the viscous stress tensor and τ_{ij}^{sgs} accounts for the unresolved subgrid-scale stresses.

In vortex shedding flows [144], the large vortices contain the majority of the turbulent kinetic energy and dominate the transport of mass, momentum, and energy within the wake. LES is therefore particularly well suited for wake-vortex studies, as it spatially filters the numerical grid scale and resolves the large-scale turbulence explicitly by the governing discretised equations while models the SGS motions through additional closure terms. The isotropic part to be modelled is typically absorbed into the filtered pressure term as it accounts only for a relatively small portion of the total turbulence energy within the flow field. Consequently, LES yields a higher fidelity in capturing the vortex structure and downstream evolution compared to URANS models. Although it incurs a significantly higher computational cost, the improved fidelity in preserving vortex core strength and capturing fine-scale turbulent dissipation makes it an essential component of the present validation study.

The numerical simulations are advanced in time using a second-order implicit backward differencing scheme to ensure numerical stability while maintaining temporal accuracy for unsteady vortex evolution. The pressure–velocity coupling is handled using a `PIMPLE`-based algorithm with a single outer corrector loop (`nOuterCorrectors=1`), resulting in `PISO`-like transient behavior. Three pressure corrector iterations are applied per time step to ensure tight coupling between velocity and pressure fields, while a momentum predictor step is activated to improve the temporal accuracy of the velocity solution.

Spatial discretization of gradient terms employs a second-order Gauss linear scheme, with cell-limited treatment applied to velocity and turbulence quantities to maintain boundedness in regions with strong gradients. Convective terms are discretized using a bounded central-differencing scheme to minimize numerical dissipation while preserving stability in regions of strong velocity gradients such as the vortex core. Diffusion terms are discretized using a Gauss linear formulation with limited non-orthogonal correction to account for mesh non-orthogonality.

To enhance the accuracy of LES in capturing the small-scale motions of the wingtip vortex, the computational mesh is selectively refined around the vortex core, thereby reducing the local filter width Δ. This meticulous refinement ensures that the LES model effectively captures the smaller scales features and intricate fluctuations near the vortex core [145]. Therefore, the accuracy of the LES in the refined region is greatly improved, approaching levels akin to Direct Numerical Simulation (DNS). The LES simulation is advanced for a minimum 20 chord-flow-through times [146] over the wing model to ensure the decay of initial transients and attain a fully converged and stable flow field for detailed vortex analysis.

3.3 Post-processing

ParaView [97] is the application developed for data extraction, to allow visualisation of vorticity fields, contours and streamlines of the velocity and pressure distributions. The software also supports the computations of the aerodynamics parameters such as lift, drag, moment and stability derivatives. The results from OpenFOAM in the present work were all extracted to ParaView for post-processing.

The vortex core location is identified at where u_y and u_z are minimum. Once the core position was established, velocity profiles across the vortex core at plane $x/c = 0$, 1, 2 and 3 were plotted for validation, as illustrated in Figure 3.3.

The validation of the URANS and LES model based on the normalised tangential velocity across the vortex core is presented in Section 3.4. The presence of wake vortex exhibited a distinct V-shaped pattern in the plots. The vortex core location is corresponding to the location of trough of the V-shape, where the tangential velocity approaches zero. The diameter of the vortex core is determined by measuring the distance between the two peak positions, where the crossflow velocity is at maximum. The tangential velocity is calculated from the resultant of transverse velocity vectors of y and z directions, defined as $u_\theta = \left(u_y{}^2 + u_z{}^2\right)^{1/2}$. This parameter is one of the critical parameters in vortex capturing as it indicates the swirling motion and strength of the vortex structure.

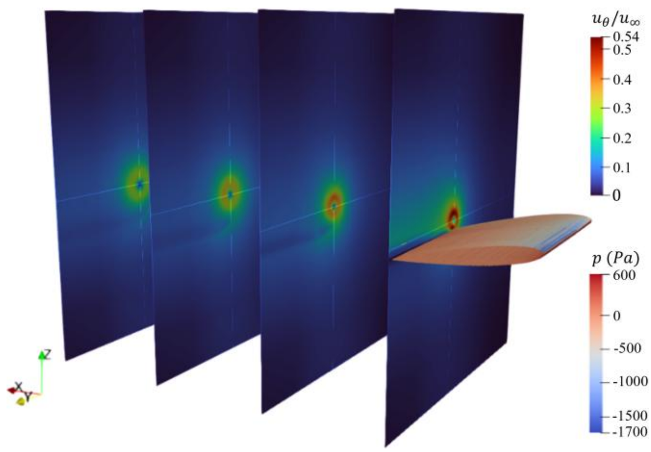

Figure 3.3 Plotting data across vortex core, for normalised u_x and u_θ.

3.4 Validating CFD with Published Data

From the results plotted in Figure 3.4, the LES performs markedly better than the URANS model as expected. Starting at $x/c = 0$, the URANS prediction is approximately 13% below experimental measurement, while LES deviates by only 5%. As the vortices developed downstream, the rapid dissipation of URANS expanded the deviation to 48% at $x/c = 3$. The LES improves this significantly by reducing the error by 21%.

In comparison, the URANS turbulence model with vorticity confinement correction from literature [111] has maintained an almost constant circulation throughout the $x/c = 0$ to $x/c = 3$, while the LES with the same confinement function tends to over-predict the vortical strength. Therefore, the present LES framework has adequately proved its capabilities in capturing the wake vortex structures and maintaining the near-field downstream characteristics with satisfactory fidelity.

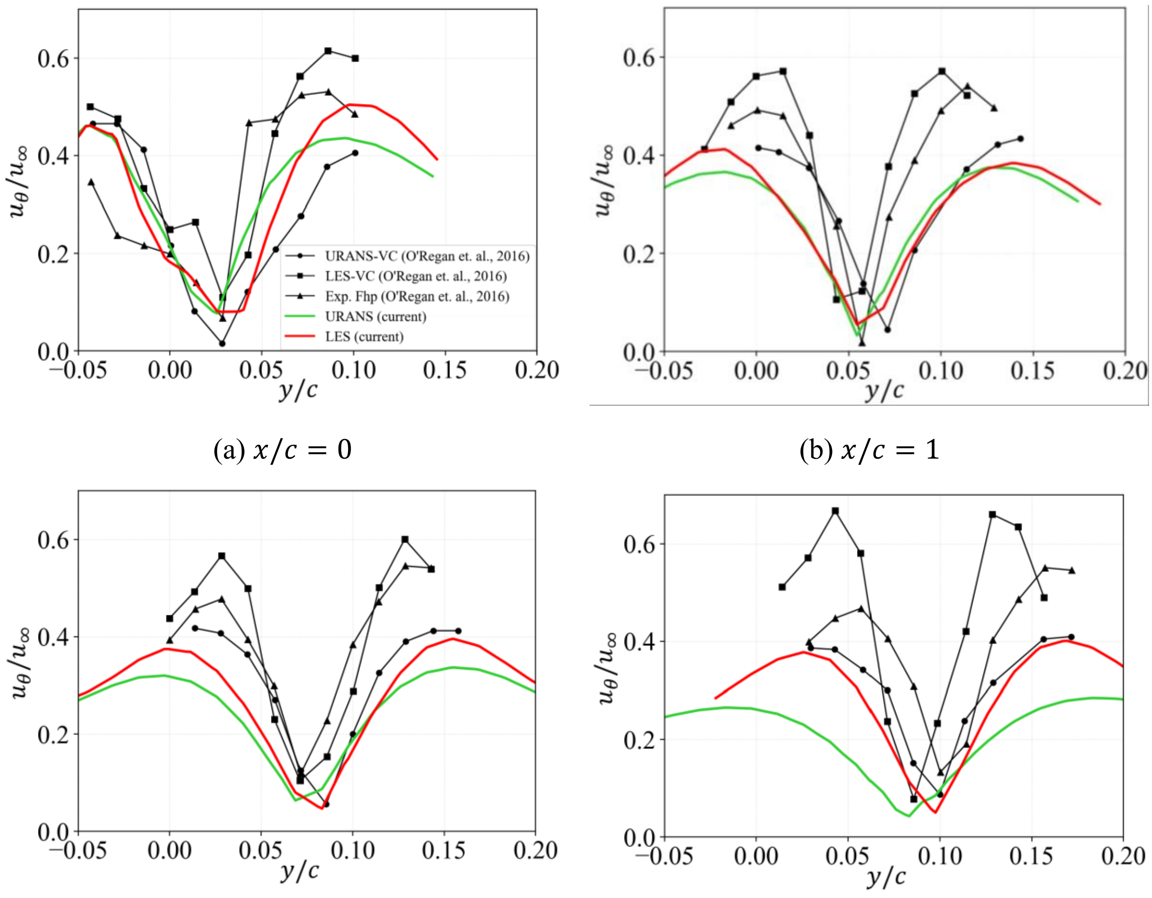

(a) $x/c = 0$ (b) $x/c = 1$

(c) $x/c = 2$ (d) $x/c = 3$

Figure 3.4 Normalised tangential velocity magnitude u_θ/u_∞ across the vortex core for $\alpha = 10°$.

In addition to the tangential velocity, the axial velocity profiles in the vicinity of the vortex core region are presented in Figure 3.5. As the wingtip vortices roll up, the rotational flow curls inwards to the vortex core centre, resulting in axial velocity deficit [138, 147]. The axial velocity deficit is inherently one of the unsteady factors in vortices. At $x/c = 0$, the axial velocities in all turbulence models and experiment are greatly fluctuated and exhibits a noticeable surplus value at the very core region. As the vortices further developed downstream, the axial velocity component within the vortex core was stabilised into a more consistent deficit form. In the present study, both the URANS and LES models have predicted the axial velocity deficit successfully. Despite the LES has a slight over-prediction, the overall deficits trends agree well with the DNS and LES results reported in the literature for similar configurations [134, 138]. Consistent with the tangential velocity comparisons, the axial velocity deficit in the LES simulation is closer to the experiment data, as compared to URANS results.

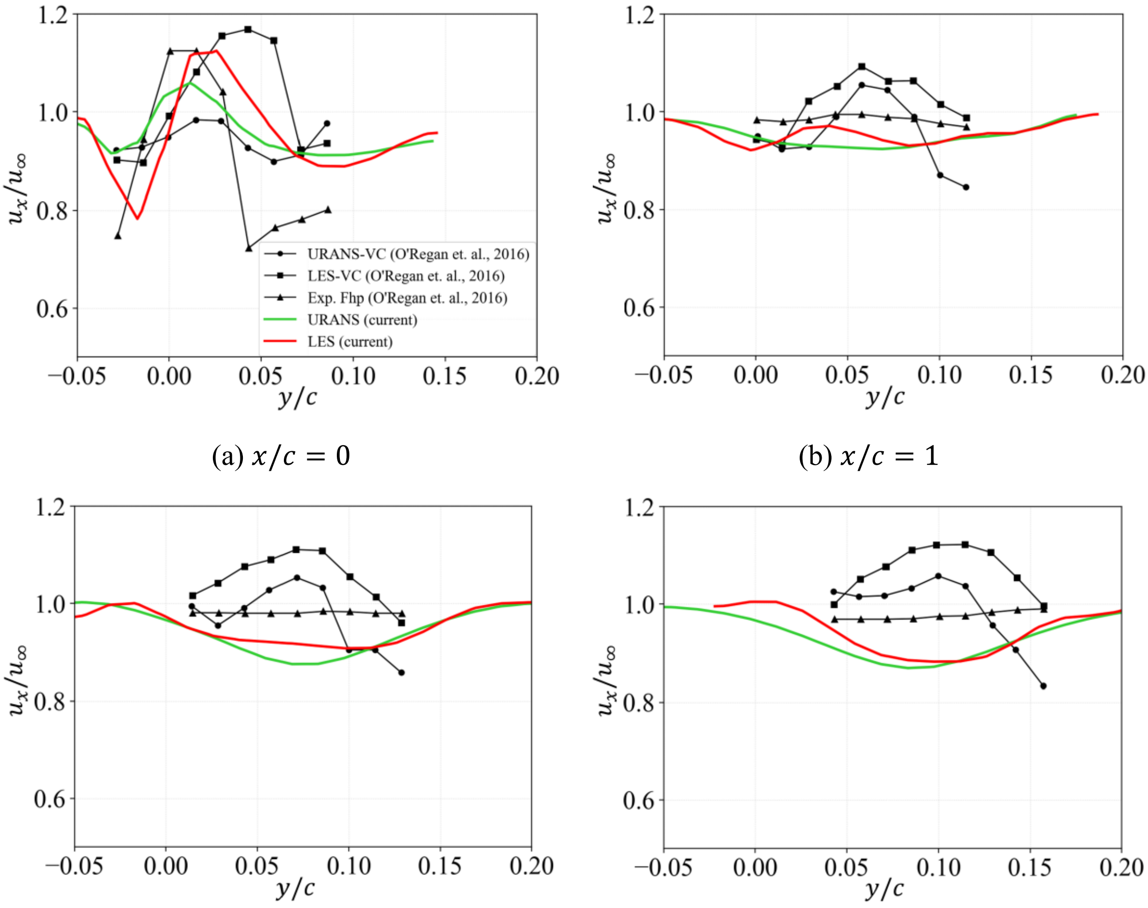

(a) $x/c = 0$ (b) $x/c = 1$

(c) $x/c = 2$ (d) $x/c = 3$

Figure 3.5 Normalised axial velocity u_x/u_∞ across the vortex core for $\alpha = 10°$.

With the tangential velocity distribution profile, the vortex core size can be easily defined by the distance of core centre to the point of maximum tangential velocity. The resulting vortex trajectory with the vortex core centre and size are plotted in Figure 3.6. As the turbulence dissipates downstream, the vortex core diffuses and grows in core radius. Both the URANS and LES track the core centre location with fair accuracy, though LES performs better in computing the vortex core size. The overall trajectory of the vortex core is moving inboard and marginally downwards, which agreed to the experimental trajectory as shown in Figure 3.6.

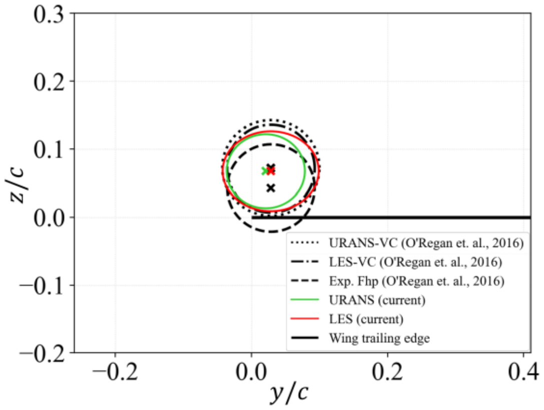

(a) $x/c = 0$

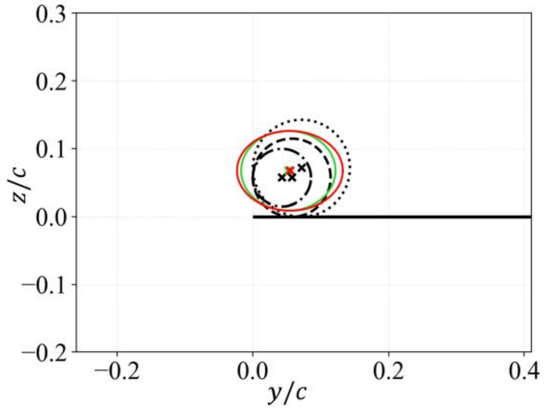

(b) $x/c = 1$

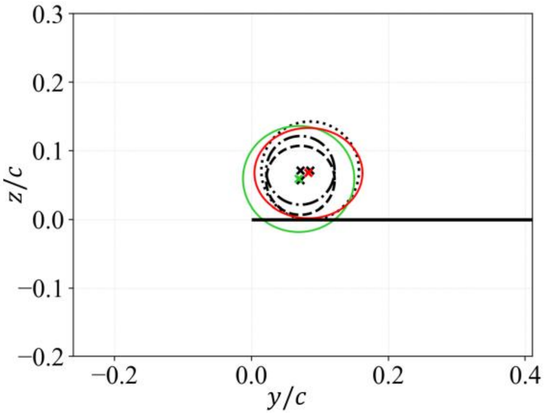

(c) $x/c = 2$

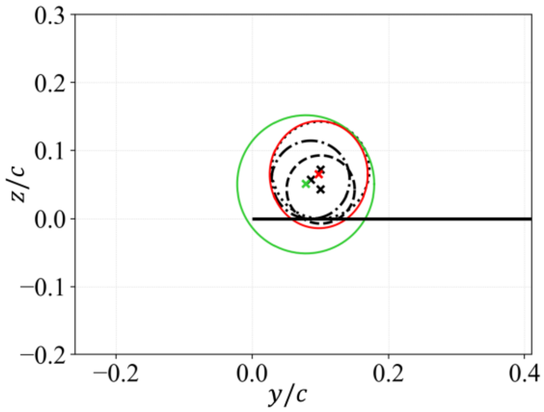

(d) $x/c = 3$

Figure 3.6 Downstream development of vortex trajectory, size, and core centre location for $\alpha = 10°$.

The validation results discussed above clearly demonstrate that LES offers superior accuracy in predicting the wake vortex physics. It is of higher confidence in resolving the turbulent structures and preserves the downstream evolution of the wingtip vortices in the near field. Thus, LES is chosen for the subsequent formation flight simulations. To quantify the aerodynamic benefits of wake vortex surfing, the general aerodynamic coefficients such as lift and drag must be accurately predicted. A further validation against the wind tunnel experiment conducted by Martínez-Aranda et al. [148] is therefore performed. The wing geometry in this experiment is using a rectangular NACA 0012 wing with chord length $c = 0.1m$, aspect ratio $AR = 2$ and Reynold's number $Re = 1.33 \times 10^5$. As shown in Figure 3.7, the predicted lift coefficient is matching well with the measurements from literature, but slightly underpredicted the drag coefficients for α below 12°.

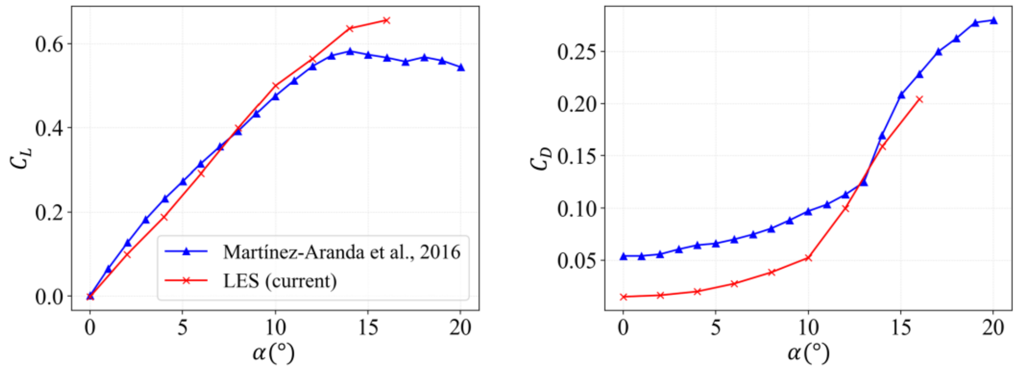

(a) Lift coefficient C_L validation (b) Drag coefficient C_D validation

Figure 3.7 Aerodynamics coefficient validation.

3.5 Validating CFD with Experimental Work

Prior to comparison with the wind tunnel observations from Chapter 2.4, the CFD framework was quantitatively verified against the published numerical and experimental investigation by O'Regan et al. [111].

The validation and analysis in the previous Section 3.4 has demonstrated the superior capability of LES in capturing the vortices behaviour and persistence compared to the unsteady RANS [8]. The LES model is validated against the literature data [111] on the tangential and axial velocity distribution across the vortex core, as well as the vortex core location and dimensions. The agreement obtained in key vortex parameters, including velocity distribution, vortex core characteristics, and circulation evolution, establishes confidence in the adopted numerical framework. Despite its high fidelity, the vortices modelled by the LES still appear to be about 4.35% – 5.56% more dissipative than the experimental results over each chord length in the streamwise direction.

In this section, the validated LES methodology [8] is applied to reproduce the present wind tunnel test condition, to validate against the wind tunnel experimental results [11, 149]. The objective of this comparison was to assess whether the numerical model could capture the experimentally observed vortex development and structure under the current configuration. The emphasis of the wind tunnel experiments was on the methodology of perspective upright correction to capture the spiral motion of smoke particles tracing the trailing vortices, while the velocity information was disregarded. Accordingly, the validation here emphasises on the near-field vortex behaviour observed in the experiments, which are the wake-spiral contours formed by the smoke visualisation.

Although the peak axial turbulence stress may occur near the vortex core and visually resemble the spiral structure, it actually represents a different aspect of flow dynamics. The widely accepted definition of vortex core radius is based on the distance from the core centre to the location of strongest vorticity or peak tangential velocity [111, 150, 151]. However, there has not been any comparative study on the relationship between the wake spiral profile and the peak tangential velocity profile. This comparison is therefore introduced as part of the present validation effort.

3.5.1 LES Preparation

The two wing geometries with the NACA 4412 aerofoil profile used in the wind tunnel experiments in Chapter 2 (Figure 2.3) were also reconstructed in 3D CAD modelling, as shown in Figure 3.8.

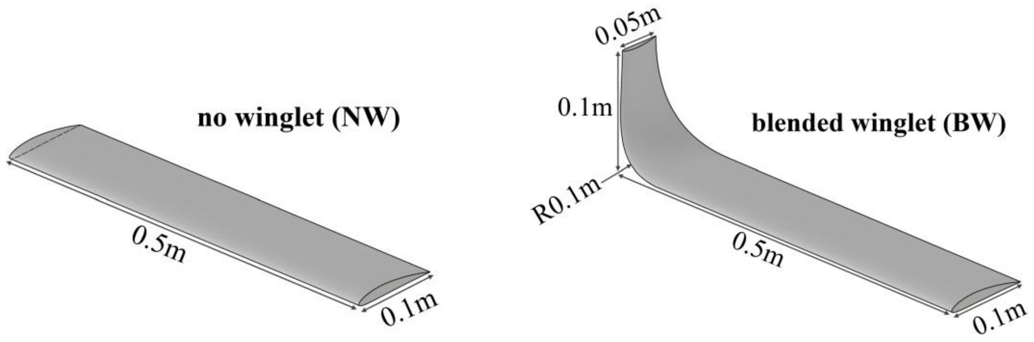

a) No winglet (NW) b) Blended winglet (BW)

Figure 3.8 NACA 4412 wing model with different winglet designs.

As shown in Figure 3.9, the wing model placement and boundary condition for the CFD validation case are in the same configurations to the wind tunnel experiment [11]. The simulation domain consists of an inlet with freestream velocity, $u_\infty = 10$m/s which corresponds to chord-based Reynolds number, $Re_c = 6.8 \times 10^4$, an outlet of constant zero pressure, and no-slip boundary condition is imposed on the wing surface to enforce zero velocity and resolve the viscous boundary layer.

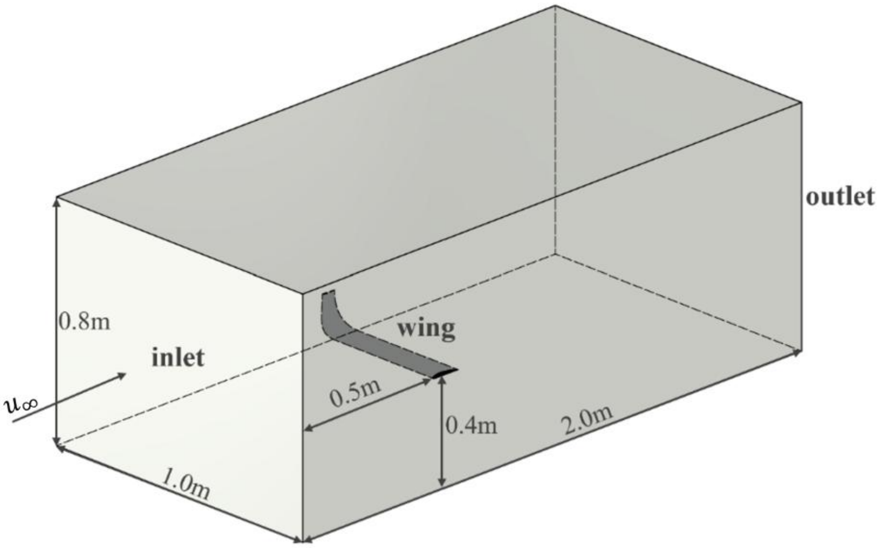

Figure 3.9 Wing model in domain for validation.

The present work will utilise the mesh refinement strategy from the previous LES validation [8], in which the grid resolution is locally refined to about 1.1% of the chord length concentrated in the volume around the vortex core, as shown in Figure 3.10. Given the freestream velocity and mesh cell size, a time step of 1×10^{-5}s is adopted to keep the maximum Courant number below one throughout the simulation. The numerical solver employed was the pisoFoam using regular Smagorinsky model coupled with the mesh refinement around vortex core [8]. The flow-field simulation iterates for a minimum of 20 chord-flow times over the wing model to attain a converged and statistically stable solution.

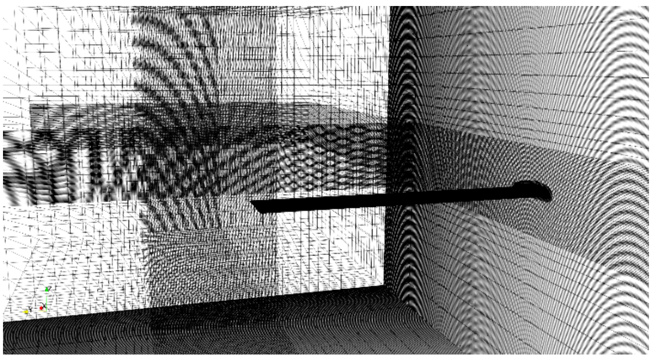

Figure 3.10 Meshing size of 0.011c at volume around the vortex core.

For the post-processing, ParaView [97] is employed to visualise the wake behaviour. A stream tracer along vertical axis (z-axis) is placed at the same location as the smoke probe in the wind tunnel and is initiated five chord lengths upstream to track and identify the motion of smoke particle motion paths passing over the wing. The behaviour of the stream tracer is examined by slicing the tracer field at planes $x/c = 0$, 1, 2, 3, 4 and 7 for validation against the experimental wake spiral visualisation results. A seeding density of 15,000 points is implemented for the stream tracer to ensure its continuity and visibility, resembling the behaviour of the experimental smoke particles. Figure 3.11 shows the illustration of the stream tracer and the slicing planes (example shown with 150 seeds for clarity) used for the assessment.

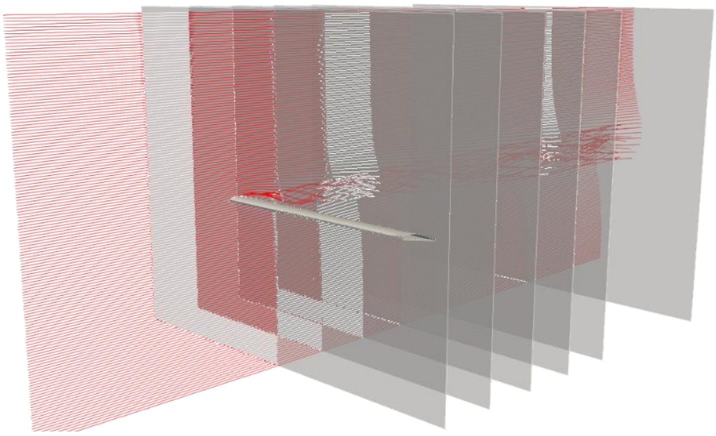

Figure 3.11 Stream tracer originated from the same position as the experimental smoke probe.

3.5.2 Validation Results

During the wind tunnel testing, the wingtip vortices were visualised with smoke particles along the vertical axis in the upstream and forming a wake spiral form after flowing over the wingtip. The LES validation is conducted to compare on the form and size of the wingtip vortices as they propagate downstream. This assessment aims to enhance confidence on the accuracy of the CFD model in representing the physical phenomena, thereby affirming its efficacy in capturing vortices. Table 3.4 summarises the validation outcomes captured at different longitudinal distance x after the trailing edge in terms of chord unit c. The vortex visualised through diffusing green smoke contours is the result from wind tunnel observations, while the vortex outlined in red colour correspond to the LES results. The purpose of the comparison in Table 3.4 is to provide a qualitative assessment of the agreement between the experiment and simulation, where similarity in vortex location, shape, and size indicates the capability of the LES model to capture the dominant features of the wingtip vortex evolution.

Table 3.4 Qualitative validation of the LES (red stream tracer) against wind tunnel experimental visualisation (green smoke contours) at different downstream locations.

x/c	No Winglet (NW)		Blended Winglet (BW)	
	$\alpha = 2°$	$\alpha = 12°$	$\alpha = 2°$	$\alpha = 12°$
0	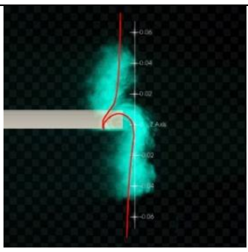	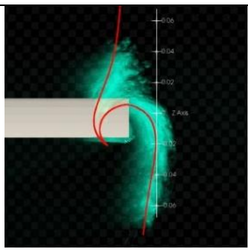	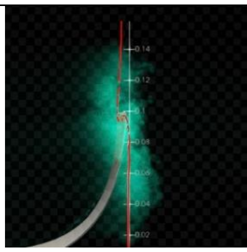	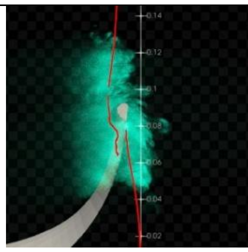
1	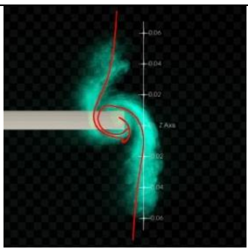	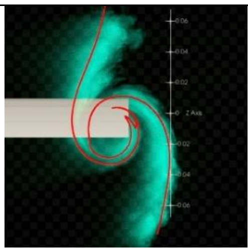	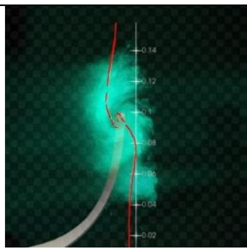	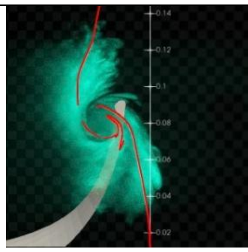
2	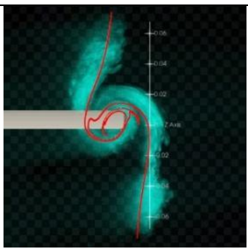	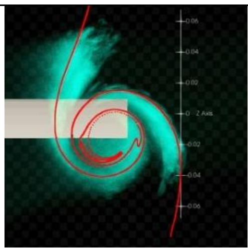	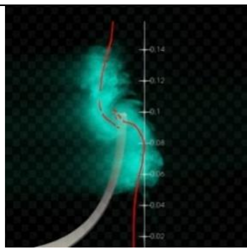	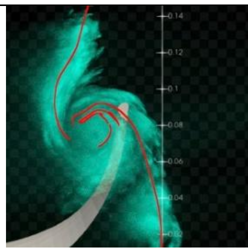
4	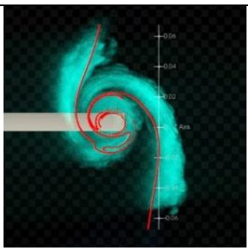	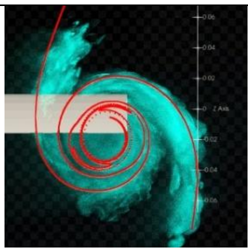	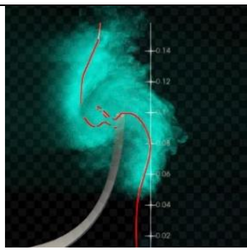	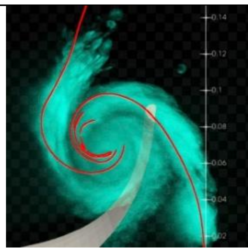
7	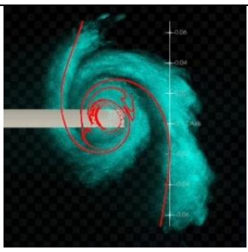	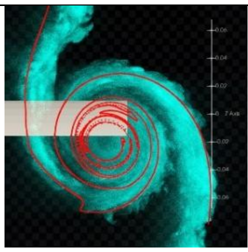	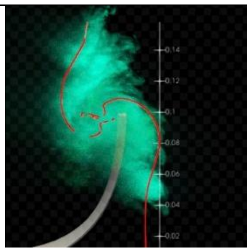	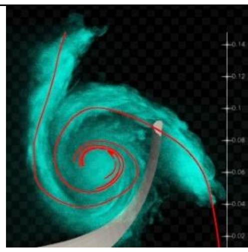

With the two profiles superimposed as presented in Table 3.4, it is evident that the red vortex spiral contour formed by the stream tracer in LES prediction highly coincides with the vortex profile obtained from the illuminated smoke particles in wind tunnel experiments. It is noteworthy that in the previous validation on tangential velocity [8], the LES model exhibited a 5% higher dissipation over each chord length in the streamwise direction. The increased dissipation resulted in subtle enlargement of the vortex core size, potentially making it difficult to discern based on the qualitative results shown in Table 3.4.

The LES model not only effectively captures the intricate form and dimensions of the vortex core, but also accurately predicts the shifting of the vortex core location. The outcomes from both the LES simulation and wind tunnel test demonstrated that higher α leads to a more pronounced vortex shed. Additionally, the results also show that the blended winglets can reduce vortex size effectively, agreeing well with literature [152, 153] about the effects of winglets inclusion. This remarkable agreement noted in the qualitative comparison highlights the precision and reliability of the LES model in simulating the complex flow dynamics of the wingtip vortex.

Devenport et al. [106] defined the contour of the wake spiral as the locus of peak axial turbulence stress, which provides insight into the vortex spiral form. Across the vortex core, the axial velocity generally peaks at the point where it returns from deficits to freestream velocity, typically located approximately one to two core radii from the centre of the core [106]. The complex spiral contour however poses challenges in precisely determining the size of the vortex core, which is crucial for accurately characterising the vortex dynamics and validating the vortex core size from LES against the wind tunnel test. In prior studies, there has not been any comparative study on the relationship between the wake spiral profile and the peak tangential velocity profile. In Table 3.5, the vortex spiral outline is overlaid on top of the tangential velocity distribution field, providing a visual representation of the position of the vortex core circumference (defined by the maximum tangential velocity contour in dark red) in relation to the spiral contour.

Table 3.5 Vortex spiral on the tangential velocity (m/s) contour at x/c = 0, 2 and 4.

x/c	NW		BW
	$\alpha = 2°$	$\alpha = 12°$	
0	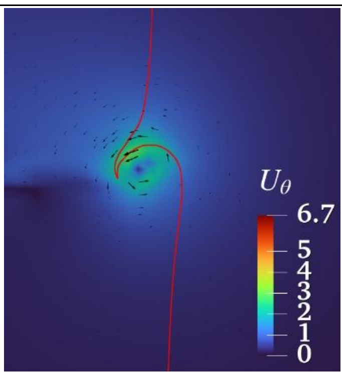	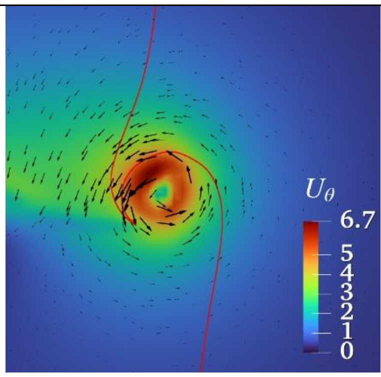	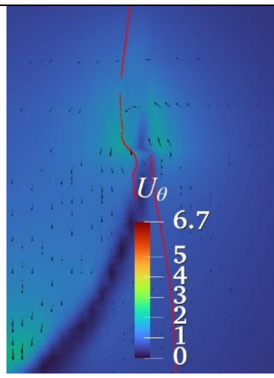

Table continues in the next page

2	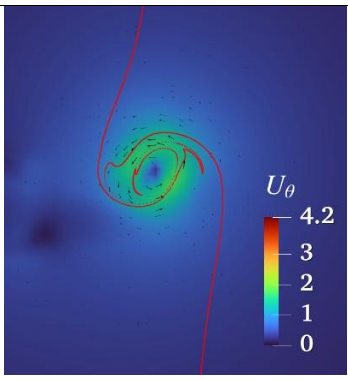	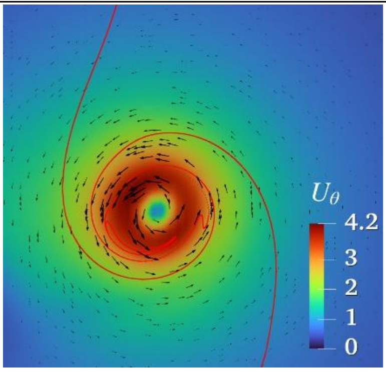	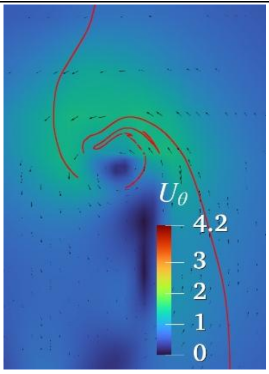
4	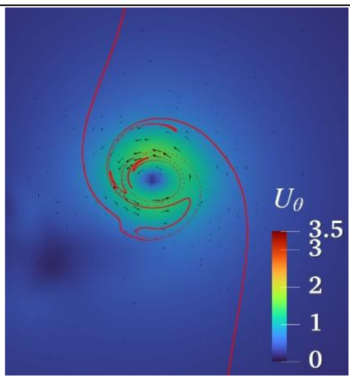	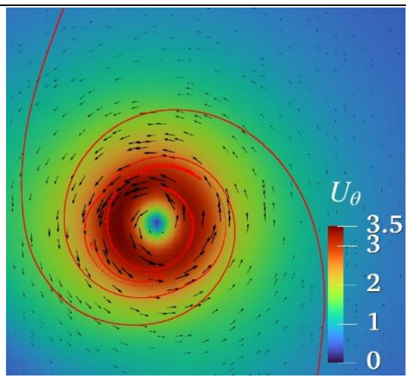	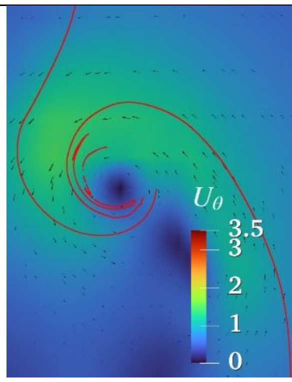

From the experimental and computational results presented in Table 3.5, an increasing number of vortex spiral layers form around the vortex as the swirling flow progresses downstream. The incorporation of the tangential velocity in Table 3.5 provides further understanding regarding how the development of the wake spiral is influenced by the magnitude of vortex strength. The highest tangential velocity induced by the NW wing at high α is more than double compared to a lower α or BW wing at same α. The more vigorous swirling motion accelerates the rotation of the vortex, causing it to develop at a faster rate and resulting in a higher count or more folds of circling rings around the vortex, as captured in both wind tunnel tests and CFD.

In general, the vortex core generated by the NW wing remains smaller than the corresponding spiral envelope, regardless of the angle of attack. Even at a farther downstream position (e.g., $x/c = 4$), where multiple layers of spiral structure emerge, the vortex core diameter remains confined within the innermost spiral ring. Conversely, BW wings tend to have peak tangential velocity profile exceeding the size of the vortex spiral shape. Given these opposing trends, it can be inferred that there is no apparent correlation between the wake spiral and the dimension of the vortex core. Hence, deriving the vortex core radius solely based on the vortex spiral obtained from wind tunnel testing remains unresolved and may lead to systematic inaccuracies.

To provide a more objective comparison, a horizontal line (along the y-axis) was plotted across the centre of the vortex core for both wing configurations at $\alpha = 12°$. The normalised tangential velocity values with respect to the freestream velocity along the plotted line are illustrated in Figure 3.12. For each dataset, the left side pertains to NW wings and right side represents BW wings. These plots offer a more objective perspective on the peak tangential velocity and dimension of vortex core compared to the wake spiral pattern from the stream tracer, providing insights beyond the constraints of the wind tunnel experiment.

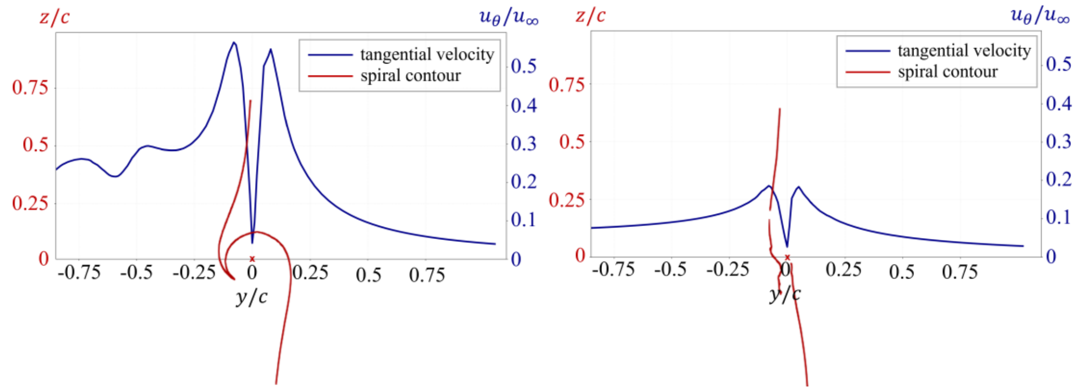

a) $x/c = 0$

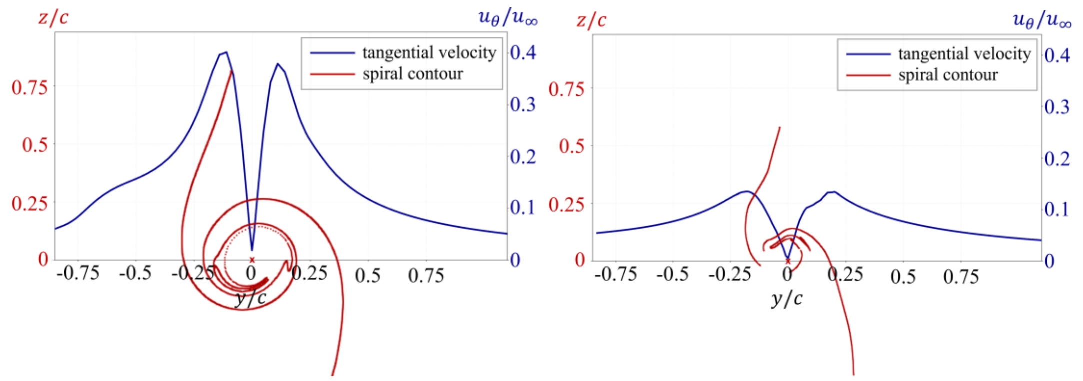

b) $x/c = 2$

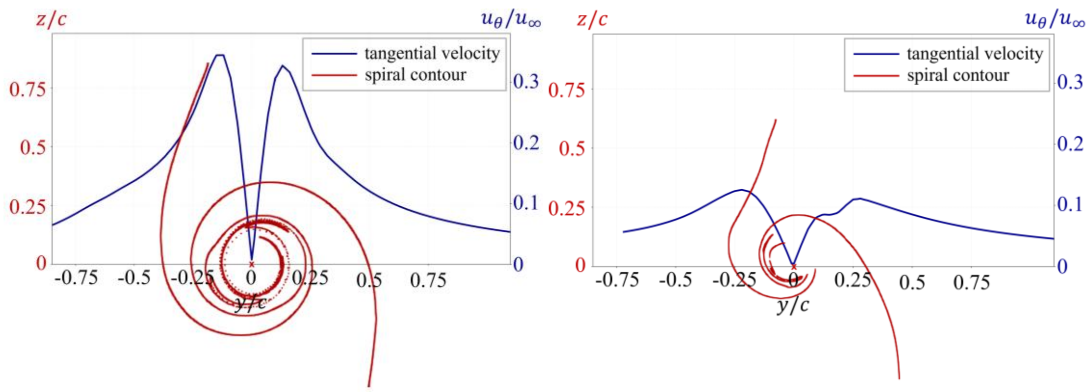

c) $x/c = 4$

Figure 3.12 Normalised tangential velocity (blue) across vortex core (red) along *y*-axis, on NW wing (left) and BW wing (right), at $\alpha = 12°$ and $x/c = 0$, 2 and 4.

From Figure 3.12, it is observed that the addition of blended winglets has resulted in a significant attenuation of approximately 67% in the peak tangential velocity compared to the plain wing. This pronounced reduction reflects the effectiveness of blended winglets in altering the flow dynamics and mitigating the impact of vortices induced drag. With the presence of two peaks in the tangential velocity profile, the computation of the vortex core radius becomes straightforward. The distance from the vortex core centre to the peaks vary for both the inboard and outboard directions. Therefore, the vortex core radius listed in Table 3.6 is determined by dividing the vortex diameter in half. Despite the reduced tangential velocity, the vortex core radius generated by the BW wing is larger than NW wing. The rate of expansion of the BW vortex is significantly higher than the NW vortex, resulting in a greater disparity in size between the two as they evolve downstream.

Table 3.6 Vortex core radius over chord (r_c/c).

α	Wing	x/c					
		0	1	2	3	4	7
2°	NW	0.060	0.065	0.075	0.080	0.110	0.110
	BW	0.060	0.110	0.145	0.185	0.205	0.285
12°	NW	0.080	0.095	0.110	0.125	0.125	0.160
	BW	0.065	0.125	0.190	0.220	0.250	0.410

The vortex core size downstream can be modelled using the time-dependent viscosity diffusion term from the Lamb-Oseen model [154]. However, Squire [155] proposed that the eddy viscosity is proportional to the vortex circulation strength. Thereafter, the eddy viscosity coefficient was formulated to be empirically determined from experimental measurements. Based on the findings in Figure 3.12 and Table 3.5, it is established that there is no discernible correlation between the wake spiral and the dimensions of the vortex core. This reinforces the importance of qualitative validation, as the LES results align well with the wind tunnel data, confirming the reliability of the LES model in capturing vortex characteristics. Interestingly, the analysis of vortex core size for the wings with and without winglet indicates contrasting trends when it comes to evaluation through either visual stream tracer or maximum tangential velocity measurement. The vortex tracing and characterisation, both computationally and experimentally, indicate that the BW appears to reduce the size of the vortex as captured visually. However, the actual size of the vortex core determined by the maximum tangential velocity is larger for the BW wing compared to the NW wing.

This contradictory phenomenon on the wingtip vortices can be clearly seen in Figure 3.12. Nevertheless, the reduced tangential velocity in the larger vortex core for the blended winglet is aligned with the theory of Lamb-Oseen model [107, 108], provided that the total vorticity is nearly equivalent. In Figure 3.13, the circulation strength was evaluated based on the time-averaged velocity field obtained after the LES reached a statistically stationary state with 20 chord flow times. In the diagram, the vortex circulation strength of BW is slightly higher than that of the NW, likely due to the higher lift experienced on the BW, as explained by Kutta Joukowski's theorem [109]. This has further proven the benefits of the blended winglet in mitigating the impact of wingtip vortices, improving the effective wingspan and enhancing the overall aerodynamic efficiency. The demonstrated accuracy and credibility of the CFD model can ensure that the future simulations in the extended field are grounded.

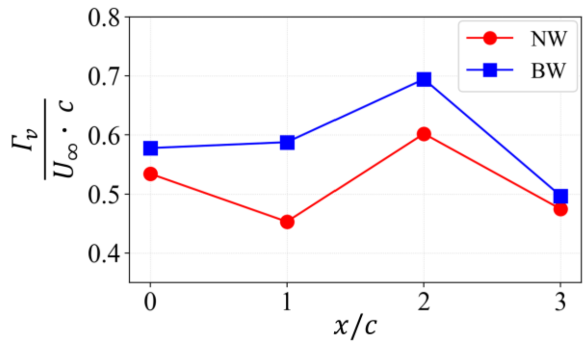

Figure 3.13 Comparison of normalised vortex circulation strength for NW and BW, $\alpha = 12°$.

3.6 Summary and Recommendations

This section has carried out the numerical simulation using both URANS and LES for vortex capturing and validated the accuracy of the different turbulence models in predicting the aerodynamics of the wake vortices. The results showed that the LES model is more accurate in anticipating the wake vortex strength and persistence, which provides a better agreement with the experimental and published reference data. URANS has achieved some degree of accuracy in estimating the vortex core centre location and axial velocity deficit, but unable to maintain the vortex physics, and the vortices diffused more quickly than the reported data from experiment. Thus, LES is identified as the more appropriate framework for modelling formation flight aerodynamics, where accurate representation of coherent vortical structures is essential for predicting the beneficial upwash encountered by a trailing wing or aircraft.

The comparative study of the LES framework against the experimentally upright corrected results has shown a positive outcome. The vortex spiral profiles generated by the LES demonstrate a high degree of qualitative consistency across various wing configurations, angles of attack, and multiple downstream planes when compared to wind tunnel data. Furthermore, the numerical simulation has provided a more in-depth analysis of the vortex core, defined by its maximum tangential velocity, against the wake spiral contours that represents the peak axial turbulence stresses. This dual-perspective analysis offers a more rigorous interpretation of vortex behaviour than either approach alone. The outcomes reveal that blended winglet effectively reduces both the visible spiral size formed and the respective circulation strength of the wake. However, it has a larger vortex core radius, characterised by the maximum tangential velocity profile can be larger for the blended winglet configurations, despite the visually smaller spiral envelope. This unexpected contrast highlights that the observable wake spiral shape does not necessarily correlate with the underlying vortex core dimensions. Such findings provide new insights into the understanding of fluid flow phenomena and shed light on the vortex core properties in aerodynamics.

The present investigation focuses on a low Reynolds number wingtip vortex configuration, as listed in Table 3.7. Therefore, while the developed framework validated on the vortex simulation and, further validation across different Reynolds number regimes is required to assess its broader applicability.

Table 3.7 Chord based Reynolds number, Re_c for different simulation cases.

Case	u_∞ (m/s)	c (m)	Re_c
LES Validation	34	0.14	3.25×10^5
Wind Tunnel Validation	10	0.10	6.48×10^4

Collectively, this chapter validates the accuracy and reliability of the LES framework for wake vortex modelling and establishes its suitability for the subsequent simulations of vortex surfing formation flight.

Chapter 4

Inlet Conditioning for Wake Vortex Simulation

As presented and proven in the previous chapters, LES offers demonstrably superior accuracy in capturing the complex, three-dimensional turbulent structures that govern aircraft wake vortices. However, applying LES to realistic formation flight scenarios remains computationally challenging. For instance, the recent extended range formation trials by Airbus fello'fly campaign [73], the longitudinal separation between the leading and trailing aircraft can span over several nautical miles. Simulating such vast domains requires extremely fine spatial discretisation, particularly in the vicinity of the trailing vortices, and sufficiently short temporal resolutions to resolve the integral turbulence length scales.

The intensive mesh grid and time step over the tremendous flight space will exacerbate to significant computational costs and extended computing core-hours, thereby limiting its feasibility of full domain LES for formation flight simulation and research. Moreover, studying multiple trailing aircraft positions often require repeating the entire simulation from the upstream of leading aircraft. This repeated simulation of the same upstream flow field multiplies the computational burden without providing new physical insights. Therefore, an approach that avoids reiterating the upstream vortex generation for each formation flight research is very much essential for improving efficiency and practicality.

A practical strategy for reducing the computational cost is to partition the full LES domain into two functional regions, namely the inlet condition (IC) domain and the main simulation (MS) domain, as shown in Figure 4.1. The IC domain contains the leading aircraft or wing that is responsible for generating the wake vortex and the MS domain in which contain the trailing aircraft or wing will operate within the prescribed wake field with the inlet boundary condition identical to the vortical flow data in the IC domain.

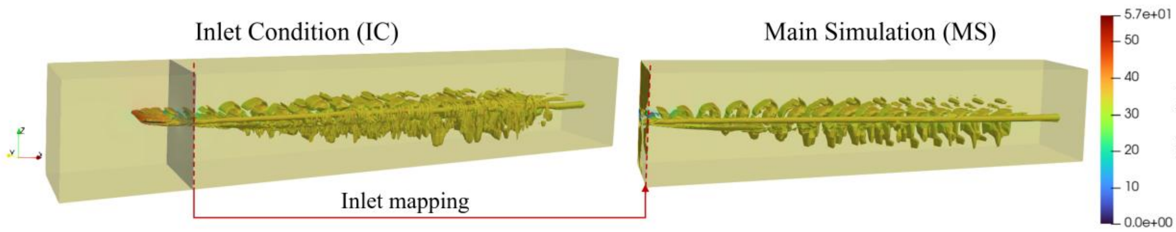

Figure 4.1 Precursor inlet mapping, with inlet condition and main simulation.

As illustrated in Figure 4.1, the fully developed wake vortex from the IC is extracted at a specified downstream plane and imposed as the inlet boundary condition for the MS domain. In such a manner, the expensive upstream vortex generation physics is simulated only once. Thereafter, multiple MS simulations with each representing a different formation flight relative position can be performed at a fraction of the original computational cost. This concept aligns with the established inlet conditioning practices [74, 75], which aim to provide realistic turbulent inflow fields without resolving the full upstream evolution within every simulation.

Recent developments in machine learning have emerged as a promising framework for synthetic turbulent inflow generation. Fukami et al. [156, 157] proposed convolutional neural network-based models for super-resolution reconstruction of turbulent flows, highlighting the ability to recover multiscale features and temporal evolution from coarse input data. In addition, physics-informed deep learning methods [158, 159] further improve inflow generation by enforcing turbulence-consistent statistics and spectral content. These developments represent a rapidly growing data-driven direction for LES inflow specification.

The primary objective of this chapter is to develop and validate an efficient inlet conditioning methodology tailored for LES of wake vortex surfing. The fidelity of the mapped inlet conditions is evaluated by the turbulent coherence, circulation strength, and downstream development of wingtip vortices. This contributes to laying the foundation for subsequent studies involving parametric evaluation of trailing aircraft positions using the MS domain without recomputing upstream vortex generation.

4.2 Inlet Condition and Main Simulation

In the IC simulation domain, the leading wing model geometry, stream field parameters and CFD framework are inherited directly from the validated wingtip vortices generation by LES presented in the previous chapters. The wing geometry comprises a NACA 0012 aerofoil profile with a chord length of $0.14m$, a semi-span of $0.15m$, and an angle of attack α of 10°. The freestream velocity is $34m/s$, corresponding to a chord-based Reynolds number of Re_c = 3.25×10^5. The mesh grid size within the volume around the vortex core is maintained to approximately 1.1% of wing chord, or equivalent to roughly 10% of the vortex core diameter at $x/c = 0$ based on the previous validation study [8]. Time step of $1 \times 10^{-5} s$ is adopted to maintain the maximum Courant number of the simulation below one. Unlike the prior validation domain, this IC domain is extended longitudinally to allow direct flow-field comparison between downstream of the selected datum plane in the IC and the corresponded planes in the MS.

From the IC simulation, the database of flow-field information and velocity fluctuations profile of the wake vortex using LES are established. This database is subsequently used to construct a physically consistent turbulent inflow conditions, to reproduce the vortex flow with the correct mean profile and fluctuation content. The cuttingPlane utility in OpenFOAM is employed to extract the relevant flow-field quantities required for inlet specification. Alternatively, the vortical mean flow parameters are augmented with synthesised temporal fluctuations to reconstruct a time-dependent inlet velocity field.

The instantaneous velocity datasets are captured at multiple streamwise stations, spanning $x/c = 0$ to $x/c = 9$ as illustrated in Figure 4.2. The time-resolved database from the IC simulation is then introduced onto the inlet of the MS domain. This approach ensures that the MS inflow contains turbulence originating from a physically resolved LES solution, thereby preserving both spatial and temporal correlations essential for the correct downstream evolution of the vortex structures.

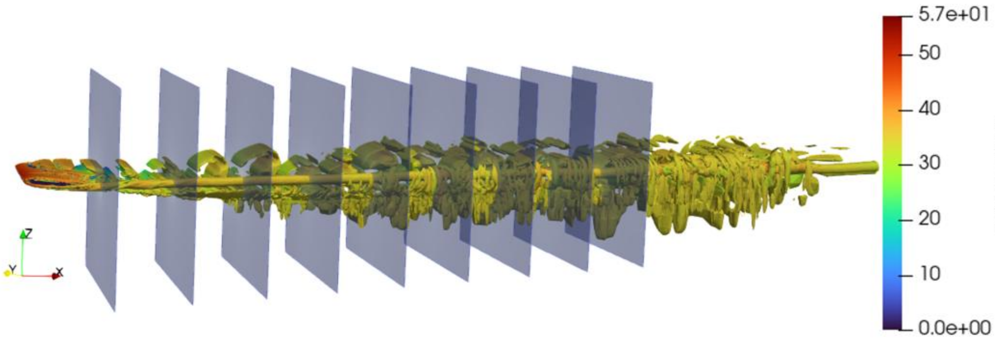

Figure 4.2 Wingtip vortex visualised with Q-criterion=200, coloured by velocity magnitude u.

Despite its advantages, inlet boundary conditioning for LES remains non-trivial. LES explicitly resolves the large eddies which contain most of the turbulent kinetic energy. The resolved turbulent kinetic energy, k is computed based on the velocity fluctuations (u'_x, u'_y, u'_z) as follows [76],

$$k = \frac{1}{2}\left({u'_x}^2 + {u'_y}^2 + {u'_z}^2\right) \tag{37}$$

where ${u'_x}^2, {u'_y}^2, {u'_z}^2$ are the mean square fluctuations of the respective velocity components. In LES, the energetically dominant scales are directly resolved, while the SGS model accounts for the effects of smaller and unresolved eddies [140]. Therefore, an accurate representation of the velocity fluctuation profile at the inlet is critical, as it directly affects the computation of the Reynolds stress tensor per unit density,

$$\tau_{ij} = \overline{u_i' u_j'} \tag{38}$$

which governs the momentum transfer, turbulent mixing and the proper cascade of energy from the resolved eddies to subgrid scales [77]. Any inaccuracies in this inflow turbulence may disrupt the energy cascade and compromise on the LES fidelity in the downstream region. Simple synthetic perturbations such as white noise forcing lack the necessary correlation and rapidly dissipate, resulting in unrealistic vortex behaviour and incorrect downstream development [77].

Prior inlet conditioning studies have conventionally focused on wall bounded turbulent flows such as channel and pipe flow [77, 160], combustor [83, 161] or nozzle simulations [80, 81], where the objective is to achieve statistically steady, fully developed turbulence. In these studies, the highly turbulent inflow conditions are often prescribed with a target swirl number or supplemented with additional forcing mechanisms such as explicit velocity corrections and imposed axial or azimuthal body forces. However, these methods are not directly applicable to wake vortex flows, which involve strongly rotational wingtip vortices evolving within an unbounded freestream field. Unlike internal wall-bounded flows, freestream vortices exhibit strongly time-dependent behaviour, where the instantaneous vortex structure governs its subsequent streamwise evolution. The challenge for vortical flow in the freestream is to preserve the dominant features of wake vortices for instances, strong azimuthal velocity, axial velocity deficit, coherent helical motion, which are far more complex to reproduce at an inflow boundary. Any loss of coherence or misrepresentation of vortex structure at the inlet would significantly compromise the accuracy of subsequent formation flight predictions. In contrast, fully developed channel flows remain largely invariant along the streamwise direction. This fundamental difference poses significant challenges in prescribing realistic inlet conditions for wake vortex simulations.

To address these challenges, the precursor-based inlet mapping and synthetic reconstruction techniques specifically for vortical inflow conditions in LES are investigated in the present work [76, 162]. These inlet condition methods aim to faithfully reproduce the physics of wingtip vortices at the inlet while drastically reducing the computational cost associated with full-domain simulation.

4.3 Precursor Method

There is very limited research on the inlet conditions strategies for wake vortex, largely because the prescribed turbulence quantities at the inlet cannot reliably reproduce the desired vortex characteristics and cannot guarantee the downstream evolution. In the inlet-outlet domain decomposition, the precursor method provides the most physically representative inflow boundary for LES because it supplies temporally and spatially correlated turbulent structures directly from an upstream simulation. For formation flight simulations, the IC domain typically includes the leading wing or aircraft, to generate a time-series of wingtip vortex dynamics data and capture the evolution of the vortex structures. The field data at a specified downstream plane are then extracted over a defined time interval and imposed as the inflow to the MS domain. This approach allows the MS domain to accurately reproduce the vortex dynamics and associated turbulence that would naturally occur if the full formation geometry were simulated within a single continuous large domain.

Before acquiring the precursor data on the velocity information of the induced vortex, the LES solution within the IC domain is first iterated for more than 20 chord-flow times to ensure the transients have subsided, and the flow has developed to a statistically steady state [146]. Once statistical convergence is established, the velocity field is sampled for an additional duration of minimum five times the integral time scale T^u [163],which provides a sufficiently long record to capture the temporal evolution of the coherent structures within the vortex. The integral time scale is computed via the integral of the autocorrelation function of the velocity fluctuations $r(\tau)$, as follows,

$$r(\tau) = \frac{\overline{u'(t)u'(t-\tau)}}{\sigma_u^2} \tag{39}$$

where τ denotes the time lag, u' is the velocity fluctuations component and σ_u^2 is the corresponding velocity variance. The integral time scale is then obtained as,

$$T^u = \int_0^\infty r(\tau)\, d\tau \tag{40}$$

which in the case of current study, it is equivalent to nearly 50 chord-flow times. The precursor data with duration exceeding T^u ensures that the inlet velocity fluctuations used in the MS domain contain the correct temporal statistics and correlation structure over a temporally representative period. For practical evaluation, the integral time scale is computed over a finite sampling duration corresponding to 50 chord-flow-through times, ensuring statistical convergence of the velocity data. The resulting integral time scale at the selected point are $T_x^u = 4.65 \times 10^{-4}s$, $T_y^u = 1.13 \times 10^{-2}s$, and $T_z^u = 7.17 \times 10^{-3}s$. The integral time scale indicates anisotropic temporal behavior where the cross-stream (tangential) velocity fluctuations exhibit longer correlation times compared to the streamwise component, reflecting the dominant rotational nature of the vortex structure.

After the sampling period, the rime-resolved precursor velocity data extracted from the selected IC plane are written into the directory /constant/boundaryData/inlet/<*time*>/ together with the associated point coordinates file stored as /constant/boundaryData/inlet/points. Following the OpenFOAM convention, each time folder contains a complete snapshot of the velocity field at the selected plane. The MS domain utilise the timeVaryingMappedFixedValue boundary condition, which reads the precursor velocity field sequentially in time and applies it directly to the corresponding spatial nodes on the inlet boundary.

With realistic and dynamic inflow conditions prescribed at the MS inlet, other flow variables such as pressure, vorticity and subgrid-scale turbulence quantities are initialised or derived from the governing equations at each time step. The precursor technique has the advantage of using time-series data from a time dependent LES to depict the inflow turbulence for the MS domain. As a result, it would have the necessary fluctuations with temporal and spatial correlations and able to reconstruct a physically realistic, time-dependent inflow that preserves the spatial coherence, turbulence intensity, and vortex structure present in the IC domain.

By mapping the precursor flow data onto the MS inlet boundary, the flow dynamics in MS domain should correspond with the region after the selected plane in IC domain. The validation on the precursor-based inflow specification in the current study uses the plane at $x/c = 0$ from the IC domain. This plane is located immediately downstream of the wing trailing edge, where the wingtip vortex has just begun to roll up and the flow field remains highly complex and transitional.

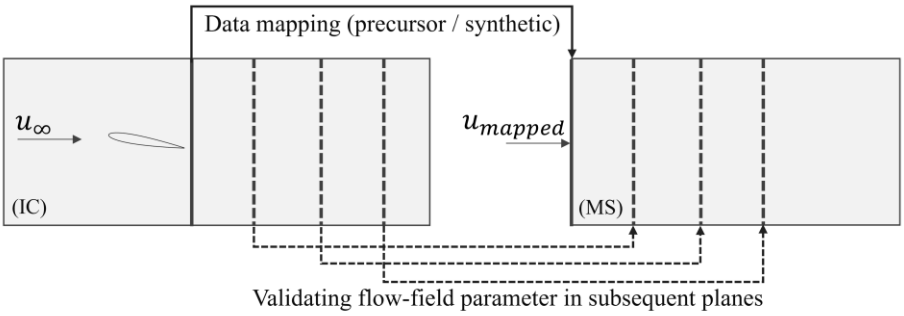

Figure 4.3 Validation on the following planes in the main simulation (MS).

The vortex development in the MS domain after the precursor inlet conditions will be validated against those corresponding planes in the IC domain, as illustrated in Figure 4.3. If the MS solution using the $x/c = 0$ as inflow condition can correctly predict the vortex trajectory, core size, and velocity structure at subsequent downstream planes, it confirms that the precursor data preserve the essential dynamics of the vortex and can reliably serve as inflow conditions for wake vortex surfing at larger separations. The mapping from any succeeding downstream plane is expected to pose lesser challenges as the flow has developed into a more organised and established vortex form.

4.3.1 Validation of Precursor Inlet

The wake vortex generated in the IC domain is visualised using the Q-criterion as shown in the Figure 4.4. The required flow field data on wingtip vortices are acquired at $x/c = 0$ and the instantaneous velocity components $u_{x,y,z}$ are among the key quantities to be mapped onto the inlet of the MS domain. With the precursor inlet data from $x/c = 0$, the turbulence quantities on the subsequent planes with one to three chord length downstream will be used to evaluate the fidelity of the reproduced vortex dynamics.

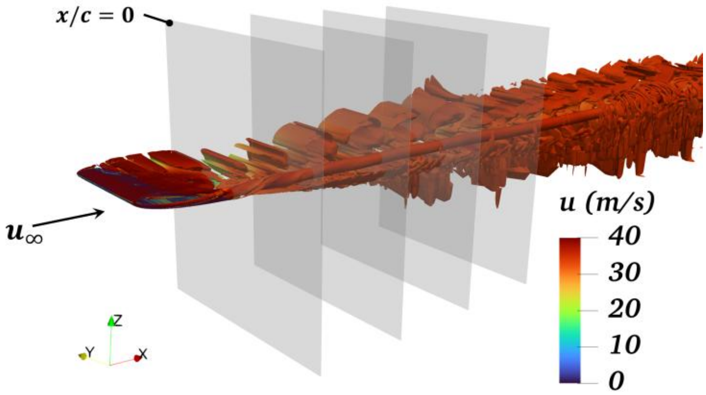

Figure 4.4 Wake vortex in IC domain visualised with Q-criterion=100, coloured by velocity magnitude u.

The use of such upstream plane in the IC may not be the optimal choice as precursor inlet, mainly due to the higher computational demands for subsequent MS domain repetitions. However, it provides a quick overview of the results and for demonstration of the methodology. In addition, the resulting MS domain vortex evolution is supported by the previous validation work [8], which has already confirmed the accuracy of the near field vortex dynamics. This further ensures that the inlet mapping approach remains credible even when applied at a plane where the vortex is not yet fully developed.

The CFD results on the MS domain using precursor-based inlet boundary extracted from the IC domain $x/c = 0$ plane is illustrated in Figure 4.5, visualised by Q-criterion and coloured by velocity magnitude. From a qualitative standpoint, the wake vortex flow field observed in the MS domain (Figure 4.5) closely resembles that of the IC domain (Figure 4.4), indicating that the mapping of time-dependent velocity field retains the essential vortical features. Overall, the MS solution does not exhibit any noticeable attenuation of downstream turbulence profile or velocity magnitude. However, the main limitation of this approach is the substantial storage required to retain the full time series of flow data.

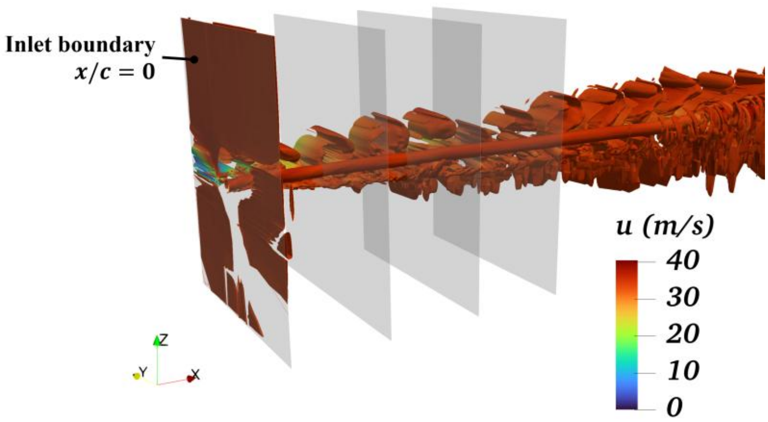

Figure 4.5 Wake vortex in MS domain with precursor vortex inflow boundary, visualised with Q-criterion=10, coloured by velocity magnitude u.

For comparison, a separate MS domain was constructed with inlet prescribed with the vortical mean velocity field $\bar{u}_{i,j,k}$, i.e., a time-invariant inflow profile. As shown in Figure 4.6, there are vortices induced after the wing body region at the initial transient phase (left), but it quickly dissipates and results in a noticeably smoother vortex evolution. While the large-scale structure and approximate core location are still captured, the absence of fluctuation content suppresses the development of small-scale turbulence and leads to an overly diffused vortex representation. This discrepancy highlights that although mean velocity inflow is capable of capturing the large-scale vortex characteristics and produces a reasonably well approximation on the vortex core, it fails to reproduce the realistic unsteady vortex dynamics required for accurate downstream predictions in wake-encounter and formation flight simulations.

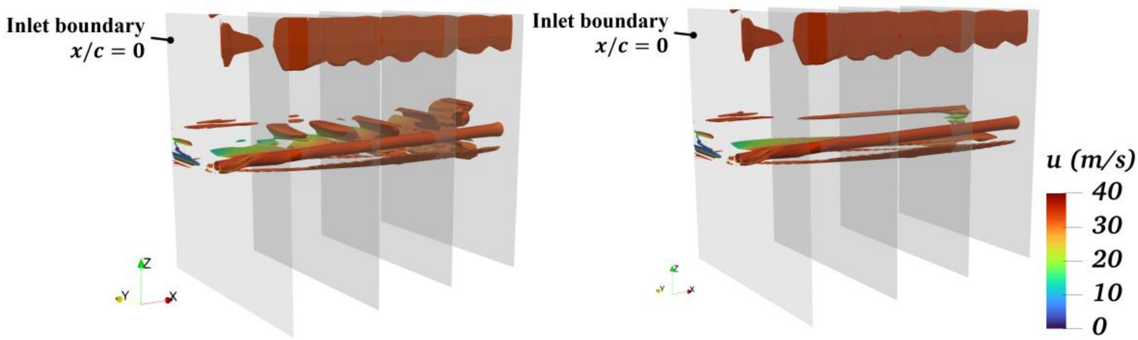

Figure 4.6 Wake vortex in MS domain with mean vortex inflow boundary, at different time stamp – 0.05s (left) and 0.1s (right), visualised with Q-criterion=100, coloured by velocity magnitude u.

From the above comparison, the precursor-based approach clearly stands out for its capability to preserve the intricate turbulent structures of wingtip vortices behaviour for downstream aerodynamic simulations. Nevertheless, a more rigorous examination of the vortex turbulent metrics is necessary to validate the accuracy of the precursor inlet boundary condition. Figure 4.7 presents the tangential velocity profile normalised by the freestream velocity, plotted across the vortex core in the spanwise direction. These profiles provide critical indicators of vortex behaviour including vortex core centre position, core radius, and vortex strength, by determining the trough, distance between peaks and the peak amplitude respectively on the same plot.

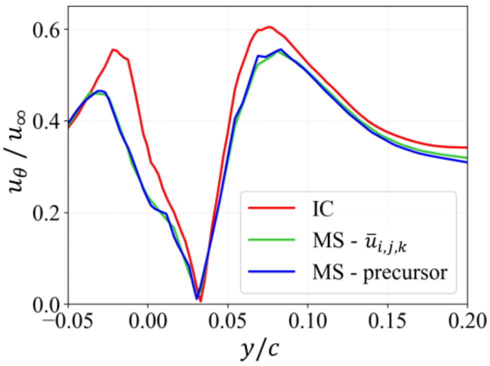

(a) $x/c = 0$

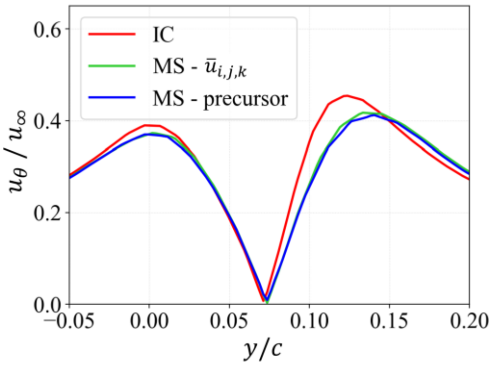

(b) $x/c = 1$

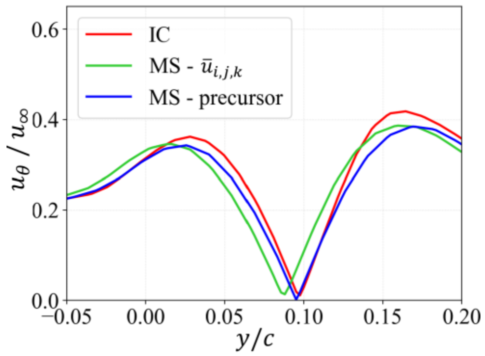

(c) $x/c = 2$

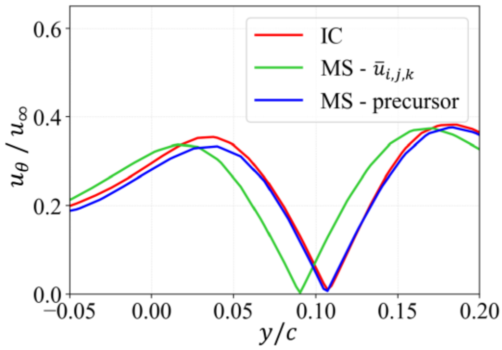

(d) $x/c = 3$

Figure 4.7 Validation on normalised tangential velocity magnitude, u_θ/u_∞ across vortex core centre.

Despite the turbulent structures showing a high degree of similarity, the precursor MS is having slight discrepancies compared to the IC tangential velocity profile at $x/c = 0$. The error is likely due to the temporal offset in data recording, where the precursor vortical data recording begins only after the IC domain has achieved steady state flow conditions. Therefore, the initial velocity data used to initialise the MS inlet boundary condition does not capture the transient phase of the IC simulation from its true starting time. This temporal discrepancy can lead to inconsistencies in the initial conditions imposed on the MS, thereby affecting the development of downstream vortex structures. Overall, the precursor MS is having a marginally lower magnitude in term of tangential velocity profile at $x/c = 0$ but restores to an almost identical tangential velocity profile thereafter ($x/c =$ 1 to 3). Interestingly, the MS with mean velocity inflow conditions closely matches this profile up to two chord lengths downstream, after which it gradually shifted less inboard. This lateral deviation is primarily due to the lack of fluctuations, resulting in an underestimation of the turbulent forces that drive the vortex core to shift more inboard.

When comparing axial velocity profiles as plotted in Figure 4.8, both MS axial velocities align well with the IC profile. The same lateral deviation as the tangential velocity plot is noticed on the MS with mean flow inlet condition after two chord lengths. All profiles exhibit an axial velocity deficit due to the induced drag and viscous effects associated with the formation and evolution of the vortex core.

This deficit occurs because the air accelerates around the vortex core, resulting in lower axial velocities within the core region [138]. These profiles generally align with the findings of Devenport et al. [106], where the velocity deficit restores to freestream velocity at about one to two core radii from the vortex centre.

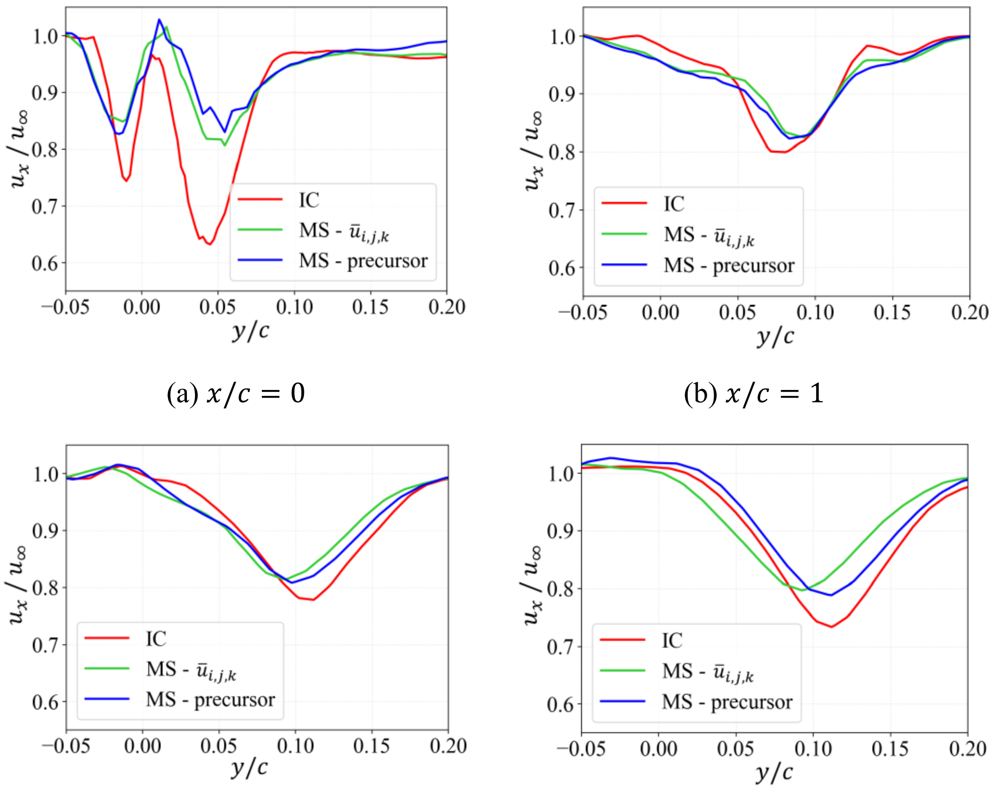

(a) $x/c = 0$ (b) $x/c = 1$

(c) $x/c = 2$ (d) $x/c = 3$

Figure 4.8 Validation on normalised axial velocity magnitude, u_x/u_∞ across vortex core centre.

While the MS tangential and axial velocity matches well with the IC profile, there is a notable discrepancy in the fluctuation intensity of the velocities across the vortex core between the MS and the IC, as shown in Figure 4.9. As expected, the MS case prescribed with a steady mean-flow inlet exhibits no fluctuations, resulting in a flat profile along the x-axis. Conversely, the precursor-driven MS retains the fluctuating behaviour but still shows discernible differences relative to the IC reference. The discrepancy may again stem from the temporal offset errors in the initiation time of the mapping data. As the simulation data are not synchronised on both domains, the time dependent fluctuations may vary quite differently.

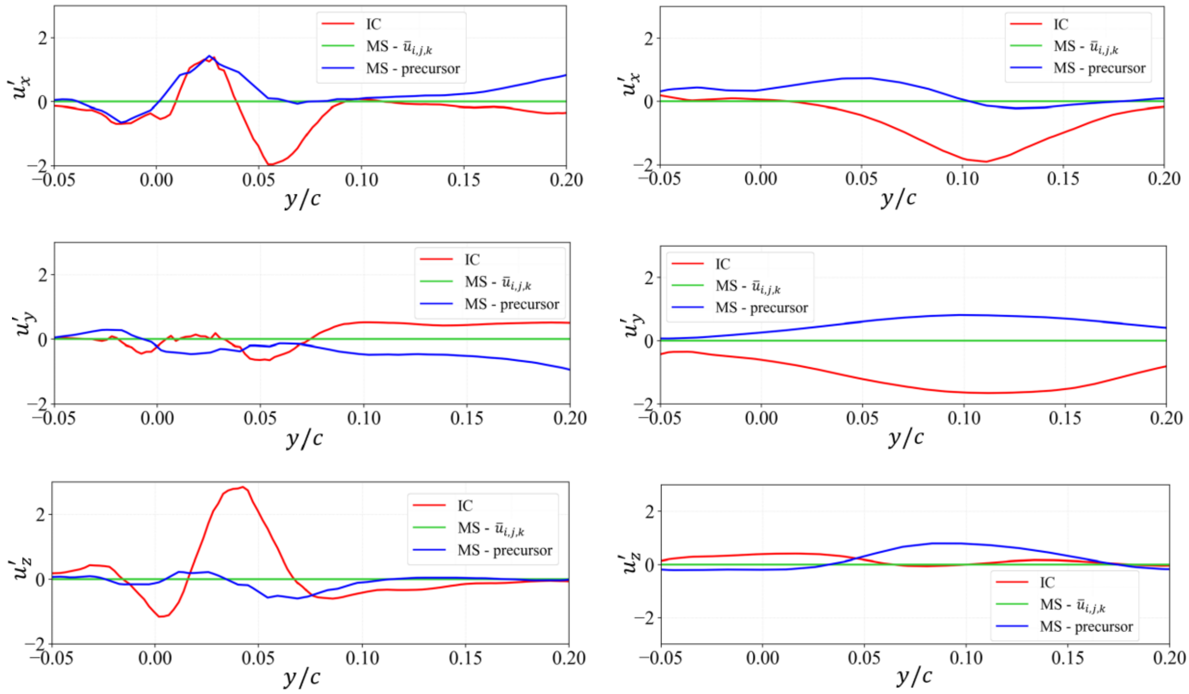

(a) $x/c = 0$ (b) $x/c = 3$

Figure 4.9 Velocity fluctuations, $u'_{x,y,z}$ across vortex core centre at the inlet and downstream.

To validate the hypothesis, a single point on the downstream plane at $x/c = 3$ with the highest tangential velocity is selected. This data point lies along the circumference of the vortex core radius. The normalised three-dimensional velocity fluctuations data of the point is plotted over time to examine its fluctuation profile in both the IC and precursor MS. The actual start time of the MS is used as the baseline for comparison. As shown in Figure 4.10, the IC velocities fed into the MS inlet lack a transient phase, as the data recording only started after 50 chord-flow times in the IC domain. In the MS domain, the point experienced freestream velocity and transient phase for approximately the first seven chord-flow times before the vortex stabilised. Thereafter it displayed a turbulent pattern that closely matched the IC domain, with only minor discrepancies at certain times. This explains the deviation of the velocity fluctuations across the vortex core in downstream planes in Figure 4.9.

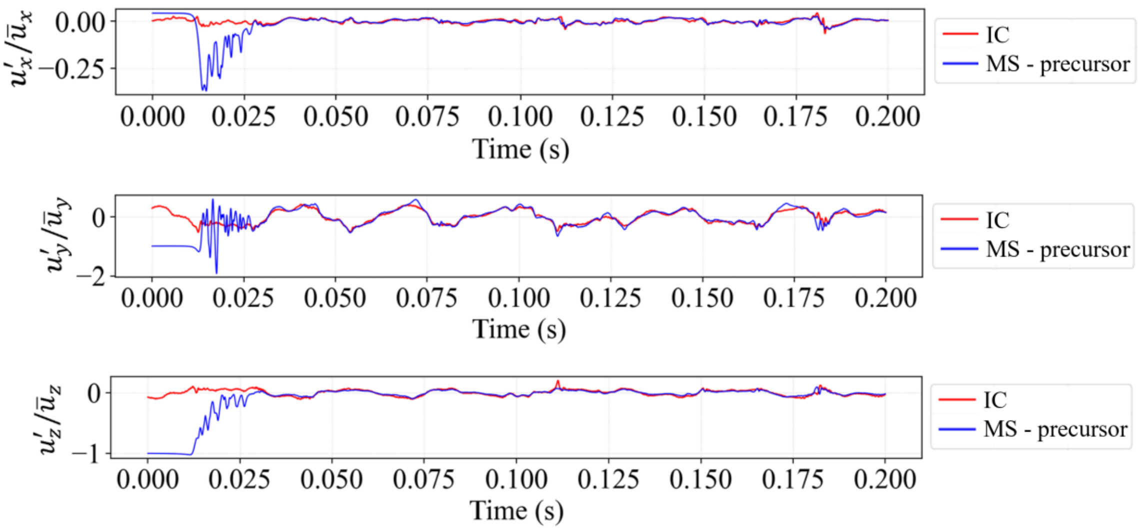

Figure 4.10 Velocity fluctuations normalised by mean velocity, $u'/\bar{u}$ across the vortex core at $x/c = 3$.

For the inlet plane, the discrepancy can be attributed by the limitations of LES. The finite volume framework employed the predominant second-order accurate central differencing scheme in gradient and Laplacian calculations, complemented by divergence schemes using upwind and limited linear methods. The central differencing schemes are effective for resolving smooth gradients, less dissipative and minimising numerical errors compared to some upwind schemes [164]. However, it can underestimate the intensity of small-scale turbulence fluctuations present in the inflow conditions. As a result, the initial turbulence characteristics at the inlet may not be fully captured, leading to discrepancies in the early stages of vortex development between the MS and IC domains. Upwind methods are typically employed in LES to handle highly advective flows and sharp gradients, ensuring that the numerical solution propagates in the direction of flow, thus preventing numerical oscillations and maintaining stability. However, upwind schemes can introduce additional numerical diffusion, which may smooth out small-scale turbulence features that are critical for accurately capturing the vortex dynamics, leading to the discrepancies observed in Figure 4.9a.

Understanding the temporal evolution of velocity fluctuations on the inlet boundary is important for the precursor MS domain. The normalised fluctuations profile at the point with the highest tangential velocity magnitude, $u_{\theta,max}$ on the inlet plane ($x/c = 0$) is plotted in time domain in Figure 4.11. As the precursor MS is taking the exact velocity dataset and grid points from the IC, suggesting there should be no interpolation issues between the two domains. Although the time-series graphs of precursor MS maintain a consistent trend throughout, there is a marginally smaller amplitude observed. The amplitude drop is likely due to the LES solver inherently filtering out some of the smaller-scale turbulence. This phenomenon does not affect the overall inlet mapping process, but it emphasises the challenges of accurately transferring and preserving the turbulent features of wake vortex across different simulation domains.

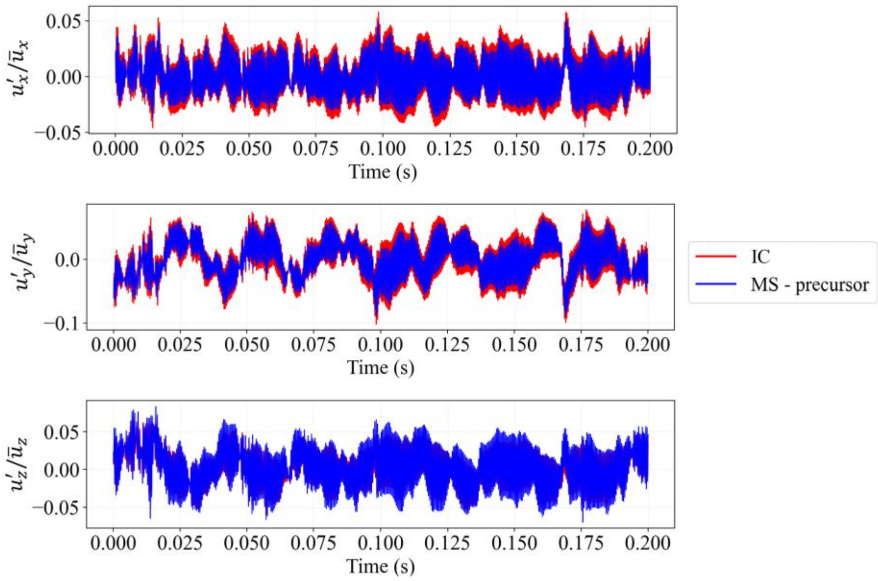

Figure 4.11 Time domain plot of the three-dimensional normalised velocity fluctuations, $u'/\bar{u}$.

Figure 4.12 shows an example of IC and precursor MS data being Fourier transformed from time domain and plotted in the frequency domain. From a validation perspective, the three-dimensional turbulence appeared to have a similar spectral profile in the frequency spectrum, with dominant energy concentrated below 500 Hz and a secondary band between approximately 2–2.5 kHz, albeit with different amplitude levels. The peaks in high-frequency spectrum (2–2.5kHz) indicate the turbulent fluctuations associated with small-scale eddies within the attached turbulent boundary layer [165]. The frequency domain analysis shown in Figure 4.12 demonstrates that the main simulation with the precursor-based inlet condition is capable of reproducing the complex yet detailed amplitude and frequency characteristics of the velocity fluctuations.

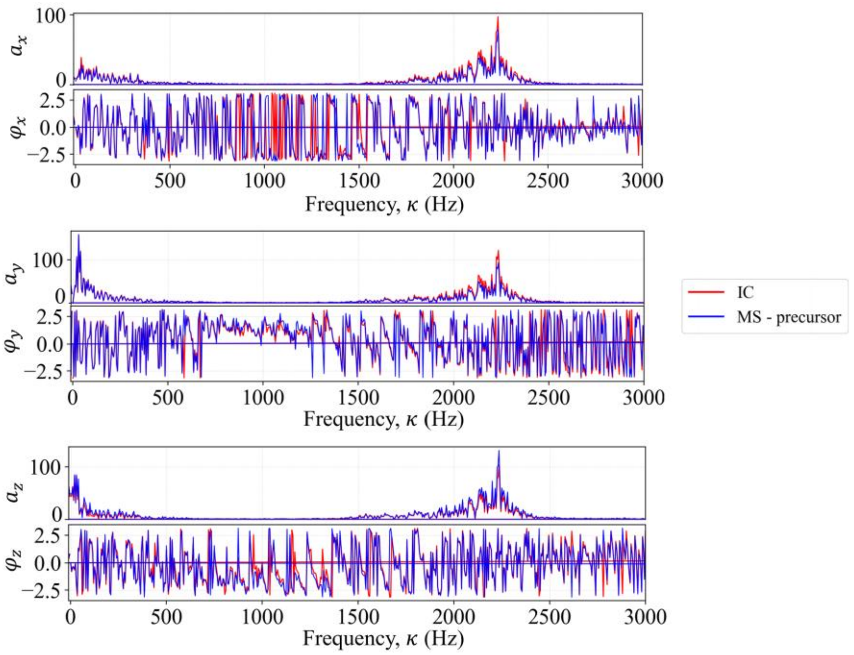

Figure 4.12 Frequency domain plot of the three-dimensional normalised velocity fluctuations, $u'/\bar{u}$ in amplitude, $a_{i,j,k}$ (top) and phase, $\phi_{i,j,k}$ (bottom) spectrum.

These small-scale eddies consist of primarily high-frequency fluctuations which will be diminished as the flow field is separated from the boundary layer, as shown in Figure 4.13 and Figure 4.14. Furthermore, the finer spatial resolution near the boundary layer can resolve smaller turbulent structures, thereby amplifying the noise at high-frequency spectrum. As the wake vortex propagating downstream, the frequency spectrum of velocity fluctuations is predominantly characterised by lower-frequency, higher-amplitude oscillations caused by the unsteady separation. The high-frequency content originating from small-scale turbulent structures near the boundary layer have progressively dissipated and is effectively absent in the more downstream region (i.e., $x/c = 3$).

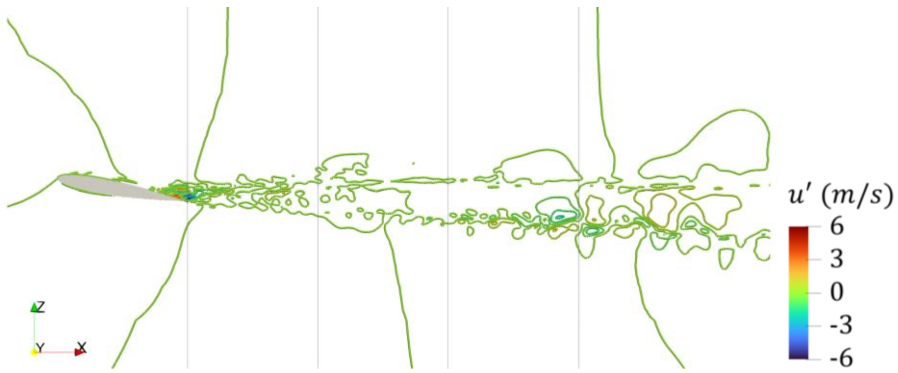

Figure 4.13 Contour in the LES IC domain, coloured by velocity fluctuations u', view from the wingtip.

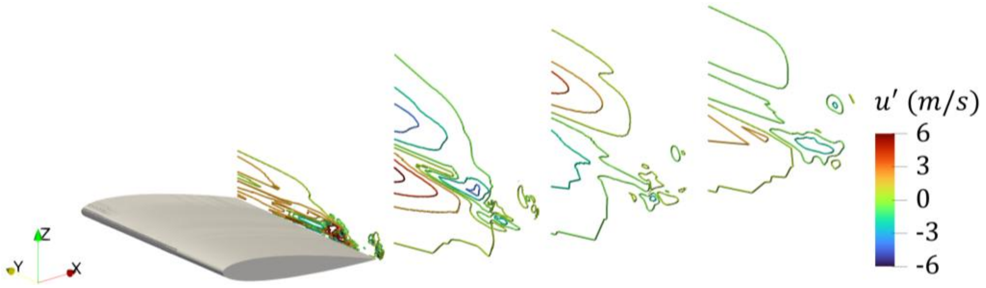

Figure 4.14 Velocity fluctuations contour at planes $x/c = 0$, 1, 2, after trailing edge.

To validate on the fluctuation characteristics, the amplitude of velocity fluctuation at $x/c = 3$ is plotted in the frequency domain, as presented in Figure 4.15. The resulting spectrum shows a significantly simplified fluctuations distribution as compared to Figure 4.12, where the dominant energy is concentrated at low frequencies while the high-frequency components have largely dissipated. This result validates that the velocity fluctuations in the further downstream planes possess a considerably simpler spectral profile. As a result, prescribing the inlet condition with a downstream location becomes a more practical approach, while it also reduces the upstream computational cost required for the simulation.

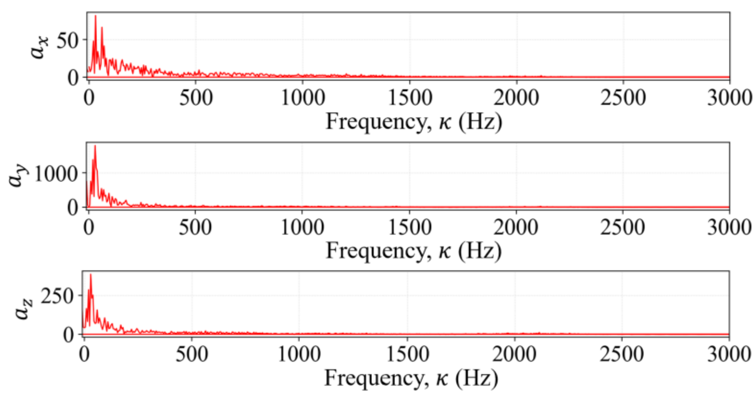

Figure 4.15 Frequency domain plot in amplitude spectrum for the highest tangential velocity $u_{\theta,max}$ point at downstream plane, $x/c = 3$.

4.4 Synthetic Method

Another approach for prescribing inflow conditions in the MS domain involves artificially generating time-dependent velocity fluctuations, also known as the synthetic method [75, 166]. The synthetic method only requires a single snapshot of mean velocity data from the IC domain that is subsequently energised by the synthetic fluctuation term. The mean velocity field is obtained via time-averaging of the resolved LES solution. Specifically, the mean velocity is defined as,

$$\bar{u}_{x,y,z}(t) = \frac{1}{T}\int_{t_0}^{t_0+T} u_{x,y,z}(t)\,dt \tag{41}$$

where t_0 denotes the start of the averaging period after the flow has reached statistical stationarity (approximately 50 chord-flow times), and T represents the averaging window following the initial transient period. In the present study, the averaging is applied to the velocity field in situ using the `fieldAverage` function object in OpenFOAM.

The synthetic fluctuation formulation is derived based on the Fourier representation of a turbulent velocity fluctuation signal. A velocity component can be decomposed into its mean and fluctuating components as,

$$u(t) = \bar{u} + u'(t) \tag{42}$$

where $\bar{u}$ represents the temporal mean velocity and $u'(t)$ represents the turbulent fluctuation. The temporal fluctuations of the point with highest tangential velocity u_θ across the selected plane in the IC domain is first recorded and analysed in the time domain and subsequently transformed into the frequency domain via a Fourier transform [167]. The velocity fluctuations components with Fourier decomposition are as follows,

$$u'_{x,y,z}(t) = \sum_{\kappa=1}^{n} a_{i,j,k} e^{i(2\pi f_{i,j,k} t + \phi_{i,j,k})} \tag{43}$$

Through the spectral analysis, the key parameters including the frequency $f_{i,j,k}$, amplitude $a_{i,j,k}$, and phase lag $\phi_{i,j,k}$ of fluctuations are extracted to characterise the temporal behaviour of velocity perturbations. The parameters extracted through the Fourier transformation were then used to formulate a series of sinusoidal expressions to synthesise velocity fluctuations on the mean flow field at each spatial node, enabling the velocity perturbations to be reconstructed using a series of harmonic functions as follows,

$$u'_{x,y,z}(t) = \sum_{\kappa=1}^{n} a_{i,j,k} \cos\left(f_{i,j,k} t + \phi_{i,j,k}\right) \tag{44}$$

With this formulation, the synthetic inflow velocity is represented as,

$$u_{x,y,z}(t) = \bar{u}_{x,y,z} + u'_{x,y,z}(t) \tag{45}$$

where the summation of the sinusoidal terms is the arbitrary synthesised fluctuation profile generated based on the turbulence behaviour of the point with highest tangential velocity across the y-z plane. The inclusion of phase information is important because the amplitude spectrum alone only describes the energy distribution among frequencies but does not preserve the temporal arrangement of the fluctuation components. Therefore, both amplitude and phase information are retained during reconstruction.

These fluctuations profiles are superimposed on the mean velocity field to reproduce the essential temporal and spatial characteristics of turbulence. Unlike the precursor approach, the synthetic method requires substantially lesser computer memory as it does not store the large time-series datasets. Instead, the turbulent fluctuations are regenerated dynamically at every LES time-step. Although the synthetic inlet method introduces a vortex profile that is spatially stationary and therefore does not reproduce the natural vortex-meandering behaviour, this limitation is acceptable in the present context. Garmann and Visbal [168, 169] demonstrated that tip-vortex meandering effect is negligible for stationary wings, particularly in steady, low-turbulence freestream conditions. Thus, the omission of meandering has minimal influence on the accuracy of the inflow representation for fixed-wing vortex simulations. In addition, the method inherently allows the enforcement of continuity constraints during the generation procedure, which improves inflow stability and numerical consistency [160].

This procedure regenerates turbulence with controllable amplitude, frequency content, and temporal coherence, while avoiding the storage burden associated with precursor datasets. Furthermore, the Fourier-series representation of fluctuations obtained from a periodic LES can be combined with mean velocity fields generated using alternative modelling approaches such as RANS or vortex methods (VM) [162, 170] to produce dynamically consistent inflow conditions tailored to different applications. This integration can transform the mean velocity profile into the desired dynamic velocity data for the MS inlet boundary.

The performance of the synthetic inlet conditions will be assessed using the same validation procedure applied to the precursor method. Taking the reference data from $x/c = 0$ in the IC domain, and the resulting flow development of the downstream planes in the synthetic MS are compared against the corresponding stations in the IC domain, as illustrated in Figure 4.3. This validation provides a direct basis for examining the fidelity of the synthetic method in reproducing the vortex inflow characteristics.

4.4.1 Validation of Synthetic Inlet

To generate the synthetic inlet fluctuations, the velocity signals extracted from the IC domain were transformed from the time domain into the frequency domain using a Fourier transform, as shown in Figure 4.16. Frequencies with discernible amplitude and the corresponding phase lag were manually selected for reconstruction, while components with negligible amplitudes were omitted. Using these extracted parameters, the inflow fluctuations were regenerated through the Fourier-series formulation in Eqs. (44) and (45)

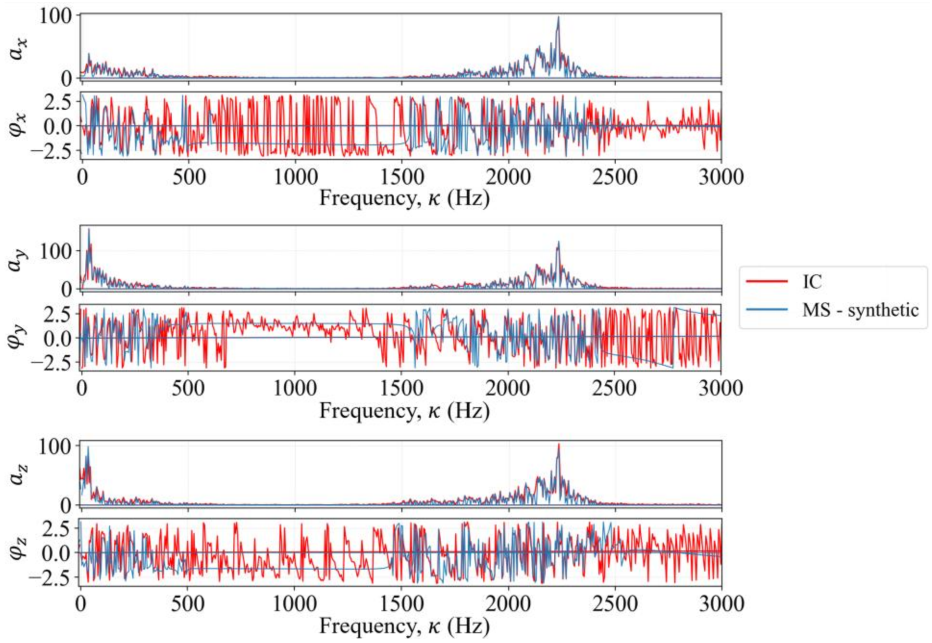

Figure 4.16 Frequency domain plot, corresponding to the time domain plot in Figure 4.17.

In Figure 4.17, the synthesised velocity fluctuations profile on the mean flow field velocity is plotted together with the original fluctuations profile from IC time domain. The comparison diagram shows that the synthesised time series plots are having consistent fluctuations magnitude bounded within the upper and lower limit of the fluctuations from IC. At certain points in the plots, the synthetic fluctuations also exhibited some dominant trends that match the fluctuations observed in the IC profile but there are also areas where the profiles do not align as closely. Unexpectedly, the cumulative effect of the ultra-low-amplitude components can lead to noticeable differences in the fluctuation profile. Despite some discrepancies in the graphs, this proves the applicability of synthetic method for the inlet condition.

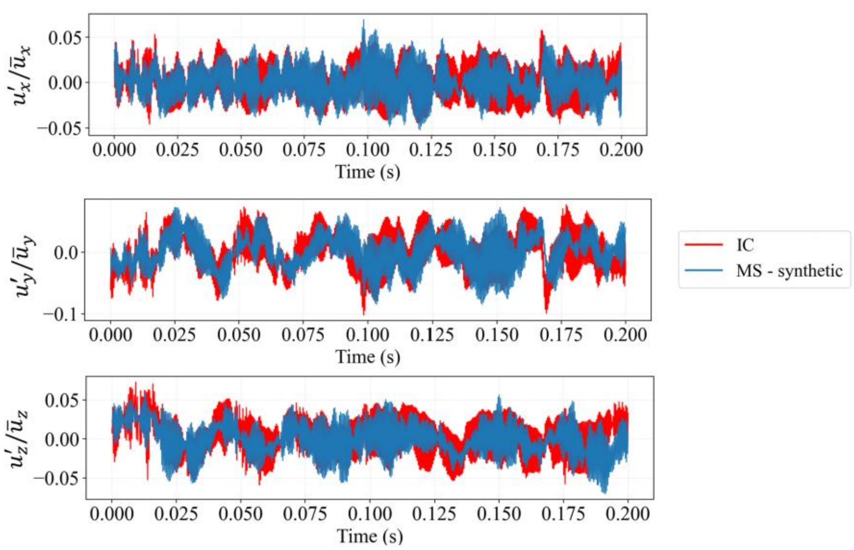

Figure 4.17 Time series fluctuation profile by synthetic method on of highest tangential velocity $u_{\theta,max}$ point.

Given the substantial variation in velocity components across the vortex core (see Figure 4.9), it may be desirable to express the fluctuations component as a percentage of its respective directional mean velocity magnitude. This normalisation ensures that the imposed fluctuations scale appropriately with the local flow intensity. To evaluate the feasibility of this approach, the instantaneous velocity fluctuations across the IC vortex core were normalised by the mean velocity magnitude at each grid point. The results were plotted along both the y- and z-axes, in Figure 4.18, to account for directional differences in the fluctuation behaviour.

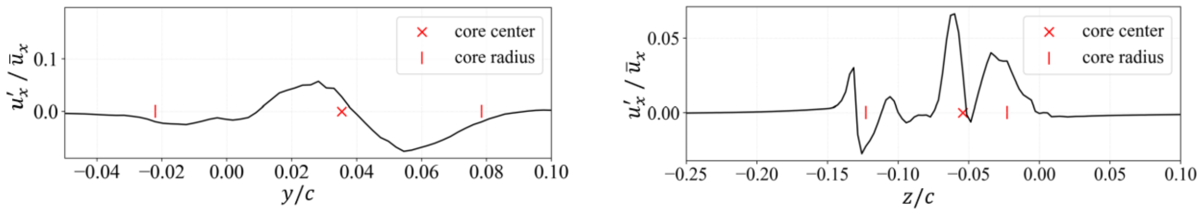

(a) x-component velocity fluctuations

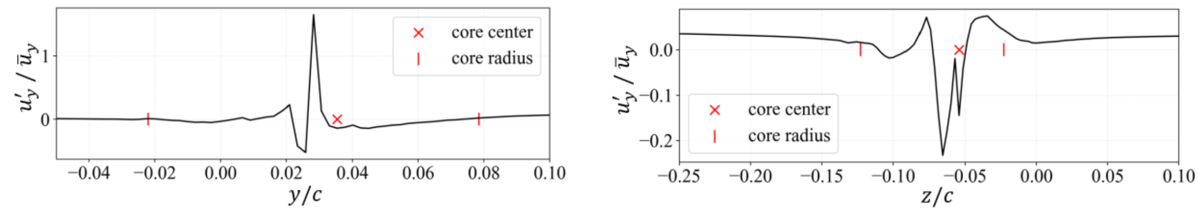

(b) y-component velocity fluctuations

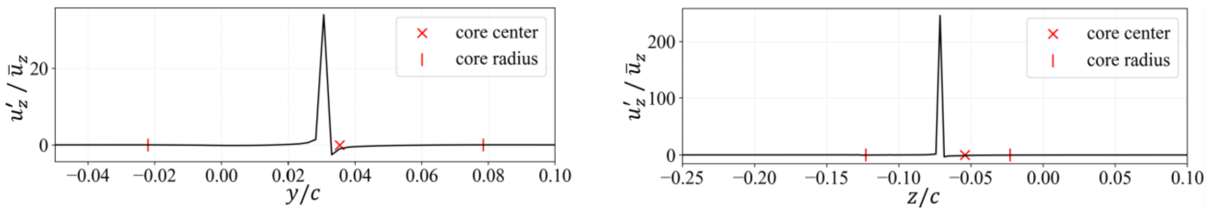

(c) z-component velocity fluctuations

Figure 4.18 Velocity fluctuations from IC normalised by mean velocity magnitude, $u'/\bar{u}$ across the vortex core in y-direction (left) and z-direction (right) at plane $x/c = 0$.

From Figure 4.18, it shows that the fluctuations magnitude is not a constant variable in relation to the mean velocity magnitude, especially within the vortex core. For the axial component, the normalised fluctuation intensity $u'_x/\bar{u}_x$ remains within approximately ±8%, indicating a relatively stable relationship. On the other hand, the normalised lateral and vertical velocity fluctuations (u'_y / $\bar{u}_y$ and u'_z / $\bar{u}_z$) show significantly high intensities near the core centre. This amplification arises from the very small mean lateral and vertical velocities in the core region, combined with strong turbulent activity and the intrinsic unsteadiness associated with vortex wandering. Consequently, the normalised fluctuations become highly erratic and lose physical representativeness.

These observations confirm that no single global scaling constant can be applied across the vortex, and therefore a direct normalisation-based synthesis strategy is not viable for this flow. The pronounced spatial variability of turbulence intensity within the rotational core highlights the inherent difficulty in reproducing the correct fluctuation field using purely synthetic inflow generation. A more robust approach would likely require conditional or region-specific fluctuation modelling, potentially incorporating separate treatments for the vortex core and for the outer flow, or leveraging additional physics-based constraints derived from precursor LES data.

4.5 Synthetic Inlet with Scaling Factor

The analysis from the prior validation on precursor method in Section 4.3.1 [76] indicated that it is more beneficial to employ data from a more downstream plane, due to the reduced high-frequency turbulent content and the smaller MS domain size required. Both contributing to lower computational cost for repeated MS simulations. Moreover, the assessment on the synthetic method using vortex data from plane $x/c = 0$ revealed notable instability in the reconstructed fluctuations and inconsistency in the synthesised turbulent structures, making the upstream plane unsuitable for inflow generation.

Therefore, the present study adopts the $x/c = 3$ plane in the IC domain as the inflow specification plane. At this location, the high-frequency turbulent content is significantly diminished, and the vortex structure has evolved into a more stable and coherent form, thereby providing a more robust and representative dataset for inlet conditioning. The subsequent downstream planes ($x/c =$ 4, 5, and 6) are then used to validate the propagation and stability of the mapped vortex structures. The flow field in the IC domain, visualised using the Q-criterion and coloured by velocity magnitude u, is presented in Figure 4.19.

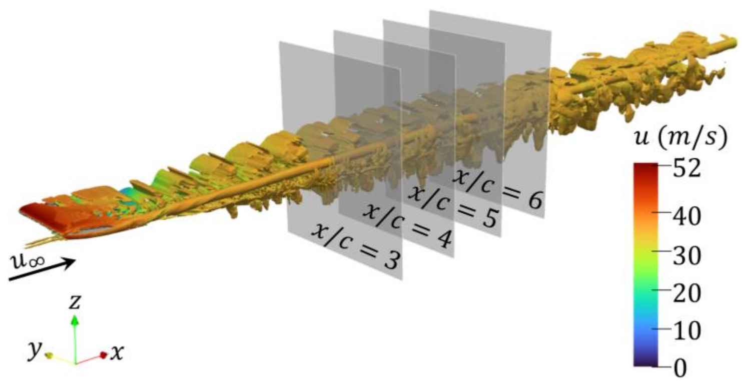

Figure 4.19 Wake vortex in IC domain visualised with Q-criterion = 100, coloured by velocity magnitude, u.

Given the chaotic and highly turbulent nature of wake vortex, it is almost impractical to have a one-solution-fit-all scaling factor across the plane. Therefore, this study simply focuses on the scaling factor that is valid for the vortex core area, where the turbulence representation is most critical. The fluctuation term in Eq. (44) is then combined with the scaling functions. The first method is by mean velocity $\bar{u}$ proportional scaling, to be presented in the later Section 4.5.1 [75, 76]. This method is to scale the temporal fluctuations profile with a factor proportional to the local mean flow intensity. Another method is by spatial correlation factor $R(\xi)$ [171, 172], to provide the fluctuation scale by radial position [173]. The spatial correlation factor was envisioned to compensate for the deviation between the mean velocity magnitudes and the corresponding fluctuation components, thereby improving the realism of the synthesised turbulence.

The two synthetic inlet conditioning strategies are summarised in Figure 4.20, where the effectiveness of both methods will be validated against downstream flow fields relative to the inlet to ensure that the synthesised turbulence not only reproduces the local vortex characteristics but also evolves consistently with the expected downstream dynamics. Ultimately, the objective of this work is to develop a synthetic model tailored for wake vortex flows that enables efficient LES with significantly reduced computational cost while maintaining an acceptable accuracy in capturing vortex coherence and turbulence fidelity. Both methods are described in the following sections respectively.

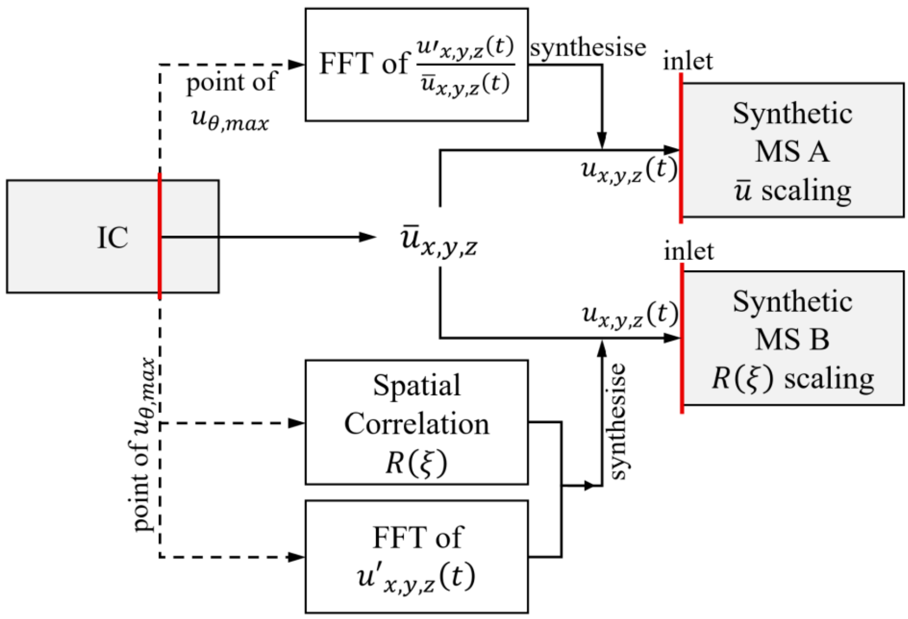

Figure 4.20 Overview of the inlet conditioning techniques in this thesis.

4.5.1 Fluctuations with Mean Velocity Scaling

On the $x/c = 3$ plane of the IC domain, the point with peak tangential velocity $u_{\theta,max}$ was selected to characterise the temporal fluctuations behaviour of the wake vortex. This data point lies along the vortex core circumference where the vortical flow is most energetic [106] and the axial velocity component has restored from deficit back to close to freestream conditions [113]. This has provided a strong signal-to-noise ratio for core vortex motions.

In cases where multiple local maxima are present due to numerical noise or secondary vortical structures, the point selection is based on the predefined vortex core circumference while excluding points in close proximity to the y- or z-axis to avoid bias arising from imbalanced lateral and vertical velocity contributions. This ensures that the selected point is associated with strong signal-to-noise ratio for primary vortex structure rather than secondary fluctuations and provides a well-balanced representation of the three-dimensional velocity components.

The low frequency meandering and core displacement also makes the vortex core spatially coherent, so the peak tangential velocity point can capture the characteristics of temporal fluctuations very well and it is a good single point proxy for the large-scale core dynamics.

The temporal velocity fluctuation signals were captured normalised by the local mean velocity and plotted over minimum five times the integral time scale T^u, as recommended by established turbulence-sampling guidelines [163]. The normalised temporal fluctuation signal for the streamwise component is presented in Figure 4.21a. The data were then transformed from the time domain to the frequency domain using the Fast Fourier Transform (FFT) toolkit in Python (NumPy), yielding the amplitude and phase spectra shown Figure 4.21b and Figure 4.21c, respectively.

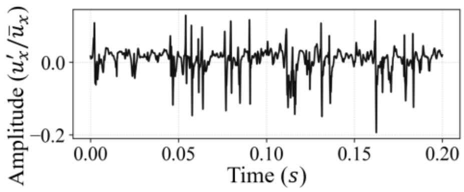

(a) Normalised velocity fluctuations in the time domain plot.

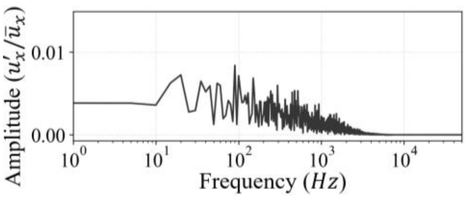

(b) Fourier transform into the frequency domain plot.

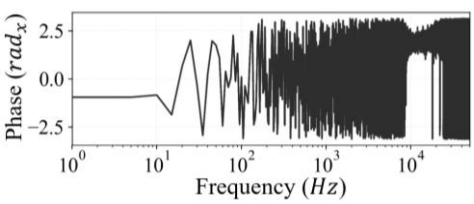

(c) Phase plot in the frequency domain.

Figure 4.21 Velocity fluctuations of x-components in time and frequency domain plot at $x/c = 3$.

From the transformed data, the dominant amplitudes in the frequency domain were identified and the corresponding phase information was extracted from the complex FFT coefficients. The same procedure was applied to the y- and z- components. To improve the resolution of synthetic fluctuation signal, any amplitudes exceeding 0.1% of the mean velocity value were extracted for inclusion in the summation of sinusoidal terms used in calculating the local velocity, as expressed in the following equation,

$$u_{x,y,z}(t) = \bar{u}_{x,y,z} + \left[\bar{u}_{x,y,z} \cdot \sum_{\kappa=1}^{n} a_{i,j,k} \cos\left(f_{i,j,k} t + \phi_{i,j,k}\right)\right] \tag{46}$$

In OpenFOAM, the synthetic inlet solver is modified to incorporate temporal fluctuations with inputs from user for amplitude, frequency and phase shift for all three directional velocity vectors. The solver will compute the velocity fluctuation terms based on the sinusoidal equations at each time step and the corresponding local velocity magnitude, to restore the turbulent profile of the wake vortex with multi-frequency oscillatory behaviour.

4.5.2 Fluctuations with Spatial Correlation Scaling

The other solution to extend the use of a single point proxy from the peak tangential velocity point is to incorporate spatial correlation coefficients $R(r)$ [174, 175]. In a wingtip vortex with a well-defined mean structure, these coefficients can represent the variation of velocity fluctuations across the core radius. The addition of spatial correlation term introduces a spatially varying factor that reflects the coherence of the vortex structure and provides a physically consistent scaling of the fluctuation amplitude across the core. The correlation of velocity fluctuations is computed from the velocity field of the IC simulation, as formulated below [171, 174],

$$R(r) = \frac{\langle u'(r_c,\, t) \cdot u'(r_c + r,\, t)\rangle}{\langle u'^2(r,\, t)\rangle} \tag{47}$$

where the numerator represents the covariance between two spatial locations and the denominator normalises the correlation to provide values between -1 and 1. In the context of wingtip vortices, this formulation allows the spatial variation of turbulent fluctuations away from the vortex core to be quantified and subsequently incorporated into the synthetic inlet reconstruction. The spatial correlation function in this study is expressed as $R(\xi)$, a function of dimensionless vortex radius ξ, representing the radial position with respect to the vortex core radius ($\xi = r/r_c$) from the vortex core centre [172].

Normalising the radial distance using vortex core radius allows the correlation distribution to be applied consistently relative to the vortex structure.

$$R(\xi) = \frac{\langle u'_{x,y,z}(x,\ y,\ z,\ t) \cdot u'_{x,y\prime,z\prime}(x,\ y + r_y, z + r_z,\ t)\rangle}{\langle u'^{2}_{x,y,z}(x,\ y,\ z,\ t)\rangle} \tag{48}$$

where $u'_{i,j,k}(x,\ y,\ z,\ t)$ represent the velocity fluctuation vector at grid point i, corresponding to the location of maximum tangential velocity $u_{\theta,max}$ evaluated over time. The terms r_y and r_z denote the spatial discretisation in the y- and z- directions with respect to the radial distance from the vortex core centre and point i. The angle bracket $\langle \cdot \rangle$ indicates the temporal averaging of the product of the dataset. The two-point spatial correlation is used to moderate the scale of fluctuating velocities across different radial positions of the wake vortex, in other words, along the radial line plotted from the vortex core centre crossing the peak tangential velocity point and extended towards $\xi = 3$, as shown in Figure 4.22.

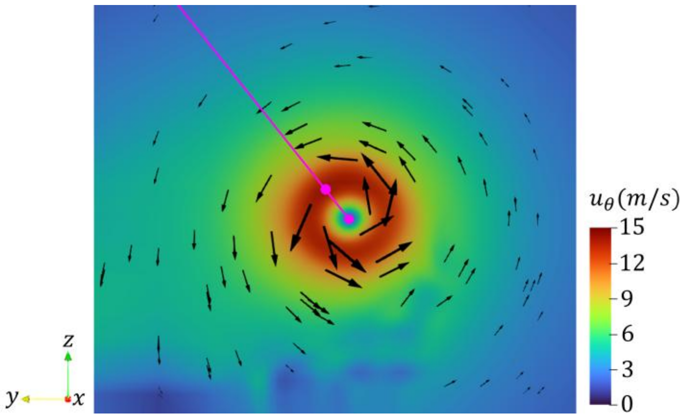

Figure 4.22 Plotting of the radial path from vortex core centre via the peak tangential velocity point.

Based on the data examined on the points along the radial path, the phase-averaged spatial correlation coefficients are computed and plotted into line chart for visualisation. From the spatial correlation plotted at different streamwise position in Figure 4.23, it is observed that the wake has not yet fully developed into a coherent vortex structure in the very near field ($x/c = 1$). At this location, the streamwise correlation exhibits oscillatory behaviour, while the azimuthal correlation remains predominantly negative, both indicate to an undeveloped and highly unsteady vortex roll-up. As the vortex matures downstream, the spatial correlation progressively strengthens and transitions toward more coherent behaviour. In addition, the spatial correlation profile varies distinctly across the radial position, it is noticed that the spatial correlation for the axial velocity $R_x(\xi)$ appeared to be different from the lateral and vertical velocity components $R_{y,z}(\xi)$.

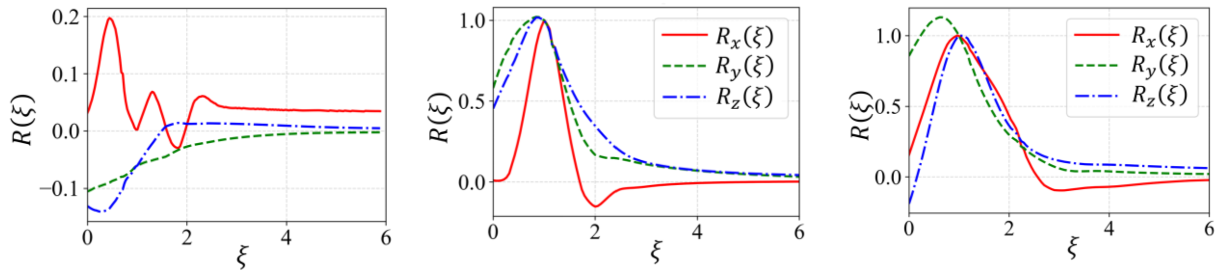

(a) $x/c = 1$ (b) $x/c = 3$ (c) $x/c = 5$

Figure 4.23 Spatial correlation of velocities along the radial path.

From the line chart, the spatial coherence of axial velocity fluctuations u_x' at the vortex core is near to zero. The correlation then experiences a Gaussian rise and peak at near $\xi = 1$. After the peak, the spatial correlation coefficient undergoes a damped cosine decay, where there is cross zero oscillatory behaviour as the flow field transitions into the freestream conditions, similar observations were reported in wind farm and acoustic fields [175, 176]. Based on the profile, the pre-peak and post-peak information had modelled them with different terms as expressed in the following,

$$R_x(\xi) = (1 - w(\xi))\left[\frac{1 - e^{-\xi^2/\sigma^2}}{1 - e^{-1/\sigma^2}}\right]^p + w(\xi)\left[\frac{e^{-\lambda(\xi-1)}cos(\beta(\xi - 1) + \phi)}{cos\,\phi}\right] \tag{49}$$

where $w(\xi) = \frac{1}{1+e^{-k(\xi-1)}}$ is a typical sigmoid function to seamlessly switch between the pre-peak and post-peak terms, with parameter k to control the transition sharpness. For the pre-peak region where it is within the core $\xi < 1$, the $w(\xi)$ is close to 0 and the spatial correlation is primarily governed by the pre-peak component. This is the Gaussian cumulative distribution profile that is commonly used in statistics or Gaussian vortex profile such as Lamb-Oseen model [108]. This term models the initial Gaussian rise of correlation factor from the core centre towards the core circumference. The numerator represents the cumulative effect of the vortex structure, parameterised by its relative width σ. This function is normalised by its value at the core radius where $\xi = 1$ to ensure unity and raised to a pre-peak exponent p to suppress a larger portion of the initial rise to remain near zero before the profile turning upwards.

When the dimensionless radial value ξ is transitioned to above one, the correlation function is then dominated by the damped oscillatory post-peak component. The exponential decay term $e^{-\lambda(\xi-1)}$ dictates the rate of spatial decay, where higher λ produced faster loss of coherence. Whereas the cosine term introduces coherent oscillations with spatial oscillation wavenumber β and phase ϕ to shift the sinuous profile, normalised by $\cos\phi$ to ensure the amplitude continuity at $\xi = 1$.

Unlike the correlation on axial velocity fluctuation, the fluctuation correlation on the tangential velocity components exhibited a non-zero coefficient at the very vortex core location, as reported in the Section 4.4.1 and Figure 4.18 Velocity fluctuations from IC normalised by mean velocity magnitude,

$\boldsymbol{u'/\bar{u}}$ across the vortex core in $\boldsymbol{y}$-direction (left) and $\boldsymbol{z}$-direction (right) at plane $\boldsymbol{x/c = 0}$. [76]. The fluctuations of both the tangential components u'_y and u'_z exhibited similar behaviour like a general damped cosine wave with peak at around $\xi = 1$ location and in some cases exceeding unity ($R_{y,z}(\xi) > 1$). This is due to the selected point with maximum tangential velocity does not necessarily coinciding with the locations of maximum lateral or vertical velocities, nor their respective fluctuation amplitudes. Consequently, other points within the vortex core may exhibit higher correlation coefficients than the reference point. The form of the spatial correlation for tangential component is expressed as,

$$R_{y,z}(\xi) = A_{j,k}e^{-\lambda_{j,k}\xi}\, cos\left(k_{j,k}\xi + \phi_{j,k}\right) + C_{j,k} \tag{50}$$

where the function model captures the wave behaviour where amplitude rises and diminishes exponentially as the radial distance increases. A is the initial amplitude to set the scale of the oscillation. Similar to the axial fluctuation correlation, the exponential decay term $e^{-\lambda\xi}$ is to represent the effects of dissipation or diffusion of coherence in the system. The oscillatory term $cos(k\xi + \phi)$ describes the periodic, wave-like nature of the profile, with k being the wavenumber and ϕ being the phase shift. Lastly the constant offset term C which accounts for a non-zero residual in the data.

Considering the velocity fluctuation distribution across the vortex core as shown in Figure 4.24, directly applying the spatial correlation to the y- and z-components individually using Eq. (50) would produce inaccurate results. For instance, along the y-axis where the $\bar{u}_y$ and its fluctuations u'_y are near zero, the correlation would still impose high fluctuation amplitudes as the model depends solely on radial distance, not the relative position to the vortex core centre.

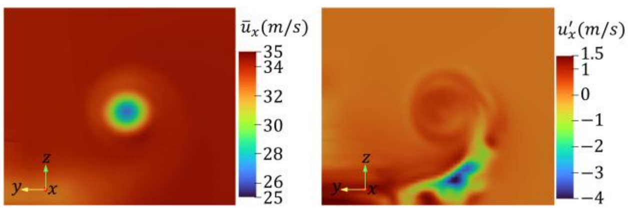

(a) x-component of velocity and fluctuations

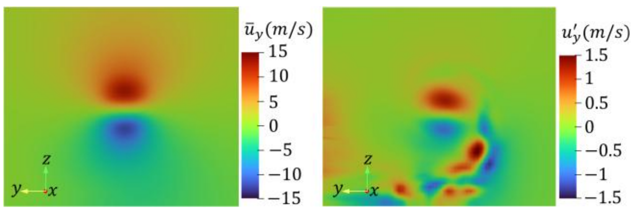

(b) y-component of velocity and fluctuations

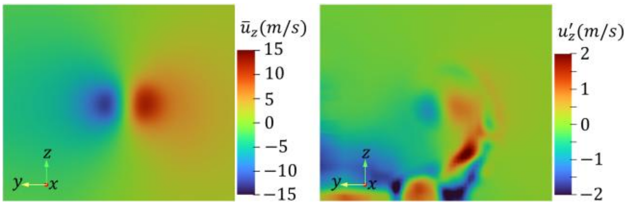

(c) z-component of velocity and fluctuations

Figure 4.24 Distribution of three-directional mean velocities (left) and fluctuations (right) around the vortex core area.

Hence, to better represent the local vortical fluctuations correlations, the two directional components were combined into a single tangential component by vector interpretation. The product is plotted in Figure 4.25, providing a clearer depiction of the spatial correlation of tangential velocity fluctuations. Its overall profile remains similar as the lateral and vertical components but with a higher magnitude, and therefore Eq. (50) remains applicable.

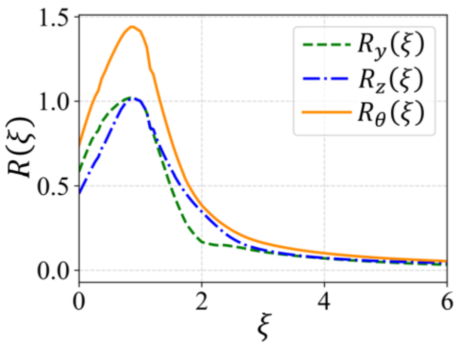

Figure 4.25 Spatial correlation of tangential velocity fluctuations at $x/c = 3$.

The model parameters for each velocity components in $R(\xi)$ terms – from Eqs. (49) and (50) were optimised using a nonlinear least-squares fitting in Python using the `curve_fit` function from the SciPy library [177]. For each turbulent component, the fitting procedure was initialised with a reasonable estimate. The optimisation algorithm then iteratively adjusted these parameters to minimise the sum of squared residuals between the modelled damped cosine function and the experimental spatial correlation data. The best fit parameters based on the precursor simulation result on the $x/c = 3$ plane are recorded as follows,

Table 4.1 Best fit parameters for the spatial correlation function at $x/c = 3$.

Axial						Tangential				
σ	p	k	λ	β	ϕ	A	λ	k	ϕ	C
0.64	1.76	7.62	1.90	2.94	-0.52	5.31	1.25	0.78	-1.48	0.04

As the resulting profiles are expressed in a mathematical model, the values in the Table 4.1 were adopted to complete the prescription of each $R(\xi)$ term and to generate inflow turbulence for the MS inlet boundary. The results are plotted in Figure 4.26 for validation and the results are highly matching, with R^2 value of 99.6% and 97.7% for the axial and tangential components respectively.

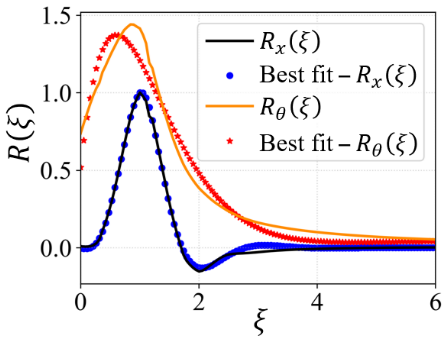

Figure 4.26 Validation of the spatial correlation model.

Subsequently, based on the spatial orientation with respect to the core centre in the y-z plane, the solver determines the azimuthal coordinate around the vortex core by evaluating the polar angle of each point, where $\theta = tan^{-1}(\Delta y/\Delta z)$. The tangential component is then decomposed back into the y and z directions using trigonometric relations,

$$R_y(\xi) = -R_\theta(\xi)\, sin\, \theta \tag{51}$$

$$R_z(\xi) = R_\theta(\xi)\, cos\, \theta \tag{52}$$

This transformation allows the synthesised velocity fluctuations to be reconstructed in the Cartesian coordinate system while preserving the azimuthal symmetry for the simulation. The need for this decomposition arises because the point of peak tangential velocity generally occurs at an arbitrary location around the vortex circumference and does not lie on either the y- or z-axis, where the u_z and u_y are at the maximum respectively. By decomposing the tangential term, the spatial correlation would restore the more accurate value at each location. Even though the wake vortices are not axisymmetric, the decomposition of tangential components by azimuthal coordinates reveals the dominant modes and reduces complexity for the anisotropic turbulence near the vortex core. With the spatial coherence factors, the synthetic velocities on the MS inlet boundary can be computed with the following expression,

$$u_{i,j,k}(t) = \bar{u}_{i,j,k} + \left[\sum_{\kappa=1}^{n} a_{i,j,k} \cos\left(f_{i,j,k}t + \phi_{i,j,k}\right) \cdot R_{x,y,z}(\xi)\right] \tag{53}$$

where the amplitude in the sinusoidal term is the absolute magnitude of the fluctuation. With either synthetic inlet condition methods, provided that the mean flow field is accurately modelled, the synthetic formulation can generate time-dependent inflow conditions even with mean flow data obtained from different modelling frameworks such as Reynolds-Averaged Navier–Stokes (RANS) or vortex methods (VM) [162, 170].

The proposed synthetic fluctuation formulation is developed based on the turbulence characteristics extracted from the reference LES case considered in this study. Therefore, the objective is to demonstrate the feasibility of reconstructing vortex-specific turbulent inflow conditions and reducing the dependency on storing large precursor datasets, rather than establishing a universal turbulence model applicable to all Reynolds number regimes. The spectral characteristics and spatial correlation functions used in the formulation may vary with flow conditions, and further investigations involving different Reynolds numbers and vortex configurations are required to assess the broader applicability of the proposed methodology.

4.5.3 Results of Synthetic Inlet with Scaling Factor

The synthetic methods are characterising the temporal velocity fluctuations using the representative points with peak tangential velocity. Hence it is crucial to validate the synthesised fluctuations on the MS domain inlet against the precursor IC data, to ensure the synthetic method reproduced the intended temporal behaviour. The time series data of u_x' , u_y' and u_z' from both MS domain with inlet conditioning by synthetic method A – scaled by the magnitude of local mean velocity $\bar{u}_{x,y,z}$, and method B – scaled by the spatial correlation coefficient $R_{x,y,z}(\xi)$ were plotted and examined in Figure 4.27. Although minor amplitude shifts were observed, they are likely attributed to the exclusion of small fluctuation components during Fourier reconstruction, and very minor deviations in the baseline mean velocity field. Nonetheless, both methods successfully synthesise the oscillatory characteristic of the wake vortex, reproducing the satisfactorily accurate amplitude, frequency, and damping trends. These results confirm that the synthetic inlet framework can accurately generate the necessary velocity fluctuations at the inlet boundary.

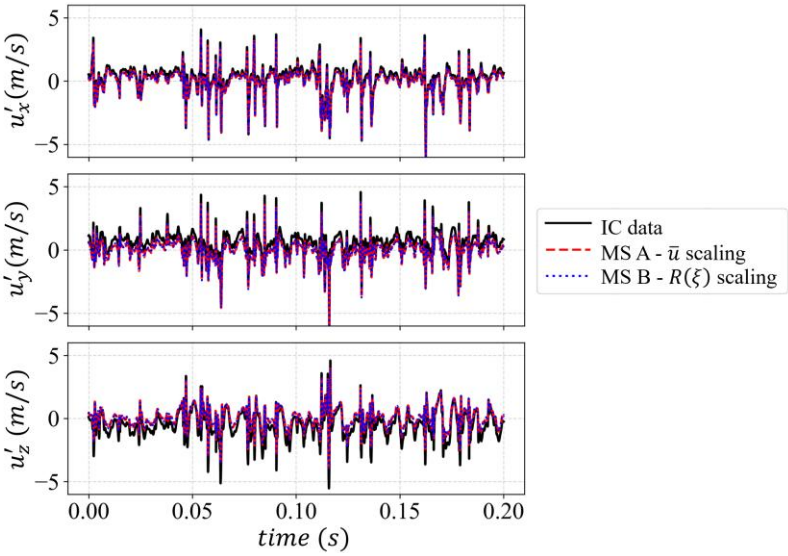

Figure 4.27 Validation on the velocity fluctuations of the representative point on the synthetic inlet ($x/c = 3$).

With the augmented fluctuations at the inflow boundary, combined with the applied scaling factor, the wake vortex development in the MS domain is expected to closely replicate the vortex coherence and turbulent characteristics observed in the IC domain. To examine the fidelity of the wake vortex turbulence structures, a snapshot of the partial wake vortex from the IC domain is captured and illustrated in Figure 4.28a, coloured by tangential velocity magnitude u_θ. The corresponding LES results in the MS domains are presented in Figure 4.28b and c, allowing a direct comparison qualitatively.

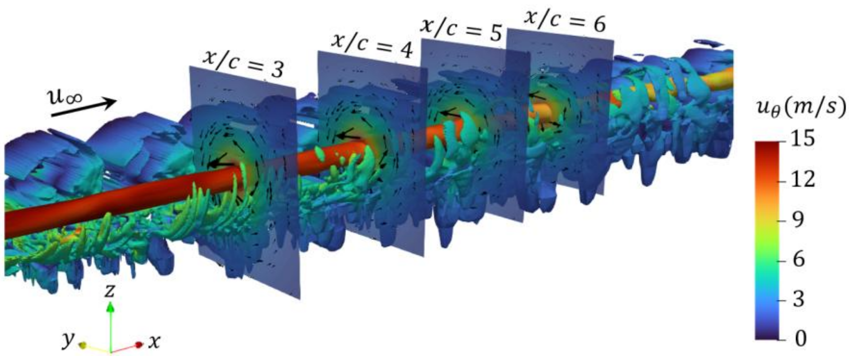

(a) IC domain with wake vortex induced by physical wing geometry.

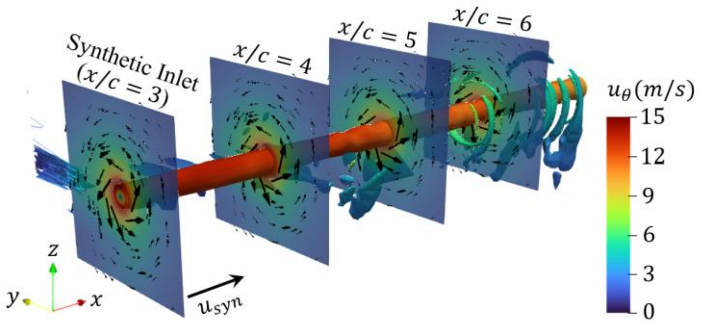

(b) MS with synthetic inlet by method A – mean velocity scaling.

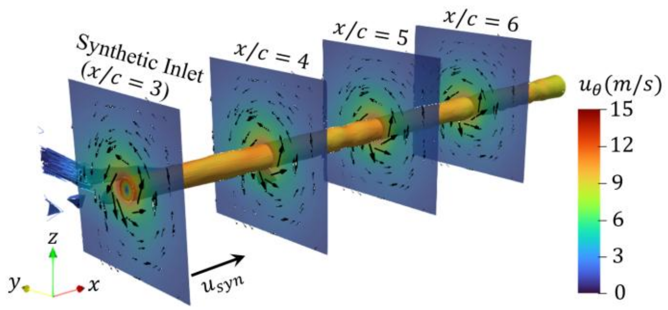

(c) MS with synthetic inlet by method B – spatial correlation scaling.

Figure 4.28 Wake vortex (core region) in the IC and MS domains with synthetic inlet conditions, visualised with Q-criterion=100, coloured by tangential velocity magnitude u_θ.

Comparing the results in Figure 4.28, both inlet strategies successfully capture the overall vortex core structure of the wake vortex. The synthetic inlet with mean velocity scaling exhibited with a more realistic turbulent structure and a closer match to the tangential velocity distribution around the vortex core. To validate the effectiveness of the synthetic inlet of vortical flow more, the flow-field parameters on the downstream planes with one to three chord length are assessed quantitatively against the corresponding location in the IC domain. The tangential velocity profiles across the vortex core in both MS domains are plotted together with the IC results in Figure 4.29. Synthetic method A matches the IC profile well ($R^2 > 95\%$ up to two chords downstream) but overpredicts at $x/c = 6$ with R^2 drops to 72%. Method B has a slightly lower near field R^2 (~90%) but better matches tangential velocity at $x/c = 6$ ($R^2 = 78\%$). Both methods track the vortex core centre and the vortex core size accurately, with less than 2% chord-length deviation. Overall, both approaches achieve a high level of fidelity in reproducing the wake vortex evolution while highlighting the trade-offs between near-field accuracy and downstream prediction.

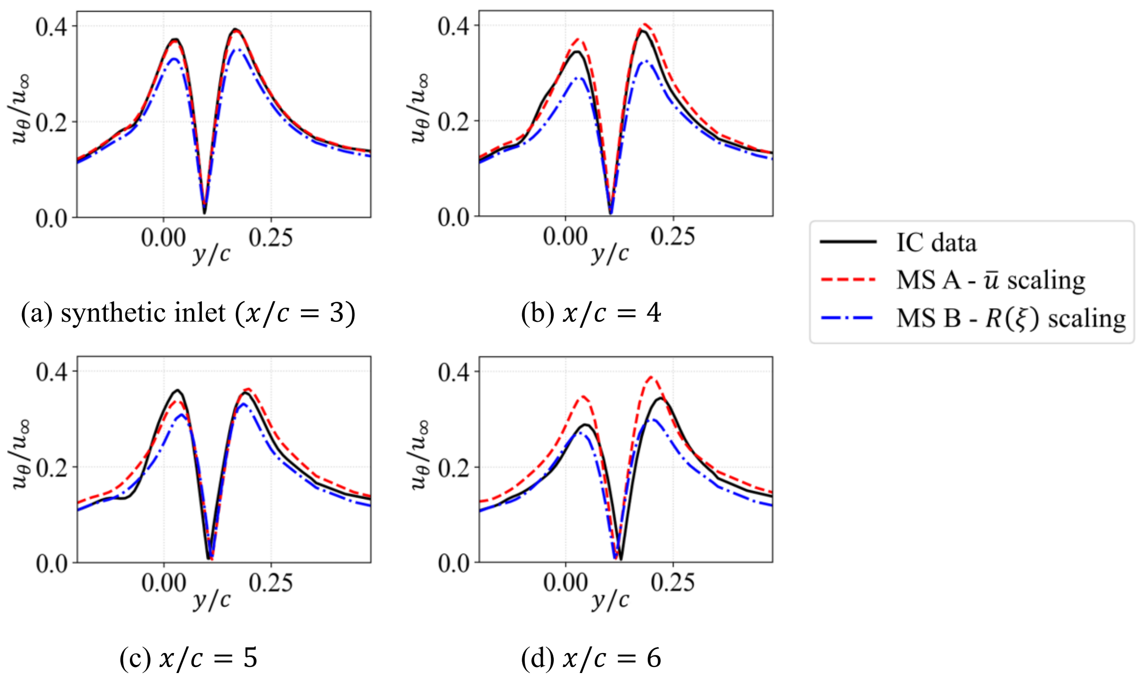

Figure 4.29 Validation on the tangential velocity profile across vortex core.

The instantaneous velocity fluctuations are further examined on x-z planes at several lateral stations to assess the spatial distribution of fluctuation turbulence. Three slices are selected at $y/c = 0$, 0.1 and 0.2, correspondingly respectively to the wingtip location, cutting directly through the vortex core centre, and a more inboard position behind the wing geometry. Figure 4.30a presents the contour plots of velocity fluctuations from the precursor IC domain, while Figure 4.30b and c show the corresponding results from the MS domain using synthetic methods A and B, respectively.

From the results, method A exhibits stronger velocity fluctuations within the vortex core region, whereas method B better preserves the fluctuation intensity in the outer regions of the vortex. This behaviour may be attributed to the scaling formulation – mean velocity scaling tends to amplify fluctuations in regions of strong mean flow [75], while spatial correlation scaling maintains a more gradual radial decay [175], consistent with the local coherence structure of the vortex.

Among the three lateral planes, the strongest turbulence intensity is observed at $y/c = 0.1$, which coincides with the vortex centre in each of the simulation domain. Whereas the planes at $y/c = 0$ and 0.2 show comparable but weaker intensities due to reduced shear effects. These findings suggest that either normalised fluctuation or spatial-correlation method does effectively capture the radial distribution of turbulence, while the mean velocity scaling approach offers a simpler yet sufficiently accurate for representing near-core turbulence.

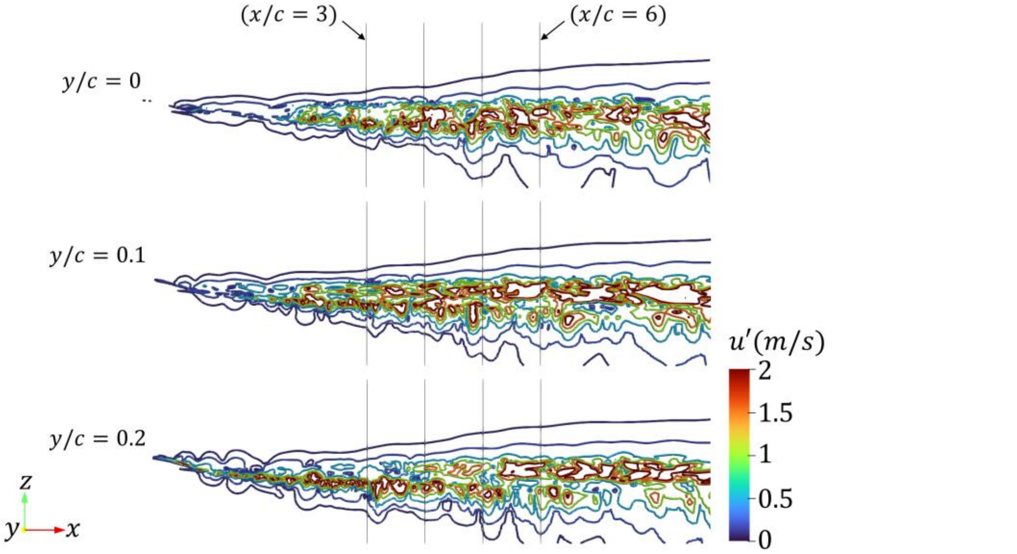

(a) IC domain with wake vortex fluctuations induced by wing geometry.

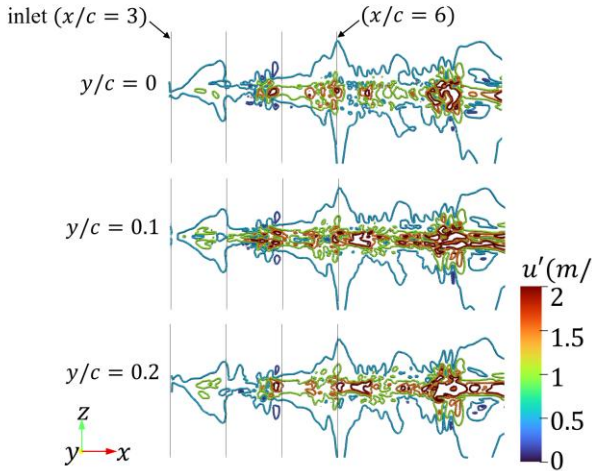

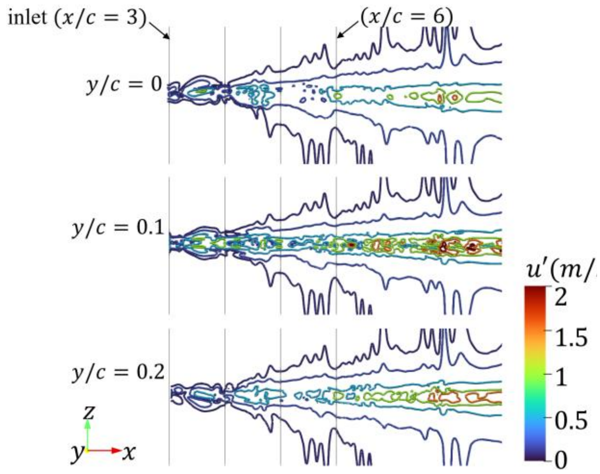

(b) MS with synthetic inlet by $\bar{u}$ scaling.

(c) MS with synthetic inlet by $R(\xi)$ scaling.

Figure 4.30 Contour of velocity fluctuations across x-z plane at different y-position.

4.6 Summary and Recommendations

This chapter has investigated and evaluated advanced inlet boundary conditioning strategies for freestream vortical flows in LES, with specific focus on wingtip vortices relevant to wake vortex surfing applications. While there are several well-established inlet conditioning methods such as precursor mapping, synthetic turbulence, and recycling-rescaling, the direct applications are in the context of wall-bounded or confined flows. The research on freestream vortical structures remains a challenging gap due to the highly fluctuating turbulences near the vortex core, and varying velocity profile across the vortex core. The specifications of these characteristics at the chosen plane for inflow conditioning are critical to maintain the physical fidelity in downstream simulations of formation flight.

The earlier part of this chapter examined the precursor method to map the time series data of the wake vortex induced by wing geometry in the IC domain onto the inlet of the MS domain. The results demonstrated the accuracy of the precursor method in reproducing the highly realistic turbulent structures and robust flow characteristics such as the vortex core dimension, position and the circulation strength. The precursor method also replicated the turbulent profile in the downstream flow, with negligible attenuation in velocity fluctuations. The primary limitation of this approach is the significant data storage requirement and the computational cost of generating long precursor sequences.

Based on the analysis of the turbulence behaviour in the precursor flow field, the necessary parameters were captured to formulate the Fourier series expression which can synthetically regenerate the velocity fluctuations based on the mean-flow-field information. However, the study revealed fundamental challenge where the vortex core fluctuations vary strongly with radial position, and no single scaling law or correlation function can accurately reconstruct the fluctuation field across the entire inlet plane. Although the synthetic method reproduced several dominant fluctuation modes and demonstrated feasibility, its accuracy remains insufficient for fully capturing the spatially varying turbulence structure of wingtip vortices. This motivates future work toward hybridisation or conditionally applied synthetic models that separately treat the vortex core and the outer flow regions.

A key insight from this chapter is that using a more downstream precursor plane (e.g., $x/c = 3$ or later) improves the stability and accuracy of the mapped inflow, as the vortex has evolved into a coherent structure with reduced high-frequency turbulent content. This reduces both mapping errors and the required MS domain length, improving overall computational efficiency for repeated trailing-aircraft simulations.

Overall, this chapter confirms that precursor-based inlet mapping offers the highest fidelity for LES of freestream vortices. Whereas the synthetic conditioning approach demonstrates the feasibility of generating vortex turbulence without storing extensive precursor datasets. While these approaches significantly reduce computational cost, additional challenges remain, particularly when extending to more complex scenarios involving multiple interacting vortices or full aircraft wake fields, where accurately capturing inter-vortex correlations and spatially varying turbulence structures will be critical. In addition, since the fluctuation characteristics are derived from a reference LES case, further investigations across different Reynolds numbers and operating conditions are required to establish the general applicability and robustness of the proposed formulation.

The novelty of the proposed synthetic conditioning approaches lies in their adaptation for wingtip vortex LES, where the turbulence characteristics exhibit strong spatial variation due to vortex-induced flow structures. Unlike conventional synthetic turbulence methods developed for uniform freestream inflows, the proposed approaches incorporate vortex-specific features through mean velocity scaling and spatial correlation-based reconstruction to improve the representation of turbulent fluctuations within and outside the vortex core. This research lay the foundation for subsequent studies involving parametric evaluation of trailing-aircraft positions using the MS domain without recomputing upstream vortex generation.

Chapter 5

Large Eddy Simulation for Formation Flight Predictions

In the formation flight simulation, the previously validated LES model in OpenFOAM is used to analyse the aerodynamic interactions between the leading and trailing wings. The leading wing corresponds to the validated configuration at NACA 0012 with $\alpha = 10°$, while the trailing wing with identical NACA 0012 aerofoil profile, chord $c = 0.14m$, wingspan, $b = 0.3m$ and $\alpha = 0°$, is placed in the downstream position as shown in Figure 5.1. Before assessing the formation flight effects, an isolated LES computation of the trailing wing is performed to establish the baseline aerodynamic coefficients. Any subsequent deviation in the lift, drag or moment during formation flight is therefore attributed solely to the influence of the wake vortex system generated by the leading wing, and thus interpreted as the vortex surfing effect.

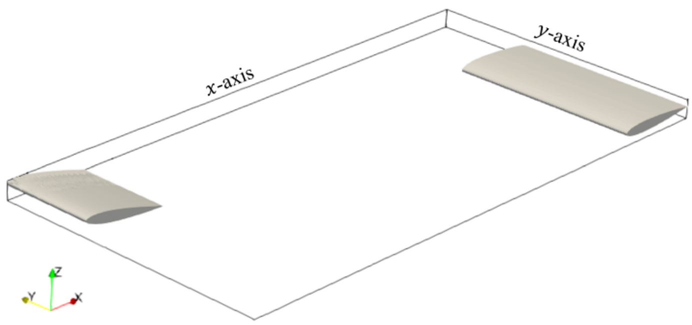

Figure 5.1 Leading and trailing wings in formation.

As the behaviour of wingtip vortices in the near field where $x/c < 6.43$ $(x/b < 3)$ remains nearly constant in both magnitude and structure [111, 178], the impact of vortex surfing on the trailing wing along the longitudinal axis is minimal in the close formation [179]. However, due to the slight degradation of the vortex in the LES model shown in validation work above, an additional assessment across different longitudinal separation (x/c) from the leading wing is required to determine the appropriate separation for formation flight analysis.

Accordingly, a series of simulations is conducted where the trailing wing is positioned at varying streamwise separations x/c behind the leading wing, while maintaining zero lateral and vertical offsets ($y/c = 0, z/c = 0$). This configuration represents the theoretically optimal arrangement for induced-drag reduction, as recommended by Lissaman and Shollenberger [14]. Once the longitudinal dependence is established, the trailing wing will be fixed at the selected x/c plane and subsequently repositioned laterally and vertically to map the full aerodynamic benefit field within the vortex upwash region. An illustration of the wake-vortex surfing configuration with the trailing wing located at $x/c = 4.29$ is provided in Figure 5.2.

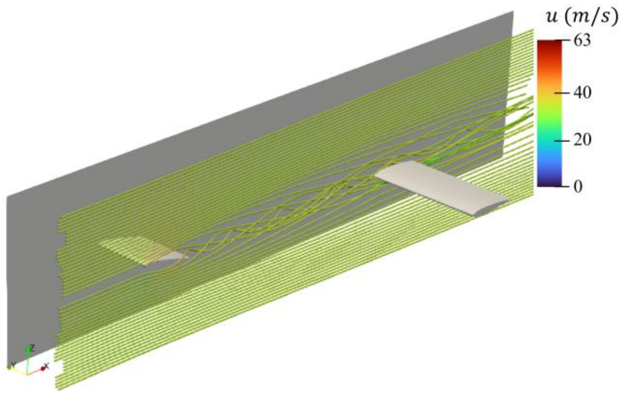

Figure 5.2. Stream tracer on wingtip vortices in formation.

5.2 Wake Surfing Effect

The CFD results on the aerodynamic coefficients of the leading and trailing wings at various longitudinal separation, x/c is presented in Figure 5.3. In the close formation flight, the leading wing with $\alpha = 10°$ does not experience any noticeable change in terms of the lift and drag characteristics when compared with its solo flight baseline. This indicates that the follower-induced aerodynamic interference is minimal. Conversely, the trailing wing with a symmetrical aerofoil profile at $\alpha = 0°$ produces nearly zero lift in an isolated flight but gains substantial aerodynamic benefits when operating within the upwash field of the leader's tip vortex.

When the lateral and vertical offsets are fixed at $y/c = 0$ and $z/c = 0$, the wake surfing effect is solely influenced by the longitudinal spacing. As the trailing wing moves progressively downstream, the aerodynamic benefits diminish slightly due to the loss of vortex strength as energy dissipates over time. However, this reduction is relatively small comparing to the aerodynamic gains made from the induced upwash generated by the wake vortex.

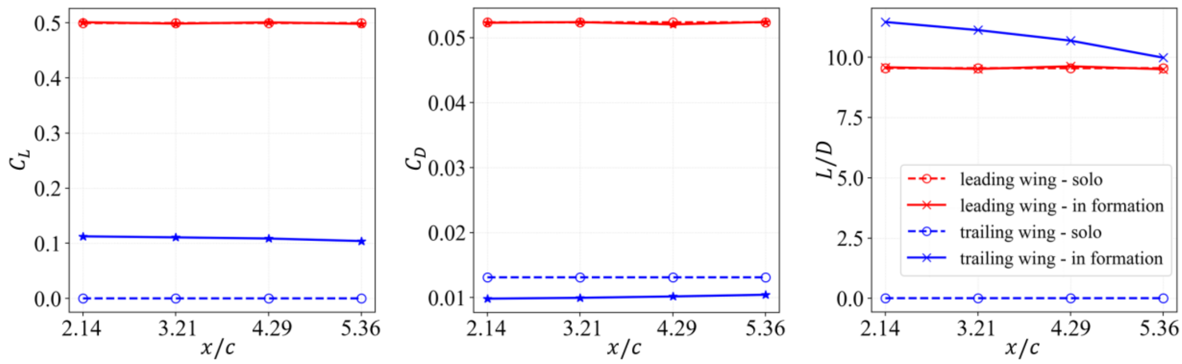

(a) Lift coefficient, C_L (b) Drag coefficient, C_D (c) Lift-to-drag ratio, L/D

Figure 5.3. Aerodynamics performance against longitudinal separation in formation.

Based on Hummel's findings [16, 180], the aerodynamic response of a trailing wing in formation is comparatively less responsive in the longitudinal separation than to the lateral spacing and vertical displacement. To investigate the effects of vortex surfing across different lateral and vertical spacing, the trailing wing is repositioned over a matrix of lateral and vertical coordinates $(y/c, z/c)$, as illustrated in Figure 5.4. All cases are evaluated at a fixed longitudinal spacing of approximately $x/c = 4.29$, or $x/b = 2$, which slightly farther downstream from the validated plane earlier ($x/c = 3$) in Section 3.4.

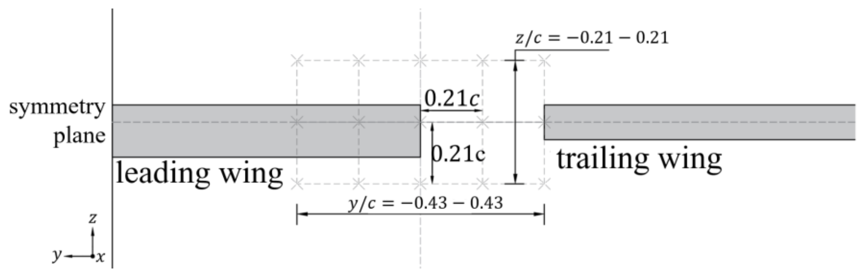

Figure 5.4. Lateral and vertical spacing for the leading-trailing wing.

The aerodynamic performance of the trailing wing under wake surfing effect across different positions is summarised in Figure 5.5. As the trailing wing traverses laterally across the vortex field, it encounters varying levels of induced upwash and vortex strength. Because the vortex core centre of the leading wing resides approximately $0.1c$ inboard of the wingtip, positions beyond this point experience an adverse aerodynamic effect. The corresponding pressure distribution contours extracted along the spanwise direction are shown in Table 5.1, providing physical insight into the wake-wing interactions at representative lateral offsets.

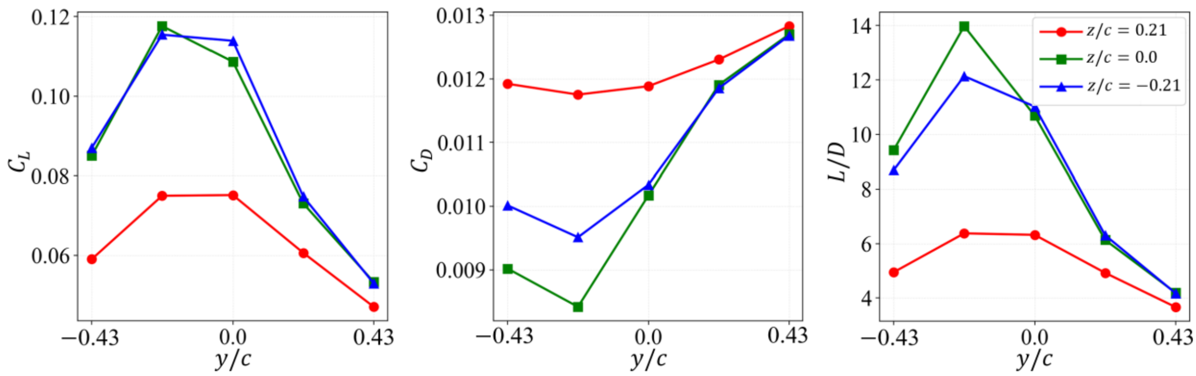

(a) Lift coefficient, C_L (b) Drag coefficient, C_D (c) Lift-to-drag ratio, L/D

Figure 5.5 Aerodynamics performance of trailing wing in different y and z positions at $x/c = 4.29$.

When positioned at $y/c = -0.43$, the wingtip of trailing wing interferes heavily across the vortex core, producing a highly distorted pressure field, which is marked by elevated pressures along the leading edge and lower surface, and severely degrades both lift and drag characteristics. At $y/c = -0.21$, a small margin of the wingtip overlaps with the vortex core, but the pressure on the suction surface is of the strongest amongst all. As a result, it leads to the highest lift coefficient observed among all lateral positions in Figure 5.5a. So that the lift coefficient is maximum when the wingtip is overlapping by 10% of the span ($y/c = -0.21$) or when the wingtip is closest to the vortex core centre. As the trailing wing moves outward past the vortex core ($y/c > -0.21$), the surfing benefit decays progressively, with lift enhancement reduced by nearly 50% between $y/c = 0$ and $y/c = 0.21$.

In terms of drag, the trailing wing experiences the strongest benefit when located near the vortex core centre, as plotted in Figure 5.5b. This reduction stems from the axial velocity deficit embedded within the core, which effectively lowers the relative dynamic pressure seen by the trailing wing. Moving either inboard or outboard from this region diminishes the beneficial deficit effect and therefore increases drag. When considering both lift enhancement and drag reduction, the resulting lift-to-drag ratio reaches its optimum at $y/c = -0.21$, where the trailing wing simultaneously exploits the local upwash and experiences minimal axial-deficit-induced drag. Nevertheless, across all lateral positions studied, the trailing wing consistently performs better than in solo flight, confirming that positive aerodynamic gains persist throughout most of the vortex field, albeit with varying magnitude.

Table 5.1 Pressure contour on the trailing wing along y-axis, at $x/c = 4.29$, $z/c = 0$.

y/c	Lower surface	Wingtip and upper surface
-0.43		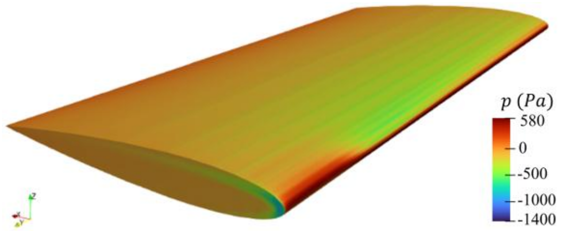
-0.21		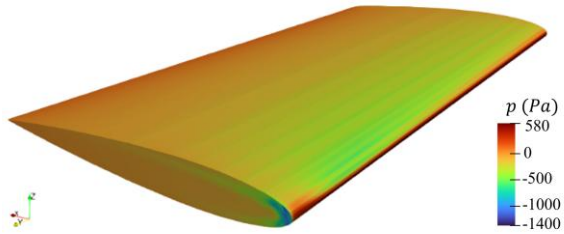
0		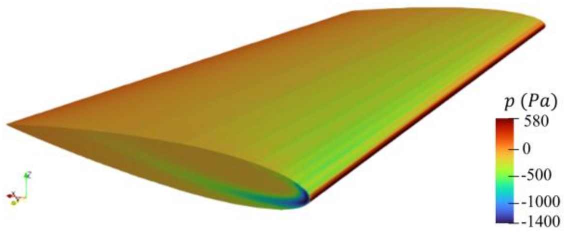
0.2		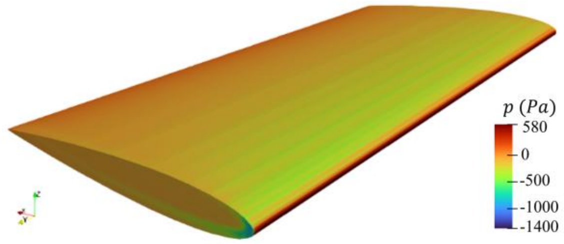
0.43		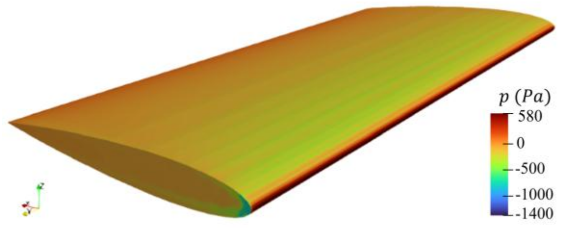

Looking at the performance in different vertical offset (z/c) in a formation flight, both the lift and drag coefficients are inferior when the trailing wing is at a higher z position, irrelevant to the lateral spacing. This is primarily attributed to the downwash field generated by the lifting action of the leading wing. As the bound circulation sheds into a pair of trailing vortices, the induced velocity field convects downward [41], causing the wake vortex to descend progressively with downstream distance. Consequently, trailing wings which fly above the waterline of the leading wing encounter a substantially weakened upwash field and therefore derive noticeably smaller aerodynamic gains. Conversely, locations below or near the wake centreline experience stronger induced upwash and thus more favourable lift-to-drag performance.

5.3 Inlet Conditioning for Wake Vortex Surfing

With the inlet conditioning methodologies established and validated in Chapter 4, the framework is now extended to the more complex two-wing formation flight. The objective of this section is to assess the robustness of the precursor and synthetic inlet conditioning approaches when applied to an interacting vortex environment, and to evaluate their impact on the aerodynamic performance of the trailing wing relative to a fully continuous simulation.

The precursor and synthetic inlet conditioning methodologies provide a computationally efficient strategy for reconstructing wake vortex inflow conditions without simulating the entire upstream domain. While the validity was demonstrated for isolated wake development in freestream conditions, their capability in representing vortex-wing interaction within a formation remains to be established. Formation flight introduces additional sensitivity to inflow structure, particularly in terms of vortex core strength, spatial coherence and turbulence fluctuations, all of which directly influence the induced lift and drag characteristics.

The leading wing configuration is identical to the validated case presented earlier in Section 3.4, which is based on a NACA 0012 aerofoil with $\alpha = 10°$. This leading wing has proven its capabilities in generating a well-defined pair of counter-rotating tip vortices which are then utilised by the trailing wing. The trailing wing is modelled with a full wingspan of $b = 0.3m$ and angle of attack of $\alpha = 0°$. As proven in the previous study presented in Section 5.2 and Figure 5.3 [8], the symmetrical wing with zero angle of attack at solo flight has proven its aerodynamics characteristics are almost fully influenced by the upstream vortex system. The formation setup is as shown in Figure 5.6a for the conventional simulation with continuous domain. The inflow plane for the formation simulation is prescribed at plane $x/c = 3$ from the leading wing, as illustrated in Figure 5.6b and Figure 5.6c. The longitudinal separation between the leading and trailing wings is systematically varied in order to examine the sensitivity of aerodynamic performance to both formation spacing and inlet reconstruction frameworks.

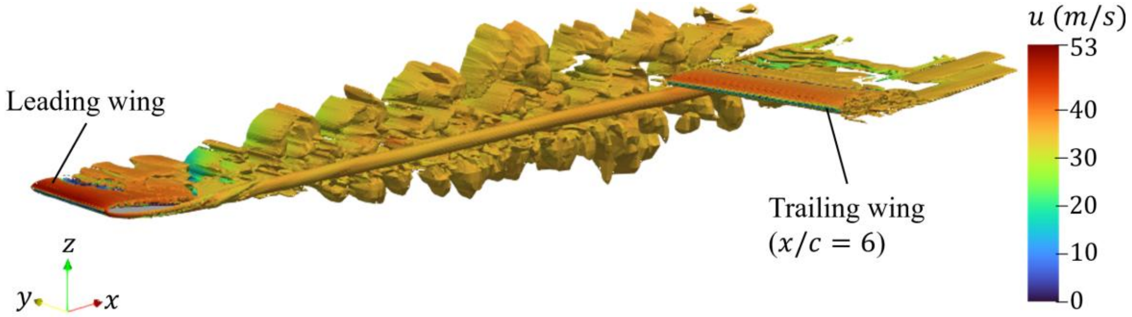

(a) Continuous domain reference simulation

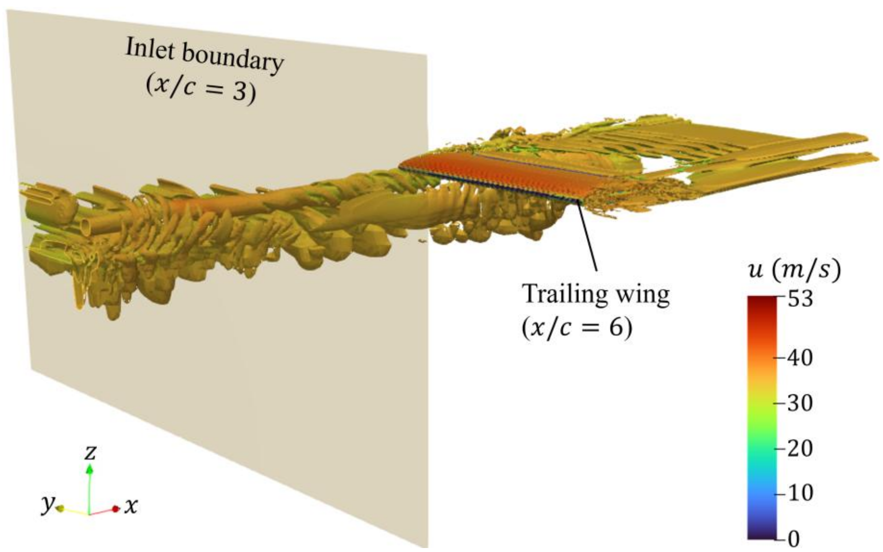

(b) Main simulation with precursor inlet conditioning method

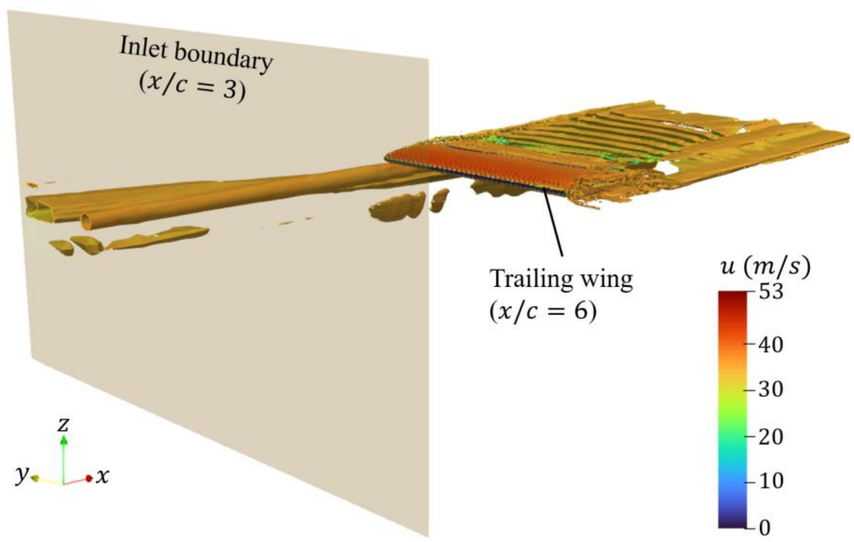

(c) Main simulation with synthetic inlet conditioning method with spatial correlation scaling

Figure 5.6 Illustration of the flight formation setup at $x/c = 6$, $y/c = 0$, $z/c = 0$.

The aerodynamic forces acting on the trailing wing with varying longitudinal positions in the formation are plotted in Figure 5.7. In general, the lift coefficient of the trailing wing (Figure 5.7a) decreases marginally as the separating distance from the leading wing increases. This trend is physically consistent with the gradual weakening and radial diffusion of the vortex pair, which reduces the upwash component available to augment the trailing wing's effective angle of attack. The reduction in induced vertical velocity diminishes the beneficial vortex-induced lift augmentation as the downstream distance increases.

The precursor method and the synthetic method scaled by spatial correlation produce lift coefficients closely matching those obtained from the continuous-domain LES reference. In contrast, the synthetic method employing mean velocity scaling consistently predicts higher lift values. This overprediction can be attributed to amplified velocity fluctuations outside the vortex core region. Since mean velocity scaling does not explicitly preserve the spatial coherence of turbulent structures, it may artificially enhance local vertical velocity components, leading to an exaggerated upwash effect on the trailing wing.

On the other hand, the drag coefficient shown in Figure 5.7b reveals a more pronounced sensitivity to inlet conditioning methodology. In the continuous domain reference, the drag coefficient increases gradually with downstream separation and reach a maximum near $x/c = 7$ before a slight reduction further downstream. In comparison, the precursor inlet exhibits the highest resemblance from the continuous domain reference, closely following both the magnitude and trend of the reference drag curve. This result is expected as the precursor method directly inherits the developed velocity field from the upstream simulation, thereby preserving the coherent vortex structure and induced velocity gradients at the inlet plane. Both synthetic methods provide a reasonable prediction on the drag coefficient in the near inlet area ($x/c = 3.5$). However, a substantial reduction in the drag is observed downstream, where the values remain consistently lower across the streamwise positions. The substantial reduction in drag indicates that the synthetic inflow is not able to preserve the same structures of the wake vortex during convection. As a result, the induced velocity field interaction with the trailing wing diminishes more rapidly and lead to a lesser drag impact.

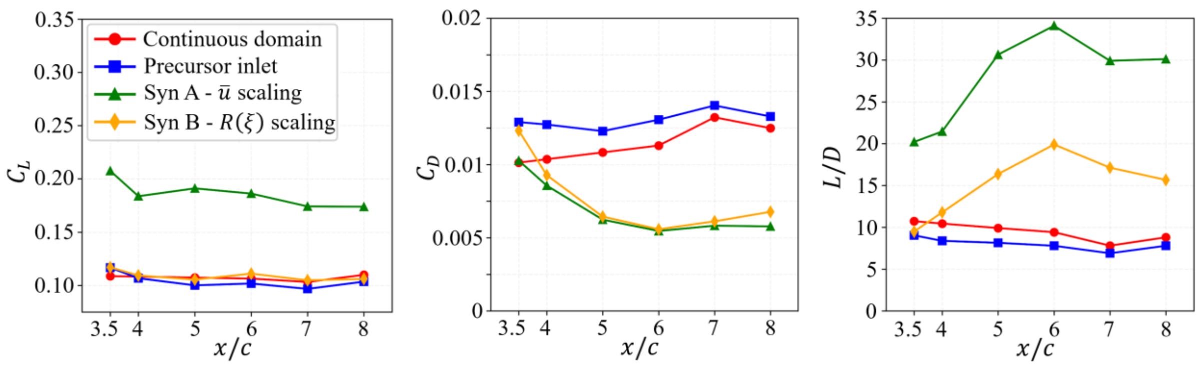

(a) Lift coefficient (b) Drag coefficient (c) Lift-to-drag ratio

Figure 5.7 Aerodynamics performance of trailing wing along longitudinal position in different inlet conditioning methods.

The combined effects on lift and drag are reflected in the lift-to-drag ratio as presented in Figure 5.7c. The results in the continuous domain indicate that the trailing wing is achieving a higher efficiency when it is positioned with a closer longitudinal separation from the leading wing, where the upwash effect of the vortex system is prominently stronger. This outcome is consistent with the reported formation flight theory [36]. As the downstream distance increases, vortex diffusion weakens the induced velocity field, leading to a successive reduction in aerodynamic benefit.

The precursor method provides the closest representation of the reference efficiency trend, while deviations in the synthetic methods arise primarily from discrepancies in drag prediction. In particular, the synthetic method by spatial correlation is having a better accuracy than the mean velocity scaling approach, where the latter produces elevated L/D values due to combined lift overprediction and drag underestimation.

The discrepancies observed in the results of synthetic inlet methods are primarily due to the limitations in reconstructing the full vortex turbulence coupling present in the precursor inflow. The approximate fluctuations characteristic does not preserve the subtle features such as the secondary induced velocities and vortex core deformation. These higher order flow structures play a critical role in determining local velocity gradients near the trailing wing and affect the boundary layer development and drag computations. Despite the limitations, the inlet conditioning methods enable high-fidelity simulation of formation flight without requiring extended upstream computational domains, offering significant savings in grid size and computational time by more than 50% while retaining predictive accuracy. These savings reinforce the importance of the synthetic inlet generation, particularly for multi-body aerodynamic interaction problems.

Using the same inflow plane at $x/c = 3$ from the initial domain as the inlet boundary, the trailing wing in the formation is fixed at a longitudinal position of three chord length in the downstream direction (i.e., equivalent to $x/c = 6$ from the leading wing) and is systematically translated across the cross-sectional plane along the y- and z-axis. The resulting aerodynamic characteristics of the trailing wing in various formational positions are plotted in Figure 5.8. From Figure 5.8, it is evident that the lift coefficient increases marginally as the trailing wing shifts laterally outboard. This trend is physically consistent with vortex-induced upwash distribution. When positioned slightly outboard of the vortex core, the trailing wing resides within a region of favourable upward induced velocity, which increases the effective angle of attack and thereby enhances lift generation. In contrast, the drag coefficient exhibits a local peak at positions slightly inboard, corresponding approximately to the vicinity of the vortex core centre. This behaviour is expected due to the intensified velocity gradients and rotational flow near the core, which increase induced drag and modify boundary layer development. As the lateral spacing increases further from the core, the induced velocity gradients weaken, leading to a gradual reduction in drag.

Even with the trailing wing positioned at $x/c = 6$ downstream of the leading wing, the combined lift-to-drag ratio remains consistently around 10 across most lateral positions. This performance is comparable to that at $x/c = 4.29$, where the L/D ratio ranges between 10 and 14, as shown in Figure 5.5. In contrast, the symmetric wing in the baseline solo flight case at $\alpha = 0°$exhibits an L/D ratio close to zero (Figure 5.3). These results therefore indicate a clear net aerodynamic benefit arising from vortex surfing.

Even the trailing wing is positioned at $x/c = 6$ downstream from the leading wing, the combined lift-to-drag ratio remains constantly around 10 across most lateral positions. This performance is comparable to that at $x/c = 4.29$, where the L/D ratio ranges between 10 and 14, as reported in Figure 5.5. Since this symmetrical wing in the baseline solo flight case at $\alpha = 0°$ exhibits an L/D ratio close to zero in Figure 5.3, these results therefore indicate a clear net aerodynamic benefit arising from vortex surfing. Notably, the aerodynamic gains are more sensitive to lateral displacement than to vertical positioning. Across the vertical offsets shown in Figure 5.8a-c, the variations in lift, drag, and efficiency is comparatively moderate. This reduced sensitivity in the vertical direction can be explained by the dominant horizontal structure of the vortex-induced velocity field, where the strongest gradients occur radially in the lateral plane rather than vertically within the limited offset range considered.

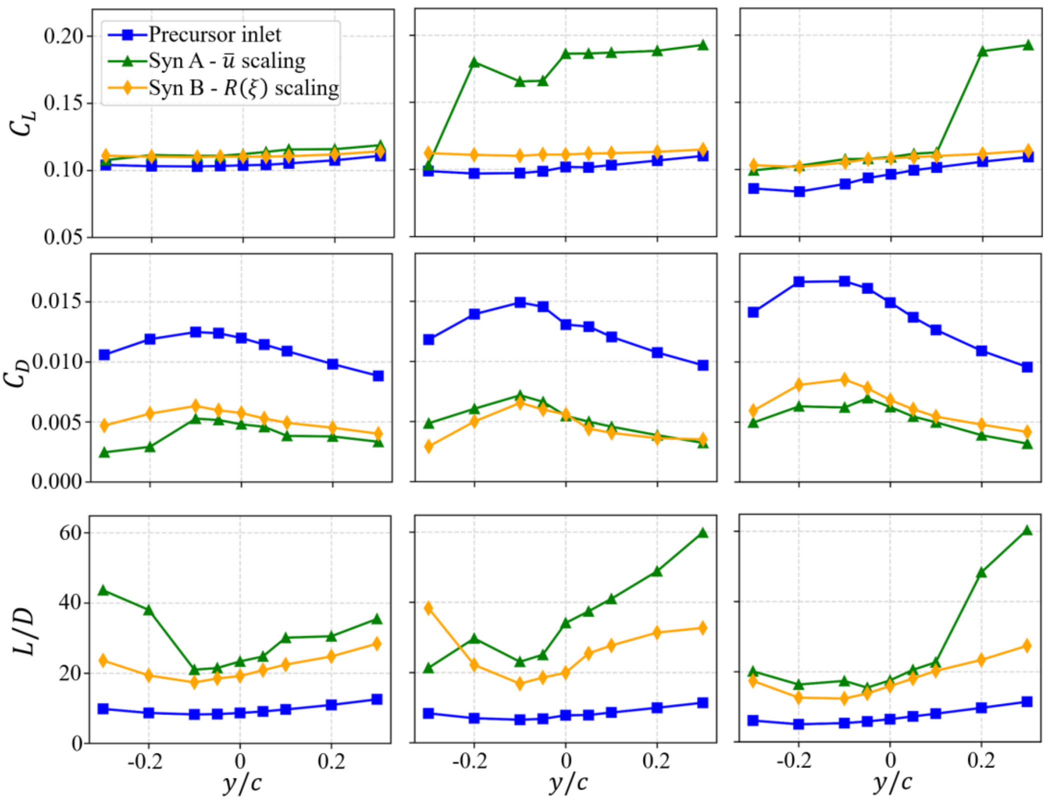

(a) $z/c = 0.1$ (b) $z/c = 0.0$ (c) $z/c = -0.1$

Figure 5.8 Aerodynamics performance of trailing wing at $x/c = 6$, at different lateral and vertical positions with precursor and synthetic inlet conditions.

Beyond lift and drag performance, the rolling moment experienced by the trailing wing is of critical importance for formation flight stability. Asymmetric induced velocities across the span generate lift imbalances, resulting in non-zero rolling moment coefficients. This effect is particularly relevant in vortex surfing applications, where aerodynamic gains must be balanced against potential instability. The rolling moment coefficients C_l are shown in Figure 5.9, illustrating how the trailing wing behave during the vortex encounter.

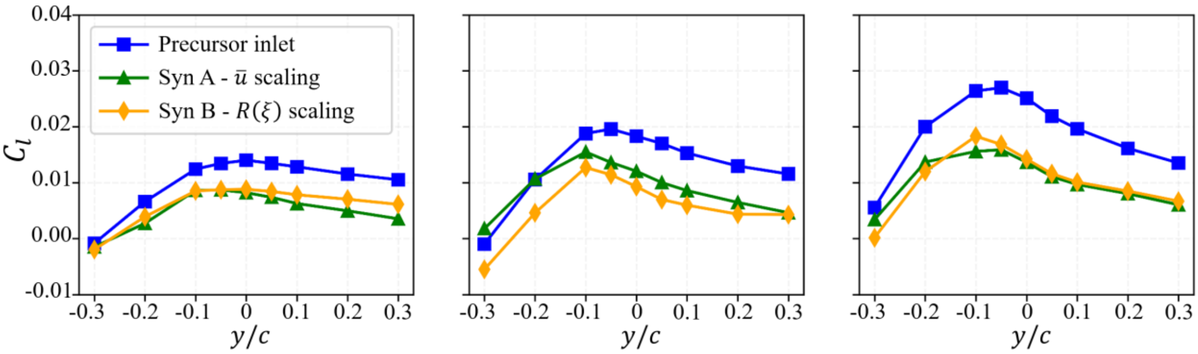

(a) $z/c = 0.1$ (b) $z/c = 0.0$ (c) $z/c = -0.1$

Figure 5.9 Rolling moment coefficient C_l of the trailing wing at different lateral and vertical positions with precursor and synthetic inlet conditions.

It is noticed that the rolling moment coefficient peaks near $y/c = -0.1$. This corresponds to the lateral position where the trailing wingtip lies closest to the vortex core centre. At this location, the trailing wing experiences the intensified upwash and the maximum lift asymmetry. As a result, the wing peaks in the rolling moment, which is consistent with previous experimental and numerical investigations [12].

As the trailing wing shifts further away from the vortex core, the induced velocity imbalance weakens, and the rolling moment magnitude decreases accordingly. This reduction improves roll stability and reduces structural loading. Conversely, when the trailing wing crosses beyond the vortex core centre, the local induced flow transitions from upwash to downwash at the wingtip. This reversal in induced velocity generates a rolling moment in the opposite rotational direction. Although the magnitude of the moment decreases, the rapid transition in loading direction introduces significant structural and control implications. The asymmetric downforce acting on one semi-span can produce abrupt changes in bending moment distribution and lead to elevated structural stress and dynamic instability [109]. Continuously shifting the wing inboard will further reduce the rolling moment until it dips into the negative regime at a certain point. This is where the induced downwash dominates over the beneficial upwash on one side of the wing, producing a net adverse rolling tendency. This behaviour is observed on the trailing wing when positioned at $y/c = -0.3$, $z/c = 0$.

When the lift, drag, and rolling moment coefficients are considered collectively, a favourable operational region emerges. This region corresponds to lateral positions slightly outboard of the vortex core, where lift-to-drag ratio is remarkable and with acceptable rolling moment levels. Positions too close to the core maximise lift but incur substantial rolling instability, whereas positions beyond the core enhance stability but sacrifice aerodynamic gains. This balance aligns with observations from Cutts and Speakman [20], who reported that pink-footed geese preferentially occupy outboard vortex positions to optimise aerodynamic efficiency while maintaining roll stability. The present LES results provide quantitative CFD based support for these biological flight patterns.

5.4 Summary and Recommendations

The aerodynamic forces on both leading and trailing wing in the formation flight were examined, and the effects of the trailing wing positioning were investigated. In general, the aerodynamic properties of the leading wing are not affected by the formation, even with a tight longitudinal separation of $x/b = 1$. In contrast, the trailing wing flies in the updraft region of the wake is benefiting from the formation with higher lift and yet lower drag. As the vortex dynamics is relatively consistent in the near field, the aerodynamic impacts on the trailing wing are not much affected by the longitudinal separation. Nevertheless, the aerodynamic of trailing wing is more susceptible to the lateral and vertical spacing. The optimal position with the resolution in this study is at $y/b = -0.1$ and $z/b = 0$, which has obtained a lift-to-drag ratio of about 14. As the trailing wing moving further away from the vortex core, it reduced the aerodynamic interactions and hence lesser gains. This optimal position may be altered slightly if more simulation is run with finer resolution in the formation spacing.

The formation flight with various inlet conditioning methodologies in LES were conducted to demonstrate the capability in reproducing the aerodynamic force trends and higher-order stability characteristics. The precursor-based inlet conditioning demonstrated the most consistent agreement with the continuous domain reference results, as the inflow field directly inherits the dynamically evolved vortex structure. Although discrepancies are observed, the synthetic inlet method incorporating spatial correlation scaling provides a better representation compare to the method scaled by mean velocity magnitude. This confirms that preservation of spatial coherence, in addition to mean velocity magnitude, is critical for accurate prediction of vortex-wing interaction. Overall, the studies established a robust framework for analysing vortex induced aerodynamic interaction in formation flight and identifies a favourable near field operating region that balances aerodynamic gain with rolling stability considerations.

The current study primarily focused on the close formation in the near field wake region. For practical implementation in extended formation flight, future research may look at a more efficient methodology for modelling the wingtip vortices evolution in the far field, to provide a more computationally viable solution for simulating large aircraft separations of industrial relevance.

Chapter 6

Conclusion

The optimisation of formation flight performance relies on accurately identifying the "sweet spot" in which the trailing aircraft can benefit from the wake vortex surfing effect. Hence, a robust modelling framework to accurately predict the wingtip vortices and its downstream development with high fidelity is much needed. This research integrates different techniques such as wind tunnel experiments, CFD models including URANS and LES, and an efficient low-order model UVLM to advance both the physical understanding and practicality of wake vortex modelling for formation flight.

The wind tunnel experiments in Chapter 2 have distinctly visualised and characterised the wingtip vortex development of different wing configurations. The novel perspective upright correction method provides an efficient yet accurate approach to extract the vortex geometry from a single, non-orthogonal camera view. The proposed methodology allows the camera or inspection device to be mounted and positioned at any possible location as long as the checkered paper for baseline initialisation can be captured within its view. This technique greatly simplifies experimental setup, minimises flow disturbance compared to conventional multi-camera alignment, and provides improved measurement accuracy over the native tilted images. Despite the limitation of the apparatus on measuring the airflow velocity, the experiments verified that blended winglets reduce the visible wake spiral size and induce a slightly larger but weaker vortex core, consistent with the Lamb–Oseen diffusion mechanism. These findings provide foundational insight for subsequent numerical validation.

In Chapter 3, the numerical simulation using both URANS and LES is conducted to validate the accuracy of the different turbulence models in predicting the aerodynamics of the wake vortices. Several techniques including adaptive mesh refinement and vorticity confinement model were assessed. However, with consideration in balancing the computational complexity and solution accuracy, the mesh refinement strategy was adopted in which specifically having grid size of about 1.1% of the characterising length concentrated around the vortex core region. The URANS model of k-omega shear stress transport (k-ω SST) model demonstrated a reasonable accuracy in estimating the vortex core centre location and axial velocity deficit, but it is unable to maintain the vortex physics, resulting in a more rapid dissipation on the vortex strength and an increased dispersion of the core diameter. On the other hand, the LES framework with Smagorinsky sub-grid scale model has validated its efficacy in accurately predicting the wake vortex strength and persistence, which provides a better agreement with the literature data.

The established LES framework also exhibited a positive outcome when comparing to the experimentally upright corrected results. The vortex spiral profiles from both the LES and wind tunnel experiment are highly coincided across various wing configurations, angles of attack, and multiple downstream planes, which further affirming the reliability of the LES model. While the wind tunnel experiments primarily capture qualitative data on the wake spiral outline, the LES framework complements this by providing quantitative data such as velocity, turbulence stresses and the real vortex core which is defined by the maximum tangential velocity. The comparison between the real vortex core and the wake spiral shape revealed that a visually larger wake spiral shape does not necessarily indicate a bigger vortex core size. This finding has provided significant insights into the properties of the vortex core and underscored the importance of numerical modelling in conducting in-depth analysis. Hence, it is recommended to adopt the validated LES framework for the formation flight modelling.

To investigate the wake vortex surfing effect in extended formation, a considerably longer and larger simulation domain is needed. The size of domain makes LES prohibitively expensive in terms of computational resources and time, let alone the repetitive simulation for numerous trailing aircraft positioning. To rationalise the simulation resources for formation flight, Chapter 4 presented the inlet boundary condition mapping approaches including precursor and synthetic methods. This technique enhances the computational efficiency of repetitive simulations within the MS domain. The precursor method mapped the time series data of the wake vortex induced by wing geometry in the IC domain onto the inlet of the MS domain. The results demonstrated the effectiveness of the precursor method in reproducing the highly realistic turbulent structures and robust flow characteristics such as the vortex core dimension, position and the circulation strength. The precursor method also replicated the turbulent profile in the downstream flow, with negligible reduction in velocity fluctuations.

For the synthetic method, the necessary parameters from the IC domain are extracted to formulate the Fourier series expression which can synthetically regenerate the velocity fluctuations based on the mean flow-field information. From the study, it is advisable to adopt a flow-field plane further downstream in the IC domain as it can reduce the MS domain size where the object of interest is located at. In addition, the wake vortex projected further downstream generally features larger core diameter and lower fluctuations frequency, thereby reducing the likelihood of mapping errors and discrepancies. However, the equation cannot accurately represent every point on the inflow plane, as the intensity of velocity fluctuations varies greatly within the vortex core region. Scaling methods using the mean velocity magnitude and spatial correlation coefficients are demonstrated and have satisfactorily reconstructed the velocity fluctuations components. The current work however focuses on the near field primarily for comparison and validation purposes. Future research will focus on further deriving the fluctuations within vortex core, investigating on a better model to represent the velocity fluctuations level across the vortex core radius and beyond.

In the LES simulations of close range formation flight detailed in Chapter 5, the aerodynamic properties of the leading wing are proved to be unaffected by the formation, even with a tight longitudinal separation of less than a wing chord distance. In contrast, the trailing wing in formation benefits from flying in the updraft region of the wake, experiencing enhanced lift and reduced drag. As the vortex dynamics remain relatively consistent in the near field, the aerodynamic effects on the trailing wing are minimally impacted by the longitudinal separation. In contrast, the aerodynamic of trailing wing is more susceptible to the lateral and vertical spacing. The optimal position identified with the resolution in this study is with 10% wingspan overlapped laterally and on the same flight level vertically, which resulted in an increased lift-to-drag ratio of up to 14 for the symmetrical trailing wing at $\alpha = 0°$. This optimal position may be altered slightly if the simulations are performed with finer resolution in the formation spacing. When the trailing wing deviates from the optimal position, the aerodynamic benefit decreases as the wing shifts away from the vortex core and the associated upwash region. Nonetheless, the reduction in aerodynamic gain remains relatively modest compared to the overall gains achieved through formation flight. Even with a lateral shift of $\pm 20\%$ chord distance, the trailing wing will continue to retain substantial benefits with the lift-to-drag ratio remaining within the range of approximately 9 to 14.

Despite the high-fidelity LES model could capture and reproduce the vortex turbulence, but it is computationally expensive even to initialise the wake vortex profile and temporal data. Therefore Appendix A introduced UVLM as an efficient model to generate the mean vortex flow field. The lower-order numerical modelling could generate the mean vortex flow field at a faster rate and more cost effective to map the mid-plane of wingtip vortex onto the inlet of a LES MS domain. This vortical flow profile from UVLM served as the inlet boundary condition for the LES main simulation, effectively reducing the computational effort in modelling the vortex. The mean flow data can be superimposed with the LES turbulence fluctuations to achieve necessary turbulence characteristics. Despite the limitations of the UVLM model such as accelerated vortex core development, accurate representation of the vortex at the inlet of LES MS domain can be achieved through careful selection of the inflow. Future research may explore the correlation between the vortex growth rate in UVLM and actual cases. This will enable the identification of specific planes within UVLM that can be mapped onto the LES inlet to represent a more downstream plane.

In conclusion, the motivation for this research is driven by the CFD application of wake vortex surfing in extended longitudinal field. The author utilised different methodologies to capture the wingtip vortices and clarified the vortex core characteristics with various efficient techniques. These techniques greatly reduce the required resources for both experimental and computational modelling efforts. For the variety of formation configurations and positioning, the presented methodologies will tremendously ease the assessment of the aerodynamics performance of trailing aircraft, especially for the extended simulation domain. This highlights the contribution of the research in advancing fluid dynamics studies on the wake vortex interactions and the wake vortex surfing application. However, it remains a challenge at this stage to accurately represent the fluctuation level of each node across the inlet plane due to the highly fluctuating turbulence behaviour near the vortex core and varying velocity profile across the vortex core.

6.2 Research Contributions

This research provides a more profound comprehension of wake vortex strength and degradation via different methods and subsequently develop a CFD framework which is able to accurately capture the wake vortex shedding from selected leading aircraft and compute the aerodynamic impact on the trailing aircraft effectively. The proposed framework can be utilised to allow industry partner to identify the most efficient formation configuration for vortex surfing and plan the flight route ahead. The key contributions are summarised as follows:

1. Development of a perspective corrected experimental methodology for wingtip vortex characterisation.
    - A perspective upright correction (PUC) methodology was developed to improve the accessibility and accuracy of wind tunnel vortex visualisation. Unlike conventional approaches requiring precise alignment between the camera and measurement plane, the proposed method enables vortex images captured from arbitrary viewing angles to be geometrically corrected. This provides a simplified experimental framework for characterising vortex trajectory, core size, and downstream evolution, supporting subsequent CFD validation.
2. Establishment and validation of a CFD framework for wake vortex prediction
    - A CFD framework based on URANS and LES modelling was established to investigate wingtip vortex development and decay. The CFD framework was validated through comparison with established literature data and further demonstrated against independent wind tunnel observations, providing confidence in its application for vortex evolution and formation flight studies. The research demonstrated the capability of LES in reproducing key vortex characteristics, including vortex core structure, tangential velocity distribution, circulation strength, and downstream evolution. This validated framework provides the foundation for reliable formation flight aerodynamic analysis. The analysis also revealed that visual vortex spirals do not necessarily represent the true vortex core size, providing new insight into the interpretation of experimental visualisation techniques.

3. Development of LES inlet conditioning strategies for wake vortex simulations, with formulation of spatial fluctuation scaling strategies for synthetic vortex inflow
    - A major contribution of this research is the extension of LES inlet conditioning methodologies from conventional canonical turbulent flows to spatially evolving vortex-dominated flows. The strong swirl, anisotropy, and radial variation of vortex turbulence intensity introduce additional challenges. A precursor-based inlet mapping approach was demonstrated to preserve coherent vortex turbulence with negligible attenuation, providing a high-fidelity but computationally efficient alternative to full-domain LES simulations.
4. Development of synthetic fluctuation reconstruction for efficient vortex inflow generation
    - A synthetic fluctuation reconstruction approach was formulated based on Fourier decomposition of LES velocity fluctuations. The method enables time-dependent turbulent inflow generation without requiring storage of large precursor datasets. Furthermore, mean-velocity-based normalisation and spatial correlation-based scaling approaches were introduced to improve the representation of turbulence variation across the vortex core. The novelty lies in the adaptation and assessment of these approaches for vortex-dominated flows, where turbulence characteristics exhibit improved spatial and temporal variations.

      The results demonstrate the feasibility of synthetic vortex inflow generation while identifying the remaining challenges associated with reproducing highly unsteady turbulence behaviour within the vortex core. This methodological advancement provides an efficient framework for assessing formation flight aerodynamics in a wide range of operational configurations.
5. Application of efficient LES inlet conditioning to formation flight aerodynamic analysis
    - Characterisation of aerodynamic benefits experienced by a trailing wing in close range formation flight across different longitudinal, lateral, and vertical separations. This establishes a clear quantitative understanding of wake surfing performance trends and provides a foundational dataset for future formation flight planning and optimisation.
6. Integration of UVLM-based mean vortical inflow with the LES fluctuations profile
    - The initial vortex profile is generated from UVLM as the inflow condition for the LES. Despite the simplified physics of UVLM, careful selection of an appropriate inlet plane enables UVLM to provide a representative mean vortex structure for LES inflow and provides a transferable framework for future parametric studies.

Collectively, these contributions form a coherent methodology as shown in Figure 6.1, which combines experiment, high fidelity LES, lower-order UVLM, and inlet mapping techniques to enable efficient and practical analysis of wake vortex interactions and formation flight aerodynamics.

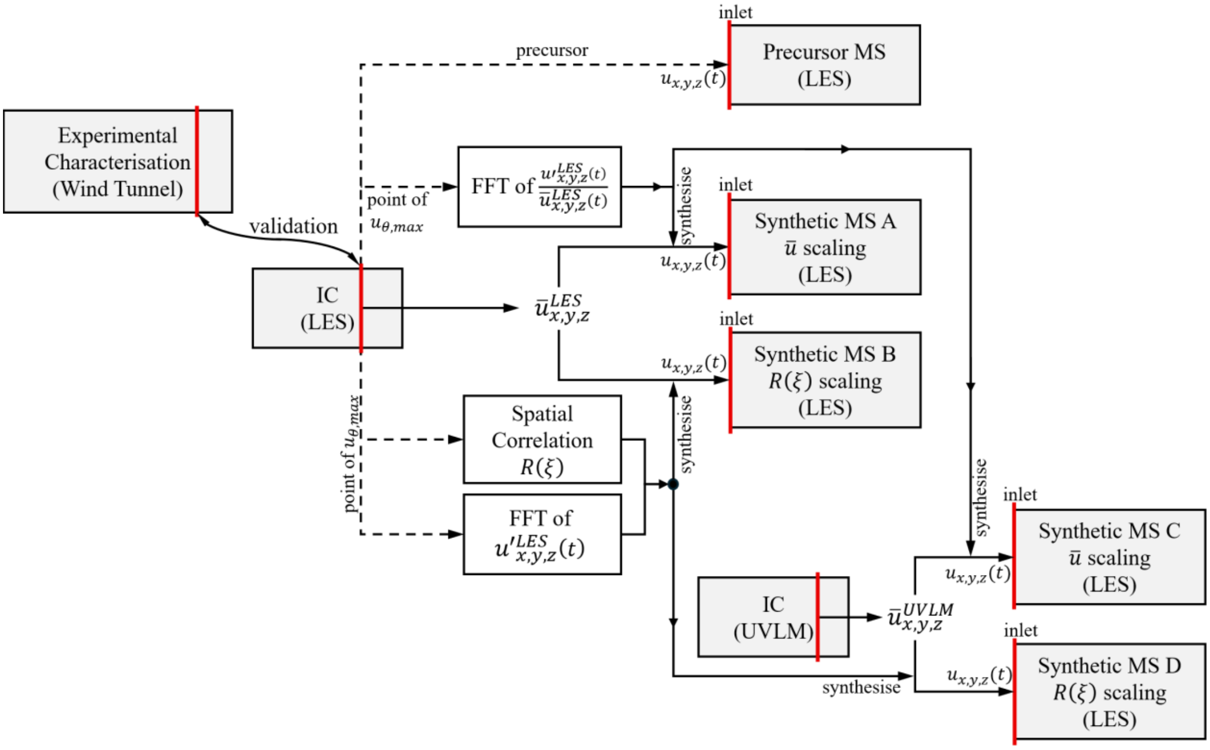

Figure 6.1 Overview of the inlet conditioning techniques in this thesis.

6.3 Recommendations for Future Work

Multiple methodologies in capturing and characterising the wingtip vortex are established and presented in the thesis. While it provides a solid foundation to enable the inlet boundary condition design, several areas remain worthwhile for future investigations:

1. The current Fourier-based synthesis struggles within the vortex core due to intense and spatially irregular fluctuation behaviour. Future work should refine the synthetic inflow conditions for vortex-dominated flows by exploring conditional fluctuation scaling functions, or additional corrective terms to accurately reconstruct turbulence across the vortex core. Alternatively, it is possible to have hybrid methods combining precursor turbulence with synthetic augmentation outside the core region.
2. Although UVLM provides efficient mean-flow initialisation, the accelerated vortex growth limits direct applicability. A systematic correlation study between UVLM, LES, and experimental vortex evolution would help identify modified UVLM wake roll-up parameters that better match realistic vortex development, enabling more accurate selection of inlet planes.
3. The methodologies developed in this thesis (Figure 6.1) enables future research to be extended to full aircraft wings, swept wings, or high-Reynolds-number regimes to improve industrial

relevance. The future investigation may also include the application for multi-vortex systems, such as with vortices generated by engine nacelles or empennage.

4. Future work should also investigate the scalability of the synthetic fluctuation reconstruction approach across a broader range of Reynolds numbers. Such investigations would enable the development of more generalised formulations where the turbulence spectral characteristics and spatial scaling parameters can be determined independently of a single reference LES case.
5. With the advancement of artificial intelligence applications [181], the adoption of adaptive or machine-learning model [182, 183] for vortex inlet condition may be a promising direction. Such models could be trained to learn the dominant fluctuation modes of wingtip vortices and automate the generation of coherent fluctuation fields without manual spectral reconstructions.

Appendix A

Inlet Initialisation with Unsteady Vortex Lattice Method

Large-eddy simulation (LES) provides a high-fidelity framework for resolving the large-scale turbulent structures that governs the wake vortex formation and evolution. In formation flight studies, the inlet conditional methods presented in Chapter 4 have greatly reduced the computational cost. Nevertheless, the upstream flow development using LES can still be computationally expensive especially when the longitudinal separation becomes significant. This limitation becomes particularly restrictive when the primary objective is to generate the dominant vortex structure at the inlet plane for subsequent main simulation rather than resolving the entire upstream flow development.

To address this limitation, the vortex-based modelling provides a reduced-order alternative for representing the dominant coherent structures of the wingtip vortex. By representing the lifting surface and its wake using discrete vortex elements, vortex methods [184] can substantially reduce the computational resources as compared to the Navier-Stokes simulations. Such reduced-order representations can therefore serve as a practical tool to initialise the vortex velocity field used in the inlet boundary conditions for downstream LES main simulations.

Vortex methods [184, 185] are generally formulated under potential flow assumptions, where the fluid is considered incompressible, inviscid and irrotational except along vortex filaments where vorticity is concentrated. Under these conditions, the velocity field can be expressed as the gradient of a scalar velocity potential and governed by the Laplace’s equation [186]. These assumptions neglect viscous effects, turbulence, and boundary layer development that are inherently resolved in LES. Consequently, the vortex methods aim to provide an efficient representation of the dominant circulation and induced velocity fields associated with lifting surfaces.

A.1 Unsteady Vortex Lattice Method (UVLM)

Among the available vortex methods, the Unsteady Vortex Lattice Method (UVLM) [64, 65] offers a convenient approach for modelling the lifting surfaces undergoing unsteady motion while capturing the time evolution of the wake system. The UVLM models a lifting surface by discretising it into a lattice of horseshoe vortices composed of bound and wake vortices. The lifting area is treated as a thin surface neglecting the aerofoil thickness effects, and assumed the surrounding flow is assumed incompressible, inviscid and irrotational. Under these potential-flow assumptions, the velocity potential scalar φ satisfies the Laplace's equation,

$$\nabla^2 \phi = 0 \tag{54}$$

and the wake vortex lattices are transported from the trailing edge with vorticity of equivalent strength to the bound vortex lattices. The corner points of the free wake lattices move with the local velocity, and the following non-penetration condition is applied to all collocation points on the wings,

$$(u_b + u_w + u_\infty - u_k) \cdot n = 0 \tag{55}$$

where u_b denotes the induced velocity produced by bound vortex lattices, u_w denotes the induced velocity produced by wake vortex lattices, u_∞ denotes the freestream velocity, u_k denotes the surface kinematic velocity, and n denotes the local normal vector at the collocation point. Another boundary condition is that the flow disturbance diminishes at infinity, as follows,

$$\lim_{\|x - x_0\| \to \infty} u = 0 \tag{56}$$

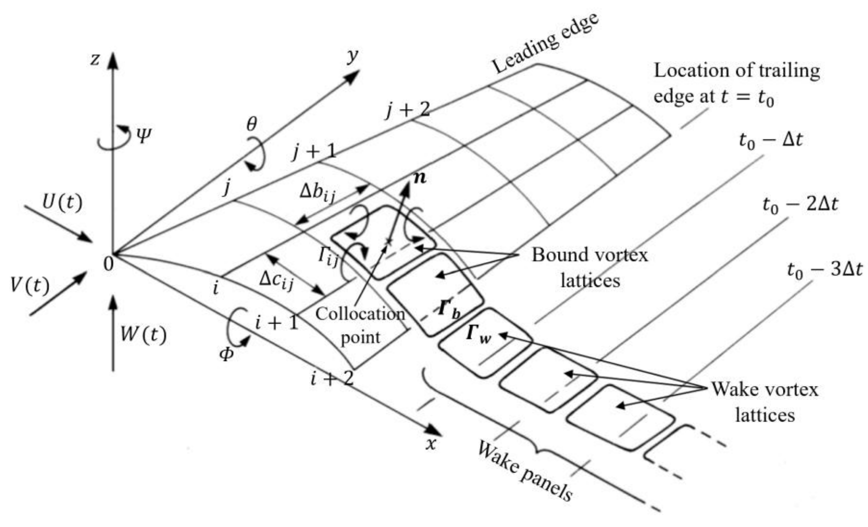

Figure A.1 Descriptive diagram of UVLM [187].

The induced velocities at each point induced by the horseshoe vortices are calculated using the Biot-Savart law. In flight condition, the UVLM models the force-free wake by forming vortex rings over the mean panel surface, as shown in Figure A.1. Each discretised quadrilateral panel is attached with bound vortex lattices, where the leading vortex ring is placed on the quarter-chord line of the panel and the rear vortex ring is placed on the next panel's quarter-chord line. The collocation point is on the three-quarter chord line, which falls at the centre of the vortex ring.

This formulation allows UVLM to efficiently resolve the unsteady aerodynamic loading and wake evolution with substantially lower computational cost than viscous CFD, making it attractive for preliminary analysis of vortex-dominated flows and formation flight interactions.

A.2 Vortex Initialisation by UVLM

The UVLM toolkit utilised in this study is SHARPy (Simulation of High-Aspect-Ratio aircraft and wind turbines in Python) [96, 188]. It is an open-source software package well-known for simulation of nonlinear aeroelastic systems, integrating structural dynamics and aerodynamic solvers [109, 189]. The UVLM is solving a system of linear algebraic equations to determine the singularity strengths at every time step [190, 191]. The induced velocity at an arbitrary field point, r due to a vortex lattice with vertices $P = \{P^i, i \in [1,4]\}$ and strength Γ can be expressed by $u(r) = A(P,r)\,\Gamma$, where $A(P,r)$ denotes the three-dimensional influence coefficient. At discrete time step $n+1$, the vorticity distribution of the bound vortex elements is determined by applying the non-penetration boundary condition, formulated as,

$$A_{cb}\Gamma_b^{n+1} + A_{cw}\Gamma_w^{n+1} + w^{n+1} = 0 \tag{57}$$

where A_{cb} and A_{cw} denotes bound-to-collocation and wake-to-collocation aerodynamic influence coefficient matrices, Γ_b and Γ_w are the circulation strength vector for bound and wake vortex rings, and $w = (u_\infty - u_k) \cdot n$ represents the normal component of all velocities except those induced by bound and wake vortex lattices at the collocation points. The induced velocity is calculated at the field points to obtain the influence matrices and the convection velocity of the wake, before the equation solves both the bound and wake vortex strength vector Γ_b and Γ_w iteratively.

The velocity induced by a vortex ring l over collocation point k can be calculated using the Biot–Savart law. For a unit circulation strength, it is expressed as,

$$\vec{u}_{i,kl} = \oint_{C_l} \frac{d\vec{s}_l \times \vec{r}_{kl}}{4\pi|\vec{r}_{kl}|^3} \tag{58}$$

where $d\vec{s}_l$ represents the differential element of the vortex segment along the ring l, that makes up the complete ring C_l, and $\vec{r}_{kl}$ is the vector from the collocation point k to the relevant vortex ring at l. This process involves four evaluations of the Biot-Savart law, corresponding to each vortex segment of the closed circuit C_l. The aerodynamic influence coefficient matrices A_{cb} and A_{cw} are determined by calculating all cross-induced velocities at the collocation points and projecting these velocities along the normal vector of the respective panel,

$$(A_{cb})_{kl} = \vec{u}_{i,kl}\vec{n}_k, \qquad k, l = 1 \dots N_b \tag{59}$$

$$(A_{cw})_{kv} = \vec{u}_{i,kv}\vec{n}_k, \qquad k, l = 1 \dots N_b, \qquad v = 1 \dots N_w \tag{60}$$

where k, l are bound (surface) panel counters, v is the vortex ring counter, and N_b is the number of total bound panels, N_w the number of wake panels, and n_k is the total number i the normal vector of the kth vortex ring (at which the induced velocity is being computed. The propagation equation for the wake circulation can be written in discrete time as follows,

$$\Gamma_w^{n+1} = C_{\Gamma b}\Gamma_b^n + C_{\Gamma w}\Gamma_w^n \tag{61}$$

where $C_{\Gamma b}$ and $C_{\Gamma w}$ map the circulation of the previous time step to the current one, and they are very sparse constant matrices which account for Kelvin's circulation theorem [192], which mandates that the total circulation of the vortex sheet shed from the trailing edge of the wing remains constant as it moves downstream. Additionally, these matrices also comply with Helmholtz's vortex theorem in the convection of the wake [192], which leads to the rolling up of the wake panels into the concentrated wingtip vortex structure.

Once the flow is fully developed, the roll-up of the wake panels downstream captures the formation of wingtip vortices, which is utilised to determine the vortex core centre locations (y_c, z_c) and their respective core radius, r_c. This process helps to establish the initial shape and size of the vortex core. The circulation strength calculated from the UVLM is used then to provide data to define the tangential velocity field of the vortical flow by the Lamb-Oseen model [107, 108],

$$u_\theta = \frac{\Gamma_v}{2\pi r}\left[1 - e^{-1.26\left(\frac{r^2}{r_c{}^2}\right)}\right] \tag{62}$$

where the circulation of wingtip vortex, Γ_v is approximately equal to the spanwise-averaged circulation strength [193, 194]. A higher Γ_v typically indicates stronger vortices, or tangential velocity. The tangential velocity at any point (y, z) is calculated based on the radial distance, r, from the vortex core centre,

$$r = \sqrt{(y - y_c)^2 + (z - z_c)^2} \tag{63}$$

The tangential velocity can then be decomposed into Cartesian velocity components u_y and u_z using trigonometeri relationships and is the angle θ from the selected point to the vortex core centre,

$$u_y = -u_\theta \sin\theta \tag{64}$$

$$u_z = u_\theta \cos\theta \tag{65}$$

After establishing the tangential velocity, the only velocity component remaining for the inlet condition is the axial velocity u_x. As wingtip vortices develop, the surrounding airflow curls inward and revolves around the centre of the vortex core. This dynamic mechanism creates an axial velocity excess right after the wing trailing edge and subsequently transitions into a deficit after a certain distance [138]. The axial velocity profile typically shows a deficit of 15% at the centre of the core and it tends to restore to freestream velocity at about one to two core radius distance from the core centre [106],

$$u_x = u_\infty \cdot \left[1 - 0.15\, e^{-1.26\left(\frac{r^2}{{r_c}^2}\right)}\right] \tag{66}$$

With the three-dimensional velocity components derived from the UVLM, inlet boundary conditions can be specified for the LES main simulation domain. While the inflow data does not fully capture the required dynamic complexities, it does provide initial vortex data to initiate the simulation with high efficiency. Validation on the vortices will be performed to assess the accuracy of this approach.

The mean-velocity, $\bar{u}_{x,y,z}^{UVLM}$ of the vortex flow at position (x, y, z) derived from the UVLM model will be integrated with the synthetic fluctuations obtained from the LES, as presented in Sections 4.4 and 4.5. This combination produces the desired time-dependent velocity profile to be applied on the inlet boundary of the MS domain, as follows,

$$u_{x,y,z}(t) = \bar{u}_{x,y,z}^{UVLM} + u'^{\,LES}_{x,y,z}(t) \tag{67}$$

By using UVLM for mean flow data, the computational effort and time required to initialise the wake vortex profile are significantly reduced compared to performing full-scale LES simulations.

A.3 Results of UVLM-Based Inlet Conditions

This study compares the outcomes of UVLM against validated reference data to determine the most suitable downstream plane for supplying mean-flow data to the LES inlet boundary. Owing to its potential-flow formulation, UVLM does not account for temporal turbulent fluctuations, and consequently exhibits discrepancies in vortex characteristics, particularly in circulation retention, core growth and trajectory evolution when used directly as an LES inflow condition. To address the issue, velocity fluctuations from a LES simulation are processed to derive an equation for reproducing the fluctuations synthetically. A detailed analysis of velocity fluctuations across the vortex core within the LES is conducted. The analysis results are used to improve the accuracy and applicability of the synthesised method for vortex dominated inlet condition.

A.3.1 UVLM Mean Flow Data for LES Main Simulation Inlet

The wing model geometry and stream field conditions employed for the UVLM validation are the same as Section 3.4. The wing geometry is a symmetrical aerofoil (NACA 0012) profile with a chord length of $0.14m$, a semi-span of $0.15m$, and an angle of attack, α of 10°. The freestream velocity is $34m/s$ in x-direction, not having dynamic inputs such as gusts and turbulence. This case setup assumes a rigid-body condition, neglecting the aeroelastic effects such as wing deformation under aerodynamic loads.

In the UVLM, each wake panel induces velocities in the surrounding fluid and at the same time experiences velocities induced by all other bound and wake panels. This mutual interaction causes the wake to convect and rotate as it progresses downstream. The positions of wake panels are iteratively updated based on these induced velocities, ensuring compliance with Kelvin's circulation theorem and Helmholtz's vortex theorems [192]. These principles collectively caused the wake panels to roll up as they convect downstream, forming coherent and concentrated tip vortex structures. The force-free wake roll-up modelled by the UVLM is presented in Figure A.2. This illustration shows the evolution of the wake behind the wing in a steady freestream flow-field condition. It shows the wake circulation strength, Γ_p peaking at the mid-span and gradually decreasing towards the wingtip, in an elliptically distributed profile. As the wake progresses in the streamwise direction, it is observed that the roll-up phenomenon becomes more prominent, leading to a noticeable enlargement in the wingtip vortex structures.

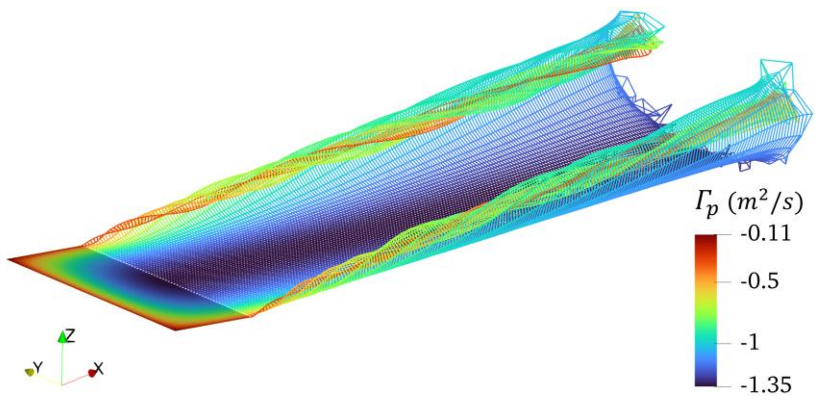

Figure A.2 Force-free wake roll-up modelled by UVLM, coloured by panel circulation Γ_p.

The wingtip vortex represented by the spanwise wake panel roll-up are captured at every chord length interval along the freestream direction, as shown in Figure A.3. The wingtip vortex circulation, Γ_v can be approximated using the spanwise-averaged wake circulation, where $\Gamma_v \approx \overline{\Gamma}_w$ at the corresponding longitudinal position [194]. For a classical elliptic distribution of bound circulation, the spanwise-averaged circulation is also perceived as $\bar{\Gamma}_w = \pi\Gamma_0/4$, where Γ_0 is the maximum circulation strength at the midspan or wing root position ($y = 0$). To affirm the vortex circulation strength estimated by the UVLM, a validation is conducted against the reported values in LES, URANS and experimental studies [111]. As shown in Figure A.4, the UVLM results fall within the reported range, confirming that the reduced-order model provides a physically consistent estimate of wingtip vortex strength suitable for generating mean inflow conditions for LES.

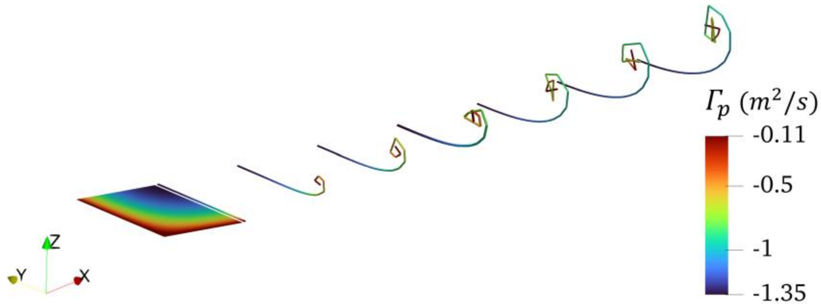

Figure A.3 Development of wingtip vortex per chord distance downstream.

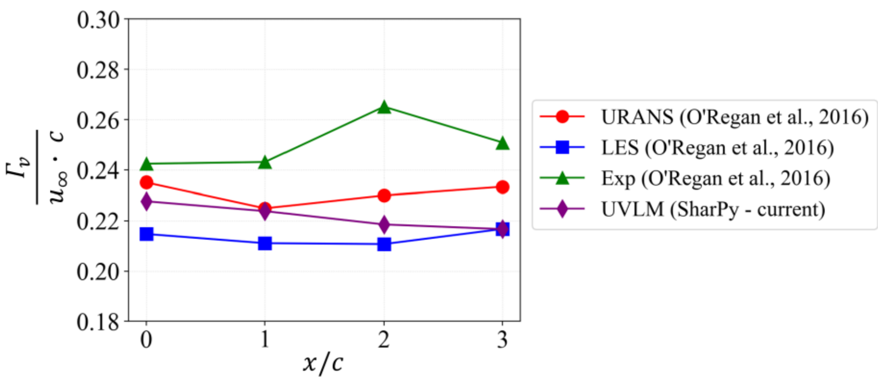

Figure A.4 Validation of normalised vortex circulation strength with downstream distance.

At plane $x/c = 0$, the wake panel does not exhibit any roll-up behaviour due to the vortex lattice at this position remains closely attached to the bound vortex sheet at the trailing edge. However, as the force-free wake panels progress downstream, the wake panels progressively roll up and form into wingtip vortex structures which provide measurable geometric data to determine the dimension and position of the vortex core. Figure A.5 presents the downstream view of the vortex filament roll-up development, clearly illustrating the presence of vortex core in relative to the wing panel (colour plot in the background).

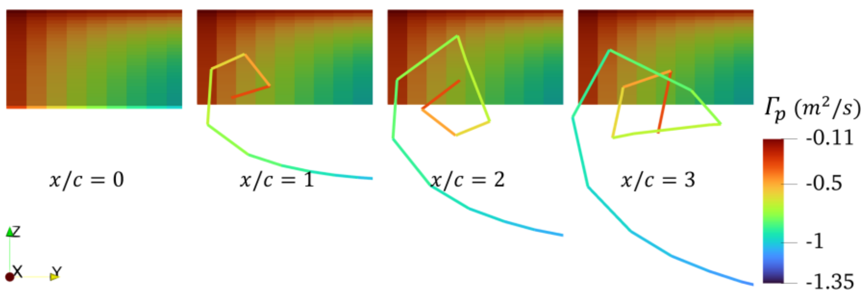

Figure A.5 Wake panel roll-up in the vortex core region, view from downstream.

In this study, vortex filaments with an overall roll-up angle exceeding 90° are classified as belonging within the vortex core region. This significant rotation indicates the presence of concentrated vortex structures typical of wingtip vortices. The resulting vortex core size in UVLM is not a resolved viscous core but rather the apparent radius of the rolled-up vortex sheet in this case. Once the core region is identified, the vortex core centre is computed by averaging the coordinates of all filament vertices within this region.

Subsequently, the radial distances from this centre to each filament vertex are then averaged to estimate the vortex core radius, r_c. Using these definitions, the downstream development of vortex core size and trajectory are plotted alongside the reference data [8, 111] for comparison, as illustrated in Figure A.6.

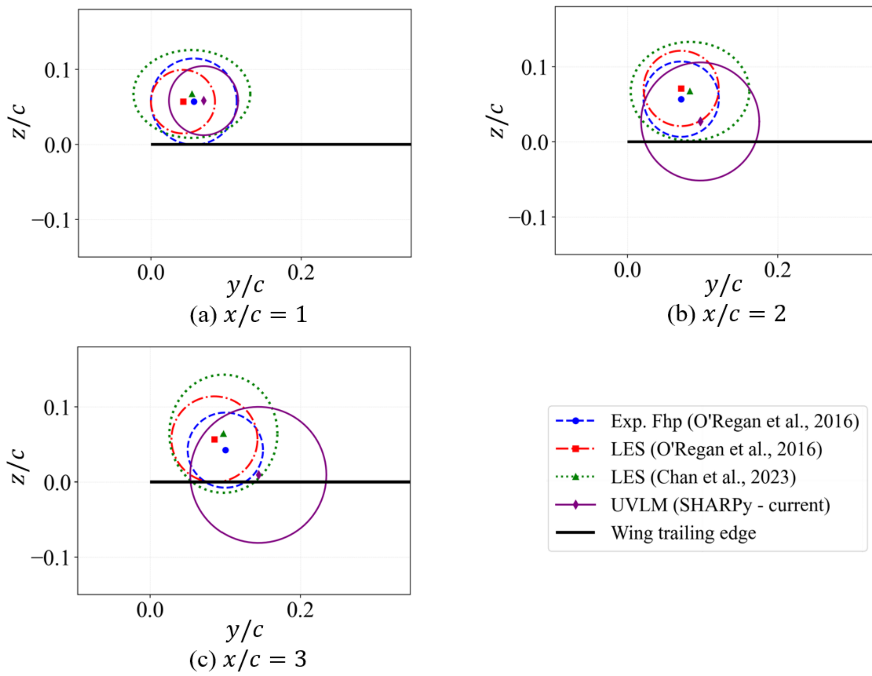

Figure A.6 Comparison on the vortex centre point position and core radius.

Comparing the results at plane $x/c = 1$, the UVLM predictions show relatively accurate results in both vortex core position and size. While vortex cores typically project towards the inboard and downward direction [11], the UVLM-predicted trajectory appears to shift too rapidly as it propagates downstream. The vortex sheet rolled-up radius also exhibits an accelerated growth rate relative to the reference core radius. The discrepancy arises because the UVLM is a numerical model that utilises discrete panel representation to approximate the wake vortex behaviour under inviscid potential flow conditions [65] where the viscous diffusion and turbulence effects governing vortex core evolution are not explicitly resolved. Furthermore, the wake is approximated by a limited number of Lagrangian filaments [195], which can cause the predicted wake development to appear larger prematurely as compared to the confined core radius observed in the experiment and LES. This reduces the computational complexity compared to higher-order models but can impact the prediction accuracy, especially for the highly dynamic wingtip vortices downstream.

Based on the wingtip circulation, vortex centre location and core radius derived from UVLM, the data at plane $x/c = 1$ demonstrates the most promising outcome amongst the planes, showing closely matched profile with reference data. Whereas the subsequent planes such as $x/c = 2$ and $x/c = 3$ in the UVLM solution are showing an enlarged vortex sheet radius that does not correspond to the physical vortex core dimension. Therefore, the plane $x/c = 1$ is utilised to populate the velocity components required for the LES MS inlet boundary conditions using the formulations prescribed in Eqs. (62) to (66). The LES MS domain with the inlet boundary specified by the $x/c = 1$ plane data from UVLM are shown in Figure A.7.

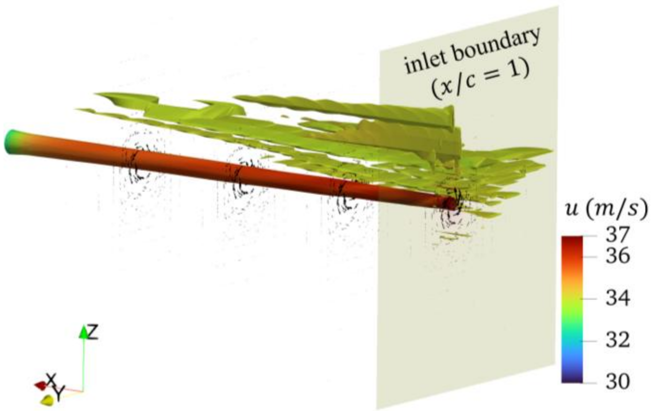

Figure A.7 LES main simulation (MS) with the mean inflow conditions derived from UVLM, visualised with Q-criterion and coloured by the velocity magnitude.

Since the mean-flow-field data prescribed with the UVLM aims to provide an efficient approach to initialise the wingtip vortex flow in a LES inlet condition, the mean vortical velocities remain constant throughout the simulation. As a result, the wingtip vortices in the LES MS do not exhibit any turbulence-like structure, as shown in Figure A.7. In contrast to the UVLM roll up shown previously in Figure A.2, the vortex core appears to maintain a relatively consistent core diameter downstream.

In the LES main simulation with the inlet boundary prescribed by the $x/c = 1$ plane data from UVLM, the flow-field quantities across the vortex core at successive downstream locations are extracted to further examine the vortex development. The tangential and axial velocity distributions were compared against the published data [8], and presented in Figure A.8 and Figure A.9, respectively.

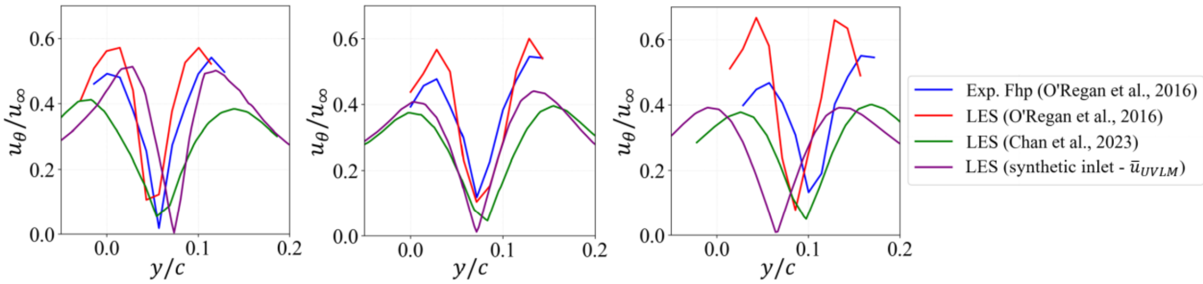

(a) $x/c = 1$ (b) $x/c = 2$ (c) $x/c = 3$

Figure A.8 Validation on normalised tangential velocity magnitude u_θ/u_∞.

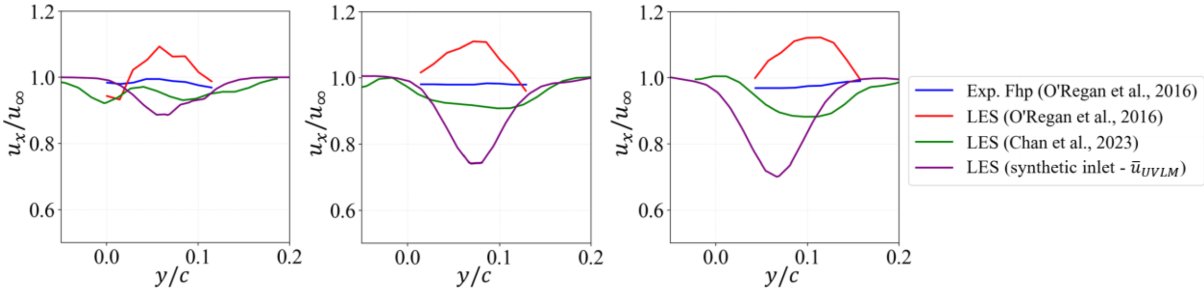

(a) $x/c = 1$ (b) $x/c = 2$ (c) $x/c = 3$

Figure A.9 Validation on normalised tangential velocity magnitude u_x/u_∞.

At the inlet boundary ($x/c = 1$), the inlet condition by UVLM produces a vortex characteristic the expected distribution profile. The tangential velocity profile exhibits correctly placed peak values and trough locations, indicating that both the vortex core centre and the core radius are consistently captured. The peak magnitude is marginally higher than the LES reference, which is attributed to the slightly smaller core radius specified from UVLM. The axial velocity also shows the appropriate deficit behaviour, with approximately 15% below the freestream level, as defined by the Eq. (66).

As the flow develops downstream, it is noticed that although the tangential velocity magnitude is largely preserved, the position of the vortex core remains stationary, with its centre fixed at $0.07c$ inboard across all planes. Similarly, the trough position of the axial velocity deficit does not shift as predicted by the LES data. Moreover, the deficit profile diverges further from the LES charts, possibly due to the overly specified initial deficit value.

The discrepancies in the core position are caused by the absence of time-varying velocity components at the inlet boundary. In LES, the fluctuation components play a crucial role in computing the kinetic energy and the Reynolds stress tensor. These parameters in turn affect the flow dynamics and turbulence characteristics within the domain, resulting in inaccuracies in vortex development. The fluctuations level of the inlet velocities is however correlated with both the spatial and temporal scale.

Hence, the following section explores the development of representative fluctuations at the inlet conditions from LES.

A.3.2 UVLM Data Synthesised with Fluctuations from LES

UVLM serves as an efficient approach for predicting the mean vortex-induced velocity field. However, the resulting flow remains inherently steady due to the inviscid potential flow assumptions. Consequently, the LES main simulation with inlet condition initialised by the UVLM as shown in Figure A.7 do not contain the turbulence like fluctuations unless sufficient downstream development distance is provided for instabilities to emerge naturally.

To introduce the unsteady characteristics required for LES, the UVLM-derived mean velocity can be combined with the fluctuation synthesis methodology previously described and demonstrated in the Section 4.5. In this framework, the mean velocity components from UVLM are treated as the baseline flow field at the inlet plane. The synthetic velocity fluctuations are then constructed using the LES-based statistical Fourier transformation.

The synthetical sinusoidal formulations, whether scaled by the mean velocity magnitude in Eq. (46) or by the spatial correlation function in Eq. (53), are then superimposed onto the UVLM mean velocity following the same procedure previously applied to the LES baseline flow in Chapter 4. The inlet velocity can therefore be represented as Eq. (67). With this hybrid formulation, the dominant vortex structure predicted by the UVLM is preserved while the synthetic fluctuations provide the temporal turbulence required to initiate a more realistic flow development within the LES domain. This strategy therefore enables the efficient initialisation of the wingtip vortex flow at the inlet without requiring an upstream high-fidelity simulation.

A.4 Summary and Recommendations

The motivation for this research is driven by the CFD application of wake vortex surfing in extended longitudinal field. With the variety of formation configurations and positioning, evaluating the effects of vortex surfing on the trailing aircraft in each permutation will require extensive simulation efforts and substantial computational resources. To streamline this process, an efficient UVLM is employed to predetermine the wingtip vortex downstream. This vortex serves as the inlet conditions for the main LES simulation, effectively reducing the simulation domain size to begin just before the trailing aircraft's position. This method also enables repeated assessments of aerodynamic performance across different aircraft types and positions.

The chapter has demonstrated the effective mapping of vortical flow from a UVLM model to the LES inlet boundary condition. Despite limitations of the UVLM model, such as accelerated vortex core development, accurate representation of the vortex at the inlet of LES MS domain can be achieved through careful selection of the inflow plane. Future research may explore the correlation between the vortex growth rate in UVLM and actual cases. This will enable the systematic selection of UVLM mapping plane that best represent any desired downstream position.

Using the fluctuations characteristics extracted from a separated LES simulation, the author formulated the Fourier series sinusoidal expression to synthesise the temporal velocity data. This hybrid UVLM-LES synthesis approach significantly reduces the computational cost associated with precursor-based inlet generation. Instead of performing a dedicated upstream LES for every simulation, the turbulence statistics extracted from a single reference LES can be reused to synthesise fluctuations, while the mean vortex structure is efficiently predicted using UVLM. Consequently, realistic inflow conditions can be generated for multiple formation configurations without repeatedly incurring the high computational core-hour cost of precursor LES simulations.

Overall, this chapter establishes an efficient inlet conditioning framework specifically tailored for freestream vortices, which are fundamentally different from the wall-bounded turbulence or internal flows. The methodology captures the unique turbulence characteristics of vortex cores, including their correlated tri-axial fluctuations and coherent rotational structures. These contributions advance the current state of CFD practice for wake vortex modelling and provide a practical foundation for future studies on formation flight aerodynamics, enabling cost effective and accurate simulation of vortex-induced performance effects on trailing aircraft.

References

[1] ICAO, “Agenda Item 16: Environmental Protection - International Aviation and Climate Change - Policy and Standardization,” International Civil Aviation Organization, 2019.

[2] B. Graver, K. Zhang and D. Rutherford, “CO2 emissions from commercial aviation, 2018,” The International Council on Clean Transportation , 2019.

[3] IATA, “Global Air Passenger Demand Reaches Record High in 2024,” IATA, 30 January 2025. [Online]. Available: https://www.iata.org/en/pressroom/2025-releases/2025-01-30-01/#:~:text=Total%20full%2Dyear%20traffic%20in,record%20for%20full%2Dyear%20traffic.. [Accessed 16 September 2025].

[4] Airbus, “Global Market Forecast 2025,” 2025. [Online]. Available: https://www.airbus.com/sites/g/files/jlcbta136/files/2025-06/Presentation%20GMF%202025-2044.pdf. [Accessed 05 September 2025].

[5] Boeing, “Commercial Market Outlook 2025-2044,” 2025. [Online]. Available: https://www.boeing.com/content/dam/boeing/boeingdotcom/market/assets/downloads/2025-commercial-market-outlook.pdf. [Accessed 05 September 2025].

[6] C. Bergero, G. Gosnell, D. Gielen, S. Kang, M. Bazilian and S. J. Davis, “Pathways to net-zero emissions from aviation,” *Nature Sustainability,* vol. 6, pp. 404-414, 2023.
DOI: 10.1038/s41893-022-01046-9

[7] I. Ransquin, D.-G. Caprace, M. Duponcheel and P. Chatelain, “Wake Vortex Detection and Tracking for Aircraft Formation Flight,” *Journal of Guidance, Control and Dynamics,* vol. 44, no. 12, pp. 2225-2243, 2021.
DOI: 10.2514/1.G006028

[8] J. C. Chan, H. Hesse and P. C. Wang, “Aerodynamic Interactions in Formation Flight for Wake Vortex Surfing,” in *AIAA AVIATION 2023 Forum*, San Diego, CA and Online, 2023.
DOI: 10.2514/6.2023-4221

[9] Y. Zhao, H. Wu, Q. Zhang and Q. Cheng, “Overview of surfing aircraft vortices for energy,” *Journal of Physics: Conference Series (The 11th Asia Conference on Mechanical and Aerospace Engineering ACMAE),* vol. 1786, no. 1, pp. 12-26, 2021.
DOI: 10.1088/1742-6596/1786/1/012026

[10] W. B. Blake, S. R. Bieniawski and T. C. Flanzer, “Surfing aircraft vortices for energy,” *The Journal of Defense Modeling and Simulation: Applications, Methodology, Technology,* vol. 12, no. 1, pp. 31-39, 2013.
DOI: 10.1177/1548512913500734

[11] J. C. Chan, H. Hesse and P. C. Wang, “Experimental Characterization of Wingtip Vortices with Perspective Upright Correction,” in *AIAA AVIATION 2023 Forum*, San Diego, CA and Online, 2023.
DOI: 10.2514/6.2023-4526

[12] J. J. Westermeyer, “Wake Surfing: Vortex Wake Energy Recovery for sUAS's,” in *AIAA SciTech 2024 Forum*, Orlando, FL, 2024.
DOI: 10.2514/6.2024-0128

[13] C. Wieselsberger, “Beitrag zur Erkl¨arung des Winkelfluges einiger Zugv¨ogel,” *Z. Flugtechnik & Motorluftschiffahrt,* vol. 5, pp. 225-229, 1914.

[14] P. B. S. Lissaman and C. A. Shollenberger, “Formation Flight of Birds,” *Journal of Science,* vol. 168, no. 3934, pp. 1003-1005, 1970.
DOI: 10.1126/science.168.3934.1003

[15] D. Hummel, “The Use of Aircraft Wakes to Achieve Power Reductions in Formation Flight,” in *Advisory Group for Aerospace Research & Development Fluid Dynamics Panel (AGARD FDP)*, Trondheim, Norway, 1996.

[16] D. Hummel, “Formation flight as an energy-saving mechanism,” *Israel Journal of Zoology,* vol. 41, no. 3, pp. 261-278, 1995.

[17] J. P. Badgerow and F. R. Hainsworth, “Energy Savings Through Formation Flight? A Re-examination of the Vee Formation,” *Journal of Theoretical Biology,* vol. 93, no. 1, pp. 41-52, 1981.
DOI: 10.1016/0022-5193(81)90055-2

[18] F. R. Hainsworth, “Precision and Dynamics of Positioning by Canada Geese Flying in Formation,” *Journal of Experimental Biology,* vol. 128, no. 1, pp. 445-462, 1987.
DOI: 10.1242/jeb.128.1.445

[19] F. R. Hainsworth, “Wing movements and positioning for aerodynamic benefit by Canada geese flying in formation,” *Canadian Journal of Zoology,* vol. 67, no. 3, pp. 585-589, 1989.
DOI: 10.1139/z89-084

[20] C. J. Cutts and J. R. Speakman, “Energy savings in formation flight of pink-footed geese,” *Journal of Experimental Biology,* vol. 189, no. 1, pp. 251-261, 1994.
DOI: 10.1242/jeb.189.1.251

[21] H. Weimerskirch, J. Martin, Y. Clerquin, P. Alexandre and S. Jiraskova, “Energy saving in flight formation,” *Nature,* vol. 413, no. 6857, pp. 697-698, 2001.
DOI: 10.1038/35099670

[22] E. C. Mills, T. K. Speer and J. L. Tate, “Formation Flight Technology,” *Aircraft Engineering and Aerospace Technology,* vol. 43, no. 7, pp. 4-8, 1970.
DOI: 10.1108/eb034785

[23] L. R. Jenkinson, R. E. Caves and D. P. Rhodes, “Automatic formation flight - A preliminary investigation into the application to civil operations,” *Aircraft Engineering, Technology, and Operations Congress,* 1995.
DOI: 10.2514/6.1995-3898

[24] D. Fleischmann and M. M. Lone, “Analysis of wake surfing benefits using a fast unsteady vortex lattice method,” *AIAA SciTech 2019 Forum,* 2019.
DOI: 10.2514/6.2019-0264

[25] DLR, “The rear aircraft ‘surfs’ on the airflow of the wake vortex,” Deutsches Zentrum für Luft-und Raumfahrt German Aerospace Center, 23 June 2021. [Online]. Available: https://www.dlr.de/content/en/images/2021/2/formic-formation-flight.html. [Accessed 03 March 2022].

[26] D. Erbschloe, A. Antczak, D. Carter, G. Dale, C. Döll, R. Luckner, T. Marks and M. Niestroy, “Operationalizing Flight Formations for Aerodynamic Benefits,” in *AIAA SciTech Forum*, Orlando, FL, 2020.
DOI: 10.2514/6.2020-1004

[27] C. Hanson, J. Ryan, M. Allen and S. Jacobson, “An Overview of Flight Test Results for a Formation Flight Autopilot,” *AIAA Guidance, Navigation, and Control Conference and Exhibit,* 2002.
DOI: 10.2514/6.2002-4755

[28] M. J. Vachon, R. J. Ray, K. R. Walsh and K. Ennix, “F/A-18 Performance Benefits Measured During the Autonomous Formation Flight Project,” NASA Drydan Flight Research Center, Edwards, California, 2003.

[29] E. Wagner, “An Analytical Study of T-38 Drag Reduction in Tight Formation Flight,” Master Thesis, Department of The Air Force, Air University, Air Force Institute of Technology, Wright-Patterson Air Force Base, Ohio, 2002.

[30] E. Wagner, D. Jacques, W. Blake and M. Pachter, “Flight Test Results of Close Formation Flight for Fuel Savings,” *AIAA Atmospheric Flight Mechanics Conference and Exhibit,* 2002. DOI: 10.2514/6.2002-4490

[31] M. T. Morgan, “A Study in Drag Reduction of Close Formation Flight Accounting for Flight Control Trim Positions and Dissimilar Formations,” Master of Science Thesis, Department of Aeronautics and Astronautics, Air Force Institute of Technology, March 2005.

[32] J. Pahle, D. Berger, M. Venti, C. Duggan, J. Faber and K. Cardinal, “An Initial Flight Investigation of Formation Flight for Drag Reduction on the C-17 Aircraft,” *AIAA Atmospheric Flight Mechanics Conference,* 2012. DOI: 10.2514/6.2012-4802

[33] S. R. Bieniawski, R. W. Clark, S. E. Rosenzweig and W. B. Blake, “Summary of Flight Testing and Results for the Formation Flight for Aerodynamic Benefit Program,” *AIAA SciTech Forum 52nd Aerospace Science Meeting,* 2014. DOI: 10.2514/6.2014-1457

[34] T. C. Flanzer and S. R. Bieniawski, “Operational Analysis for the Formation Flight for Aerodynamic Benefit Program,” in *AIAA SciTech 52nd Aerospace Sciences Meeting*, Maryland, 2014. DOI: 10.2514/6.2014-1460

[35] B. Whitehead, “Surfing Aircraft Vortices for Energy ATD Technical Report Improved Software Review & Flight,” AFRL Technical Report, 2017.

[36] R. K. Nangia, N. Brown, D. Erbschloe and Carter Dennis, “Formation Flying (Air-Wake Surfing) for Efficient Operations,” *AIAA SciTech Forum,* 2020. DOI: 10.2514/6.2020-1001

[37] Airbus, “Airbus joined by European partners to demonstrate reduced emission fello'fly operations,” 9 September 2020. [Online]. Available: https://www.airbus.com/sites/g/files/jlcbta136/files/d71469db351c7374f2eb9a0faa20da6e_

Airbus-joined-by-partners-to-demonstrate-reduced-emission-fellowfly-operations.pdf. [Accessed 20 May 2022].

[38] Airbus, “fello'fly Wake Energy Retrieval Concept of Operations,” August 2021. [Online]. Available: https://flipbook.mms-airbus.com/fellofly/index.html#/page/0. [Accessed 20 May 2022].

[39] M. Kaushik, Theoretical and Experimental Aerodynamics, Kharagpur, West Bengal, India: Springer, 2019.

DOI: 10.1007/978-981-13-1678-4

[40] G. Michea, “Formation and early development of wingtip vortices,” *PhD Thesis, University of Glasgow,* 2013.

[41] C. Breitsamter, “Wake vortex characteristics of transport aircraft,” *Progress in Aerospace Sciences,* vol. 47, no. 2, pp. 89-134, 2011.

DOI: 10.1016/j.paerosci.2010.09.002

[42] H. Lamb, Hydrodynamics, 6th ed., New York: Dover, 1945.

[43] V. J. Rossow and K. D. James, “Wake-Vortex Hazards During Cruise,” NASA Ames Research Center, Moffett Field, California, 1998.

[44] B. Makgantai, N. Subaschandar and R. S. Jamisola Jr., “Design Optimization of Wingtip Devices to Reduce Induced Drag on Fixed-Wings,” in *International Conference on Unmanned Aircraft Systems (ICUAS)*, Athens, Greece, 2021.

DOI: 10.1109/ICUAS51884.2021.9476801

[45] H. S. M. Helal, E. E. Khalil, O. E. Abdellatif and G. M. Elhariry, “Aircraft-Blended Winglet Performance Analyses,” in *55th AIAA Aerospace Sciences Meeting, AIAA SciTech Forum*, Grapevine, Texas, 2017.

DOI: 10.2514/6.2017-1838

[46] B. S. de Mattos, P. J. Komatsu and J. T. Tomita, “Optimal wingtip device design for transport airplane,” *Aircraft Engineering and Aerospace Technology,* vol. 90, no. 5, pp. 743-763, 2018.

DOI: 10.1108/AEAT-07-2015-0183

[47] V. R. Corsiglia, R. A. Jacobsen and N. Chigier, “An Experimental Investigation of Trailing Vortices Behind a Wing with a Vortex Dissipator,” in *Aircraft Wake Turbulence and Its Detection*, Boston, MA, Springer, 1971, pp. 229-242.

DOI: 10.1007/978-1-4684-8346-8_14

[48] S. Raorane, “The development of method (tool) to model propeller propulsion models to be implemented in the potential flow simulation software "Tornado",” Master’s thesis, Department of Management and Engineering, Linköping University, Linköping, Sweden, 2017.

[49] M. Marion and R. Temam, “Navier-Stokes Equations: Theory and Approximation,” in *Handbook of Numerical Analysis*, Elsevier, 1998, pp. 503-689.
DOI: 10.1016/S1570-8659(98)80010-0

[50] J. F. Wendt, J. D. Anderson Jr., J. Degroote, G. Degrez, E. Dick, R. Grundmann and J. Vierendeels, Computational Fluid Dynamics: An Introduction, Waterloo, Belgium: Springer, 1995.
DOI: 10.1007/978-3-662-11350-9

[51] R. S. Scorer and L. J. Davenport, “Contrails and aircraft downwash,” *Journal of Fluid Mechanics,* vol. 43, no. 3, pp. 451-464, 1970.
DOI: 10.1017/S0022112070002501

[52] K. Sassen, “Contrails-Cirrus and Their Potential for Regional Climate Change,” *Bulletin of the American Meteorological Society,* vol. 787, no. 9, pp. 1885-1903, 1997.
DOI: 10.1175/1520-0477(1997)078<1885:CCATPF>2.0.CO;2

[53] Y. S. Lim, P. C. Wang, J. J. Yeo and S. C. M. Yu, “Experimental and numerical studies for flow over a sierpinski tetrahedron for potential windbreak application,” *Journal of Wind Engineering & Industrial Aerodynamics,* vol. 216, 2021.
DOI: 10.1016/j.jweia.2021.104712

[54] B. Chanetz, J. Délery, P. Gilliéron, P. Gnemmi, E. R. Gowree and P. Perrier, Experimental Aerodynamics An Introductory Guide, Cham, Switzerland: Springer, 2020.
DOI: 10.1007/978-3-030-35562-3

[55] M. H. Sohn and J. W. Chang, “Visualization and PIV study of wing-tip vortices for three different tip configurations,” *Aerospace Science and Technology,* vol. 16, pp. 40-46, 2012.
DOI: 10.1016/j.ast.2011.02.005

[56] M. J. Bhagwat, F. X. Caradonna and M. Ramasamy, “Wing-vortex interaction: unraveling the flowfield of a hovering rotor,” *Experiments in Fluids,* vol. 1, p. 56, 2015.
DOI: 10.1007/s00348-014-1893-3

[57] P. Panagiotou, G. Ioannidis, I. Tzivinikos and K. Yakinthos, “Experimental Investigation of theWake and the Wingtip Vortices of a UAV Model,” *Aerospace,* vol. 4, no. 53, 2017.

DOI: 10.3390/aerospace4040053

[58] D. Nagarathinam, J.-W. Hong, B.-K. Ahn, C. Park, G.-D. Kim and I.-S. Moon, “Dynamics of tip vortex flow over three dimensional hydrofoils by LDV measurements,” *Ocean Engineering,* vol. 266, no. 1, 2022.

DOI: 10.1016/j.oceaneng.2022.112748

[59] J. J. Serrano-Aguilera, J. H. García-Ortiz and A. Gallardo-Claros, “Experimental characterization of wingtip vortices in the near field using smoke flow visualizations,” *Exp Fluids,* vol. 57, no. 137, 2016.

DOI: 10.1007/s00348-016-2222-9

[60] W. F. Philips, Mechanics of Flight, John Wiley & Sons Ltd, 2009.

[61] B. Chaouat, “The State of Art of Hybrid RANS/LES Modeling for the Simulation of Turbulent Flows,” Springer Science+Business Media, 2017, pp. 279-327.

DOI: 10.1007/s10494-017-9828-8

[62] B. K. J. Tan, H. Hesse and P. C. Wang, “Numerical Capture and Validation of a Massively Separated Bluff-Body Wake,” in *AIAA AVIATION 2020 FORUM*, Virtual Event, 2020.

DOI: 10.2514/6.2020-2713

[63] R. H. Bush, T. Chyczewsky, K. Duraisamy, B. Eisfeld, C. L. Rumsey and B. R. Smith, “Recommendations for Future Efforts in RANS Modeling and Simulation,” *AIAA SciTech Forum,* 2019.

DOI: 10.2514/6.2019-0317

[64] J. Katz and A. Plotkin, Low-speed aerodynamics, Cambridge: Cambridge University Press, 2001.

DOI: 10.1017/CBO9780511810329

[65] J. Murua, R. Palacios and J. M. R. Graham, “Applications of the unsteady vortex-lattice method in aircraft aeroelasticity and flight dynamics,” *Progress in Aerospace Sciences,* vol. 55, pp. 46-72, 2012.

DOI: 10.1016/j.paerosci.2012.06.001

[66] E. Trumic and K. S. Swamy, “Aerodynamic Performance Analysis of a UAV using CFD and VLM,” *Master's Thesis, Linkoping University,* 2021.

[67] A. Septiyana, K. Hidayat, A. Rizaldi, M. L. Ramadiansyah, R. A. Ramadhan, P. Suseno, E. B. Jayanti, N. Atmasari and A. Rashydi, “Analysis of Aerodynamic Characteristics Using

the Vortex Lattice Method on Twin Tail Boom Unmanned Aircraft," *AIP Conference Proceedings,* 2020.

DOI: 10.1063/5.0002337

[68] D. J. Halaas, S. R. Bieniswski, B. Whitehead and W. B. Blake, "Formation Flight for Aerodynamic Benefit Simulation Development and Validation," *52nd Aerospace Sciences Meeting,* 2014.

DOI: 10.2514/6.2014-1459

[69] D. Singh, A. F. Antoniadis, P. Tsoutsanis, H.-S. Shin, A. Tsourdos, S. Mathekga and K. W. Jenkins, "A Multi-Fidelity Approach for Aerodynamic," *Aerospace,* vol. 5, no. 2, p. 66, 2018.

DOI: 10.3390/aerospace5020066

[70] D. Zhang, Y. Chen, X. Dong, Z. Liu and Y. Zhou, "Numerical Aerodynamic Characteristics Analysis of the Close Formation Flight," *Mathematical Problems in Engineering,* pp. 1-13, 2018.

DOI: 10.1155/2018/3136519

[71] D. Vechtel, D. Fischenberg and J. Schwithal, "Flight dynamics simulation of formation flight for

energy saving using LES-generated wake flow fields," *CEAS Aeronautical Journal,* vol. 9, no. 4, pp. 735-746, 2018.

DOI: 10.1007/s13272-018-0318-z

[72] C. H. Moeng and P. P. Sullivan, Large-Eddy Simulation, Boulder, CO, USA: National Center for Atmospheric Research, 2015.

DOI: 10.1016/B978-0-12-382225-3.00201-2

[73] Airbus, "Airbus and SESAR partners are taking wake energy retrieval to the next level," 27 September 2024. [Online]. Available: https://www.airbus.com/en/newsroom/stories/2024-09-airbus-and-sesar-partners-are-taking-wake-energy-retrieval-to-the-next. [Accessed 6 August 2025].

[74] M. H. Baba-Ahmadi and G. R. Tabor, "Inlet conditions for LES using mapping and feedback control," *Computers & Fluids,* vol. 38, no. 6, pp. 1299-1311, 2009.

DOI: 10.1016/j.compfluid.2009.02.001

[75] G. R. Tabor and M. H. Baba-Ahmadi, "Inlet conditions for large eddy simulation: A review," *Computer & Fluids,* vol. 39, no. 4, pp. 553-567, 2010.

DOI: 10.1016/j.compfluid.2009.10.007

[76] J. C. Chan, H. Hesse and P. C. Wang, "Inlet Mapping of Wingtip Vortices in LES for Wake Vortex Surfing," in *AIAA Aviation Forum*, Las Vegas, Nevada, 2024.

DOI: 10.2514/6.2024-4016

[77] P. C. Wang and J. J. McGuirk, "Large Eddy Simulation of High Speed Nozzle Flows - Assessment & Validation of Synthetic Turbulence Inlet Conditions," in *20th AIAA Computational Fluid Dynamics Conference*, Honolulu, Hawaii, 2011.

DOI: 10.2514/6.2011-3555

[78] E. D. Villers, "The Potential of Large Eddy Simulation for the Modelling of Wall Bounded Flows," Department of Mechanical Engineering Imperial College London, London, 2006.

[79] A. Montorfano, F. Piscaglia and G. Ferrari, "Inlet boundary conditions for incompressible LES: A comparative study.," *MathemaTical and Computer Modelling,* vol. 57, no. 7-8, pp. 1640-1647, 2013.

DOI: 10.1016/j.mcm.2011.10.077

[80] P. C. Wang and J. J. McGuirk, "Large Eddy Simulation of supersonic jet plumes from rectangular con-di nozzles," *International Journal of Heat and Fluid Flow,* vol. 43, pp. 62-73, 2013.

DOI: 10.1016/j.ijheatfluidflow.2013.06.002

[81] P. C. Wang and J. J. McGuirk, "Validation of a large eddy simulation methodology for accelerated nozzle flows," *The Aeronautical Journal,* vol. 124, no. 1277, pp. 1070-1098, 2020.

DOI: 10.1017/aer.2020.12

[82] N. S. Dhamankar, G. A. Blaisdell and A. S. Lyrintzis, "Overview of Turbulent Inflow Boundary Conditions for Large-Eddy Simulations," *AIAA Journal,* vol. 56, no. 4, 2017.

DOI: 10.2514/1.J055528

[83] J. U. Schlüter, H. Pitsch and P. Moin, "Large Eddy Simulation Inflow Conditions for Coupling with Reynolds-Averaged Flow Solvers," *AIAA Journal,* vol. 42, no. 3, pp. 478-484, 2004.

DOI: 10.2514/1.3488

[84] C. D. Pierce and P. Moin, "Method for Generating Equilibrium Swirling Inflow Conditions," *AIAA Journal,* vol. 36, no. 7, pp. 1325-1327, 1998.

DOI: 10.2514/2.518

[85] X. Jiang, G. A. Siamas and L. C. Wrobel, “Analytical Equilibrium Swirling Inflow Conditions for Computational Fluid Dynamics,” *AIAA Journal,* vol. 46, no. 4, pp. 1015-1018, 2008.
DOI: 10.2514/1.29439

[86] “Singapore Institute of Technology,” [Online]. Available: https://www.singaporetech.edu.sg/. [Accessed 28 August 2022].

[87] “Interchangeable-lens Cameras | Alpha 7C Compact full-frame camera | ILCE-7C/ILCE-7CL,” Sony, 2022. [Online]. Available: https://www.sony.com.sg/interchangeable-lens-cameras/products/ilce-7c?locale=en_SG&cpint=HOMEPAGE_TOPBANNER_DIILCE7C_8524. [Accessed 27 June 2022].

[88] “28-70mm F2.8 DG DN | Contemporary,” Sigma, 2022. [Online]. Available: https://www.sigma-global.com/en/lenses/c021_28_70_28/. [Accessed 10 July 2022].

[89] “Aiguru Laser Level Green Line 4B1H comes with Remote | Model: LASER-AGR-LD5150-4B1H,” Aik Chin Hin Hardware & Machinery, 2022. [Online]. Available: https://www.aikchinhin.sg/products/aiguru-laser-level-green-line-4b1h-c-w-remote-model-laser-agr-ld5150-4b1h. [Accessed 04 September 2022].

[90] “Adobe Lightroom Classic,” Adobe, 2022. [Online]. Available: https://www.adobe.com/sg/products/photoshop-lightroom.html. [Accessed 1 September 2022].

[91] “Adobe Photoshop,” Adobe, 2022. [Online]. Available: https://www.adobe.com/sg/products/photoshop.html. [Accessed 28 August 2022].

[92] “AMD Ryzen Threadripper PRO 5995WX,” CPU Benchmarks, [Online]. Available: https://www.cpubenchmark.net/cpu.php?cpu=AMD+Ryzen+Threadripper+PRO+5995WX&id=4764. [Accessed 05 May 2022].

[93] “Autodesk Inventor: 3D modeling software for designers and engineers,” Autodesk, [Online]. Available: https://www.autodesk.com/products/inventor/overview?us_oa=dotcom-us&us_si=10725494-1df6-4460-856f-43b56eda96e3&us_pt=INVNTOR&us_at=Overview. [Accessed 07 April 2022].

[94] “OpenFOAM,” OpenFOAM, [Online]. Available: https://www.openfoam.com/. [Accessed 07 May 2022].

[95] "OpenFOAM," The OpenFOAM Foundation, [Online]. Available: https://openfoam.org/. [Accessed 07 May 2022].

[96] R. Palacios, "SHARPy: Simulation of High-Aspect-Ratio aircraft and wind turbines in Python," Imperial College London, 12 September 2023. [Online]. Available: https://www.imperial.ac.uk/aeroelastics/sharpy/. [Accessed 12 February 2024].

[97] "ParaView," kitware, 2023. [Online]. Available: https://www.paraview.org/. [Accessed 29 November 2023].

[98] "Python," Python, [Online]. Available: https://www.python.org/. [Accessed 09 November 2023].

[99] H. Chevalier, "Flight Test Studies of the Formation and Dissipation of Trailing Vortices," *SAE Technical Paper 730295,* 1973.
DOI: 10.4271/730295

[100] D. McLean, "Wingtip Devices: What They Do and How They Do It," in *Performance and Flight Operations Engineering Conference*, Seattle, WA, 2005.

[101] H. S. Helal, E. E. Khalil, O. E. Abdellatif and G. M. Elhariry, "Aerodynamic Analyses of Aircraft-Blended Winglet Performance," *IOSR Journal of Mechanical and Civil Engineering (IOSR-JMCE),* vol. 13, no. 3, pp. 65-72, 2016.
DOI: 10.9790/1684-1303046572

[102] M. N. Haque, M. Ali and I. Ara, "Experimental Investigation on the Performance of NACA 4412 Aerofoil with Curved Leading Edge Planform," *Journal of Procedia Engineering,* vol. 105, pp. 232-240, 2015.
DOI: 10.1016/j.proeng.2015.05.099

[103] D. S. Körpe, Ö. Ö. Kanat and T. Oktay, "The Effects of Initial y plus: Numerical Analysis of 3D NACA 4412 Wing Using γ-Reθ SST Turbulence Model," *European Journal of Science and Technology,* no. 17, pp. 692-702, 2019.
DOI: 10.31590/ejosat.631135

[104] K. B. M. Q. Zaman, A. F. Fagan and M. R. Mankbadi, "An Experimental Study and Database for Tip Vortex Flow From an Airfoil," in *NASA Technical Memorandum*, Cleveland, Ohio, 2017.

[105] A. Rohatgi, "WebPlotDigitizer v4.6," [Online]. Available: https://apps.automeris.io/wpd/. [Accessed 28 March 2023].

[106] W. J. Devenport, M. C. Rife, S. I. Liapis and G. J. Follin, “The structure and development of a wing-tip vortex,” *Journal of Fluid Mechanics,* vol. 312, pp. 67-106, 1996.

DOI: 10.1017/S0022112096001929

[107] F. Holzapfel, T. Gerz, M. Frech and A. Dornbrack, “Wake Vortices in Convective Boundary Layer and Their Influence on Following Aircraft,” *Journal of Aircraft,* vol. 37, no. 6, pp. 1001-1007, 2000.

DOI: 10.2514/2.2727

[108] N. N. Ahmad, F. H. Proctor, F. M. L. Duparcmeur and D. Jacob, “Review of Idealized Aircraft Wake Vortex Models,” in *AIAA SciTech 52nd Aerospace Sciences Meeting*, National Harbour, Maryland, 2014.

DOI: 10.2514/6.2014-0927

[109] H. Hesse and R. Palacios, “Dynamic Load Alleviation in Wake Vortex Encounters,” *Journal of Guidance, Control, and Dynamics,* vol. 39, no. 4, pp. 801-813, 2016.

DOI: 10.2514/1.G000715

[110] I. Ara, M. Ali, M. Q. Islam and M. N. Akhter, “An Experimental Investigation on the Aerodynamic Characteristics of NACA 4412 with Winglets,” in *AIP Conference Proceedings 2121*, 2019.

DOI: 10.1063/1.5115905

[111] M. S. O'Regan, P. C. Griffin and T. M. Young, “A vorticity confinement model applied to URANS and LES simulations of a wing-tip vortex in the near-field,” *International Journal of Heat and Fluid Flow,* vol. 61, no. 2016, pp. 355-365, 2016.

DOI: 10.1016/j.ijheatfluidflow.2016.05.014

[112] B. K. J. Tan, P. C. Wang and S. Srigrarom, “Computational Modelling of Wing Downwash Profile with Reynolds-Averaged and Delayed Detached-Eddy Simulations,” in *23rd AIAA Computational Fluid Dynamics Conference*, Denver, Colorado, 2017.

DOI: 10.2514/6.2017-3960

[113] M. Giuni and B. Emmanuel, “Analytical/experimental comparison of the axial velocity in trailing vortices,” in *49th AIAA Aerospace Sciences Meeting including the New Horizons Forum and Aerospace Exposition*, Orlando, FL, 2011.

DOI: 10.2514/6.2011-990

[114] N. N. Ahmad, F. H. Proctor and R. B. Perry, “Numerical Simulation of the Aircraft Wake Vortex Flowfield,” in *5th AIAA Atmospheric and Space Environments Conference*, San Diago, CA, 2013.

10.2514/6.2013-2552

[115] A. Revell, G. Iaccarino and X. Wu, “Advanced RANS modeling of wingtip vortex flows,” in *Center for Turbulence Research - Proceedings of the Summer Program*, 2006.

[116] Autodesk, “Autodesk Inventor: 3D modeling software for designers and engineers,” [Online]. Available: https://www.autodesk.com/sg/products/inventor/overview. [Accessed 27 June 2022].

[117] T. Snyder and M. Braun, “Comparison of Perturbed Reynolds Equation and CFD Models for the Prediction of Dynamic Coefficients of Sliding Bearings,” *Lubricants,* vol. 6, no. 1, p. 5, 2018.

DOI: 10.3390/lubricants6010005

[118] C. Greenshields, “5.3 Mesh generation with the blockMesh utility,” CFD Direct, 12 July 2022. [Online]. Available: https://doc.cfd.direct/openfoam/user-guide-v10/blockmesh. [Accessed 9 November 2022].

[119] C. Greenshields, “OpenFOAM v10 User Guide - 5.4 Mesh generation with the snappyHexMesh utility,” CFD Direct, 12 July 2022. [Online]. Available: https://doc.cfd.direct/openfoam/user-guide-v10/snappyhexmesh. [Accessed 9 November 2022].

[120] M. S. O'Regan, P. C. Griffin and T. M. Young, “Numerical and experimental investigation of the mean and turbulent characteristics of a wing-tip vortex in the near field,” *Journal of Aerospace Engineering,* vol. 228, no. 13, pp. 2516-2529, 2014.

DOI: 10.1177/0954410013519598

[121] N. Kasmai, D. Thompson, E. Luke, M. Jankun-Kelly and R. Machiraju, “Feature-based adaptive mesh refinement for wingtip vortices,” *International Journal for Numerical Methods in Fluids,* vol. 66, pp. 1274-1294, 2011.

DOI: 10.1002/fld.2312

[122] O. Lehmkuhl, U. Piomelli and G. Houzeaux, “On the extension of the interal length-scale approximation model to complex geometries,” *International Journal of Heat and Fluid Flows,* vol. 78, pp. 1-12, 2019.

DOI: 10.1016/j.ijheatfluidflow.2019.108422

[123] M. S. Salim, M. Ariff and S. C. Cheah, “Wall y+ approach for dealing with turbulent flows over a wall mounted cube,” *Progress in Computational Fluid Dynamics, an International Journal,* vol. 10, no. 5-6, pp. 341-351, 2010.

DOI: 10.1504/PCFD.2010.035368

[124] C. Greenshields, “OpenFOAM v10 User Guide - 3.6 Standard utilities,” CFD Direct, 12 July 2022. [Online]. Available: https://doc.cfd.direct/openfoam/user-guide-v10/standard-solvers. [Accessed 9 November 2022].

[125] J. D. Anderson, G. Degrez, E. Dick and R. Grundmann, Computational fluid dynamics: an introduction, Springer Science & Business Media, 2013.

[126] H. K. Versteeg, An introduction to computational fluid dynamics: the finite volume method, 2nd edition, Pearson Education India, 2007.

DOI: 10.1007/978-3-642-14767-8

[127] A. Dewan, Tackling Turbulent Flows in Engineering, New Delhi: Springer, 2011.

[128] P. R. Spalart and S. R. Allmaras, “A one-equation turbulence model for aerodynamic flows,” *30th aerospace sciences meeting and exhibit,* p. 439, 1992.

DOI: 10.2514/6.1992-439

[129] P. R. Spalart, “Turbulence modeling for CFD,” *International Journal of Heat and Fluid Flow,* vol. 21, pp. 252-263, 2000.

DOI: 10.1016/S0142-727X(00)00007-2

[130] C. L. Rumsey and P. R. Spalart, “Turbulence model behavior in low Reynolds number regoins of aerodynamic flowfields,” *AIAA Journal,* vol. 47, no. 4, pp. 982-993, 2009.

DOI: 10.2514/1.39947

[131] X. Tan, W. Chen, G. Wu and J. Yang, “Study of airflow in a cold-region tunnel using a standard k-ε turbulence model and air-rock heat transfer characteristics: validation of the CFD results,” *Heat Mass Transfer,* vol. 49, pp. 327-336, 2013.

DOI: 10.1007/s00231-012-1081-z

[132] D. M. Hargreaves and N. G. Wright, “On the use of the k–ε model in commercial CFD software to model the neutral atmospheric boundary layer,” *Journal of Wind Energy,* vol. 95, pp. 355-369, 2007.

DOI: 10.1016/j.jweia.2006.08.002

[133] B. Aupoix and P. R. Spalart, “Extensions of the Spalart–Allmaras turbulence model to account for wall roughness,” *International Journal of Heat and Fluid Flow,* vol. 24, pp. 454-462, 2003.

DOI: 10.1016/S0142-727X(03)00043-2

[134] F. R. Menter, “Zonal two equation k-ω turbulence models for aerodynamics flows,” in *24th Fluid Dynamics Conference*, Orlando, 1993.

DOI: 10.2514/6.1993-2906

[135] F. R. Menter, M. Kuntz and R. Langtry, “Ten years of industrial experience with the SST turbulence model,” *Turbulence, heat and mass transfer,* vol. 4, no. 1, pp. 625-632, 2003.

DOI: 10.2514/3.12149

[136] A. J. Menter, “Two-equation eddy-viscosity turbulence models for engineering applications,” *AIAA Journal,* vol. 32, no. 8, pp. 1598-1605, 1994.

[137] R. Lohner, “On limiters for minimal vorticity dissipation,” in *47th AIAA Aerospace Sciences Meeting Including The New Horizons Forum and Aerospace Exposition*, Orlando, 2009.

[138] S. Ragab and M. Sreedhar, “Numerical simulation of vortices with axial velocity deficits,” *Physics of Fluids,* vol. 1, no. 3, pp. 549-558, 1995.

DOI: 10.1063/1.868582

[139] D. Kolomenskiy, R. Paoli and J.-F. Boussuge, “Hybrid RANS-LES simulation of wingtip vortex dynamics,” in *Proceedings of the ASME 2014 4th Joint US-European Fluids Engineering Division Summer Meeting* , Chicago, 2014.

DOI: 10.1115/FEDSM2014-21349

[140] K.-S. Yang and J. H. Ferziger, “Large-Eddy Simulation of Turbulent Obstacle Flow Using a Dynamic Subgrid-Scale Model,” *AIAA Journal,* vol. 31, no. 8, pp. 1406-1413, 1993.

DOI: 10.2514/3.49081

[141] P. Sagaut, Large eddy simulation for incompressible flows, Berlin, Heidelberg: Springer Berlin Heidelberg, 2006.

[142] J. Smagorinsky, “General circulation experiments with the primitive equations,” *Monthly Weather Review,* vol. 91, no. 3, pp. 99-164, 1963.

DOI: 10.1175/1520-0493(1963)091<0099:GCEWTP>2.3.CO;2

[143] N. D. Katopodes, “Turbulent Flow,” in *Free-Surface Flow: Environmental Fluid Mechanics*, Butterworth-Heinemann, 2018, pp. 567-650.

DOI: 10.1201/9781003323037

[144] F. Rezaei, E. Roohi and M. Pasandideh-Fard, “Stall simulation of flow around an airfoil using LES model and comparison of RANS models at low angles of attack,” in *15th Conference On Fluid Dynamics*, Bandar Abbas, Iran, 2013.

[145] D. Carati, G. S. Winckelmans and H. Jeanmart, “On the modelling of the subgrid-scale and filtered-scale stress tensors in large-eddy simulation,” *Journal of Fluid Mechanics,* vol. 441, pp. 119-138, 2001.

DOI: 10.1017/S0022112001004773

[146] T. A. Smith and Y. Ventikos, “Wing-tip vortex dynamics at moderate Reynolds numbers,” *Physics of Fluids,* vol. 33, no. 3, 2021.

DOI: 10.1063/5.0039492

[147] D. H. Thompson, “Experimental study of axial flow in wing tip vortices,” *Journal of Aircraft,* vol. 12, no. 11, pp. 910-911, 1975.

DOI: 10.2514/3.44500

[148] S. Martínez-Aranda, A. L. García-González, L. Parras, J. F. Velázquez-Navarro and C. del Pino, “Comparison of the Aerodynamic Characteristics of the NACA0012 Airfoil at Low-to-Moderate Reynolds Numbers for any Aspect Ratio,” *International Journal of Aerospace Sciences,* vol. 4, no. 1, pp. 1-8, 2016.

DOI: 10.5923/j.aerospace.20160401.01

[149] J. C. Chan, H. Hesse and P. C. Wang, “LES validation on near-field wingtip vortex evolution with wind tunnel characterization at low Reynolds number,” *Journal of Aerospace Science and Technology,* vol. 157, 2025.

DOI: 10.1016/j.ast.2024.109789

[150] D. -F. Feder, M. Dhone, N. Kornev and M. Abdel-Maksoud, “Comparison of different approaches tracking a wing-tip vortex,” *Ocean Engineering,* vol. 147, pp. 659-675, 2018. DOI: 10.1016/j.oceaneng.2017.09.036

[151] S. N. Skinner, R. B. Green and H. Zare-Behtash, “Wingtip vortex structure in the near-field of swept-tapered wings,” *Physics of Fluids,* vol. 32, no. 9, 2020.

DOI: 10.1063/5.0016353

[152] S. Merryisha and P. Rajendran, “Review of Winglets on Tip Vortex, Drag and Airfoil Geometry,” *Journal of Advanced Research in Fluid Mechanics and Thermal Sciences,* vol. 63, no. 2, pp. 218-237, 2019.

[153] G. Narayan and B. John, “Effect of winglets induced tip vortex structure on the performance of subsonic wings,” *Aerospace Science and Technology,* vol. 58, pp. 328-340, 2016.
DOI: 10.1016/j.ast.2016.08.031

[154] M. J. Bhagwat and J. G. Leishman, “Generalized viscous vortex model for application to free-vortex wake and aeroacoustic calculations,” *Annual forum proceedings - American helicopter society, Inc,* vol. 58, no. 2, pp. 2042-2057, 2002.

[155] H. B. Squire, “The Growth of a Vortex In Turbulent Flow,” *Aeronautical Quarterly,* vol. 16, no. 3, pp. 302-306, 1965.
DOI: 10.1017/S0001925900003516

[156] K. Fukami, K. Fukagata and K. Taira, “Super-resolution reconstruction of turbulent flows with machine learning,” *Journal of Fluid Mechanics,* vol. 870, pp. 106-120, 2019.
DOI:10.1017/jfm.2019.238

[157] K. Fukami, K. Fukagata and K. Taira, “Machine-learning-based spatio-temporal super resolution reconstruction of turbulent flows,” *Journal of Fluid Mechanics,* vol. 909, p. A9, 2021.
DOI:10.1017/jfm.2020.948

[158] M. Z. Yousif, L. Yu and H. Lim, “Physics-guided deep learning for generating turbulent inflow conditions,” *Journal of Fluid Mechanics,* vol. 936, p. A21, 2022.
DOI:10.1017/jfm.2022.61

[159] D. Kim and J. Lee, “A Review of Physics Informed Neural Networks for Multiscale Analysis and Inverse Problems,” *Multiscale Science and Engineering,* vol. 6, no. 1, pp. 1-11, 2024.
DOI: 10.1007/s42493-024-00106-w

[160] K. Kondo, S. Murakami and A. Mochida, “Generation of velocity fluctuations for inflow boundary condition of LES,” *Journal of Wind Engineering and Industrial Aerodynamics,* vol. 67&68, pp. 51-64, 1997.
DOI: 10.1016/S0167-6105(97)00062-7

[161] C. D. Pierce and P. Moin, “Method for Generating Equilibrium Swirling Inflow Conditions,” *AIAA Journal,* vol. 36, no. 7, pp. 1325-1327, 1998.
DOI: 10.2514/2.518

[162] J. C. Chan, P. C. Wang, J. J. Y. Tan and H. Hesse, “Characterization of LES Inlet Conditions with Mapped Wingtip Vortices using UVLM Mean Flow Field Data,” in *Twelfth*

International Conference on Computational Fluid Dynamics (ICCFD12), Kobe, Japan, 2024.

[163] H. Liu, I. Hayat, Y. Jin and L. P. Chamorro, "On the Evolution of the Integral Time Scale within Wind Farms," *Energies,* vol. 11, no. 93, 2018.
DOI: 10.3390/en11010093

[164] D. Tafti, "Comparison of some upwind-biased high-order formulations with a second-order central-difference scheme for time integration of the incompressible Navier-Stokes equations," *Computers & fluids,* vol. 25, no. 7, pp. 647-665, 1996.
DOI: 10.1016/0045-7930(96)00015-1

[165] M. Wang and P. Moin, "Computation of Trailing-Edge Flow and Noise Using Large-Eddy Simulation," *AIAA Journal,* vol. 38, no. 12, pp. 2201-2209, 2000.
DOI: 10.2514/2.895

[166] X. Wu, "Inflow Turbulence Generation Methods," *Annual Review of Fluid Mechanics,* vol. 49, pp. 23-49, 2017.
DOI: 10.1146/annurev-fluid-010816-060322

[167] R. G. Deissler, "Turbulent Fluid Motion V-Fourier Analysis, the Spectral Form of the Continuum Equations, and Homogeneous Turbulence," NASA Lewis Research Center, Cleveland, Ohio, 1996.

[168] D. J. Garmann and M. R. Visbal, "Unsteady Evolution of the Tip Vortex on a Stationary and Oscillating NACA0012 Wing," in *54th AIAA Aerospace Sciences Meeting*, San Diego, California, 2016.
DOI: 10.2514/6.2016-0328

[169] D. J. Garmann and M. R. Visbal, "Analysis of Tip Vortex Near-Wake Evolution for Stationary and Oscillating Wings," *AIAA Journal,* vol. 55, no. 8, pp. 2686-2702, 2017.
DOI: 10.2514/1.J055574

[170] F. Mathey, D. Cokljat, J. P. Bertoglio and E. Sergent, "Assessment of the vortex method for Large Eddy Simulation inlet conditions," *Progress in Computational Fluid Dynamics,* vol. 6, no. 1/2/3, pp. 58-67, 2006.
DOI: 10.1504/PCFD.2006.009483

[171] L. Guo, D. Li, Zhang Xing and G.-W. He, "LES prediction of space-time correlations in turbulent shear flows," *Acta Mechanica Sinica,* vol. 28, no. 4, pp. 993-998, 2012.
DOI: 10.1007/s10409-012-0088-5

[172] G. H. Vatistas, G. D. Panagiotakakos and F. I. Manikis, “Extension of the n-Vortex Model to Approximate the Effects of Turbulence,” *Journal of Aircraft,* vol. 52, no. 5, pp. 1721-1725, 2015.

DOI: 10.2514/1.C033238

[173] L. J. Lukassen, R. J. A. M. Stevens, C. Meneveau and M. Wilczek, “Modeling space-time correlations of velocity fluctuations in wind farms,” *Wind energy,* vol. 21, no. 7, pp. 474-487, 2018.

DOI: 10.1002/we.2172

[174] M. R. Cholemari and J. H. Arakeri, “A model relating Eulerian spatial and temporal velocity correlations,” *Journal of Fluid Mechanics,* vol. 551, pp. 19-29, 2006.

DOI: 10.1017/S0022112005008074

[175] H. Takahashi, H. Oso, T. Kouchi, G. Masuya and M. Hirota, “Scalar Spatial Correlations in a Supersonic Mixing Flowfield,” *AIAA Journal,* vol. 48, no. 2, pp. 443-452, 2010.

DOI: 10.2514/1.44684

[176] R. B. Davis, “Spatial Correlation Function of Cylinders in Diffuse Acoustic Fields,” *AIAA Journal,* vol. 55, no. 11, pp. 4005-4010, 2017.

DOI: 10.2514/1.J055805

[177] The SciPy community, “scipy.optimize.curve_fit,” SciPy, [Online]. Available: https://docs.scipy.org/doc/scipy-1.15.2/reference/generated/scipy.optimize.curve_fit.html. [Accessed 03 December 2025].

[178] A. Shekarriz, T. C. Fu and J. Katz, “Near-field behavior of a tip vortex,” *AIAA Journal,* vol. 31, no. 1, 1993.

DOI: 10.2514/3.11326

[179] M. Munk, The minimum induced drag of Aerofoils, Technical Report Archive & Image Library, 1923.

[180] D. Hummel, “Aerodynamic aspects of formation flight in birds,” *Journal of Theoretical Biology,* vol. 104, no. 3, pp. 321-347, 1983.

DOI: 10.1016/0022-5193(83)90110-8

[181] R. Vinuesa and S. L. Brunton, “Emerging Trends in Machine Learning for Computational Fluid Dynamics,” *IEEE Computing in Science & Engineering,* vol. 24, no. 5, pp. 33-41, 2022.

DOI: 10.1109/MCSE.2023.3264340

[182] K. Fukami, K. Fukagata and K. Taira, “Machine-learning-based spatio-temporal super resolution reconstruction of turbulent flows,” *Journal of Fluid Mechanics,* vol. 909, no. A9, 2021.

DOI: 10.1017/jfm.2020.948

[183] L. Guastoni, A. Güemes, A. Ianiro, S. Discetti, P. Schlatter, H. Azizpour and R. Vinuesa, “Convolutional-network models to predict wall-bounded turbulence from wall quantities,” *Journal of Fluid Mechanics,* vol. 928, no. A27, 2021.

DOI: 10.1017/jfm.2021.812

[184] S. G. Voutsinas, “Vortex methods in aeronautics: how to make things work,” *International Journal of Computational Fluid Dynamics,* vol. 20, no. 1, pp. 3-18, 2006.

DOI: 10.1080/10618560600566059

[185] C. Mimeau and I. Mortazavi, “A Review of Vortex Methods and Their Applications: From Creation to Recent Advances,” *Fluid,* vol. 6, no. 2, p. 68, 2021.

DOI: 10.3390/fluids6020068

[186] G. Winckelmans, R. Cocle, L. Dufresne and R. Capart, “Vortex methods and their application to trailing wake vortex simulations,” *Comptes Rendus Physique,* vol. 6, no. 4-5, pp. 467-486, 2005.

DOI: 10.1016/j.crhy.2005.05.001

[187] M. Parenteau, E. Laurendeau, F. Plante and M. Costes, “Unsteady Coupling Algorithm for Lifting-Line Methods,” in *55th AIAA Aerospace Sciences Meeting*, Grapevine, Texas, 2017.

DOI: 10.2514/6.2017-0951

[188] A. del Carre, A. Muñoz-Simón, N. Goizuera and R. Palacios, “SHARPy: A dynamic aeroelastic simulation toolbox for,” *Journal of Open Source Software,* vol. 4, no. 44, p. 1885, 2019.

DOI: 10.21105/joss.01885

[189] S. Düssler and R. Palacios, “Enhanced Unsteady Vortex Lattice Aerodynamics for Nonlinear Flexible Aircraft Dynamic Simulation,” *AIAA Journal,* vol. 62, no. 3, pp. 1179-1194, 2024.

DOI: 10.2514/1.J063174

[190] J. Murua, R. Palacios and J. M. R. Graham, “Assessment of Wake-Tail Interference Effects on the Dynamics of Flexible Aircraft,” *AIAA Journal,* vol. 50, no. 7, pp. 1575-1585, 2012.

DOI: 10.2514/1.J051543

[191] S. Deng, C. Jiang, Y. Wang and H. Wang, "Acceleration of unsteady vortex lattice method via dipole panel fast multipole method," *Chinese Journal of Aeronautics,* vol. 34, no. 2, pp. 265-278, 2021.

DOI: 10.1016/j.cja.2020.06.029

[192] G. K. Batchelor, "An introduction to fluid dynamics," *Cambridge University Press,* 2000.

[193] S. Gudmundsson, "Chapter 9 - The Anatomy of the Wing," in *General aviation aircraft design: Applied Methods and Procedures*, Butterworth-Heinemann, 2014, pp. 299-399.

DOI: 10.1016/B978-0-12-397308-5.00014-3

[194] M. Xu, H. Cheng, B. Ji and X. Peng, "Prediction method of tip vortex circulation based on hydrofoil load," *Ocean Engineering,* vol. 288, p. 116176, 2023.

DOI: 10.1016/j.oceaneng.2023.116176

[195] A. Perez, O. Lopez, S. Poroseva and J. Escobar, "Computational Study of a Small Rotor at Hover Using CFD and UVLM," in *AIAA Scitech Forum*, San Diego, 2019.

DOI: 10.2514/6.2019-0597